

Hafnium dioxide for memristive applications

DISSERTATION

FOR THE DEGREE OF DOCTOR OF ENGINEERING (DR.-ING.)



SUBMITTED TO THE FACULTY OF ELECTRICAL AND INFORMATION
ENGINEERING OF KIEL UNIVERSITY

By

Richard Volker Marquardt

Kiel University

2024

Examiners of the dissertation

Prof. Dr. Hermann Kohlstedt (Supervisor)

Prof. Dr. Holger Kersten

Prof. Dr. Nagarajan Valanoor

Examination committee of the disputation (February 14, 2024)

Prof. Dr. Rainer Adelung (Chairman)

Prof. Dr. Hermann Kohlstedt (Supervisor)

Prof. Dr. Holger Kersten

Prof. Dr. Jan Steinkühler

Abstract

The ever-increasing energy demand of modern society, further reinforced by emerging technologies such as artificial intelligence, presents us with a significant challenge. The shift from digital to analog data processing, inspired by neural structures, fits with the analog data provided by the environment. However, simulating or emulating the existing digital technology is enormously energy-hungry and is far surpassed in terms of efficiency in processing data by the brain working in parallel. A solution to this energy dilemma is given by neuromorphic engineering, which has as its objective the construction of an electrical equivalent of different brain and nerve branches, which, like the biological model, should enable analog and parallel data processing utilizing oscillating spikes. This technology has the potential to be several orders of magnitude more energy efficient than existing digital Complementary Metal Oxide Semiconductor (CMOS) technology depending on the task at hand and the data available. While CMOS technology dominates in algebraic tasks, it is outperformed by its neuromorphic competitor in pattern recognition. The coexistence of these two technologies with interwoven structures for the most efficient processing of the whole task spectrum is therefore most likely for future systems. Material integration of neuromorphic components is a non-negligible task due to the high requirements of the CMOS technology manufacturing process.

Hafnium dioxide (HfO_2), seems to be a candidate worth discussing due to its compatibility with existing technologies and its versatile electrical properties. In addition, it is considered to be an already well-researched material due to its decades-long application in nuclear technology, power electronics as well as CMOS technology. This work deals with comprehensive analyses of the electrical properties of HfO_2 concerning an application as a memristive device, which together with the oscillator, are considered one of the two basic elementary building blocks.

After an introduction to the fundamentals relevant to the analyses, the first three publications cover the recently discovered ferroelectric properties of HfO_2 and the superconducting properties of niobium nitride electrodes. Ferroelectric films, which, as is the case with HfO_2 , have a scalability down to the single-digit nanometer range, have versatile applications and high potential in both digital and analog technologies. A particular focus of the investigations is on the training effect known from other ferroelectric films, which is particularly strong for HfO_2 , as well as the domain wall behavior and ultimately the compatible deposition of superconducting electrodes and ferroelectric thin films. As cause for the ferroelectric training effect a ferroelastic 90° domain switching of $[110]$ oriented grains can be found. A Rayleigh

analysis reveals that the domain wall behavior can be characterized into four different modes including their transitions.

In the two following publications, the memristive behavior and the underlying structure of HfO_2 , which are already integrated into a fully functional memristive device, are investigated. In the course of the analysis, it is shown that memristive switching is enabled by a manipulation of a space charge region due to the charging and discharging of electron traps in the HfO_2 layer. Double positively charged oxygen defects with two different effective cross sections can be defined as necessary defects for the memristive effect in this system.

The results shown in this work provide profound information on the application of HfO_2 in memory elements, which is particularly useful with respect to its application in neural networks and thus in the transition from digital to analog technology.

German Abstract

Der stets wachsende Energiebedarf der modernen Gesellschaft, welcher durch aufstrebende Technologien wie künstliche Intelligenzen zusätzlich bestärkt wird, stellt uns vor eine wesentliche Herausforderung. Der Wechsel von der digitalen hin zur analogen Datenverarbeitung, welche durch neuronale Strukturen inspiriert ist, scheint in Anbetracht der aus der Umwelt bereitgestellten analogen Daten mehr als sinnvoll zu sein. Jedoch ist das Simulieren beziehungsweise Emulieren auf der bestehenden digitalen Technologie enorm energieaufwändig und wird in Bezug auf die Effizienz in der Verarbeitung von Daten durch das parallel arbeitende Gehirn bei Weitem übertroffen. Eine Lösung dieses Energiedilemmas verspricht das Neuromorphe Engineering, welches als Zielsetzung den Aufbau eines elektrischen Äquivalents von verschiedenen Hirn- und Nervenarealen hat, welche gleich dem biologischen Vorbild eine analoge und parallele Datenverarbeitung anhand von oszillierenden Spikes ermöglichen soll. Diese Technologie hat das Potenzial um mehrere Größenordnungen energiesparsamer, als die bisher bestehende digitale Siliziumtechnologie abhängig von der gestellten Aufgabe und den zur Verfügung stehenden Daten, zu sein. Während bei algebraischen Aufgaben die Siliziumtechnologie dominiert, wird sie im Bereich der Mustererkennung klar von ihrem neuromorphen Konkurrenten übertroffen. Eine Koexistenz dieser beiden Technologien mit ineinander verwobenen Strukturen für eine möglichst effiziente Bearbeitung des gesamten Aufgabenspektrums ist daher für zukünftige Systeme sehr wahrscheinlich. Eine Materialintegration von neuromorphen Komponenten ist aufgrund hoher Anforderungen des Herstel-

lungsprozesses der Siliziumtechnologie eine nicht zu vernachlässigende Aufgabe.

Hafniumdioxid (HfO_2) scheint aufgrund seiner Kompatibilität mit bestehenden Technologien sowie seiner vielseitigen elektrischen Eigenschaften ein vielversprechender Kandidat. Zusätzlich gilt es durch seine jahrzehntelange Anwendung in der Kerntechnik, Leistungselektronik und Siliziumtechnologie als bereits gut erforschtes Material. Diese Arbeit behandelt umfassende Analysen der elektrischen Eigenschaften von HfO_2 in Bezug auf eine Anwendung als memristives Bauteil, welches zusammen mit dem Oszillator als einer der beiden elementaren Grundbausteine gilt. Nach einer Einführung in die für die Analysen relevanten Grundlagen behandeln die ersten drei Publikationen die kürzlich entdeckten ferroelektrischen Eigenschaften von HfO_2 sowie die supraleitenden Eigenschaften der Niobiumnitrid Elektroden. Ferroelektrische Schichten, welche, wie es bei HfO_2 der Fall ist, eine Skalierbarkeit bis in den einstelligen Nanometerbereich besitzen, haben sowohl in der digitalen als auch analogen Technologie vielseitige Anwendungsmöglichkeiten und hohes Potenzial. Ein besonderes Augenmerk der Untersuchungen liegt auf dem durch andere ferroelektrische Schichten bekannten Trainingseffekt, welcher bei HfO_2 , besonders stark auftritt, sowie auf dem Domänenwandverhalten und letztlich der kompatiblen Abscheidung von supraleitenden Elektroden und ferroelektrischen Dünnschichten. Während für das ferroelektrische Training Hinweise auf ein ferroelastisches 90° Domänenschalten von $[110]$ orientierten Körnern als Ursache gefunden werden können, kann das Verhalten der Domänenwände in vier verschiedene Modi inklusive deren Übergänge charakterisiert werden.

In den zwei folgenden Publikationen wird das memristive Verhalten sowie dessen zugrundeliegende Struktur von HfO_2 , welches bereits in einem vollfunktionsfähigen memristiven Bauteil integriert ist, untersucht. Im Zuge der Analyse zeigt sich, dass das memristive Schalten durch eine Manipulation einer Raumladungszone, welche durch das Laden und Entladen von Elektronen-Fallen in der HfO_2 Schicht ermöglicht wird. Doppelt positiv geladenen Sauerstofffehlstellen mit zwei unterschiedlichen Wirkungsquerschnitten können in diesem System als notwendige Defekte für den memristiven Effekt definiert werden.

Die in dieser Arbeit gezeigten Ergebnisse geben tiefgreifende Informationen zur Anwendung von HfO_2 in Speicherelementen, welche besonders im Hinblick auf die Anwendung in neuronalen Netzen und somit im Wandel von der digitalen zur analogen Technik von großem Nutzen sind.

Acknowledgement

I want to thank:

- Hermann Kohlstedt for his mentoring, support, encouragement, and patience in all aspects of the past years
- The Chair of Nanoelectronics for a family-like environment, entertaining lunch discussions, and fun team activities
- Jürgen Carstensen and George Popkirov for stimulating discussions as well as for their advice and support in collecting and analyzing data
- Finn Zahari and Rouven Lamprecht for conversations and jokes that made working together even more pleasant
- Adrian Petraru and Christoph Ochmann for their practical help in various projects
- Ole Gronenberg for his effort during the TEM investigations as well as his shared insights on this topic
- Johannes Marquardt for opening up new perspectives on scientific topics for me and his advice on correct scientific practice
- My Family for all the encouragement and understanding that I could have ever wished for
- The Deutsche Forschungsgemeinschaft (DFG, German Research Foundation) for funding the research projects — Project number RU 2093 and Project-ID 434434223—SFB 1461

Contents

Preamble

Introduction	14
Neuromorphic computing	17
2.1 Biological model	17
2.1.1 Neuron	18
2.1.2 Synapse	19
2.2 Memristive devices	20
Hafnium dioxide	25
3.1 Ferroelectricity in Hafnium dioxid (HfO_2)	25
3.2 Charge trapping in HfO_2	30
Fabrication process	33
4.1 Sputtering	33
4.2 Rapid Thermal Processing	36
Analytics	38
5.1 Impedance spectroscopy	38
5.1.1 Fundamental Principles	38
5.1.2 Frequency Dispersion	39
5.1.3 Equivalent Circuit Elements	41
5.2 Plasma Measurements	45
5.3 X-ray diffraction Measurements	45
5.4 Transmission Electron Microscopy	46
5.4.1 Electron Energy-loss Spectroscopy	47
5.5 X-ray Photoelectron Spectroscopy	48
Brief combined summary of the Publications	50
Conclusions	54
Outlook and future work	56

Publications

The impact of rapid thermal annealing for the ferroelectricity of HfO_2 ...	71
Correlation between sputtered niobium nitride films and plasma parameters ...	85
Domain Wall Movement in Undoped Ferroelectric HfO_2 ...	98
Trap-Assisted Memristive Switching in HfO_2 -Based Devices ...	110
Impedance Spectroscopy on Hafnium Oxide-Based Memristive Devices ...	129

Appendix

Complete list of publications	147
Eidesstattliche Erklärung	149

List of Figures

1.1	Trends in training computed by floating point operations (FLOPs) of 102 milestone systems between 2010 and 2022 on a semilogarithmic scale. The trend in the remaining models stayed the same before and after 2016. Adapted from Sevilla et al.[Sev+22], the unnamed data points can be looked up in the source.	15
2.1	Sketch of a neuron including an enlarged sketch of a synapse and the illustration of a single action potential, a spike. [BK22]	18
2.2	Five different Principles of resistive switching in memristive devices for neuromorphic computing with their on- and off-states. Three of these principles namely Electrochemical Metallization (ECM), Valence Change Mechanism (VCM) and Electrostatic/Electronic Effect Mechanism (EEM) have already been implemented using HfO ₂ as active memristive layer [Wei+15; Cüp+19; Mar+23; Zah+23].	22
2.3	Four different Electrostatic/Electronic Effects Mechanisms for resistive switching. The two left principles are based on the charging and discharging of electron traps, while the two right principles use the polarizability of ferroelectric layers to change their resistive state.	23
3.1	Phase diagram of bulk HfO ₂ accompanied by the schematic structures of the unit cells of various polymorphs. The ferroelectric <i>Pca</i> 2 ₁ phase cannot be a stable phase for any temperature and pressure in bulk HfO ₂ , whereas ferroelectricity can be induced in doped HfO ₂ or Hf _{1-x} Zr _x O ₂ films deposited by various techniques. There are two different kinds of <i>Pbca</i> orthorhombic phases: anti-polar and nonpolar, which should be carefully distinguished [Sch+22a]. Reproduced with permission from Springer Nature.	26

3.2	Polar orthorhombic $Pca2_1$ phase with down polarization (left) and up polarization (right). Reprinted from [MKK15], with the permission of AIP Publishing.	29
3.3	Electronic energy levels (Kohn–Sham states) in the band gap of m-HfO ₂ for oxygen vacancies in different charge states: (a) calculated for c-HfO ₂ in Ref. [Xio+05] with respect to the band edges of Si; (b) for four-coordinated oxygen vacancy from Ref. [Gav+06]; (c) for three- and four-coordinated oxygen vacancy from Ref. [BP06]. Reprinted from [GPI16], with permission from Elsevier.	31
4.1	Thornton diagram illustrating the nanostructures of thin films prepared by sputtering at different argon pressures and substrate temperatures. Reprinted from [Tho77], with the permission of Annual Reviews, Inc.	34
4.2	IR camera images taken at one-second intervals shortly after an Rapid Thermal Processing (RTP) in the self-built oven. . .	36
5.1	I) A physical system with multiple connected centers of mass is excited by a perturbation $F(t)$ and gives a response $R(t)$. II) A physical system filled with a fluid that dampens the perturbation. III) A combination of I) and II).	39
5.2	Measurement routine for the characterization of a physical system using Impedance Spectroscopy (ImpSpec) (adapted from Barsoukov and Macdonald)[BM05].	40

List of Abbreviations

DNN	Deep Neural Networks
SNN	Spiking Neural Networks
CMOS	Complementary Metal Oxide Semiconductor
HfO₂	Hafnium dioxid
SiO₂	Silicon dioxid
TiN	Titanium nitrid
NbN	Niobium nitrid
Al₂O₃	Aluminium oxid
PCM	Phase Change Mechanism
TCM	Thermochemical Mechanism
CF	Conductive Filament
ECM	Electrochemical Metallization
VCM	Valence Change Mechanism
EEM	Electrostatic/Electronic Effect Mechanism
SCR	Space charge region
SCLC	Space-Charge Limitid Conduction
DW	Domain wall
VO	Oxygen Vaccancies
SZD	Thornton's structural zone diagram

RTP	Rapid Thermal Processing
CFP	Conventional Furnace Process
LP	Langmuir Probe
PTP	Passive Thermal Probe
XRD	X-ray Diffraction
PES	Photoelectron Spectroscopy
XPS	X-ray Photoelectron Spectroscopy
HAXPES	Hard X-ray Photoelectron Spectroscopy
EDS	Energy-dispersive X-ray Spectrometry
TEM	Transmission Electron Microscopy
STEM	Scanning Transmission Electron Microscopy
EELS	Electron Energy-loss Spectroscopy
ImpSpec	Impedance Spectroscopy
FFT	Fast Fourier transformation
EC	Equivalent Circuit

Preamble

"Eine Kalibrierung kann dir in die Augen schauen und trotzdem lügen." - "A calibration can look you straight in the eye and still lie to you."

George Popkirov, 2022

"Ein gutes Bauteil ist das, das Gutes tut." - "A good device is the one that does good."

Jürgen Carstensen, 2021

"Stoßgebet zum Herrn, dass das klappt..." - "Quick prayer to the Lord that this will work..."

Hermann Kohlstedt, 2020

1. Introduction

The exponential increase in data volume due to emerging Big Data technology, such as Internet of Things, Machine Learning, consume data processing in server farms, as well as the burgeoning autonomy, leads to a societal as well as governmental need for a scalable and energy-efficient information technology adapted to these complex new tasks. The hitherto existing holy grail of Complementary Metal Oxide Semiconductor (CMOS) technology seems to be no longer adapted to the new variety of challenges, such as processing unstructured data, that have developed around traditional arithmetic tasks in recent years[CSA19]. The gap in the performance of memory and processor in the traditional Van Neumann architecture will lead to an encounter with the well-known "memory wall" soon[McK04]. This circumstance is due to the physical limits of process manufacturing, which will cause a soon end of paradigms such as Moore's Law which for decades were considered the solid cornerstone of information technology[TW17; Man00].

An additional demand on the new technology, apart from coping with the data volumes, is to maintain a high level of energy efficiency in the processing of this task. While the average worldwide electrical energy demand is increasing by 3% annually, the proportion of energy consumed by digital devices each year is rising much faster at 7% [IEA21]. To put this energy hunger of modern information processing in perspective, Berkeley Lab researched the annual energy consumption of 70 billion kilowatt hours to keep the Internet running [She+16]. This energy consumption is equivalent to the total energy generated in Switzerland. In a society where there are more active mobile devices than people [Alv22], reducing the energy consumed by information processing and thus reducing emissions of climate-damaging gases is an equally important part of designing a technology that succeeds or complements CMOS technology. Machine learning systems account for an increasing share of the information processing energy consumption (Fig. 1.1), which emulates analog data processing based on the biological model of a brain.

Various approaches as alternatives or supplements to CMOS technology have been discussed in the scientific world in the last two decades. It should be noted that each of these approaches has its strengths and challenges. Be-

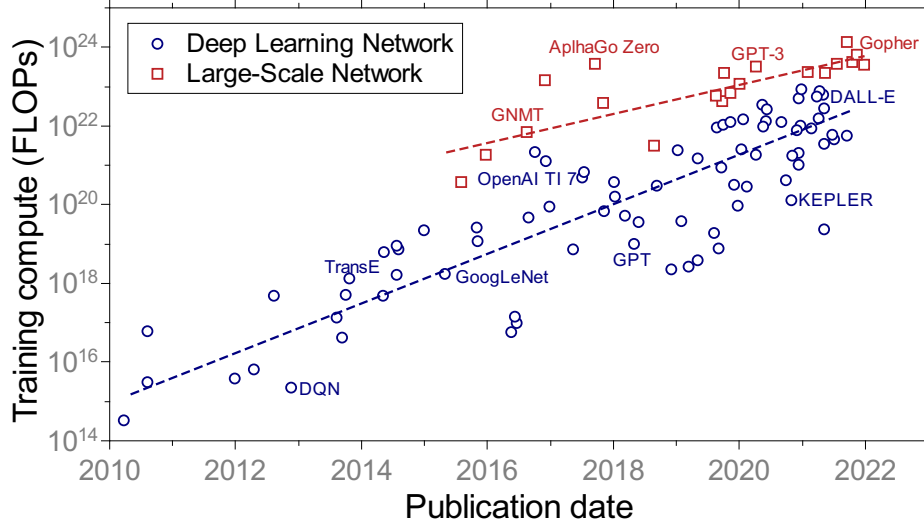


Figure 1.1: Trends in training computed by floating point operations (FLOPs) of 102 milestone systems between 2010 and 2022 on a semilogarithmic scale. The trend in the remaining models stayed the same before and after 2016. Adapted from Sevilla et al.[Sev+22], the unnamed data points can be looked up in the source.

sides Quantum computing, Neuromorphic computing is one of the main hopefuls [CGW21]. The basic idea of neuromorphic computing is constructing an architecture based on the human brain, consisting of neurons as information processing centers, which are connected by modelable synapses. The emulation of the information processing of a brain thus made possible enables robust and parallel processing of complex tasks. Especially in the area of pattern recognition, neural networks outperform conventional technology by far, especially when the energy consumption for processing the tasks is taken into account. Harnessing the biology that has been shaped by evolution for more than a billion years promises enormous potential as a complement to existing computing systems when implemented with the right technology. In addition, it is possible to produce a part of the already developed neuromorphic technologies compatible with the existing manufacturing processes of traditional CMOS technology. This makes integrating existing systems easier, and existing processes can be maintained.

A recent implementation of the neuromorphic approach is the Loihi 2 chip from IBM, which with its approximately one million neurons and 120 million synaptic connections [Orc+21], has already reached the scale of complex

beings such as a honey bee. The Loihi 2 chip is based on digital technology, which emulates analog switching. An analog modulation of the connection-weights between neurons would come closer to the biological model and promise a higher energy efficiency and fault tolerance. The basic building block for such a connection is an analog switch which is the technical equivalent of the biological synapse and is called a memristor or memristive device.

This work focuses on the operation and possibilities of the CMOS technology process compatible material HfO_2 in applying two different analog-switching memristive device concepts. The first case focuses on a memristive device utilizing a trap-assisted field effect for a change in the resistive state. Here, the HfO_2 layer acts as an active layer that modulates a space charge region by charging and discharging electron traps. For the second case, the recently discovered ferroelectric switching of HfO_2 is investigated, which promises great potential for application in memristive devices due to its scalability. The analyses focuses on ImpSpec, supported by Hard X-ray Photoelectron Spectroscopy (HAXPES) and Transmission Electron Microscopy (TEM).

2. Neuromorphic computing

The origin of neuromorphic technology is the attempt to create an information processing system based on the biological model of a hierarchical network structure of neurons and synapses [MP43]. The first efforts of an artificial reconstruction of the learning behavior of humans are attributed to Farley and Clark in the 1950s, who developed a simple artificial neural network based on the design of the perceptron, which was able to represent a self-organized learning algorithm [FC54; Ros58]. The far-reaching further development of backpropagation was added to neural network theory about 20 years later by Werbos [Wer74; Wer90] and broadened the horizon for possible applications. With the help of error backpropagation, it was possible to perform efficient supervised learning on neural networks. These digital emulations of analog processes are often computationally expensive due to the analytical mathematics of error backpropagation.

In order to meet the different requirements of complex tasks, a variety of different neural networks has already been developed based on the perceptron. These can be roughly divided into Deep Neural Networks (DNN) and Spiking Neural Networks (SNN)[WS22]. While the DNN approach is closer to existing technology and allows easy embedding into CMOS technology by a reduced representation of neurons and synapses, SNN follows an approach very close to the biological model. Through information transfer and processing which, like in the human brain are based on spikes and events, SNN assume a more energy-efficient processing[GA09].

The biological cornerstones both types of networks use are neurons and synapses. Their functions and possible artificial replicas are explained in more detail below.

2.1 Biological model

Biological nervous systems exhibit distinct characteristics in information processing. These systems are known for their highly parallel energy-efficient and adaptive architecture. Regarding pattern recognition, tolerance to failures, and cognitive tasks, even simple organisms surpass supercomputers,

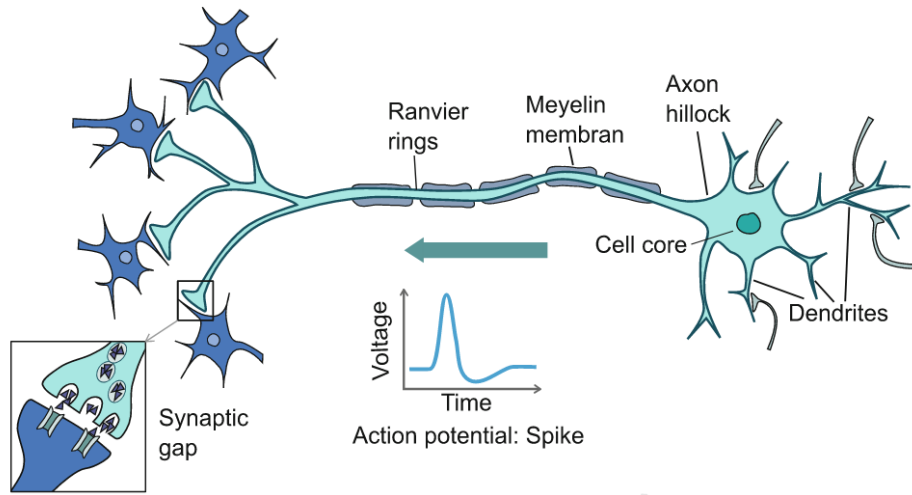


Figure 2.1: Sketch of a neuron including an enlarged sketch of a synapse and the illustration of a single action potential, a spike. [BK22]

especially in power efficiency [BK22]. The exceptional properties of these systems come from fundamental building blocks that utilize neurons as central processing units. These neurons are interconnected through synapses, forming a complex three-dimensional network called the connectome. Fig. 2.1 illustrates the structure of a neuron, including the soma, dendrites, axon, and synaptic connections with other neurons [She88].

2.1.1 Neuron

Neurons are specialized cells in the nervous system that transmit and process electrical and chemical signals, facilitating communication within the nervous system. The neuron serves as the fundamental unit of the nervous system, enabling the transmission of information between different parts of the body and facilitating various physiological and cognitive functions. The structure of a typical neuron includes the cell body (soma), dendrites, axon, and axon terminals. The cell body contains the nucleus and is responsible for essential cellular processes and signal integration. Dendrites extend from the cell body and receive incoming signals from other neurons through synapses. Axons carry electrical signals away from the cell body, while axon terminals, located at the end of the axon, contain synaptic vesicles filled with neurotransmitters. The function of a neuron involves several key processes. Neurons receive incoming signals through dendrites, which are stimulated by neurotransmitters released from neighboring neurons. The neuron inte-

grates these signals in the cell body and if the combined signals surpass a certain threshold, it generates an action potential. An action potential is an electrical signal initiated at the axon hillock, propagating along the axon. This rapid depolarization of the neuron's membrane enables the transmission of the electrical signal toward the axon terminals. A myelin sheath aids in increasing the speed of signal propagation through saltatory conduction [Smi03; Rud08].

When the action potential reaches the axon terminals, it triggers the release of neurotransmitters into the synaptic gap. These neurotransmitters diffuse across the synaptic gap and bind to receptors on the dendrites of neighboring neurons, initiating electrical signals in those neurons. This transmission process continues, allowing for the relay of information from one neuron to another [Ham01].

2.1.2 Synapse

A synapse is a specialized junction between two neurons that enables communication and signal transmission within the nervous system. Its primary function is to transmit information from a presynaptic neuron to a postsynaptic neuron through the release and reception of chemical messengers known as neurotransmitters. At a synapse signals are transmitted when an electrical impulse, called action potential, reaches the axon terminals of the presynaptic neuron. This triggers the release of neurotransmitters stored in synaptic vesicles into the synaptic gap. The neurotransmitters then diffuse across the synaptic gap and bind to receptors located on the postsynaptic neuron. This binding initiates chemical signaling in the postsynaptic neuron, leading to the generation of postsynaptic potentials. These potentials can be either excitatory, depolarizing the postsynaptic neuron and increasing the likelihood of an action potential, or inhibitory, hyperpolarizing the postsynaptic neuron and reducing the likelihood of an action potential. The postsynaptic neuron integrates the excitatory and inhibitory signals it receives from multiple synapses. If the combined signals reach the threshold for an action potential, the postsynaptic neuron generates its own action potential, propagating the signal to the next neuron [Ham01].

To ensure proper signaling, neurotransmitters in the synapse are swiftly removed. They can be taken back up into the presynaptic neuron through reuptake or broken down by enzymes in the synaptic gap. A synapse could be therefore seen as a junction that facilitates the transmission of signals from one neuron to another. It involves the release, diffusion, and binding of neurotransmitters, leading to the generation of postsynaptic potentials in the receiving neuron. This synaptic communication allows for the integration and

processing of signals, enabling the transfer of information and coordination within the nervous system [BS11].

2.2 Memristive devices

The memristive device is one of the most important units of neuromorphic networks and is as diverse as the field of application in which it is used. While the first memristor was built by H. Davy as early as 1801 [LCH14], it took several more years for the concept and potential to be properly understood. With the mathematical definition of Chua [Chu71], which was revised several years later [Chu14], and the growing interest caused by the approaching memory wall, the field gained more attention. Over the course of the last few decades, a large toolbox of the most diverse functionalities of memristive devices has accumulated, in which each is adapted to the specific criteria of the application. A uniform evaluation of the devices on the basis of defined criteria is therefore not trivial, it is more advisable to take a valuation-free view with respect to the intended field of application.

The largest number of memristive devices with two contacts and usually consisting of a metal-insulator-metal sequence can be categorized into five physical processes (Fig. 2.2). While most publications distinguish between unipolar/bipolar switching or between electronic or redox-based processes, this work focuses on the feasibility of using CMOS-compatible HfO_2 as an insulating layer.

Phase Change Mechanism

One possible physical mechanism for memristive switching is the structural change in a material, altering the resistive state. This mechanism is called Phase Change Mechanism (PCM). An often-chosen mechanism is the phase change between an amorphous (disordered state) and crystalline phase (ordered state) of chalcogenides [Xu+20]. In addition, vanadium oxide is gaining increasing interest in the field of PCM due to its low phase change temperature [LMH19; Ord+19; Dri+09]. During the operation of a memristive device, a voltage is applied across the device, causing an electric current to flow through it. This current prompts the chalcogenide material to undergo a phase change. The movement of atoms or molecules within the material leads to a change in its resistive state. Specifically, in the amorphous phase, the material exhibits higher resistance, while in the crystalline phase, it shows lower resistance. The key mechanism is the migration of ions within the material. When an electrical current passes through the device, cer-

tain ions migrate from one region to another, inducing the transformation from amorphous to crystalline or vice versa. This migration is facilitated by applying an external electric field and the heat generated by the flowing current. What’s particularly intriguing about this phase change mechanism is its non-volatile nature. Once the material transitions between phases, it maintains its new resistive state even after removing the voltage. This property enables memristive devices to function as memory elements, capable of storing information by encoding data as distinct resistance levels associated with the different phases.

Thermochemical Mechanism

The PCM and the Thermochemical Mechanism (TCM) are both considered unipolar switching types of process. However, the switching mechanisms are quite different. Switching to the on-state in the TCM is, simply stated, enabled by a dielectric breakdown of the insulator. Increasing the current flow through the insulator, usually made possible by a Poole-Frenkel effect, leads to a thermal runaway. Using the example of a metal oxide as an insulator, the thermal runaway can be described as splitting into metallic and oxide ions, which experience an opposite diffusion due to the strong temperature gradient in the surrounding insulating material. This results in forming a Conductive Filament (CF) consisting of the thermally more stable metal ions surrounded by a slightly more oxidized layer of metal oxide [IBW11; Yan+12]. The formed CF is "frozen" in the conductive state in most cases by using current compliance.

Switching back to the non-leading off-state of the device is made possible by omitting the current compliance. This allows the current to be increased above the limit used to form the CF, which is necessary to cause a partial or total breakdown of the CF by a thermally activated process. A partial breakdown leads to the reoxidation of the CF in the thinnest place, mainly in the center of the insulating layer due to its hourglass-like shape [CSA19]. The TCM assumes the formation of a switching filament, made possible by a redox-related process. High temperatures and currents are required to enable the memristive switching processes.

Electrochemical Mechanism

The switching mechanism in an ECM device is enabled by the field-driven migration of metallic cations. This requires either an active metal electrode in combination with a solid electrolyte layer through which the cations of the active electrodes can move or, alternatively, an insulator layer doped with

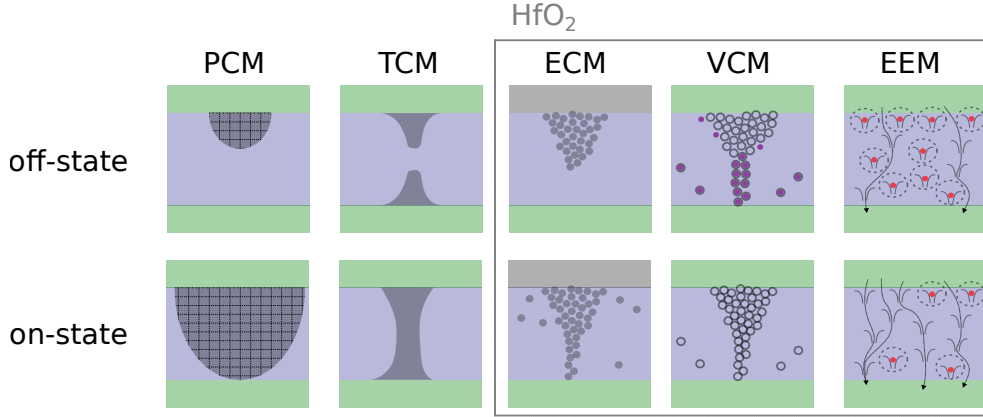


Figure 2.2: Five different Principles of resistive switching in memristive devices for neuromorphic computing with their on- and off-states. Three of these principles namely ECM, VCM and EEM have already been implemented using HfO_2 as active memristive layer [Wei+15; Cüp+19; Mar+23; Zah+23].

mobile cations. The movable cations here are often silver or copper, which are driven by a solid electrolyte often made of binary oxides such as Silicon dioxid (SiO_2) or HfO_2 [Kim+23; Wei+15; Tap+11].

In the first step of switching from the off-state to the on-state, cations are generated by oxidation of the active electrode. These migrate, driven by the applied electric field through the solid electrolyte to the inert counter electrode at whose surface they undergo reduction. There, the metal atoms accumulate in a self-reinforcing stochastic process, forming a CF between the active and inert electrodes. Applying a negative voltage dissolves the CF by reversing the redox process.

Valence Change Mechanism

In the Valence Change Mechanism (VCM), the active species are not introduced into the system by an electrochemical process as in the Electrostatic/Electronic Effect Mechanism (ECM). Instead, they are formed during the manufacturing process by the formation of defects [Kwo+10]. Therefore, knowledge about defect density and defect chemistry is essential to get a basic understanding of the switching processes. In the forming step, gas atoms, mostly oxygen or nitrogen, are moved in an insulating layer with a low migration barrier by applying an external voltage, which leads to a non-stoichiometry of the insulating material [Par+13]. This local non-stoichiometry, caused by the occupation of vacancies, influences the conduc-

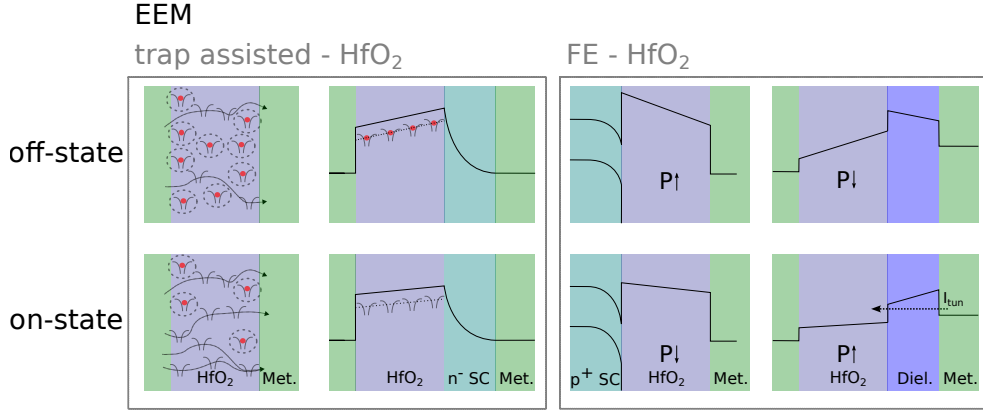


Figure 2.3: Four different Electrostatic/Electronic Effects Mechanisms for resistive switching. The two left principles are based on the charging and discharging of electron traps, while the two right principles use the polarizability of ferroelectric layers to change their resistive state.

tivity of the insulating material. In general, the switching mechanisms of the VCM are divided into two types: filamentary and interface-based [CSA19]. Like TCM, ECM, and the VCM also assume the formation of a switching filament, which is made possible by a redox-related process. In contrast to TCM, however, no high temperatures and currents are required here, but only the applied electric fields enable the memristive switching processes to be driven. In addition, the switching and switching back of ECM and VCM-based components require the application of electrical voltages in both polarities, which is why they are counted among the bipolar switching processes [Str+11].

Electrostatic/Electronic Effect Mechanism

Another resistive switching mechanism that can appear both as a binary effect and as an analog effect is the memristive Electrostatic/Electronic Effect Mechanism (EEM). This broad term covers many effects that play an essential role in this work. The two memristive effects discussed in this thesis are the Space-Charge Limited Conduction (SCLC) effect and the ferroelectric effect. In addition, a direct influence of Poole-Frenkel emission and Fowler-Nordheim tunnels by electron traps are also counted among the EEM, which are outlined in Fig. 2.3. A direct influence of the charge carrier flux dominated by either Poole-Frenkel emission or Fowler-Nordheim tunneling is carried by the change of state of electron traps located inside the bulk or at the interfaces [Sch+22b; Mai+23].

The SCLC is enabled by the presence of electron traps whose occupation

state can be changed by applying external electric voltages. The trapping and releasing of electrons in the electron traps modulate a space charge zone due to the internal field change, which influences the charge carrier flow and thus enables switching between different resistive states. The position and influence of the space charge zone can be different. On the one hand, the space charge region can form in the wide band gap semiconductor, providing a sufficient amount of electron traps that behave as dopants[Liu+08]. On the other hand, this can also happen in a semiconducting layer adjacent to the dielectric containing traps[Mar+23; Zah+23]. The second case is sketched on the left side of Fig. 2.3 and can lead to analog resistive switching in the right configuration. A detailed analysis and modeling of a memristive device based on this physical mechanism can be found in the two publications 4 and 5 of this thesis.

Kohlstedt et al. demonstrated one of the first applications of ferroelectric layers in random access memories that exhibited pinched hysteresis[Mey+04]. The memristive property is achieved by modeling a tunnel barrier adjacent to the ferroelectric layer. A change in polarity in the ferroelectric layer leads to a change in the effective path length to be tunneled for the charge carriers and thus alters the device's resistance. A sketch of the mechanism is shown on the right side of Fig. 2.3. In recent times, there has been a variety of HfO_2 -based memristive devices that have taken advantage of the mechanism shown by Kohlstedt et al.[Mik+20; Yan+23; Du+21]. Another possibility of resistive switching using ferroelectric layers is shown by Mikheev et al. by modeling a space charge region of an adjacent semiconductor by the alternating ferroelectric polarization instead of a tunnel barrier[Mik+19]. This mechanism can also be called SCLC, which is based on the polarization change of a ferroelectric instead of the field effect of electron traps. A sketch of this mechanism is also shown in Fig. 2.3. An alternative approach, in which the information is not stored in the ferroelectric domain but in the domain wall, has already been demonstrated for the ferroelectric BiFeO_3 (BFO). Here, ON-OFF ratios of about three orders of magnitude were obtained by precisely controlling the domain wall length [Sha+17].

3. Hafnium dioxide

Hafnium dioxide has already been in industrial use for several decades as a refractory insulator thanks to its high melting point and high polymorphic transformation temperature together with its low thermal conductivity (1.5 W/mK) [GK85; WLS92; MIK03]. In the early 2000s, HfO_2 was discovered as a possible replacement for amorphous SiO_2 in gate dielectric applications, which until then had been considered the gold standard [DN05]. The reason for this was the scalability of transistors, which was hindered by SiO_2 , in which the small layer thickness and the relatively low dielectric constant of SiO_2 (3.9) led to parasitic effects such as leakage currents. In the course of the search for high- k materials, HfO_2 , which was already known as a thermally stable material thanks to its high dielectric constant (16-30), was the logical choice as a replacement for SiO_2 . The newly discovered field of application of HfO_2 was followed by decades of research aimed at investigating the dielectric, mechanical, electrical, and thermal properties of HfO_2 in its application as a gate dielectric [SHF19]. Only about a decade later, two further applications for the fluorite-type oxide were discovered, in 2011 as a ferroelectric [Bös+11] and a short time later as a resistive switch for neuromorphic applications [Cov+15; Cov+16; Mat+15]. Both discoveries provide growing interest in the oxide type, which is reflected in the number of publications. In the following two subsections, the most important aspects of ferroelectricity and charge trapping in HfO_2 will be discussed.

3.1 Ferroelectricity in HfO_2

About 100 years ago, four decades after the discovery of piezoelectricity [CC80], ferroelectric behavior was discovered in Rochelle salt by J. Valasek [Val21]. The same behavior was also demonstrated in the mid-19th century in perovskite structures, which were used from then on as the basic building blocks for two essential elements of digital computing, i.e. the ferroelectric random-access memory (FeRAM) and the ferroelectric field-effect transistor (FeFET). However, a lack of compatibility with CMOS processes, together with scaling problems in the sub-100 nm range, stood in the way of in-

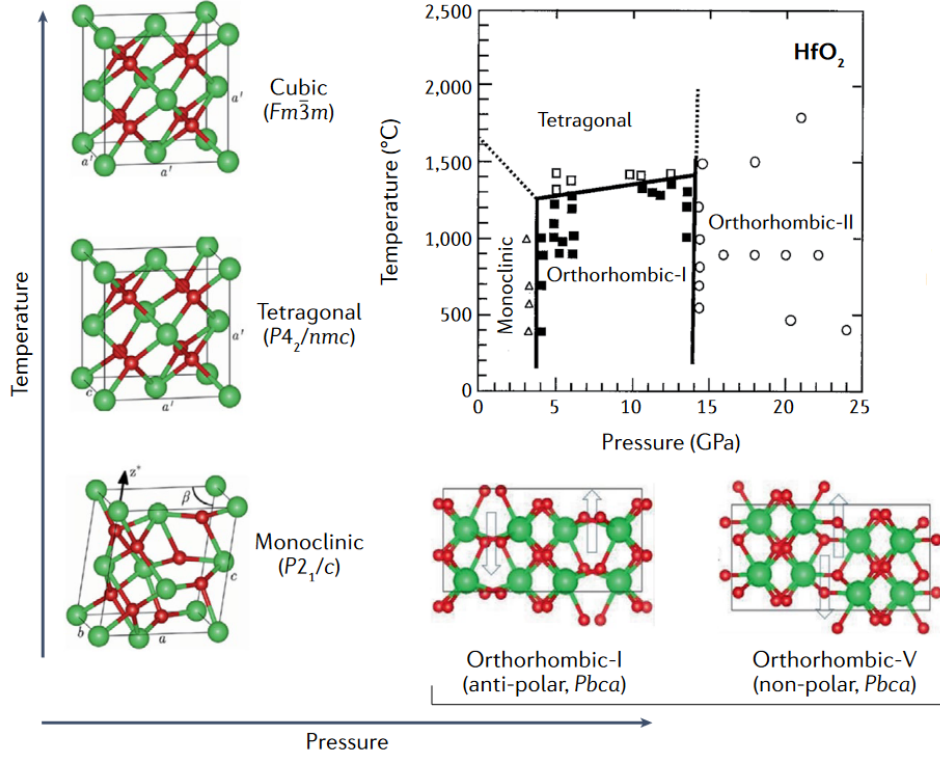


Figure 3.1: Phase diagram of bulk HfO_2 accompanied by the schematic structures of the unit cells of various polymorphs. The ferroelectric $Pca2_1$ phase cannot be a stable phase for any temperature and pressure in bulk HfO_2 , whereas ferroelectricity can be induced in doped HfO_2 or $\text{Hf}_{1-x}\text{Zr}_x\text{O}_2$ films deposited by various techniques. There are two different kinds of $Pbca$ orthorhombic phases: anti-polar and nonpolar, which should be carefully distinguished [Sch+22a]. Reproduced with permission from Springer Nature.

corporation of the perovskite-structured ferroelectric devices into integrated circuits on silicon basis [Sch+22a]. Although the scalability issues of ferroelectric perovskites have been overcome over the last couple years [Nag+04], the discovery of ferroelectricity in HfO_2 due to its CMOS compatibility has led to increased interest in the field of ferroelectric memory and process devices and expanded it to include applications such as logic-in-memory and neuromorphic computing.

The discovery by Börscke et al. is even more surprising because up to this point, it was assumed that the phase diagrams of fluorite structures, in particular HfO_2 , had already been sufficiently explored to rule out a stable polar phase [Oht+01]. As can be seen from the phase diagram in Fig. 3.1, the

stable phase of HfO_2 at room temperature is the monoclinic phase ($P2_1/c$). With a temperature feed at constant ambient pressure, a phase transformation into the tetragonal phase ($P4_2/nmc$) can take place, which begins at about 1800 K. If the pressure is increased, the transition temperature from monoclinic phase to tetragonal phase can be lowered up to a pressure of about 4 GPa. If the pressure of 4 GPa is exceeded, the antipolar orthorhombic I phase ($Pbca$), not to be confused with the non-polar orthorhombic V phase [KF21], and the orthorhombic II phase ($Pnma$) can also be stabilized at lower temperatures [Sch+22a]. Stabilization of the polar orthorhombic-III (Fig. 3.2) phase was thus not expected and the causes for the formation of this phase were unclear at the outset due to the nontrivial observability of the phase transition between the oIII phase and the t phase without forming the m phase. After a large number of studies, a confluence of several factors consisting of doping density, oxygen deficiency, surface energies, quenching rate, as well as mechanical stress and strain, was found to be the cause of this metastable phase transition. Due to the acting shear forces, together with the thermal quenching of the phase transition, this diffusionless transformation process can be described as martensitic [SHF19]. The fabrication steps and their physical significance for stabilizing the polar oIII phase are described subsequently.

During the deposition of an oxygen-defective undoped or doped HfO_2 film, an amorphous structure is assumed, which may contain small crystal seeds. The subsequent rapid heating step to a temperature above 400°C leads to a crystallization of the film, which follows the Ostwald rule [Van84]. This rule states that a system passes through several metastable intermediate stages on its way from a high-energy state to an energetically favorable state [Ost97]. Crystallization during the rapid heating starts with the nucleation of the t phase due to its reduced free energy, small surface and interface energy in the temperature range 400°C to 1000°C compared to other crystalline phases of HfO_2 [Par+19; PLH19]. As the grain sizes increase, the energetic advantage of low interfacial energies of the t phase over the other phase decreases. A phase transition to the polar oIII phase and then finally to the m phase, which has the lowest bulk free energy follows. This phase transition is nucleation limited and can be described by classical nucleation theories based on the thermodynamic parameters of the three phases. Using simulated parameters leads to a lower nucleation barrier for the t-to-oIII phase transition than for a t-to-m phase transition and a much higher nucleation barrier for the oIII-to-m transition. These results are consistent with the assumption of formation from a metastable oIII phase along the lines of the Ostwald rule [PLH19; Bat+17; KMK17].

Thus, "freezing" the favored oIII phase requires an appropriate cooling

rate after the RTP. Investigations into the cooling rate showed that the strongest possible quenching of the sample is advantageous. While a slow cooling favors a t to m phase transformation and an abrupt quenching allows the stabilization of the oIII phase, a cooling rate between these two leads to the formation of the anti-polar oI phase [Ku+20].

Since the t phase acts as the basis for the subsequent stabilization of the oIII phase, it is important to create favorable conditions for its formation during crystallization. In polycrystalline layers, small grain sizes below 15 nm serve this purpose [Par+18; MKK15], which can be achieved either by the presence of Oxygen Vacancies (VO) [Sch+22a] or by a grain structure of small size in the underlying electrode layer. VO prevents crystallization of the HfO_2 layer during deposition and thus inhibits the growth of crystalline grains. However, while the introduction of too many VO can lead to parasitic effects such as leakage currents [SD00], a high density of pinning centers for domain walls and resistive switching [Cov+16; Cov+15], a too hypo-stoichiometric oxygen concentration favors the growth of the m phase [Mit+19]. A sensitive tunability of the oxygen content during deposition, together with a fast cooling rate, is thus an essential tool for preparing ferroelectric HfO_2 films.

HfO_2 differs from other ferroelectrics not only in the method of production but also in polarization characteristics. While conventional perovskite ferroelectrics usually have a decentralized position of a cation describing the polarization, HfO_2 shows a shift of half of the oxygen atoms within a unit cell [MKK15] (Fig. 3.2). This property leads to unique domain and domain wall characteristics. While different domain wall types, such as Bloch types [Vas+13] or Ising-Neel types [BGN16], can be observed in perovskites, the fluorite structures of HfO_2 show highly localized domain walls and domains which can be as small as the size of a unit cell [Led+22]. This is possible due to extremely flat phonon bands that inhibit the interaction between dipoles, making them individually switchable [Lee+20]. Despite the highly localized domains, Rayleigh behavior could be demonstrated for the movement of the mass centers of the domain walls, which thus appear to interact with the pinning centers in a similar way to the Ising walls (Publication 3). A change in the polarity of the aforementioned off-center oxygen ions is indicated by the movement from one tetrahedron face to another via the tetrahedron centers [Yua+22]. The two polarity states of the oIII phase can be seen in Fig. 3.2.

In addition to the many advantages over conventional ferroelectrics, however, HfO_2 also has hurdles regarding integration capability for memory elements. One of these is the so-called "wake-up effect", which describes the gradual increase in polarization over the number of switching cycles [Jia+21]. Such behavior can also be observed in perovskites [Fen+17], but in contrast

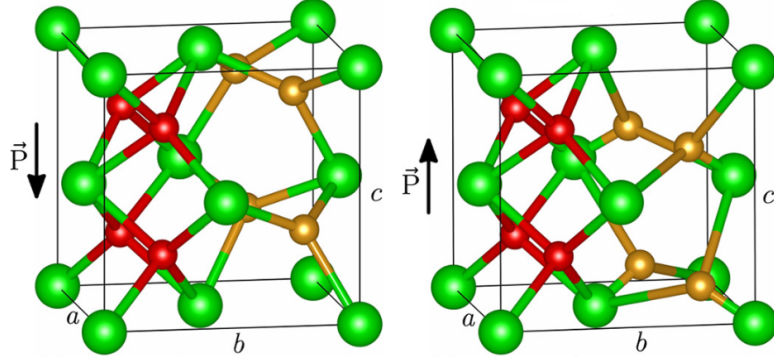


Figure 3.2: Polar orthorhombic $Pca2_1$ phase with down polarization (left) and up polarization (right). Reprinted from [MKK15], with the permission of AIP Publishing.

to fluorite ferroelectrics, it is completed after only a few cycles. The cause of the wake-up effect in doped HfO_2 is widely believed to be the influence of redistribution of VO and the phase transformation from the non-ferroelectric phase to the ferroelectric phase. The successive redistribution of VO during cycling ensures the degradation of internal electric fields, which in turn leads to the depinning of the ferroelectric domains. Thus, the number of domains involved in the polar switching process increases, and the remanent polarization increases with the number of cycles [Jia+21].

For undoped ferroelectric HfO_2 films, (020)/(002) d-values for [110] texturing determined by TEM images were found to indicate structural rearrangement. The change in d-values during training indicates a gradual ferroelastic 90° domain switching, where a change of the in-plane b-axis to the out-of-plane c-axis occurs. This process should be facilitated by a redistribution or uniform distribution of VO, just as in the case of doped layers, which induce a helpful structural disorder by compensating for the missing negative charge [He+21]. The increase in parasitic leakage currents with a number of cycles during wake-up indicates such redistribution of oxygen vacancies in the undoped layers studied. The observations on the training process in undoped HfO_2 layers and the influence of temperature during RTP can be read about in more detail in publication 1. General information about ferroelectricity and its application in information storage elements can be obtained from the following literature [Ish12].

3.2 Charge trapping in HfO_2

The Shockley-Read-Hall (SRH) theory is a widely used model in semiconductor physics to describe the recombination and generation of charge carriers (electrons and holes) in a material. The theory was developed by William Shockley, Walter H. Read, and Robert N. Hall in the 1950s [Sho+50; SR52; Hal52].

The SRH theory focuses on the defects or impurities present in a semiconductor material that can act as recombination centers for charge carriers. The model can also be applied to wide-band gap semiconductors with defects like HfO_2 . These defects can arise from various sources, such as crystal lattice imperfections, impurity atoms, material impurities, or interface states [Ruc+21]. Defects introduce energy levels within the semiconductor bandgap, which can trap and release charge carriers.

According to the SRH theory, the recombination and generation rates of charge carriers in a semiconductor material containing defects are determined by three main processes: capture, emission, and thermal equilibrium [Kha05; SLN21].

1. **Capture:** When a charge carrier (either an electron or a hole) approaches a defect, it can be captured by the defect and get trapped in one of the energy levels associated with it. This process depends on the availability of energy states and the density of the defects.
2. **Emission:** Trapped charge carriers can be released or emitted from the defect energy levels and recombine with a carrier of the opposite type (e.g., an electron and a hole). The emitted carrier can contribute to the material's electrical current flow.
3. **Thermal Equilibrium:** In the presence of thermal energy, charge carriers in a material have a certain probability of occupying energy levels within the bandgap. This probability depends on the temperature and the energy levels available. The thermal equilibrium process involves the redistribution of carriers among different energy levels, including those associated with defects.

The SRH theory introduces two key parameters: the capture cross-section (σ) and the carrier lifetime (τ). The capture cross-section represents the probability that a charge carrier will be captured by a defect when it comes into contact with it. The carrier lifetime represents the average time a charge carrier survives before recombining with another carrier. The lifetime is inversely proportional to the recombination rate [SLN21].

A mathematical description of the SRH theory can be made by using detailed balance equations and statistical mechanics principles. Analyzing the rates of carrier capture and emission provides insights into the efficiency, performance and defect types as well as defect distribution of insulating and semiconducting devices such as solar cells, transistors, photo- and tunnel-diodes. For a simple case τ of a charge carrier trapped in the energy level E_t below the conduction band E_c can be described by [SR52]:

$$\tau = \frac{1}{N_C \sigma v_{th}} \exp\left(\frac{E_c - E_t}{k_B T}\right) \quad (3.1)$$

with N_C as defect density, v_{th} as mean thermal and velocity of the charge carriers. For a better understanding of the electron trapping process, literature on the Franck-Condon principle [Con47; Lax52] and elastic electron tunneling [Goe+10], whose transmission rate is dependent on the charge carrier lifetime, is recommended.

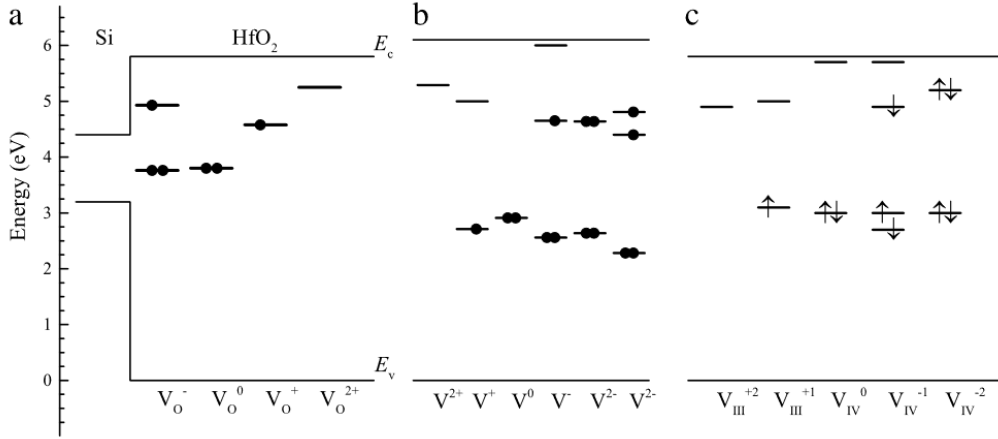


Figure 3.3: Electronic energy levels (Kohn-Sham states) in the band gap of m-HfO₂ for oxygen vacancies in different charge states: (a) calculated for c-HfO₂ in Ref. [Xio+05] with respect to the band edges of Si; (b) for four-coordinated oxygen vacancy from Ref. [Gav+06]; (c) for three- and four-coordinated oxygen vacancy from Ref. [BP06]. Reprinted from [GPI16], with permission from Elsevier.

Due to the many different configurations of oxygen defects in HfO₂ [GPI16], numerous charge-trapping processes at various energy levels are conceivable for a defect-rich material (Fig. 3.3). While these defects cause problems for the application as an insulator, for example in a transistor gate stack, they can be helpful in other devices.

In SONOS (silicon-oxide-nitride-oxide-silicon) cells, for example, a defect-rich electron trap layer can be used to create an analog memory mechanism, which is well suited for neuromorphic networks due to its high accuracy and low information loss over time [Yi+22; Xia+22]. Similar applications can be found for analog switching NAND memories, which exploit the defect structure of HfO_2 among others [Kim+17; Yoo+15].

4. Fabrication process

In the course of this work mesa structures with HfO_2 as the active layer for the resistive switching process and ferroelectric capacitors with HfO_2 as ferroelectric with and without superconducting electrodes were fabricated. Niobium nitrid (NbN) was used as a superconducting electrode, and Titanium nitrid (TiN) as a non-superconducting electrode. Both electrodes are characterized by their inertness to oxidation processes[BR03]. All prepared layers were deposited by sputter deposition. In the case of the ferroelectric capacitors, the deposition of the ferroelectric was followed by a RTP process. The structuring of the devices is done by photo-lithography and lift-off techniques. The lithography process is explained in detail in the following literature[Mor12; Lev05]. The exact process parameters of the various devices can be found in the publication.

4.1 Sputtering

All samples fabricated in this work were prepared using the sputter deposition method. This sputtering method allows the deposition of conductive and non-conductive films by ballistic removal of atoms from a target using ionized gas atoms accelerated in an electric field. The extracted target atoms condense on the substrate surface after the impact process. To enable the ionization of gas atoms and the subsequent collision processes, the depositions usually occur in a pressure range between 10^{-3} mbar and 10^{-2} mbar. The process gas can be Ar, which is an inert gas, or reactive gases such as O_2 or N_2 , which are necessary for the production of alloys.

The deposition equipment used was, the Univex 450B and a self-built sputtering system. In both systems background pressure of $2 - 8 \cdot 10^{-7}$ mbar was achieved, while the process pressure was between $5 \cdot 10^{-3}$ mbar and $5 \cdot 10^{-2}$ mbar. All conductive layers were deposited using the DC magnetron sputtering process. For the non-conductive HfO_2 layers, the DC magnetron process was also used in the case of the memristive devices based on the trap-supported field effect, while AC magnetron sputtering was used for the ferroelectric HfO_2 layers. Different sputtering methods were utilized by using

a ceramic target for the ferroelectric HfO_2 process, while a metallic target was taken for the deposition of the HfO_2 layer for the memristive device. Due to the varying target configurations for the HfO_2 deposition processes, the process gases were also chosen differently. While an inert process gas consisting of pure argon was used for the deposition process of the ferroelectric layers, a reactive gas mixture consisting of Ar and O_2 was used for the memristive HfO_2 layers.

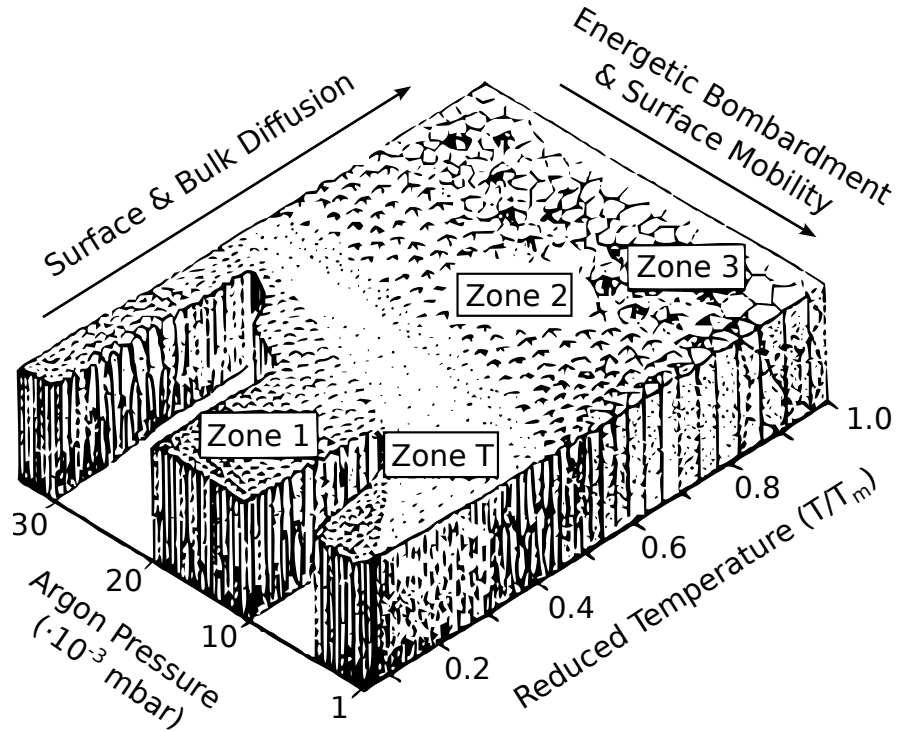


Figure 4.1: Thornton diagram illustrating the nanostructures of thin films prepared by sputtering at different argon pressures and substrate temperatures. Reprinted from [Tho77], with the permission of Annual Reviews, Inc.

Sputtering processes offer major advantages over other deposition techniques in terms of deposition rate and process parameter variation [Mit+19]. This results in a high degree of flexibility in the area of stoichiometry and morphology of the deposited layers. This advantage of sputter deposition is relevant in many aspects of the coatings produced in this work. For the HfO_2 layers in the memristive range, the number of oxygen defects is decisive for the resistive switching effect [Zah+23], and the oxygen content is also relevant for the ferroelectric layers, whose crystal structure is largely determined by the resulting stress [Mit+19]. In the case of the fabricated su-

perconducting NbN electrodes, the morphology, particularly the crystallinity and grain size, is crucial for superconducting properties, such as the transition temperature. This is due to a relation between the coherence length and the morphology of the crystal lattice assuming superconducting grains in a non-superconducting matrix [Jon75; DIG74]. In order to grow layers with different desired physical properties, such as superconductivity and ferroelectricity on top of each other, with one layer preferring epitaxial growth or large grains and the following layer preferring small grains, it is necessary to harmonize the morphologies. For this purpose, plasma diagnostics, as well as the model of Thornton et al. were used, which shows the influence of the sputtering process parameters pressure and temperature on the microstructure in a most illustrative way (Fig. 4.1)[Tho74; Tho75; Klu+03; And10].

Zone 1 of Thornton's structural zone diagram (SZD) describes the growth of a low-density layer due to low surface diffusion. Characteristics of this zone are needle-like grains and the high density of defects. This zone changes to the more dense T zone when the process pressure is reduced, or the temperature is increased. The T zone shows much lower surface roughness and larger fiber-like grains than zone 1. The increased adatom mobility leads to columnar growth of grains with narrow lateral extension in zone 2. Zone 3 is defined by in situ recrystallization due to mass diffusion during the deposition process. The coatings produced under these process conditions usually exhibit high morphological similarity to the target material. A classification of NbN films deposited by sputter deposition in the SZD and the plasma parameters existing during the process can be found in the publication 2.

4.2 Rapid Thermal Processing

RTP has been practiced in the semiconductor industry and semiconductor research for about four decades and describes the rapid heating of electronic devices. This technique was developed as an incentive to make processes in the semiconductor industry more agile and to shorten them in order to meet the time-to-market requirements for new products. The main difference to Conventional Furnace Process (CFP) is the source of heat generation and heat transfer. While the CFP uses resistive heating, which is transferred by direct heat conduction through mechanical contact or convection, the RTP usually uses radiant heat, which is generated, for example, in light sources such as halogen or quartz lamps.

The advantages of the RTP compared to the CFP are the apparent shortening of the process duration and the reduction of the process activation energy. The homogeneity of the heat distribution and the measurability during the heating process, which in turn influences the controllability of the process, are disadvantages of the RTP [Fuk03].

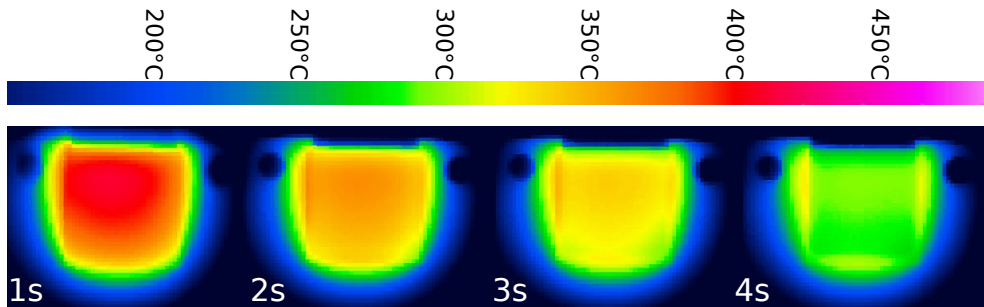


Figure 4.2: IR camera images taken at one-second intervals shortly after an RTP in the self-built oven.

One use in current technology processes is heating thin high-k materials to adjust their dielectric properties for nano-scaled MOSFET applications. A study of HfO_2 , which has been established as a high-k material since 2007, showed reduced capacitance-voltage hysteresis and leakage current for an RTP in nitrogen atmosphere [Sin+12]. Under the same process conditions, ferroelectric behavior in Si-doped HfO_2 was published five years after the first experiments [Bös+11; Sch+22a]. The RTP gained new fame through the new application area of manufacturing FE HfO_2 devices and the associated commotion.

The furnace used in this work for RTP is self-built and consists of a stainless steel vacuum chamber in which two projector lamps with 500W each are mounted above and below a sample holder with an area of 10 mm x

10 mm. A background pressure of 5×10^{-5} mbar was achieved by means of a turbo vacuum pump. Nitrogen and oxygen were available for the brightening process, which was carried out at ambient pressure. To measure the temperature, a type K thermocouple was attached directly below the sample holder, which recorded the process values for regulation by the proportional-integral-derivative (PID) controller. This setup allowed the processing of small substrates at high speed during this work. However, the disproportion between lamp footprint and sample size and the different reflection properties of the sample and thermocouple surface leads to the previously mentioned disadvantages of such an RTP setup. The different reflective properties of the surfaces make it difficult to determine the process temperature precisely, which is why it is regarded as a relative value or reference value in this work. The inhomogeneity of the heat distribution on the processed sample, caused by the mismatch of lamp imprint and sample size, resulted in a radial temperature gradient. While a temperature gradient is a yield issue for industrial processes, it can be useful to obtain information about temperature variations in a research application. For this purpose, temperature images were taken with an IR camera of a sample shortly after an RTP (Fig. 4.2).

5. Analytics

5.1 Impedance spectroscopy

5.1.1 Fundamental Principles

ImpSpec aims to identify physical mechanisms in a system that affect the flow of charge carriers through that system. For this purpose, the system is excited with a perturbation that generates a response modulated in amplitude and phase [Las02]. The causes of the modulation can be manifold and can be exemplified by a mechanical analogy, which can be seen in Fig. 5.1. Here we assume a black box filled with interconnected mass centers for the first case, with a liquid for the second case, and a combination of the first two examples for the third case. All three cases lead to an alteration of the perturbation signal but with different causes. Distinction of the mechanisms and corresponding model development is only possible by a suitable combination of several experiments.

From the analogy, one can already guess the complexity of the superposition of diverse mechanisms in the response given by the system, which illustrates the advantages and disadvantages of this method of investigation. Simply phrased: The advantage of ImpSpec is the simplicity of use; the disadvantage is the scope for interpretation of the spectra.

For an electrical or electrochemical system, the ImpSpec procedure can be described close to the mechanical analogy: A time-invariant system is excited with a perturbation signal which will excite many fundamental microscopic processes, ranging from the transport of electrons by different transport mechanisms like diverse tunneling phenomena and Schottky contact behavior to the interactions and/or movement of ions. As mentioned by the examples for electron transport, the interfaces play a crucial role since, at the interface, all physical properties of the bulk material are abruptly and dramatically changed. Unfortunately, extracting information about, i.e., a specific interface from an impedance of a multilayer system is not trivial. Therefore different measurement modes are used, which will be explained later in detail. In a superordinate definition, three main measurement modes can be distin-

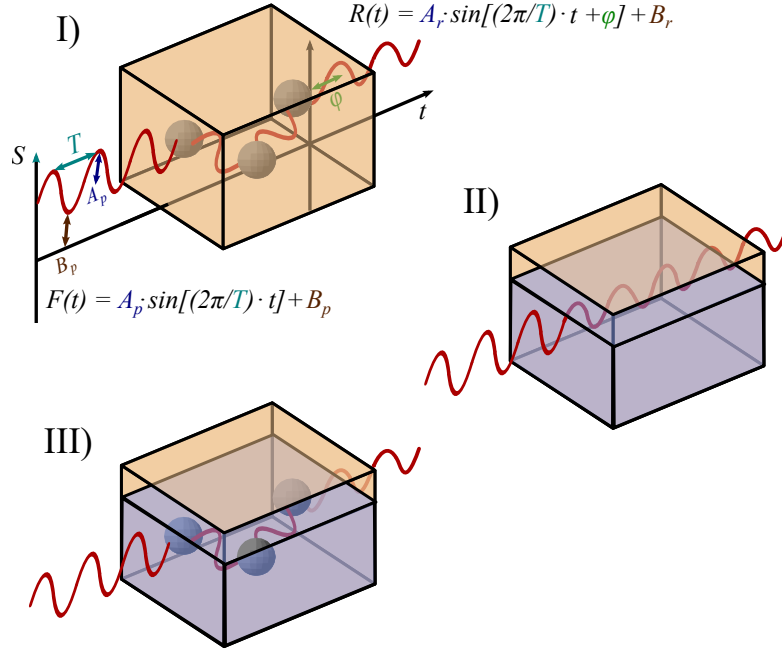


Figure 5.1: I) A physical system with multiple connected centers of mass is excited by a perturbation $F(t)$ and gives a response $R(t)$. II) A physical system filled with a fluid that dampens the perturbation. III) A combination of I) and II).

guished: Transient analysis, white noise analysis, and frequency response analysis [Wan+21; CP10]. The latter is the most frequently used analysis method which can also be used as a Fast Fourier transformation (FFT) analysis [PS93; Val+19]. For FFT analysis, all frequencies of the desired spectrum are applied at once, which is near to white noise analysis with a defined spectrum. This approach makes it possible to measure systems that are not time-invariant, such as memory or switch systems that are measured beyond their threshold voltage [Mar+23]. These measurement operands are embedded in a routine developed by Barsoukov and Macdonald to characterize physical systems using ImpSpec (Fig. 5.2) [BM05].

5.1.2 Frequency Dispersion

Frequency dispersion in ImpSpec refers to impedance variation as a function of the frequency of an applied AC signal. It is commonly observed in systems and materials that possess electrical or electrochemical properties and it provides valuable information about the dynamic behavior and characteristics of the studied system. During the measurements, an AC signal with a small

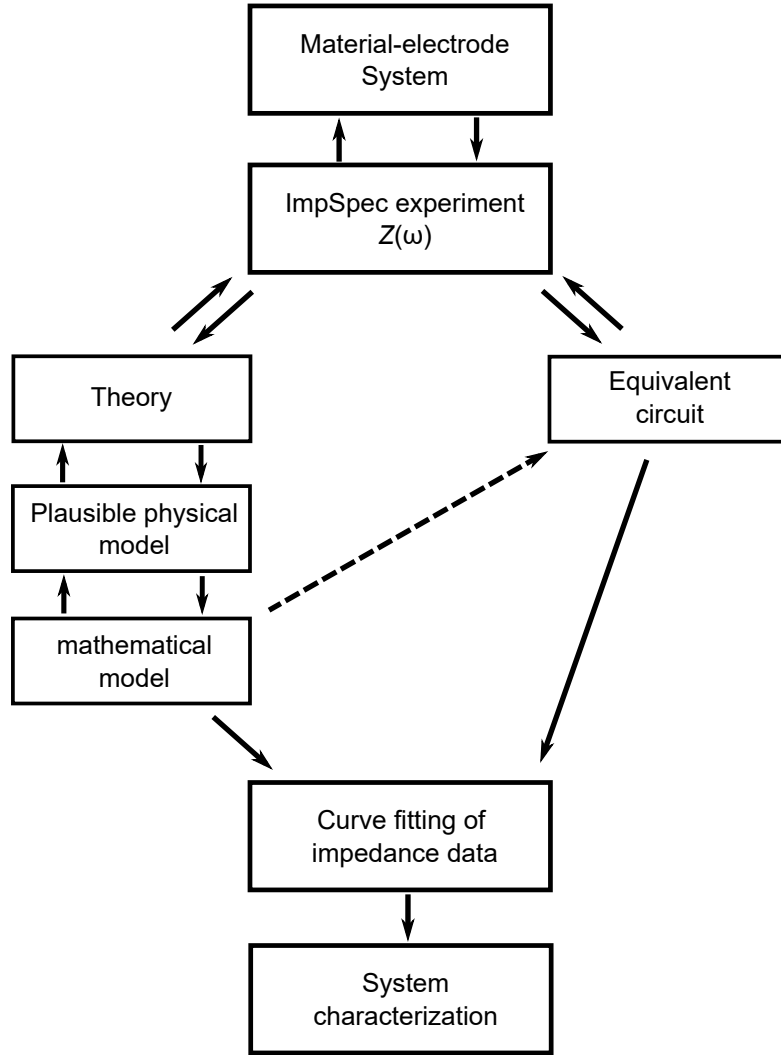


Figure 5.2: Measurement routine for the characterization of a physical system using ImpSpec (adapted from Barsoukov and Macdonald)[BM05].

amplitude is applied across the system at different frequencies. The response of the system is measured in terms of complex impedance, which includes both resistive and reactive components [BM05].

Frequency dispersion arises due to the interaction between the applied AC signal and the intrinsic electrical properties of the system. It can be attributed to various phenomena, including capacitive or inductive effects, charge transfer processes, interfacial effects, and dielectric relaxation. While a capacitive element exhibits decreasing impedance with increasing frequency, an inductive element displays increasing impedance[PF20; Las02].

In electrochemical as well as purely electric systems, frequency dispersion often arises from charge transfer processes occurring at the electrode-electrolyte interface [CCC96]. The kinetics of these processes, such as charge transfer reactions or diffusion, contribute to frequency-dependent impedance behavior. Interfacial effects between different phases of the same material can also contribute to frequency dispersion[PJ17].

Materials with polarization effects, like dielectric relaxation in insulating materials or ferroelectric/ferromagnetic polarization, can also display frequency dispersion. Relaxation processes involving the realignment of dipoles or charge carriers result in frequency-dependent impedance behavior. An example of such processes can be seen in the Rayleigh principle of ferromagnetic and ferroelectric domain wall displacements [Sch+18; Bec+20].

Analyzing the frequency dispersion involves the above-mentioned fitting of impedance spectra to mathematical models and equivalent circuits. This allows the extraction of parameters such as resistances, capacitances, and time constants associated with the different processes contributing to the impedance response. Frequency dispersion in ImpSpec finds applications in various fields, enabling the characterization of electrical properties, investigation of charge transport mechanisms, and evaluation of interfacial phenomena.

5.1.3 Equivalent Circuit Elements

Physical models for equivalent circuits are used to represent the chemical and physical processes that can be excited and observed during the applied perturbation[BM05]. The equivalent circuit created with the help of these models can thus be understood as a mathematical equivalent of the physical system under investigation. These are essential for the understanding and interpretation of impedance data. In the next step, by fitting the equivalent circuit to the measured impedance data, essential parameters of the system's own processes can be determined. This results in a more complex understanding of the studied system.

The three basic physical models consist of the passive elements of resistance, capacitance, and inductance [Las02]. In addition to these three elements, the pinning element, which describes the dispersion of the electric field by the domain wall motion, is also important for the ferroelectric systems studied in this work. These models are paraphrased in more detail below.

RC Element

The impedance of an RC (resistor-capacitor) element refers to the total opposition the RC circuit presents to the flow of alternating current (AC). Unlike a resistor alone, an RC element includes both resistance and reactance, where reactance is associated with the capacitive behavior of the circuit.

In an RC circuit, the resistor (R) restricts the current flow, while the capacitor (C) introduces a reactance that depends on the frequency ω of the AC signal. The impedance of the RC element is denoted by the symbol Z and is a complex quantity that combines resistance and reactance. The impedance of an RC element can be calculated using the following formula:

$$|Z_{RC}| = \frac{1}{\sqrt{(\frac{1}{R})^2 + (\frac{1}{\omega C})^2}} \quad (5.1)$$

with the phase difference:

$$\phi = \tan^{-1}(-\omega CR) \quad (5.2)$$

where Z_{RC} is the modulus of the impedance of the RC element, R is the resistance of the resistor, C is the capacitance of the capacitor, and ω is the angular frequency of the AC signal (in radians per second), given by $\omega = 2\pi f$, where f is the frequency. The term $(1/(\omega C))$ represents the capacitive reactance (X_c) of the RC element. Capacitive reactance is inversely proportional to the frequency of the AC signal and is given by:

$$X_c = \frac{1}{\omega C} \quad (5.3)$$

The impedance Z combines the resistance and the reactance, considering their magnitudes and the phase relationship between them. It's important to note that in an RC circuit, as the frequency of the AC signal increases, the capacitive reactance decreases, leading to a decrease in the overall impedance. Conversely, as the frequency decreases, the capacitive reactance increases, resulting in an increase in the overall impedance [PF20].

Pinning Element

While the two preceding circuit elements, resistor and capacitor, have been an integral part of impedance analyses for decades, the pinning element has only

been part of scientific discussions for the last few years [Sch+18; Bec+22]. The pinning element is used to analyze Rayleigh behavior in ferroelectric layers.

The term Rayleigh behavior, in this case, refers to an analogy between the behavior of ferroelectric domains in an applied electric field and the behavior of ferromagnetic domains in an applied magnetic field [DD96]. The magnetization of a material can be described by the displacement potential energy of the Domain wall (DW), which can be defined as follows [Ray87; Jil15]:

$$(B_0) = \mu_{init}H_0 + \alpha H_0^2, \quad (5.4)$$

$$\mu = \mu_{init} + \alpha H_0, \quad (5.5)$$

with as B_0 and H_0 as the amplitude of the magnetic induction, μ is the magnetic permeability (with μ_{init} as initial value at zero magnetic field), and α as Rayleigh constant. Analogously, without the quadratic dependence of the field, the following was found for the complex relative permittivity of ferroelectrics in the region between the threshold field $\epsilon_r = \epsilon'_r - i\epsilon''_r$ and the partially switching electric field E_{PS} ($E_T < E_O < E_{PS}$), where dielectric polarization already becomes nonlinear [Sch+18; HS99]:

$$\epsilon'_r(E_0) = \epsilon'_{r,in} + \alpha' E_0, \quad (5.6)$$

$$\epsilon''_r(E_0) = \epsilon''_{r,in} + \alpha'' E_0, \quad (5.7)$$

with E_0 as amplitude of the electric field, $\epsilon'_{r,in}$ and $\epsilon''_{r,in}$ as real and imaginary part of the reversible Rayleigh parameter $\epsilon_{r,in}$, and α' and α'' as real and imaginary part of the Rayleigh constant. The irreversible DW motion is described by $\alpha' E_0$. Thus, the real part of the Rayleigh constant can be interpreted as a measure of the mobility of the DW. Constraints on DW mobility are determined by the number of pinning centers, the film thickness, and the density of the DW [Bas+07].

The Rayleigh equation for the ferroelectric P - E hysteresis loop follows a proportionality between the real part and the imaginary part of the Rayleigh constant:

$$\alpha'' = \frac{4}{3\pi} \alpha'. \quad (5.8)$$

The logarithmic frequency dependence for the transition of DW in a rough energy landscape, with a high density of local energetic minima, between two

metastable states[FMS04] added by Becker et al.[Bec+22] can be described by:

$$\epsilon'_{r,in}(f) = \epsilon'_{r,in,0} + \Delta\epsilon'_{r,in} \ln\left(\frac{1Hz}{2\pi f}\right), \quad (5.9)$$

$$\alpha'(f) = \alpha'_0 + \Delta\alpha' \ln\left(\frac{1Hz}{2\pi f}\right). \quad (5.10)$$

From Equations 5.6, 5.7 and 5.9, 5.10 follows the redefinition of the real part of the relative permittivity:

$$\epsilon'_r(E_0, f) = \epsilon'_{r,in,0} + \alpha'_0 E_0 + [\Delta\epsilon'_{r,in} + \Delta\alpha' E_0] \ln\left(\frac{1Hz}{2\pi f}\right), \quad (5.11)$$

with $\epsilon'_{r,in,0}$ as the frequency-independent component of the reversible DW displacement, $\Delta\epsilon'_{r,in}$ as the zero-field contribution to the logarithmic dispersion strength, α'_0 as the frequency-independent component of the Rayleigh constant, and α' as the coupling strength between dielectric non-linearity and frequency dispersion. The latter is defined as the change of logarithmic frequency dispersion strength with field amplitude or equivalently as the change of the irreversible Rayleigh parameter with the logarithm of the frequency.

For the imaginary part of the complex permittivity applies:

$$\epsilon''_r(E_0) = \epsilon''_{r,in} + \alpha'' E_0. \quad (5.12)$$

As can be seen in Eq. 5.12, the complex part of the permittivity responds independently of the changing electric field. However, it contains a factor $\epsilon''_{r,in}$, which represents the zero field contribution and is therefore 0 in non-stressed ferroelectrics without an internal field.

As a result of the assumptions above an equivalent circuit element, the so-called pinning element Z_{DW} was extracted by Becker et al. [Bec+20; Bec+22]:

$$Z_{DW} = \frac{\epsilon''_{r,0} - i[\epsilon'_{r,0} + \Delta\epsilon'_r \ln(\frac{1Hz}{2\pi f})]}{2\pi f C_0 \{[\epsilon'_{r,0} + \Delta\epsilon'_r \ln(\frac{1Hz}{2\pi f})]^2 + \} \epsilon''_{r,0}^2} \quad (5.13)$$

Detailed information on the determination of dispersion parameters can be found in the publication "Domain Wall Movement in Undoped Ferroelectric HfO₂: A Rayleigh Analysis".

5.2 Plasma Measurements

The physical parameters of the process plasma for thin film deposition, such as floating potential, electron temperature, and the energy flux to the substrate, are crucial for the morphology and stoichiometry of the deposited layers as well as the defect density of the layers underneath. Insights into plasma parameters are therefore of great advantage when tuning layer properties. To determine the plasma conditions during the magnetron sputtering processes, the energy fluxes during the deposition of the layers were measured. A planar probe consisting of a copper plate to which a type K thermocouple and a bias cable are attached served as a Passive Thermal Probe (PTP) as well as a Langmuir Probe (LP) [Gau+17; GHK19; ML26]. This probe served both as a passive thermal probe and as a Langmuir probe. The copper plate with a diameter of 11 mm and thickness of 100 μm is surrounded by a cylindrical shield made of stainless steel. In order to have equal field conditions for the deposition process and the measurements, an additional stainless steel shield with the dimensions of the sample holder was attached to the probe.

All plasma measurements were performed under the same process conditions as the sample deposition. While no potential was applied to the copper plate for the PTP measurements, a voltage between -30 V and +15V was applied for the LP measurements [Cip+20]. The shield of the sample was meanwhile permanently at the ground potential, as was the sample holder during the deposition process. An illustration of the probe and the theoretical basis for analyzing the data acquired using PTP and LP can be found in Publication 2. The development of the probe as well as the measurement technology for recording the data, was carried out at the Chair of Experimental Physics of Prof. Dr. Kersten.

5.3 X-ray diffraction Measurements

X-ray diffraction is a powerful technique used to study the atomic and molecular structure of materials. It is based on the principle that when X-rays pass through a crystal, they interact with the electrons and nuclei of the atoms within the crystal lattice, resulting in constructive and destructive interference of the X-ray waves [War90]. By measuring the resulting diffraction pattern, one can determine the arrangement of atoms within a crystal and obtain valuable information about its properties. The following key points are relevant to the basic understanding of this measurement method [WA86]:

1. Interaction with Crystals: When X-rays interact with a crystal, they undergo elastic scattering, which means they change direction with-

out losing energy. The crystal acts as a three-dimensional diffraction grating, scattering the incident X-rays in different directions.

2. Bragg's Law: The diffraction of X-rays can be explained using Bragg's law, which relates the angles at which X-rays are diffracted to the spacing between the crystal planes [EJ66]. It is given by the equation:

$$n\lambda = 2d\sin(\theta) \quad (5.14)$$

where n is an integer, λ is the wavelength of the X-rays, d is the distance between the crystal planes, and θ is the angle of incidence or diffraction.

3. Diffraction Pattern: When a crystal is exposed to X-rays, a diffraction pattern is formed due to the constructive and destructive interference of the diffracted X-rays. The pattern consists of a series of spots or peaks corresponding to the different crystallographic planes within the crystal.
4. Crystal Structure Determination: By analyzing the positions and intensities of the diffraction spots in the pattern, the arrangement of atoms within the crystal lattice is deduced. This information is then used to determine the crystal structure, including the unit cell dimensions, atomic positions, and bonding arrangements.

An example of an X-ray Diffraction (XRD) pattern of HfO_2 in a mixed crystal form of cubic and orthorhombic can be found in Publication 2. For a deeper insight into the XRD analysis, the following textbooks are recommended [War90; WA86; BUA15].

5.4 Transmission Electron Microscopy

TEM has become the primary tool for characterizing the microstructure of materials. While X-ray methods offer more quantitative diffraction patterns, electrons have an advantage in being easily focused. This allows for measuring diffraction patterns from microscopic regions and selecting single microcrystals for analysis.

The general working principle of TEM consists of the transmission of a coherent and focused electron beam through a thin (typically around 50-100 nm) specimen. The interactions of the beam with the probe structure, while passing through, result in scattering and energy loss of the electrons. After

the Transmission, the electron beam forms an image of the specimen on the detector. This image depends on the different interactions of electrons with the specimen resulting in varying contrast levels and therefore highlighting different features within the specimen. Samples with the necessary thickness of 100nm and below can be prepared using Focused Ion Beam Etching [HS07].

Electron optics enable imaging of electron intensity variations in thin specimens, leading to "diffraction contrast" microscopy, useful for detecting defects like dislocations, interfaces, and second phase particles. In "high-resolution" transmission electron microscopy (HRTEM), phase-contrast imaging preserves the phase of diffracted electron waves, allowing the formation of precise images of atom columns. Additionally, electron nanobeams and high-angle annular dark-field imaging enhance high-resolution imaging capabilities. Analytical TEM employs Energy-dispersive X-ray Spectrometry (EDS) and Electron Energy-loss Spectroscopy (EELS) to obtain chemical information by analyzing electronic excitations in the specimen [FH12].

Modern TEM offer diverse imaging modes, including diffraction contrast imaging, phase contrast imaging, and spectroscopy with focused electron beams. Scanning Transmission Electron Microscopy (STEM) utilizes a focused electron beam in a raster pattern, enabling data acquisition for spectroscopy work and chemical mapping of samples.

All TEM and EELS data shown in the publications were collected by Ole Gronenberg from the chair "Synthesis and Real Structure" of Professor Kienle.

5.4.1 Electron Energy-loss Spectroscopy

The increasing demand for high spatial resolution imaging, diffraction, and spectroscopy methods to understand atomic processes in solids has been driven by the growing interest in nanoscience and nanotechnology. TEM is particularly valuable as it provides structural information with exceptional spatial resolution, down to atomic dimensions, through high-resolution TEM imaging and electron diffraction. Chemical information from the same specimen region can be obtained using analytical techniques such as EDS and EELS [Bry20].

EELS, due to its broad range of inelastic interactions with high-energy electrons, offers unique possibilities for advanced materials analysis. The energy-filtering technique in TEM has led to practical applications in both materials and biological sciences. Modern TEM with high-brightness electron sources and spherical aberration correctors have pushed the image resolution to the 50 picometre level, especially in STEM equipped with Cs-probe correctors. EELS is based on inelastically scattered electrons interacting with

atomic electrons in the specimen, leading to energy loss and bending of the electron beam. The energy distribution of these scattered electrons provides information about the local atomic environment, which relates to the physical and chemical properties of the specimen. The electron energy-loss spectrum shows characteristic features, including a zero-loss peak representing transmitted electrons and valence peaks containing information about the band structure and dielectric properties of the material. At higher energy losses, ionization edges appear, providing information about the ionization energy and qualitative analysis of chemical elements [Hof+16].

5.5 X-ray Photoelectron Spectroscopy

All photoelectronic spectroscopic are based on the photoelectronic effect, which Einstein and Rutherford described as the interaction between photons and atoms leading to various outcomes, such as the emittance of electrons. Capturing the energy of emitted electrons, which were excited by photons, sums up the basic principle of Photoelectron Spectroscopy (PES) in simple words. However, from the development of the concept of the idea of the photoelectronic effect to the first measurements of copper Core levels by the Group of Siegbahn and reliable calibration of a PES setup took several decades [NSS57; SD20]. Given by the desire to be able to detect inner core level energies of copper atoms, the emergence of HAXPES was taking place concisely with the first steps of PES development. HAXPES, which is defined by its higher photon energies (>2 keV) for the excitation of electrons, is especially in terms of extracting depth information of examined structures [WW16]. Thus surface phenomena such as charging etc. can be neglected.

To determine the electronic structure of a material composition or element, the sample is illuminated with photons in the X-ray range, whose energy input can be described as $h\nu$ by the Planck relation. Then the kinetic energy (KE) of the emitted electrons is measured by influencing their trajectory with a spherical electric field. This allows the recording of a spectrum of the kinetic energies of emitted electrons as a function of their velocity. A formal description of the process shows in simple terms the possibility of calculating the binding energy (BE) between the emitted electron and the binding atomic nucleus:

$$BE = h\nu - KE - \phi_{WF} \quad (5.15)$$

As an additional quantity for the calculation, the work function ϕ_{WF} of the spectrometer is required, which can be regarded as the calibration

constant of the measurement setup. A representation of the binding energies is done by plotting the measured intensities over the binding energy. Here, the measured nuclear levels ideally appear as a narrow peak, which can be assigned by means of a notation containing the corresponding element and emitting orbital. To get a clear picture of the electronic structure, it is recommended to use a monochromatic source to avoid satellite peaks and similar artifacts, which can overlap with the desired measurement data.

To gain additional information about the depth dependency of the electronic structure, angle-resolved X-ray Photoelectron Spectroscopy (XPS) could be utilized. In angle-resolved HAXPES, the photoelectrons are measured at different angles with respect to the sample surface. By varying the angle of detection, information about the photoelectron emission angle with respect to the sample surface can be obtained. This allows the determination of the momentum and the in-plane electronic band structure of the material [WW16]. A schematic drawing of this measurement method can be found in Fig. 1 of Publication 4. All data presented in Publication 4 were recorded by Finn Zahari from Professor Kohlstedt's Nanoelectronics group at DESY.

Further information on the subject can be found in these textbooks [Van11; WW16].

6. Brief combined summary of the Publications

The five presented publications are divided into two different areas of application of HfO_2 in memristive devices. The first three manuscripts cover the fabrication of both ferroelectric HfO_2 and superconducting NbN films by magnetron sputter deposition. Ferroelectric materials are promising candidates for neuromorphic computing synaptic devices due to the nonvolatile multiplicity of spontaneous polarization. The last two publications, already cover an application of HfO_2 in a synaptic memristive device, which shows analog area-based switching due to a trap-assisted field effect. The analysis methods used are TEM, HAXPES and ImpSpec as well as LP and PTP for plasma probing.

Ferroelectric HfO_2 for memristive applications

First Publication: Initially, TEM analyses are used to investigate a system consisting of TiN electrodes and undoped HfO_2 . The focus of this TEM analysis is the training effect of pristine HfO_2 layers, the interdiffusion at the interfaces to the electrodes, and the variation of the temperature in the RTP due to the previously mentioned (Ch. 4.2) temperature gradient.

The most important findings obtained during this analysis are the indications of the rotation of the orthorhombic grains from an in-plane orientation to an out-of-plane orientation during the training phase. This rotation probably occurs by swapping the b and c axes. In addition, depending on the temperature during the RTP, different regions can be distinguished, varying in electrical properties and morphology. The differences in morphology can be defined in particular by the varying strength of the interdiffusion.

Second Publication: In this subsequent work, the correlations of plasma parameters of magnetron sputtering processes and structural and electrical properties of NbN films are investigated. Compared to the previously described TiN electrodes, NbN electrodes show better inertness with respect to interdiffusion at interfaces. In addition, the superconducting property allows a variety of new applications. However, the use of superconducting NbN as

electrodes necessitates a compromise since an essential parameter of superconductivity, the coherence length, depends on the grain size to an opposite extent, as does the ferroelectricity of the HfO_2 layer. This means, that for good superconductivity, a growth of large grains is necessary, while for stabilizing the ferroelectric orthorhombic phase, small grains are advantageous.

In order to be able to control this trade-off, profound information about the production process is required. The process pressure and the target-substrate distance could be determined as important parameters for manipulating the grain size during sputter deposition. Their influence is directly related to the mean free path of the particles to be deposited, which in turn influences their energy during impact on the substrate surface. If the particle energy is too low, the necessary adatom mobility to form a crystalline layer is missing, and if the energy is too high, defects can form in the layer.

Third Publication: The third publication combines the findings on ferroelectric HfO_2 and superconducting NbN of the first two publications in one device. The ferroelectric capacitor structure is chemically and structurally analyzed by TEM and EELS. Furthermore, its ferroelectric switching behavior, which is due to the movement of domain walls, is investigated by Rayleigh analysis based on ImpSpec.

The Rayleigh analysis method allows us to obtain a comprehensive understanding of the flexibility of domain walls. The flexibility of the domain walls is, in turn, conditioned by the interaction with pinning centers, which must be overcome as hurdles. Thus, on the one hand, statements can be made about the density of pinning centers, and, on the other hand, a classification can be made for the different modes of motion of the center of mass of a domain wall in dependence of the applied electric field strength and frequency. The motion modes are especially interesting for application in synaptic memristive devices since partial switching can be induced by an appropriate frequency adjustment of the applied electric field.

The role of HfO_2 in synaptic memristive device

The following two publications four and five are a complementary analysis of the behavior of HfO_2 in a memristive device consisting of a multilayer stack exhibiting area-based switching. Among other applications, such devices are considered an essential building block of bio-inspired neuromorphic architectures, which aim to replicate the data processing of nervous systems since they can be exploited to emulate the plastic behavior of biological synapses in electronic circuits. The Nb/NbO_x/Aluminium oxid (Al_2O_3)/ HfO_2 /Au memristive device shows similar switching behavior to other devices reported previously [Han+15]. A profound understanding of the mechanisms responsible

for the resistive switching effect is essential for tailoring the electrical characteristics for specific applications and can pave the way for developing devices compatible with traditional CMOS technology. The complex physics behind this low-power resistive switching is investigated electrically and chemically in the following two publications.

Fourth Publication: In the fourth publication, the memristive devices under investigation exhibit filament-free interface-type analog resistive switching, high I-V non-linearity, and low power consumption characterized using the spectroscopic methods of XPS, HAXPES and EELS as well as TEM. The switching from a high-resistance state (HRS) to a low-resistance state (LRS) is achieved by applying a positive voltage to the top electrode.

First, the quasi-static IV characteristics of the device, as well as the switching and retention of the memristive effect, are analyzed. This reveals a diode-like IV behavior, which indicates the existence of an Space charge region (SCR), as well as an analog area-based memristive switching without electroforming. An EELS analysis of the multilayer stack reveals a complete oxidation of the HfO_2 and Al_2O_3 layers as well as an anoxidation of the bottom electrode with a thickness of about $d_{\text{NbO}_x} = 5 \text{ nm} \pm 2 \text{ nm}$. This circumstance can be attributed to the reactive sputtering process of the HfO_2 layer, which leads to anoxidation of the layers underneath. The degree of oxidation of the anoxidised bottom electrode can be explained as a mixture of Nb_2O_5 and NbO_2 . A pronounced plasmon peak at 23 eV indicates a stoichiometric HfO_2 . In addition, the TEM images from the cross-section show a rough interface between the NbO_x and the Al_2O_3 layers. During the memristive switching from HRS to LRS, a positive BE shift, which cannot be explained by a chemical change of about 110 meV, can be detected for the core levels of the Hf^{4+} species by XPS. Depth-resolved HAXPES measurements complete the picture of the electronic structure and show that the SCR is neither in the HfO_2 layer nor in the Al_2O_3 layer and is therefore assumed to be in the anoxidised bottom electrode. This assumption is confirmed by the investigations on similar devices with different bottom electrodes, which show a clearly deviating IV characteristic. In addition, the HAXPES investigations show a drop in the binding energy in the direction of the bottom electrode.

The results obtained from the investigations can be described by means of a metal-insulator-semiconductor (MIS) model, in which manipulation of the SCR located in the semiconductor by charging and discharging electron traps located in the insulator enables memristive switching. Experimental evidence for this model is also shown in the companion paper, described below.

Fifth Publication:

The fifth study explores various aspects of the aforementioned memristive devices, including their characteristics, switching mechanisms, Equivalent Circuit (EC) representation, time-dependent behavior, and the role of surface states and defects in the charge transport process by ImpSpec.

As mentioned before, the devices consist of a semiconducting partially oxidized Nb back electrode (NbO_x 5 nm) and an Al_2O_3 layer with varying thickness and nano-scale roughness at the interface with NbO_x . Spectral analysis of ImpSpec measurements reveals a single half circuit in the EC. The current transport mechanism is attributed to thermionic emission and thus indicates the existence of a SCR, while capacitive behavior hints towards a superposition of an SCR and an insulator. Changing the resistive state does not require altering the EC but rather involves a quantitative change in the physical process of charge carrier transport. The change in barrier height and ideality factor is associated with variations in the SCR, leading to changes in the resistive state. The slope of the capacitance-voltage (C-V) curve indicates the existence of surface states, and the ideality factor is mirrored in a dimensionless capacitance factor. Resistive switching is observed for voltages above 1V after a 30-second measurement interval, while voltages above 2V exhibit an "inductive hook." A possible explanation for this behavior is a slow process that gradually reduces resistance over time.

Transient analysis is employed to extract more information about the switching process, and a bi-exponential function is found to be necessary for accurate fitting of the transients, indicating the presence of two time constants. Likewise, in the retention measurements, two time constants slower by three orders of magnitude are observed with the same factor among them. All observations can be interpreted by fitting with the Shockley-Read-Hall model. The electron traps associated with energetic and spatial distribution exhibit multiple time constants, with a trap depth of approximately 0.89 eV, matching the literature-measured depth of VO^{2+} . Furthermore, it is suggested that interface traps with smaller capture cross sections are responsible for long-time memory, while bulk traps are responsible for short-time memory. The charging and discharging of these electron traps cause the SCR to change its charge, affecting the device's resistive state.

7. Conclusions

The presented work shows a detailed analysis of the element HfO_2 , with the first part focusing on its ferroelectric properties and in the latter regarding the memristive behavior due to the charging and discharging of electron traps. In both cases, the aim is to integrate the two investigated properties into memristive devices, which are to be used as artificial synapses in neuromorphic circuits. HfO_2 is particularly suitable for this task due to its compatibility with existing CMOS technology and the wide range of applications as presented in this work.

The first three Publications study the effects of temperature treatment and sputtering parameters on thin ferroelectric HfO_2 films and superconducting NbN electrodes. RTP with temperature gradients influenced the concentration of VO and leakage current of $\text{TiN}/\text{HfO}_2/\text{TiN}$ capacitors. Higher RTP temperatures increased VO concentrations and leakage current, while lower temperatures resulted in lower concentrations. Temperature treatment also impacted the microstructural evolution and ferroelectric behavior of HfO_2 . Wake-up effects and polarization characteristics varied depending on RTP temperature. Cycling of devices revealed a gradual ferroelastic 90° domain switching of $[110]$ oriented grains with in-plane polarization, which convincingly explains the evolution of the remnant polarization from 0 to up to $26 \mu\text{C}/\text{cm}^2$ during the wake-up.

Plasma parameters and sputtering conditions influenced the growth and properties of NbN films. Plasma particle energies affected structural layer properties and transition temperatures. Lowering the process pressure results in a rise of charged plasma particles with lower kinetic energies, leading to a significant deterioration in the structural layer's properties through a reduction in grain size. This reduction in grain size is directly linked to the transition temperature of the superconducting thin film. Additionally, structural analyses allowed for the classification of films by Thornton's diagram, confirming that the NbN film exhibited the highest crystallinity at a pressure of 10^{-2} mbar.

With the results of the two previous investigations it was possible to develop a novel material combination of stabilized HfO_2 films on superconducting NbN electrodes. The study explored domain wall dynamics by ex-

exploiting a Rayleigh analysis using the pinning element. Polycrystalline ferroelectric HfO_2 films exhibit considerably less domain wall flexibility compared to perovskite ferroelectrics, indicating a higher concentration of pinning sites. These pinning sites are typically associated with point defects, which, in ferroelectric HfO_2 , are primarily composed of oxygen vacancies or intact domain structures, such as nonferroelectric spacer layers situated between the ferroelectric layers. Detailed analysis using EELS and electrical data demonstrates a chemically stable interface between HfO_2 and NbN electrodes, revealing no detectable interdiffusion of oxygen or nitrogen. Consequently, it is presumed that intact domain structures and portions of the nonferroelectric monoclinic crystal phase are the primary contributors to the reduced polarization values. The comprehensive research provided valuable insights into the optimization and understanding of temperature treatment, plasma parameters, and material combinations for enhancing the behavior and properties of thin ferroelectric HfO_2 films and superconducting NbN electrodes, thereby advancing the potential applications in memristive electronic devices.

Furthermore, comprehensive characterizations of analog memristive switching devices were conducted. The devices consisted of Nb/NbO_x/Al₂O₃/HfO₂/Au layers, showing diode-like current-voltage ($|J|$ -V) characteristics. The stoichiometry of HfO₂ and Al₂O₃ was confirmed, and the oxidation state of NbO_x was determined. The memristive switching behavior was found to be electronic, with no evidence of ionic drift. The diode-like behavior was attributed to the NbO_x layer, while Al₂O₃ was not crucial for switching. A proposed memristive device model involved electron traps within the insulator modulating the space-charge region and overall device resistance. Spectroscopic evidence supported the charging and discharging of electron traps as the fundamental origin of resistive switching. In the companion study, ImpSpec analysis was employed to gain insights into the state-sensitive interfaces and functionalities of memristive devices. The analysis identified a single barrier and an imperfect Schottky contact, with a space-charge region sensitive to the device state. Capacitance analysis and time constants revealed the presence of electron traps. Trap-assisted field-effect altering the space-charge region was identified as the dominant switching mechanism, acting as an amplifier for charge state changes. The ImpSpec results were consistent with experiments on HAXPES and TEM, providing a more comprehensive understanding of the physical processes involved.

This work analyzed two different methods for using hafnium oxide in information storage devices. Both the ferroelectric effect with the modelable domain wall properties and the charge trapping with the relatively deep electron traps are promising for integration in memristive devices since both allow gradual switching.

8. Outlook and future work

Future work on integrating ferroelectric hafnium oxide could be in the fabrication of ferroelectric tunnel junctions (FTJ). This could enable a CMOS technology compatible artificial synapse with good retention. Further Rayleigh analysis on ferroelectric HfO_2 with different morphology would be recommended for tuning such a device. Furthermore, the use of superconducting electrodes for the FTJ would be conceivable. This would allow low energy use at cryogenic temperatures and tunneling spectroscopy for further investigations of the ferroelectric properties.

For the memristive devices, which are based on the modulation of the space charge zone by the charge state change of electron traps, a replacement of the non-CMOS technology compatible materials is recommended. Replacing the semiconducting niobium oxide with silicon, which is easier to control regarding doping level, could open up new possibilities in adapting to special applications. Likewise, changing the intermediate oxide layer from Al_2O_3 to other oxides could be interesting since the capture cross section is changed, which is decisive for the retention. A similarly inert material such as TiN must replace the Au electrode to achieve full CMOS technology compatibility.

Finally, the concepts of memristive devices presented here would need to be integrated into a neuromorphic circuit as artificial synapses with artificial neurons in the form of an oscillator network. Such networks would then have to be adapted to the corresponding tasks, which in turn would require tuning the functions of the memristive devices again.

Bibliography

- [CC80] Jacques Curie and Pierre Curie. “Développement par compression de l’électricité polaire dans les cristaux hémiedres à faces inclinées”. In: *Bulletin de minéralogie* 3.4 (1880), pp. 90–93.
- [Ray87] Lord Rayleigh. “XXV. Notes on electricity and magnetism.—III. On the behaviour of iron and steel under the operation of feeble magnetic forces”. In: *The London, Edinburgh, and Dublin Philosophical Magazine and Journal of Science* 23.142 (1887), pp. 225–245.
- [Ost97] Wilhelm Ostwald. “Studien über die Bildung und Umwandlung fester Körper”. In: *Zeitschrift für physikalische Chemie* 22.1 (1897), pp. 289–330.
- [Val21] Joseph Valasek. “Piezo-electric and allied phenomena in Rochelle salt”. In: *Physical review* 17.4 (1921), p. 475.
- [ML26] Harold M Mott-Smith and Irving Langmuir. “The theory of collectors in gaseous discharges”. In: *Physical review* 28.4 (1926), p. 727.
- [MP43] Warren S McCulloch and Walter Pitts. “A logical calculus of the ideas immanent in nervous activity”. In: *The bulletin of mathematical biophysics* 5 (1943), pp. 115–133.
- [Con47] Edward U Condon. “The Franck-Condon principle and related topics”. In: *American journal of physics* 15.5 (1947), pp. 365–374.
- [Sho+50] William Shockley et al. “Electrons and Holes in Semiconductors”. In: (1950).
- [Hal52] Robert Noel Hall. “Electron-hole recombination in germanium”. In: *Physical review* 87.2 (1952), p. 387.
- [Lax52] Melvin Lax. “The Franck-Condon principle and its application to crystals”. In: *The Journal of chemical physics* 20.11 (1952), pp. 1752–1760.

- [SR52] William Bradford Shockley and William Thornton Read Jr. “Statistics of the recombinations of holes and electrons”. In: *Physical review* 87.5 (1952), p. 835.
- [FC54] B Farley and W Clark. “Simulation of self-organizing systems by digital computer”. In: *Transactions of the IRE Professional Group on Information Theory* 4.4 (1954), pp. 76–84.
- [NSS57] Carl Nordling, Evelyn Sokolowski, and Kai Siegbahn. “Precision method for obtaining absolute values of atomic binding energies”. In: *Physical Review* 105.5 (1957), p. 1676.
- [Ros58] Frank Rosenblatt. “The perceptron: a probabilistic model for information storage and organization in the brain.” In: *Psychological review* 65.6 (1958), p. 386.
- [EJ66] LRB Elton and Daphne F Jackson. “X-ray diffraction and the Bragg law”. In: *American Journal of Physics* 34.11 (1966), pp. 1036–1038.
- [Chu71] Leon Chua. “Memristor-the missing circuit element”. In: *IEEE Transactions on circuit theory* 18.5 (1971), pp. 507–519.
- [DIG74] G Deutscher, Y Imry, and L Gunther. “Superconducting phase transitions in granular systems”. In: *Physical Review B* 10.11 (1974), p. 4598.
- [Tho74] John A Thornton. “Influence of apparatus geometry and deposition conditions on the structure and topography of thick sputtered coatings”. In: *Journal of Vacuum Science and Technology* 11.4 (1974), pp. 666–670.
- [Wer74] Paul Werbos. “Beyond regression: New tools for prediction and analysis in the behavioral sciences”. In: *PhD thesis, Committee on Applied Mathematics, Harvard University, Cambridge, MA* (1974).
- [Jon75] Harris C Jones. “Some properties of granular thin films of high-field superconductors”. In: *Applied Physics Letters* 27.8 (1975), pp. 471–473.
- [Tho75] John A Thornton. “Influence of substrate temperature and deposition rate on structure of thick sputtered Cu coatings”. In: *Journal of Vacuum Science and Technology* 12.4 (1975), pp. 830–835.
- [Tho77] John A Thornton. “High rate thick film growth”. In: *Annual review of materials science* 7.1 (1977), pp. 239–260.

- [Van84] RA Van Santen. “The Ostwald step rule”. In: *The Journal of Physical Chemistry* 88.24 (1984), pp. 5768–5769.
- [GK85] VB Glushkova and MV Kravchinskaya. “HfO₂-based refractory compounds and solid solutions: I. Phase diagrams of the systems HfO₂ M₂O₃ and HfO₂ MO”. In: *Ceramics international* 11.2 (1985), pp. 56–65.
- [WA86] LD Whittig and WR Allardice. “X-ray diffraction techniques”. In: *Methods of Soil Analysis: Part 1 Physical and Mineralogical Methods* 5 (1986), pp. 331–362.
- [She88] Gordon M Shepherd. *Neurobiology*. Oxford University Press, 1988, pp. 1–39.
- [War90] Bertram Eugene Warren. *X-ray Diffraction*. Courier Corporation, 1990.
- [Wer90] Paul J Werbos. “Backpropagation through time: what it does and how to do it”. In: *Proceedings of the IEEE* 78.10 (1990), pp. 1550–1560.
- [WLS92] J Wang, HP Li, and R Stevens. “Hafnia and hafnia-toughened ceramics”. In: *Journal of materials science* 27 (1992), pp. 5397–5430.
- [PS93] GS Popkirov and RN Schindler. “Validation of experimental data in electrochemical impedance spectroscopy”. In: *Electrochimica acta* 38.7 (1993), pp. 861–867.
- [CCC96] Hans GL Coster, Terry C Chilcott, and Adelle CF Coster. “Impedance spectroscopy of interfaces, membranes and ultrastructures”. In: *Bioelectrochemistry and Bioenergetics* 40.2 (1996), pp. 79–98.
- [DD96] Dragan Damjanovic and Marlyse Demartin. “The Rayleigh law in piezoelectric ceramics”. In: *Journal of Physics D: Applied Physics* 29.7 (1996), p. 2057.
- [HS99] David A Hall and Paul J Stevenson. “High field dielectric behaviour of ferroelectric ceramics”. In: *Ferroelectrics* 228.1 (1999), pp. 139–158.
- [Man00] Charles C Mann. “The end of Moore’s law?” In: *Technology Review* 103.3 (2000), pp. 42–42.
- [SD00] JF Scott and Matthew Dawber. “Oxygen-vacancy ordering as a fatigue mechanism in perovskite ferroelectrics”. In: *Applied Physics Letters* 76.25 (2000), pp. 3801–3803.

- [Ham01] Constance Hammond. *Cellular and Molecular Neurobiology (Deluxe Edition)*. Academic Press, 2001.
- [Oht+01] Osamu Ohtaka et al. “Phase relations and volume changes of hafnia under high pressure and high temperature”. In: *Journal of the American Ceramic Society* 84.6 (2001), pp. 1369–1373.
- [Las02] Andrzej Lasia. *Electrochemical impedance spectroscopy and its applications*. Springer, 2002.
- [BR03] Harish C Barshilia and KS Rajam. “Nanolayered TiN/NbN Multilayers as New Superhard Materials”. In: (2003).
- [Fuk03] Hisashi Fukuda. *Rapid thermal processing for future semiconductor devices*. Elsevier, 2003, pp. 1–9.
- [Klu+03] Oliver Kluth et al. “Modified Thornton model for magnetron sputtered zinc oxide: film structure and etching behaviour”. In: *Thin solid films* 442.1-2 (2003), pp. 80–85.
- [MIK03] Kazuhide Matsumoto, Yoshiyasu Itoh, and Tsuneji Kameda. “EB-PVD process and thermal properties of hafnia-based thermal barrier coating”. In: *Science and Technology of Advanced Materials* 4.2 (2003), p. 153.
- [Smi03] Christopher Upham Murray Smith. *Elements of molecular neurobiology*. John Wiley & Sons, 2003.
- [FMS04] Andrei A Fedorenko, Volkmar Mueller, and Semjon Stepanow. “Dielectric response due to stochastic motion of pinned domain walls”. In: *Physical Review B* 70.22 (2004), p. 224104.
- [McK04] Sally A McKee. “Reflections on the memory wall”. In: *Proceedings of the 1st conference on Computing frontiers*. 2004, p. 162.
- [Mey+04] R Meyer et al. “On a novel ferro resistive random access memory (FRRAM): Basic model and first experiments”. In: *Integrated Ferroelectrics* 64.1 (2004), pp. 77–88.
- [Nag+04] V Nagarajan et al. “Size effects in ultrathin epitaxial ferroelectric heterostructures”. In: *Applied Physics Letters* 84.25 (2004), pp. 5225–5227.
- [BM05] Evgenij Barsoukov and J Ross Macdonald. “Impedance spectroscopy theory, experiment, and applications”. In: *Applications, 2nd ed. (Hoboken, NJ: John Wiley & Sons, Inc.)* (2005).
- [DN05] Alexander A Demkov and Alexandra Navrotsky. *Materials fundamentals of gate dielectrics*. Vol. 256. Springer, 2005, pp. 9–20.

- [Kha05] Vinod Kumar Khanna. “Physical understanding and technological control of carrier lifetimes in semiconductor materials and devices: A critique of conceptual development, state of the art and applications”. In: *Progress in quantum electronics* 29.2 (2005), pp. 59–163.
- [Lev05] Harry J Levinson. *Principles of lithography*. Vol. 146. SPIE press, 2005.
- [Xio+05] K Xiong et al. “Defect energy levels in HfO₂ high-dielectric-constant gate oxide”. In: *Applied physics letters* 87.18 (2005).
- [BP06] Peter Broqvist and Alfredo Pasquarello. “Oxygen vacancy in monoclinic HfO₂: A consistent interpretation of trap assisted conduction, direct electron injection, and optical absorption experiments”. In: *Applied physics letters* 89.26 (2006).
- [Gav+06] JL Gavartin et al. “Negative oxygen vacancies in HfO₂ as charge traps in high-k stacks”. In: *Applied Physics Letters* 89.8 (2006).
- [Bas+07] Nazanin Bassiri-Gharb et al. “Domain wall contributions to the properties of piezoelectric thin films”. In: *Journal of Electroceramics* 19 (2007), pp. 49–67.
- [HS07] Peter W Hawkes and John CH Spence. *Science of microscopy*. Vol. 1. Springer, 2007.
- [Liu+08] Qi Liu et al. “Resistive switching memory effect of ZrO₂ films with Zr⁺ implanted”. In: *Applied physics letters* 92.1 (2008), p. 012117.
- [Rud08] Jerry W Rudy. *The neurobiology of learning and memory*. Sinauer Associates, 2008.
- [Dri+09] Tom Driscoll et al. “Phase-transition driven memristive system”. In: *Applied physics letters* 95.4 (2009).
- [GA09] Samanwoy Ghosh-Dastidar and Hojjat Adeli. “Spiking neural networks”. In: *International journal of neural systems* 19.04 (2009), pp. 295–308.
- [And10] André Anders. “A structure zone diagram including plasma-based deposition and ion etching”. In: *Thin Solid Films* 518.15 (2010), pp. 4087–4090.
- [CP10] Byoung-Yong Chang and Su-Moon Park. “Electrochemical impedance spectroscopy”. In: *Annual Review of Analytical Chemistry* 3 (2010), pp. 207–229.

- [Goe+10] Wolfgang Goes et al. “Charge trapping and the negative bias temperature instability”. In: *ECS Transactions* 33.3 (2010), p. 565.
- [Kwo+10] Deok-Hwang Kwon et al. “Atomic structure of conducting nanofilaments in TiO_2 resistive switching memory”. In: *Nature nanotechnology* 5.2 (2010), pp. 148–153.
- [Bös+11] TS Böske et al. “Ferroelectricity in hafnium oxide thin films”. In: *Applied Physics Letters* 99.10 (2011), p. 102903.
- [BS11] Scott Brady and George Siegel. *Basic neurochemistry: principles of molecular, cellular, and medical neurobiology*. Academic press, 2011, pp. 235–258.
- [IBW11] Daniele Ielmini, Rainer Bruchhaus, and Rainer Waser. “Thermochemical resistive switching: materials, mechanisms, and scaling projections”. In: *Phase Transitions* 84.7 (2011), pp. 570–602.
- [Str+11] John Paul Strachan et al. “The switching location of a bipolar memristor: chemical, thermal and structural mapping”. In: *Nanotechnology* 22.25 (2011), p. 254015.
- [Tap+11] Stefan Tappertzhofen et al. “Proton mobility in SiO_2 thin films and impact of hydrogen and humidity on the resistive switching effect”. In: *MRS Online Proceedings Library (OPL)* 1330 (2011).
- [Van11] Paul Van der Heide. *X-ray photoelectron spectroscopy: an introduction to principles and practices*. John Wiley & Sons, 2011.
- [FH12] Brent Fultz and James M Howe. *Transmission electron microscopy and diffractometry of materials*. Springer Science & Business Media, 2012.
- [Ish12] Hiroshi Ishiwara. “Ferroelectric random access memories”. In: *Journal of nanoscience and nanotechnology* 12.10 (2012), pp. 7619–7627.
- [Mor12] Wayne M Moreau. *Semiconductor lithography: principles, practices, and materials*. Springer Science & Business Media, 2012.
- [Sin+12] Vikram Singh et al. “Study of rapid thermal annealing on ultra thin high-k HfO_2 films properties for nano scaled MOSFET technology”. In: *Microelectronic Engineering* 91 (2012), pp. 137–143.
- [Yan+12] J Joshua Yang et al. “Metal oxide memories based on thermochemical and valence change mechanisms”. In: *MRS bulletin* 37.2 (2012), pp. 131–137.

- [Par+13] Gyeong-Su Park et al. “In situ observation of filamentary conducting channels in an asymmetric $\text{Ta}_2\text{O}_{5-x}/\text{TaO}_{2-x}$ bilayer structure”. In: *Nature communications* 4.1 (2013), p. 2382.
- [Vas+13] Rama K Vasudevan et al. “Domain wall conduction and polarization-mediated transport in ferroelectrics”. In: *Advanced Functional Materials* 23.20 (2013), pp. 2592–2616.
- [Chu14] Leon Chua. “If it’s pinched it’s a memristor”. In: *Semiconductor Science and Technology* 29.10 (2014), p. 104001.
- [LCH14] Deyan Lin, Leon Chua, and Shu-Yuen Hui. “The first man-made memristor: Circa 1801 [scanning our past]”. In: *Proceedings of the IEEE* 103.1 (2014), pp. 131–136.
- [BUA15] Andrei A Bunaciu, Elena Gabriela UdrişTioiu, and Hassan Y Aboul-Enein. “X-ray diffraction: instrumentation and applications”. In: *Critical reviews in analytical chemistry* 45.4 (2015), pp. 289–299.
- [Cov+15] E Covi et al. “Synaptic potentiation and depression in Al:HfO_2 -based memristor”. In: *Microelectronic Engineering* 147 (2015), pp. 41–44.
- [Han+15] Mirko Hansen et al. “A double barrier memristive device”. In: *Scientific reports* 5.1 (2015), p. 13753.
- [Jil15] David Jiles. *Introduction to magnetism and magnetic materials*. CRC press, 2015, pp. 157–168.
- [MKK15] Robin Materlik, Christopher Künneth, and AJJOAP Kersch. “The origin of ferroelectricity in $\text{Hf}_{1-x}\text{Zr}_x\text{O}_2$: A computational investigation and a surface energy model”. In: *Journal of Applied Physics* 117.13 (2015), p. 134109.
- [Mat+15] Yu Matveyev et al. “Resistive switching and synaptic properties of fully atomic layer deposition grown $\text{TiN/HfO}_2/\text{TiN}$ devices”. In: *Journal of Applied Physics* 117.4 (2015), p. 044901.
- [Wei+15] Li Wei Zhou et al. “Interface engineering for improving reliability of resistance switching in $\text{Cu/HfO}_2/\text{TiO}_2/\text{Pt}$ structure”. In: *Applied Physics Letters* 107.7 (2015).
- [Yoo+15] Jung Ho Yoon et al. “ $\text{Pt/Ta}_2\text{O}_5/\text{HfO}_{2-x}/\text{Ti}$ resistive switching memory competing with multilevel NAND flash”. In: *Advanced Materials* 27.25 (2015), pp. 3811–3816.

- [BGN16] Stuart R Burns, J Marty Gregg, and Valanoor Nagarajan. “Nanos-
tructuring ferroelectrics via focused ion beam methodologies”. In: *Advanced Functional Materials* 26.46 (2016), pp. 8367–8381.
- [Cov+16] Erika Covi et al. “HfO₂-based memristors for neuromorphic ap-
plications”. In: *2016 IEEE International Symposium on Circuits
and Systems (ISCAS)*. IEEE. 2016, pp. 393–396.
- [GPI16] Vladimir A Gritsenko, Timofey V Perevalov, and Damir R Is-
lamov. “Electronic properties of hafnium oxide: A contribution
from defects and traps”. In: *Physics Reports* 613 (2016), pp. 1–
20.
- [Hof+16] Ferdinand Hofer et al. “Fundamentals of electron energy-loss
spectroscopy”. In: *IOP conference series: Materials science and
engineering*. Vol. 109. 1. IOP Publishing. 2016, p. 012007.
- [She+16] Arman Shehabi et al. “United states data center energy usage
report”. In: (2016).
- [WW16] Joseph C Woicik and Joseph Woicik. “Hard X-ray photoelectron
spectroscopy (HAXPES)”. In: (2016).
- [Bat+17] Rohit Batra et al. “Dopants promoting ferroelectricity in hafnia:
Insights from a comprehensive chemical space exploration”. In:
Chemistry of Materials 29.21 (2017), pp. 9102–9109.
- [Fen+17] Franz PG Fengler et al. “Domain pinning: Comparison of hafnia
and PZT based ferroelectrics”. In: *Advanced Electronic Materials*
3.4 (2017), p. 1600505.
- [Gau+17] Sven Gauter et al. “Calorimetric probe measurements for a high
voltage pulsed substrate (PBII) in a HiPIMS process”. In: *Plasma
Sources Science and Technology* 26.6 (2017), p. 065013.
- [Kim+17] Gun Hwan Kim et al. “Four-Bits-Per-Cell Operation in an HfO₂-
Based Resistive Switching Device”. In: *Small* 13.40 (2017), p. 1701781.
- [KMK17] Christopher Künneth, Robin Materlik, and Alfred Kersch. “Mod-
eling ferroelectric film properties and size effects from tetragonal
interlayer in Hf_{1-x} Zr_x O₂ grains”. In: *Journal of Applied Physics*
121.20 (2017), p. 205304.
- [PJ17] Tamás Pajkossy and Rafal Jurczakowski. “Electrochemical impedance
spectroscopy in interfacial studies”. In: *Current Opinion in Elec-
trochemistry* 1.1 (2017), pp. 53–58.
- [Sha+17] Pankaj Sharma et al. “Nonvolatile ferroelectric domain wall mem-
ory”. In: *Science advances* 3.6 (2017), e1700512.

- [TW17] Thomas N Theis and H-S Philip Wong. “The end of moore’s law: A new beginning for information technology”. In: *Computing in Science & Engineering* 19.2 (2017), pp. 41–50.
- [Par+18] Min Hyuk Park et al. “Understanding the formation of the metastable ferroelectric phase in hafnia–zirconia solid solution thin films”. In: *Nanoscale* 10.2 (2018), pp. 716–725.
- [Sch+18] T Schenk et al. “Physical approach to ferroelectric impedance spectroscopy: The Rayleigh element”. In: *Physical Review Applied* 10.6 (2018), p. 064004.
- [CSA19] Leon Chua, Georgios Ch Sirakoulis, and Andrew Adamatzky. *Handbook of Memristor Networks*. Springer Nature, 2019, pp. 527–529.
- [Cüp+19] Felix Cüppers et al. “Exploiting the switching dynamics of HfO₂-based ReRAM devices for reliable analog memristive behavior”. In: *APL materials* 7.9 (2019).
- [GHK19] Sven Gauter, Fabian Haase, and Holger Kersten. “Experimentally unraveling the energy flux originating from a DC magnetron sputtering source”. In: *Thin Solid Films* 669 (2019), pp. 8–18.
- [LMH19] J Lappalainen, J Mizsei, and M Huotari. “Neuromorphic thermal-electric circuits based on phase-change VO₂ thin-film memristor elements”. In: *Journal of Applied Physics* 125.4 (2019).
- [Mik+19] Vitalii Mikheev et al. “Ferroelectric second-order memristor”. In: *ACS applied materials & interfaces* 11.35 (2019), pp. 32108–32114.
- [Mit+19] Terence Mittmann et al. “Origin of ferroelectric phase in undoped HfO₂ films deposited by sputtering”. In: *Advanced Materials Interfaces* 6.11 (2019), p. 1900042.
- [Ord+19] Jose Ordonez-Miranda et al. “Radiative thermal memristor”. In: *Physical review letters* 123.2 (2019), p. 025901.
- [PLH19] Min Hyuk Park, Young Hwan Lee, and Cheol Seong Hwang. “Understanding ferroelectric phase formation in doped HfO₂ thin films based on classical nucleation theory”. In: *Nanoscale* 11.41 (2019), pp. 19477–19487.
- [Par+19] Min Hyuk Park et al. “Thermodynamic and kinetic origins of ferroelectricity in fluorite structure oxides”. In: *Advanced Electronic Materials* 5.3 (2019), p. 1800522.

- [SHF19] Uwe Schroeder, Cheol Seong Hwang, and Hiroshi Funakubo. *Ferroelectricity in doped hafnium oxide: materials, properties and devices*. Woodhead Publishing, 2019, pp. 25–26.
- [Val+19] Aušra Valiūnienė et al. “Redox-probe-free scanning electrochemical microscopy combined with fast Fourier transform electrochemical impedance spectroscopy”. In: *Physical Chemistry Chemical Physics* 21.19 (2019), pp. 9831–9836.
- [Bec+20] M Becker et al. “Rayleigh analysis and dielectric dispersion in polycrystalline $0.5(\text{Ba}_{0.7}\text{Ca}_{0.3})\text{TiO}_3$ – $0.5\text{Ba}(\text{Zr}_{0.2}\text{Ti}_{0.8})\text{O}_3$ ferroelectric thin films by domain-wall pinning element modeling”. In: *Journal of Applied Physics* 128.15 (2020), p. 154103.
- [Bry20] Rik Brydson. *Electron energy loss spectroscopy*. Garland Science, 2020.
- [Cip+20] Julia Cipo et al. “Diagnostics of process plasma used for the production of memristive devices”. In: *Journal of Physics: Conference Series*. Vol. 1492. 1. IOP Publishing, 2020, p. 012002.
- [Ku+20] Boncheol Ku et al. “Fast thermal quenching on the ferroelectric Al: HfO_2 thin film with record polarization density and flash memory application”. In: *2020 IEEE symposium on VLSI technology*. IEEE, 2020, pp. 1–2.
- [Lee+20] Hyun-Jae Lee et al. “Scale-free ferroelectricity induced by flat phonon bands in HfO_2 ”. In: *Science* 369.6509 (2020), pp. 1343–1347.
- [Mik+20] V Mikheev et al. “Memristor with a ferroelectric HfO_2 layer: in which case it is a ferroelectric tunnel junction”. In: *Nanotechnology* 31.21 (2020), p. 215205.
- [PF20] Dale R Patrick and Stephen W Fardo. *Electricity and electronics fundamentals*. CRC Press, 2020, pp. 75–110.
- [SD20] Fred A Stevie and Carrie L Donley. “Introduction to x-ray photoelectron spectroscopy”. In: *Journal of Vacuum Science & Technology A* 38.6 (2020).
- [Xu+20] Ming Xu et al. “Recent advances on neuromorphic devices based on chalcogenide phase-change materials”. In: *Advanced Functional Materials* 30.50 (2020), p. 2003419.

- [CGW21] Malgorzata Chrzanowska-Jeske, Stephen M Goodnick, and Martin N Wybourne. “Nanoelectronics—Beyond CMOS Computing [Guest Editorial]”. In: *IEEE Nanotechnology Magazine* 15.6 (2021), pp. 6–7.
- [Du+21] Xinzhe Du et al. “High-Speed Switching and Giant Electroresistance in an Epitaxial $\text{Hf}_{0.5}\text{Zr}_{0.5}\text{O}_2$ -Based Ferroelectric Tunnel Junction Memristor”. In: *ACS Applied Materials & Interfaces* 14.1 (2021), pp. 1355–1361.
- [He+21] Ri He et al. “Charged oxygen vacancy induced ferroelectric structure transition in hafnium oxide”. In: *arXiv preprint arXiv:2106.12159* (2021).
- [IEA21] IEA. *Electricity Information: Overview*. 2021. URL: <https://www.iea.org/reports/electricity-information-overview>.
- [Jia+21] Pengfei Jiang et al. “Wake-Up Effect in HfO_2 -Based Ferroelectric Films”. In: *Advanced Electronic Materials* 7.1 (2021), p. 2000728.
- [KF21] Alfred Kersch and Max Falkowski. “New Low-Energy Crystal Structures in ZrO_2 and HfO_2 ”. In: *physica status solidi (RRL)–Rapid Research Letters* 15.5 (2021), p. 2100074.
- [Orc+21] Garrick Orchard et al. “Efficient neuromorphic signal processing with loihi 2”. In: *2021 IEEE Workshop on Signal Processing Systems (SiPS)*. IEEE. 2021, pp. 254–259.
- [Ruc+21] Bernhard Ruch et al. “Applicability of Shockley–Read–Hall theory for interface states”. In: *IEEE Transactions on Electron Devices* 68.4 (2021), pp. 2092–2097.
- [SLN21] Simon M Sze, Yiming Li, and Kwok K Ng. *Physics of semiconductor devices*. John wiley & sons, 2021, pp. 40–45.
- [Wan+21] Shangshang Wang et al. “Electrochemical impedance spectroscopy”. In: *Nature Reviews Methods Primers* 1.1 (2021), p. 41.
- [Alv22] Pablo Alvarez. *Charted: The Rise of Mobile Device Subscriptions Worldwide*. 2022. URL: <https://www.visualcapitalist.com/cp/two-decades-of-mobile-device-subscriptions-worldwide/>.
- [Bec+22] Maximilian T Becker et al. “Impedance spectroscopy of ferroelectrics: The domain wall pinning element”. In: *Journal of Applied Physics* 132.4 (2022), p. 044104.
- [BK22] Tom Birkoben and Hermann Kohlstedt. “Matter & Mind Matter”. In: *arXiv preprint arXiv:2204.12774* (2022).

- [Led+22] Maximilian Lederer et al. “Review on the microstructure of ferroelectric hafnium oxides”. In: *physica status solidi (RRL)–Rapid Research Letters* 16.10 (2022), p. 2200168.
- [Sch+22a] Uwe Schroeder et al. “The fundamentals and applications of ferroelectric HfO₂”. In: *Nature Reviews Materials* 7.8 (2022), pp. 653–669.
- [Sch+22b] Richard Schroedter et al. “Physics-based modeling of a bi-layer Al₂O₃/Nb₂O₅ analog memristive device”. In: *IEEE International Symposium on Circuits and Systems (ISCAS)*. 2022.
- [Sev+22] Jaime Sevilla et al. “Compute trends across three eras of machine learning”. In: *2022 International Joint Conference on Neural Networks (IJCNN)*. IEEE. 2022, pp. 1–8.
- [WS22] Qing Wan and Yi Shi. “Neuromorphic devices for brain-inspired computing: artificial intelligence, perception and robotics”. In: *(No Title)* (2022).
- [Xia+22] T Patrick Xiao et al. “An accurate, error-tolerant, and energy-efficient neural network inference engine based on SONOS analog memory”. In: *IEEE Transactions on Circuits and Systems I: Regular Papers* 69.4 (2022), pp. 1480–1493.
- [Yi+22] Su-in Yi et al. “Physical Compact Model for Three-Terminal SONOS Synaptic Circuit Element”. In: *Advanced Intelligent Systems* 4.9 (2022), p. 2200070.
- [Yua+22] Jun-Hui Yuan et al. “Ferroelectricity in HfO₂ from a chemical perspective”. In: *arXiv preprint arXiv:2201.00210* (2022).
- [Kim+23] Taewook Kim et al. “Oxide thickness-dependent resistive switching characteristics of Cu/HfO₂/Pt ECM devices”. In: *Applied Physics Letters* 122.2 (2023).
- [Mai+23] Punya Mainali et al. “The Impact of Trap-Assisted Tunneling and Poole–Frenkel Emission on Synaptic Potentiation in an α -Fe₂O₃/p-Si Memristive Device”. In: *Sci* 5.1 (2023), p. 3.
- [Mar+23] Richard Marquardt et al. “Impedance Spectroscopy on Hafnium Oxide-Based Memristive Devices”. In: *Advanced Electronic Materials* (2023), p. 2201227.
- [Yan+23] Xiaobing Yan et al. “A low-power Si: HfO₂ ferroelectric tunnel memristor for spiking neural networks”. In: *Nano Energy* 107 (2023), p. 108091.

- [Zah+23] Finn Zahari et al. “Trap-Assisted Memristive Switching in HfO₂-Based Devices Studied by In Situ Soft and Hard X-Ray Photoelectron Spectroscopy”. In: *Advanced Electronic Materials* (2023), p. 2201226.

Publications

The impact of rapid thermal annealing for the ferroelectricity of HfO_2 ...	71
Correlation between sputtered niobium nitride films and plasma parameters ...	85
Domain Wall Movement in Undoped Ferroelectric HfO_2 ...	98
Trap-Assisted Memristive Switching in HfO_2 -Based Devices ...	110
Impedance Spectroscopy on Hafnium Oxide-Based Memristive Devices ...	129

I. The impact of rapid thermal annealing for the ferroelectricity of undoped sputtered HfO₂ and its wake-up effect

Bibliographic Information

Gronenberg, O., **Marquardt, R.**, Lamprecht, R., Ekici, Y., Schürmann, U., Kohlstedt, H., Kienle, L.; The impact of rapid thermal annealing for the ferroelectricity of undoped sputtered HfO₂ and its wake-up effect. *Journal of Applied Physics* 7 September 2022; 132 (9): 094101.
<https://doi.org/10.1063/5.0100562>

Author's contribution

The author contributed to:

- Partial construction of the measurement setup
- Guiding sample preparation
- Measurement and evaluation of the electrical data
- Partial writing of the manuscript

Copyright Notice

©2024 AIP. Reprinted from <https://doi.org/10.1063/5.0100562>, with the permission of AIP Publishing.

I.1 Summary

This work describes the process and results of plan-view and cross section TEM sample preparation and the electrical and structural characterization of ferroelectric devices. Sample preparation for plan-view TEM involved cutting Si wafers into small pieces and punching out sample blanks. An acetone-soluble resin was applied as a protective layer. The TEM samples were prepared by thinning the material using SiC sandpaper, a dimpler, and ion polishing. Electrical characterization of the devices on a Si chip revealed inhomogeneities in polarization and leakage currents. Three areas (Pos 1, Pos 2, and Pos 3) showed different electrical properties. Pos 1 exhibited a wake-up effect, visible polarization, and displacement current. Pos 3 had lower polarization and higher leakage currents. Pos 2 showed intermediate behavior. Leakage current density and breakdown voltages also varied among the positions.

Structural characterization revealed the presence a TiO_xN_y interlayer between a TiN top electrode and the HfO_2 layer. The TiN columnar structure was interrupted by the interlayer with different structure and composition. The TE is intentionally oxidized during reactive sputtering, and the higher concentration of VO in the TE for higher annealing temperatures results in a thinner interlayer. Electron diffraction analysis indicated the presence of TiN with a cubic structure and HfO_2 with a mixed crystal orientation. Texture analysis showed a $\langle 111 \rangle$ texture for TiN and multiple orientations for HfO_2 grains. Microstructural analysis and HRTEM revealed a phase pure orthorhombic HfO_2 thin film, and a structural rearrangement involving the exchange of in-plane axes with in-plane c-axis switching to the b-axis is proposed as the cause of the observed wake-up effect. The in-plane c-axis switched to the b-axis in certain regions of the devices. The different wake-up behavior of devices from different positions on the wafer is attributed to the oxygen vacancy concentration and the crystallographic orientation of HfO_2 . The differences in electrical behavior and microstructure were attributed to variations in annealing temperature during the RTP and inhomogeneities in sputter deposition.

The work provides a detailed account of the sample preparation, electrical characterization, and structural analysis of ferroelectric devices properties in dependence of fabrication parameters using plan-view TEM.

The impact of rapid thermal annealing for the ferroelectricity of undoped sputtered HfO_2 and its wake-up effect

Cite as: J. Appl. Phys. **132**, 094101 (2022); doi: [10.1063/5.0100562](https://doi.org/10.1063/5.0100562)

Submitted: 25 May 2022 · Accepted: 2 August 2022 ·

Published Online: 1 September 2022



O. Gronenberg,^{1,a)} R. Marquardt,² R. Lamprecht,² Y. Ekici,¹ U. Schürmann,¹ H. Kohlstedt,²  and L. Kienle^{1,b)} 

AFFILIATIONS

¹Synthesis and Real Structure, Institute for Materials Science, Faculty of Engineering, Kiel University, 24143 Kiel, Germany

²Nanoelectronics, Institute of Electrical Engineering and Information Engineering, Kiel University, 24143 Kiel, Germany

^{a)}Electronic mail: og@tf.uni-kiel.de

^{b)}Author to whom correspondence should be addressed: lk@tf.uni-kiel.de

ABSTRACT

Fundamental aspects of ferroelectric HfO_2 , a fluorite-type oxide, are not understood yet. This is evident by different theories regarding, e.g., the wake-up effect or the antiferroelectric-like behavior of HfO_2 manufactured with different doping or deposition techniques. Therefore, we focus on sputtered and undoped HfO_2 to gain deeper understanding of the ferroelectric properties of pure HfO_2 . A temperature gradient on a $10 \times 10 \text{ mm}^2$ substrate during rapid thermal annealing led to different ferroelectric device performances in terms of remnant polarization and the wake-up effect. The results from the electrical characterization are compared to observations by transmission electron microscopy, performed on pristine and trained samples in plan-view as well as in cross section. We observed that different temperature treatments caused effects at the interfaces of the TiN electrodes and also affected the microstructure and defect concentration of the HfO_2 itself. Devices from the hot corner showed wake-up free ferroelectricity with a remnant polarization below $10 \mu\text{C}/\text{cm}^2$, whereas devices from the cold corner showed a strong wake-up effect with remnant polarization starting from 0 to above $20 \mu\text{C}/\text{cm}^2$ after 10^6 cycles. After observing a small structural transformation in trained devices, we attributed this strong wake-up effect to gradual ferroelastic switching of pristine [110] oriented grains with in-plane polarization to partially out-of-plane polarization, while the predominantly $\langle 111 \rangle$ oriented grains in the hot corner can suppress the wake-up effect.

Published under an exclusive license by AIP Publishing. <https://doi.org/10.1063/5.0100562>

I. INTRODUCTION

In the last few years, HfO_2 and related compounds attracted considerable interest as high-k gate insulators for advanced nanometer-scaled field effect transistors^{1,2} and non-volatile storage elements. These include resistive random access memories (ReRAMs),³ ferroelectric (FE) random access memories (FeRAMs),⁴ and ferroelectric field effect transistors (FeFETs).⁵ For memory-related applications, intrinsic or interfacial oxygen vacancies (V_O) strongly affect the functionality and device performance.^{6–8} In non-ferroelectric ReRAM-cells, the formation and rupture of conductive filaments is related to the formation and migration of V_O .^{6,9} For ferroelectric HfO_2 , V_O lead to a stabilization of the FE phase^{10,11} and play an essential role during the wake-up procedure.^{12–14}

In order to understand the ferroelectric behavior of HfO_2 , the crystal structures observed at room temperature need to be discussed.

Figure 1 shows the phase transitions of HfO_2 from the tetragonal (T) ($P4_2/nmc$) high-temperature phase. This T phase is also stable in very small grains and with high defect and doping concentrations.¹⁹ At room temperature, the thermodynamically stable phase of HfO_2 is the centrosymmetric monoclinic (M) ($P2_1/c$) phase which develops during cooling from the T phase via a symmetric distortion. The orthorhombic ($Pca2_1$) phase (O-FE) is believed to be responsible for the ferroelectricity of polycrystalline HfO_2 ²⁰ which develops by an asymmetric distortion of the T phase.¹⁸ Four of the eight oxygen ions are located in the center of Hf^{4+} -tetrahedrons (red in Fig. 1), while the rest are located on non-centrosymmetric tetrahedron faces (yellow in Fig. 1). These four anions cause the ferroelectric switching from one tetrahedron face to another via the tetrahedron centers (i.e., via an intermediate T-like phase).^{18,21} Figure 1 also depicts the similarity with the fluorite structure, which complicates

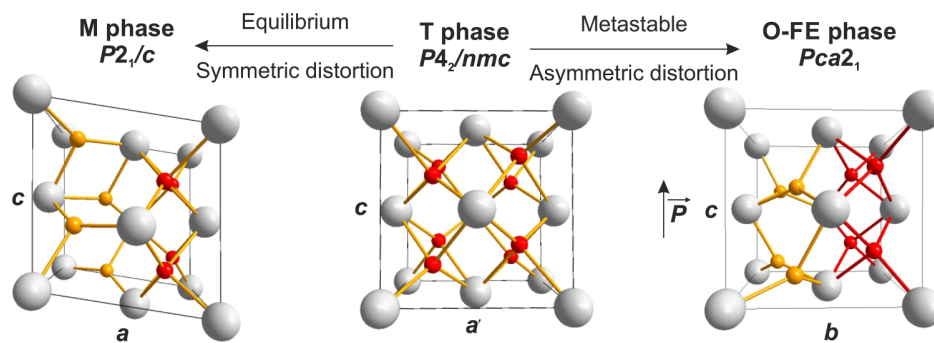


FIG. 1. Models of different unit cells of HfO_2 in fluorite-type setup. The equilibrium M phase¹⁵ forms by a symmetric distortion from the high-temperature T phase,¹⁶ while the metastable O-FE phase¹⁷ forms by an asymmetric distortion. In both cases of distortion, the coordination number of four oxygen ions changes from four to three. The oxygen ions in tetrahedron centers are colored in red, while oxygen ions on tetrahedron faces (triangles) are colored in yellow. These yellow oxygen ions are responsible for the ferroelectric switching from the lower tetrahedron face to the upper one.¹⁸ In the T phase, the a' vector represents the $\langle 110 \rangle$ directions of the T phase without c -components.

the determination of the exact phase and crystallographic directions as they differ mainly by the coordination of the anions. The O-FE phase is metastable at room temperature, and different routes have been proposed to stabilize it against the M phase. The main factors are thin film thickness,^{10,22} stress (epitaxial),^{23,24} oxygen deficiency,^{10,25} doping,²⁶ and small grain sizes induced by rapid thermal annealing (RTA)¹⁰ or by amorphous interlayers.²⁷ Also, TiN electrodes seem to play an important role for stabilizing the O-FE phase in polycrystalline HfO_2 .²⁸ The oxygen scavenging of TiN during deposition and RTA²⁹ is believed to create V_O , which are essential for stabilizing the O-FE phase.^{10,11} High concentrations of V_O are expected especially at the interfaces to the electrodes. Therefore, different approaches have been proposed to optimize the electrode interfaces for the ferroelectric HfO_2 , e.g., by optimizing the Ar/ N_2 ratio during reactive sputtering of the TE^{30–32} or by applying a NH_3 plasma treatment on both interfaces.³³ All studies showed improved endurance of the devices with N-rich TiN and concluded that less V_O are formed at the interfaces of the optimized electrodes. Also, the insertion of a diffusion barrier like Al_2O_3 ,²⁸ TiO_2 ,^{34,35} or HfO_xN_y ³⁶ has been reported to be beneficial for the ferroelectricity.

Compared to conventional ferroelectric materials such as lead zirconate titanate (PZT) or barium titanate (BTO),³⁷ hafnia is distinguished by its necessity of electric field cycling to induce or increase the ferroelectric polarization. This so-called wake-up effect was attributed to two main mechanisms: field-induced structural transformations as well as changes in the defect chemistry. Several structural transformations have been reported, namely, from M to O-FE³⁸ and from T to O-FE.³⁹ During wake-up of Si^{5-} or Zr^{4-} -doped HfO_2 , this T to O-FE transition is accompanied by an antiferroelectric (AFE)-like behavior and by the occurrence of double peaks in the $I(V)$ curves. This phase transition could be reversibly driven by the depolarization field in the T phase at low electric fields.⁴⁰ Changing the Si- or Zr-doping concentration can suppress the AFE-like behavior.⁴⁵ More recently, the electric field-induced transition from the AFE orthorhombic

phase (AFE-O) $Pbca$ to O-FE has been reported for Zr-doped HfO_2 . This phase explains more convincingly the observed one unit-cell wide 180 domain walls (Cheng 2022).⁶⁹ The second mechanism that explains the wake-up effect origins from defect related changes and the commonly discussed defects in HfO_2 are oxygen vacancies (V_O).¹¹ A pure defect redistribution without generation of additional defects was proposed by Pesic *et al.*⁴¹ The highest defect concentration in the pristine state is likely to be at the electrode interfaces in the case of oxygen scavenging electrodes like TiN and TaN.²⁵ Here, V_O might pin domain motion, as proposed by Zhou *et al.*⁴² and confirmed by piezoresponse force microscopy (PFM).^{43,44} The redistribution of such defects might release pinned domains. However, it is likely that the defect concentration and distribution are interconnected with structural transformations, e.g., the T phase being stabilized at higher V_O -concentrations.⁴⁵ Density functional theory (DFT) calculations further showed that charged V_O can stabilize the FE-O phase.¹¹

Nukala *et al.* observed reversible migration of V_O through Zr-doped HfO_2 in a scanning transmission electron microscope (STEM) during *operando* field cycling of Zr-doped HfO_2 and proved the participation of the V_O during field cycling.¹³ Nevertheless, the ferroelectricity and the wake-up effect of HfO_2 cannot be explained solely by the generation, redistribution, or migration of oxygen vacancies because ferroelectricity is a strongly anisotropic structural material property and is, therefore, related to the microstructure. The optimal orientation for the highest ferroelectric polarization is $[001]$, where the polarization vector is parallel to the electric field (i.e., out-of-plane of the thin film). In epitaxial films, a pure $[001]$ orientation is hard to achieve since $[010]$ almost has the same lattice spacing. Hence, on a (001) oriented yttria-stabilized zirconia substrate with a Sn-doped In_2O_3 electrode with Y-substituted HfO_2 , Shimizu *et al.* observed a mixed $[010]$ and $[001]$ oriented thin film. This has a predominantly $[010]$ orientation with in-plane polarization which may reduce electrostatic energy. However, field cycling induced ferroelastic 90 domain switching leads to a predominantly $[001]$ orientation of the HfO_2 .⁴⁶

Lederer *et al.* reported ferroelastic switching in polycrystalline HfO_2 thin films.^{47–49} In non-epitactic, polycrystalline thin films, the orientation control is much harder and only few reports investigated the orientation dependence of the ferroelectricity of HfO_2 . Lee *et al.* have shown the benefit of [112] oriented grains in 2 nm thick Zr-doped HfO_2 , where the *c*-axis is closer to the plane normal *E*-field in comparison to [111] or random orientation.⁵⁰ Chenk *et al.* further concluded that La doping can induce a small [001] texture improving the remnant polarization (P_r) and reducing the wake-up effect.²⁶

Concluding this overview, ferroelectricity of HfO_2 is quite sensitive to doping,^{4,5,26} V_{O} -concentration,¹⁰ heat treatment,^{29,51} and electrode interfaces.^{28,33,34,36} The deposition technique also matters because of the possible introduction of impurities³⁵ and different energies during thin film growth. Therefore, in this work, we investigated radio frequency (RF) sputtered HfO_2 to get a deeper understanding of ferroelectricity in pure HfO_2 with TiN electrodes. For sputtered and undoped FE HfO_2 , Mittmann *et al.* reported a strong temperature dependence for the ferroelectric and dielectric properties.¹⁰ Here, we present results of samples after RTA with a large temperature gradient across a $10 \times 10 \text{ mm}^2$ substrate with TiN/ HfO_2 /TiN devices. The temperature gradient during RTA eliminates any device-to-device variability from different depositions and facilitates data interpretation.

A combination of electrical characterization and transmission electron microscopy (TEM) analysis in plan-view and in cross section in *ex situ* experiments was applied. The plan-view samples with trained devices have the benefit of better statistics in diffraction analysis due to larger analyzed volumes. While cross sections of thin films with grain sizes smaller than the lamella thickness, on the other hand, have the inherent problem of superimposed grains. This hinders precise orientation and phase determination in cross section of the HfO_2 phases which are hard to distinguish anyway. Only the M phase differs significantly from the O-FE and T phase due to its monoclinic {111}M-splitting. The T and O-FE phases, however, can be hardly distinguished by means of diffraction. In the T phase, the (001)T planes correspond to the (100)O planes in the O-FE phase and the {110}T planes without *c*-components correspond to the (020)O and the (002)O planes with almost equivalent *d*-values. Mainly, the anion coordination is different between these two phases as shown in Fig. 1. The combination of plan-view and cross section has shown at least two preferential orientations of HfO_2 grains: {111} and [110]. In the hot corner, the {111} orientation dominates, which is able to show wake-up free ferroelectric polarization. While in the cold corner, the stronger [110] preferred orientation with in-plane polarization induces a strong wake-up effect due to ferroelastic 90 domain switching which could be observed by a slight structural rearrangement.

II. EXPERIMENTAL DETAILS

A. Device preparation and characterization

TiN back electrodes (BE) were deposited by reactive direct current (DC) sputtering of a Ti target with 18 SCCM Ar and 6 SCCM N_2 . Subsequently, HfO_2 was RF sputtered from a ceramic hafnia target. A homemade RTA setup was applied to crystallize the films using a projector lamp in a N_2 -atmosphere. The temperature

was set with a thermocouple near the $10 \times 10 \text{ mm}^2$ Si wafer substrate. By this, approximately 600°C is maintained for 10 s. The TiN top electrode (TE) was deposited with the same parameters as the BE after UV-lithography and was patterned by a lift-off process. Further deposition parameters are given in the [supplementary material](#). We characterized devices with TEs of sizes of approximately 25×25 and $50 \times 50 \mu\text{m}^2$. Current–voltage [*I*(*V*)] and polarization–voltage [*P*(*V*)] measurements as well as fatigue measurements are recorded using a ferroelectric analyzer TF2000 from aixACCT. Corrected *P*(*V*) curves were acquired using a Precision Premiere II from radiant technologies. Capacitance–voltage [*C*(*V*)] data were measured using an HP 4284A Precision LCR Meter from HP.

Infrared (IR) thermal imaging using an Infratec PIR 180 camera with a temperature resolution of 0.08 K at 303 K was performed directly after RTA during cooling with a time-delay of below 2 s.

B. TEM sample preparation and analysis

For plan-view TEM sample preparation, we first cut the Si wafer piece into $5 \times 5 \text{ mm}^2$ pieces by using a diamond band saw. With an ultrasonic disk-cutter and a SiC solution, sample blanks with a diameter of 3 mm were punched out. Since the SiC prevents electrical contacting with the electrodes, an acetone-soluble resin (Photoresist: AZ 5214E MicroChemicals) was spin coated on top of the TEs as the protective layer. This resin was completely removed from the sample blank to train all devices in the center of the sample with an oscilloscope 10^5 cycles at 6 Vpp. Subsequently, TEM preparation in the conventional mechanical way was performed by removing the material starting from the backside so the devices on top could be investigated. For this purpose, the sample was pre-thinned to a thickness of approximately $100 \mu\text{m}$ with different SiC sandpaper thicknesses (1200, 2500, and 4000). Hereafter, the sample was thinned in the dimpler (Dimple Grinder Model 656 from Gatan Inc.) with diamond grinding paste: a $3 \mu\text{m}$ paste and a copper wheel were used to remove a depression to a depth of approximately $30 \mu\text{m}$, and then, a felt wheel and a paste with $1 \mu\text{m}$ grain were used to thin three times for 2 min. The final polishing step was done by argon ions using a Precision Ion Polishing System (PIPS, Model 691 from Gatan Inc.). The initial acceleration voltage was set to 3.5 kV for 30 min and was reduced to finally 2.0 kV until a hole with electron transparent edges was created. Cross-sectional TEM samples were prepared with a Focused Ion Beam (FIB) in a FEI Helios Nanolab system. Prior to Ga-ion etching, a protective Pt layer was deposited with a gas injection source inside the FIB system. PIPS plan-view and FIB cross-sectional TEM samples were prepared from Position (Pos) 1 with the best and from Pos 3 with the worst ferroelectric properties to analyze the microstructural differences. The edges of the PIPS holes were more or less rolled up, maybe due to internal stress. We performed tilting series for selected area electron diffraction (SAED) to determine the actual plan-view. Here, the background level was lowest and no segmented diffraction rings appeared due to preferential growing directions. All tilting angles in this paper are given relative to the angle of the determined plan-view. The electron diffractograms were further processed for deeper analysis. First, we formed rotational averages and subtracted the background with a Python script by fitting a

polynomial of degree 6 to manually selected background regions. These regions in the diffraction patterns were the same for all samples to increase comparability. SAED of plan-view samples and analysis of cross sections were performed at a FEI Tecnai F30 G² with 300 kV and a field emission gun. Dark field imaging was performed at a Jeol JEM-2100 with 200 kV from a LaB₆ cathode.

III. RESULTS

A. Electrical characterization

Electrical analysis of the devices on the $10 \times 10 \text{ mm}^2$ Si chip showed inhomogeneities in terms of polarization and leakage currents. For a general classification, three areas were identified which showed characteristic features in their current–voltage [I(V)] behavior. Figure 2 shows a comparison of the electrical properties of these three areas together with a local assignment on the Si chip. Pos 1 can be defined by an observable wake-up effect, a clearly visible polarization and displacement current after the wake-up procedure, as well as low leakage current components.

In contrast, Pos 3 showed little to no influence from training, as well as lower polarization and higher leakage currents. Between these two extremes was Pos 2 which showed some influence of the training routine and less leakage current than Pos 3. The remnant values of Pos 2 and Pos 3 were comparable after wake-up. The comparison of the two extreme cases, Pos 1 and Pos 3, in the pristine state showed a pre-existing remnant polarization (P_r) at Pos 3 of $8.4 \mu\text{C}/\text{cm}^2$ while Pos 1 showed no displacement current peaks [see Fig. 2(c)] and, therefore, no remnant ferroelectric polarization.

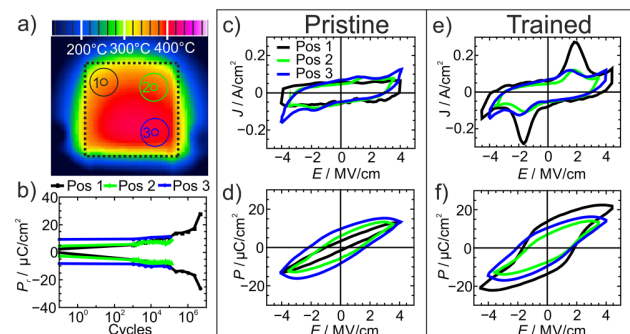


FIG. 2. (a) IR temperature image of the wafer piece (dashed square), which was lying in the RTA holder taken less than 2 s after RTA at 600°C . The dashed square marks the $10 \times 10 \text{ mm}^2$ Si chip. Circles mark the positions where PIPS TEM samples were extracted and prepared. The temperature in the small circle was 352°C in Pos 1, 380°C in Pos 2, and 405°C in Pos 3. (b) shows the remnant polarization over the cycle numbers for Pos 1, 2, and 3. The $J(E)$ [(c) and (e)] and $P(E)$ [(d) and (f)] characteristics are shown in the pristine state (left side) and in the trained state (right side) after 10^5 cycles for Pos 2 and 3 before breakdown and after 10^6 cycles for Pos 1. In the pristine state, devices from Pos 2 and 3 show a peak from the ferroelectric displacement currents in the $J(E)$ curves in (c), while devices from Pos 1 need field cycling to induce ferroelectric polarization. After the wake-up procedure devices from Pos 1 develop a prominent displacement current peak in (e) and a stronger polarization than devices from Pos 2 and 3.

It should be mentioned that uncorrected polarization values, such as recorded here, and a dynamic hysteresis measurement may be distorted by the influence of leakage currents. There are also differences with regard to leakage current density in the pristine state of those two positions. Devices close to Pos 1 showed a leakage current density of $20 \mu\text{A}/\text{cm}^2$ at 2 V which was lower by one order of magnitude compared to devices close to Pos 3 with $200 \mu\text{A}/\text{cm}^2$ at the same voltage (see Fig. S1 in the [supplementary material](#)). After a wake-up of 10^6 cycles with 8 V peak to peak (V_{pp}) devices from Pos 1 developed a P_r of $13.7 \mu\text{C}/\text{cm}^2$ without strong increase of the leakage contribution. Ultimately, after 10^6 cycles the leakage contribution increased before breakdown. Therefore, the last measured P_r value of $27.9 \mu\text{C}/\text{cm}^2$ at 4.6×10^6 cycles in Fig. 2(b) is likely to be overestimated, as here the leakage current distorts the determined polarization. On the other hand, devices from Pos 3 do not show a significant increase in P_r after 10^5 cycles before they break down. In addition, devices in Pos 3 showed a significantly lower yield in terms of measurability of ferroelectric behavior due to low breakdown voltages close to the coercive field and poor endurance of the devices in this region.

We tracked down the different ferroelectric performance depending on the position of the ferroelectric devices on the $10 \times 10 \text{ mm}^2$ Si wafer piece to the RTA process by thermal imaging. Figure 2(a) shows a temperature image of a wafer piece immediately after the RTA process (less than 2 s) during cooling at air. Three positions are marked from where PIPS samples were prepared. In the small circles, which indicate the hole from the PIPS sample, we measured a temperature of 352°C in Pos 1, 380°C in Pos 2, and 405°C in Pos 3. During RTA, the temperature difference should be even higher as the gradient tends to equalize during cooling down. The reason for this gradient is the slightly disaligned filament inside the projector lamp in the homemade RTA setup.

A different defect structure or morphology due to inhomogeneous sputter deposition parameters depending on the position relative to the target center was reported for the same sputter deposition chamber.⁵² However, this source of inhomogeneity is unlikely since deposition was done with a 4-in. target and on the $10 \times 10 \text{ mm}^2$ Si substrate placed close to the center the sputter parameters should be homogeneous.

B. Structural characterization

The cross-sectional images in Fig. 3 show a columnar TiN BE with a width around 5 nm, a 9.8 nm HfO_2 layer, and a TiO_xN_y interlayer between the HfO_2 and the TiN TE. This interlayer has a thickness of $6 \pm 2 \text{ nm}$ in Pos 1 and $4 \pm 2 \text{ nm}$ in Pos 3. In Fig. 3(c), the interlayer is rather thick for Pos 3, while in Fig. 6(c), the interlayer has a thickness well below 3 nm. The TiN columnar structure of the TE is interrupted by this interlayer, which has an amorphous to nanocrystalline structure different from the rock salt structure of TiN. The higher O- and lower N-content in this interlayer was proven by electron energy loss spectroscopy (EELS) as shown in Fig. 3(d). Figure S9 in the [supplementary material](#) shows additionally an EEL spectrum of the BE, which is well comparable with the TE. These measurements were performed in STEM-mode with a scanning window in the respective regions. STEM (EDX or EELS) line-scans were not possible, as this interlayer is more

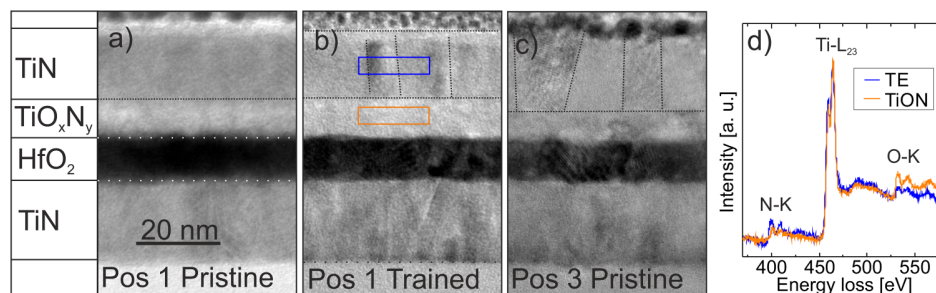


FIG. 3. Cross-sectional TEM images of three devices: (a) pristine device from Pos 1, (b) trained (10^5 cycles with 6 Vpp), and (c) pristine device from Pos 3. The sketch on the left side shows the device structure. (d) Background subtracted EEL spectra acquired in scanning TEM (STEM) mode with a scanning window on the TE (marked in blue) and the TiO_xN_y interlayer (marked in orange). The interlayer has the higher O-K edge and the lower N-K edge relative to Ti-L_{23} .

susceptible to electron beam damage and decomposes during the measurements even with reduced dose-rates.

Phase-analysis by electron diffraction revealed in all positions, the cubic ($Fm\bar{3}m$) structure of TiN with smaller lattice parameters of 4.20 Å compared to the bulk of 4.24 Å.⁵³ For HfO_2 , the phase-analysis is not so straightforward as the T, O-FE, and M phases have almost the same lattice spacings. Therefore, a detailed discussion can be found in the respective section. In both positions, however, the monoclinic phase can be ruled out since no {111} reflection splitting is observed and the d -value of the most intense diffraction ring in Fig. 4 with a d -value of 2.96 Å fits well with the {111} reflections of the O-FE phase but is very close to the {011} reflection of the T phase. The accuracy of the SAED measurements was confirmed with XRD [in-plane (IP) and grazing incidence (GI)] measurements (see Fig. S4 in the [supplementary material](#)). During these measurements, a systematic error of approximately 0.4 was evidenced in GIXRD due to refraction of the x-ray beam in the HfO_2 thin film.^{54–56} A detailed description can be found in the [supplementary material](#).

For texture analysis, we performed tilting series of the plan-view samples due to the higher number of grains in the SAED pattern compared to the cross sections. In all plan-view samples, all reflections are homogeneously distributed on the diffraction rings indicating rotational freedom of all grains [see Fig. 4(a)]. Furthermore, almost all reflections are present, except for the (200), (311), and the low intensity 120 of O-FE HfO_2 . However, upon tilting to 50°, segmented rings proved preferential orientations of both TiN and HfO_2 grains [see Figs. 4(a)–4(d)]. In the case of HfO_2 , the missing (200) and (311) reflections are tilted into the diffraction pattern indicating that no a -vector is oriented in-plane but approximately 45° out-of-plane. Due to the different d -values of the main lattice vectors (a)–(c), a serpent shape is formed in Fig. 4(d).

The SAED patterns of the cross section, aligned in zone axis of the Si substrate to guarantee perpendicular view on the interfaces, are well suited to determine the texture of TiN. Figure 5(a) shows clearly the {111} texture of TiN by an out-of-plane concentration of the {111} reflections. These {111} directions of the TiN columns are inclined by up to 10° to the film normal. For convenience, we denote all {111} oriented grains deviating up to 10° as being perpendicular to the film. A pure {111} textured TiN would

show only {220} reflections in the plan-view SAED pattern in Figs. 4(a) and 4(b). The presence of {111} and {200} reflections show a small amount of differently oriented grains.

For HfO_2 , however, the preferred orientation cannot that easily be seen in Fig. 5(a) due to the bigger grain size. Like TiN, HfO_2 shows also out-of-plane orientated {111} reflections. However, a strong {111} texture of HfO_2 cannot explain the plan-view electron diffraction pattern with high {111} intensity and

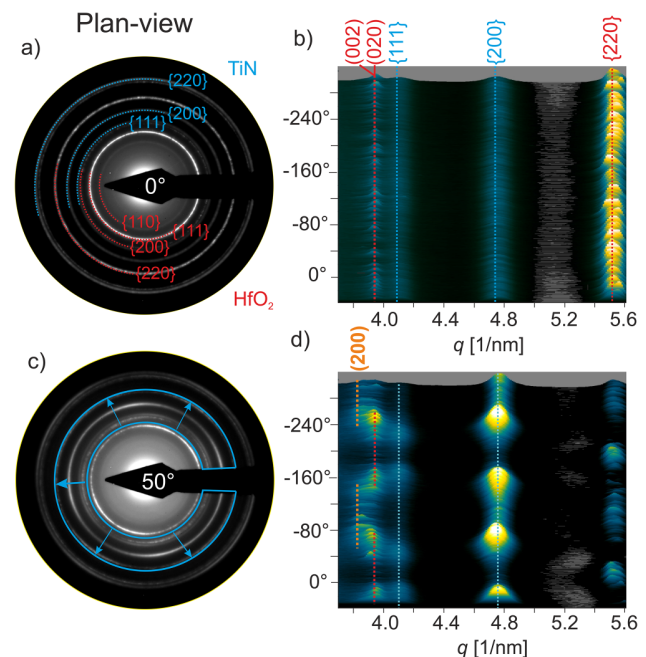


FIG. 4. SAED pattern of a pristine region in Pos 1 at 0° in (a) and 50° tilting angle in (c) (the contrast is increased for better visibility of the segmented rings). The surface plots in (b) and (d) illustrate the angle dependent intensity of the diffraction rings of TiN (blue) and HfO_2 (red). The respective region used for the surface plots is marked in (c).

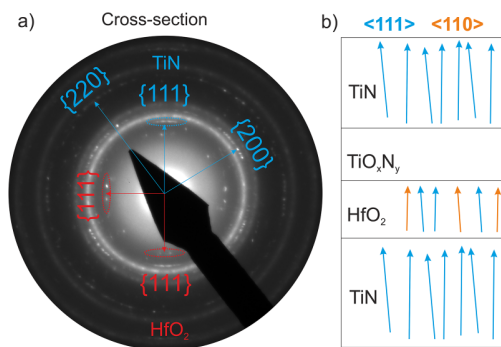


FIG. 5. (a) SAED pattern of the cross section from Pos 1 showing strong $\{111\}$ texture of TiN. The TiN diffraction pattern can be explained by multiple $\langle 110 \rangle$ zone axis with $\{111\}$ reflections oriented out-of-plane with approximately 10 tilt relative to the film normal. The HfO_2 does not show such pronounced single texture. Some $\{111\}$ reflections are oriented out-of-plane and some are oriented in-plane. The closed diffraction rings originate from the FIB-Pt with random orientation. The sketch in (b) illustrates the out-of-plane directions of TiN and HfO_2 . These are the viewing directions (zone axes) in the plan-view samples in Figs. 4(a) and 4(b).

missing (200) and (311) reflections. Therefore, we performed high resolution TEM (HRTEM) analysis of the cross sections for HfO_2 . Frequently, $\langle 111 \rangle$ and $\langle 110 \rangle$ out-of-plane directions (and few $\langle 100 \rangle$) were observed [see Figs. 5(b) and 5(c) and Fig. S8 in the supplementary material]. With these two main orientations of HfO_2 , the plan-view diffraction pattern can be explained as depicted in Fig. 4(b). $\langle 111 \rangle$ texture produces high $\{220\}$ intensity, while $\langle 110 \rangle$ grains explain the remaining diffraction rings. Especially, the missing (200) and (311) reflections can be produced by $[110]$ and $[101]$ orientations in plan-view. The (200) reflection can be tilted into the diffraction pattern at 45° as observed in Figs. 4(c) and 4(d). Furthermore, the observed in-plane $\{111\}$ reflections in Fig. 4(a) could arise from, e.g., a $[-110]$ out-of-plane orientation as being perpendicular to $[111]$.

To correlate the microstructure with the different electric responses, we performed SAED of plan-view PIPS samples and HRTEM analysis of cross sections from Pos 1 and 3 (see Fig. 6). The main difference between Pos 1 and Pos 3 is the intensity of the HfO_2 $\{220\}$ reflections in the SAED patterns (relative to $\{111\}$) in Fig. 6(a). In general, the intensity of $\{220\}$ serves as a fingerprint of a $\langle 111 \rangle$ texture, as these planes are the main reflections in a $\langle 111 \rangle$ zone axes pattern. Accordingly, Pos 3 with higher annealing temperature had a stronger $\langle 111 \rangle$ texture in comparison to Pos 1 (see Fig. 6). The quality of the PIPS sample from Pos 3 was much worse. First, the sample was contaminated with KCl [see indicated reflections in Fig. 6(a)]. Second, the analyzed film at the PIPS hole was thicker, resulting in a higher background level and stronger contributions by the TiN BE. To compare the diffraction pattern from Pos 1 and 3 nevertheless, the background was subtracted by the same routine with a polynomial of degree 6 and the intensity was normalized to the $\{111\}$ reflections of HfO_2 .

The grain size was analyzed via dark field (DF) imaging by selecting diffracted intensity with the objective aperture from HfO_2

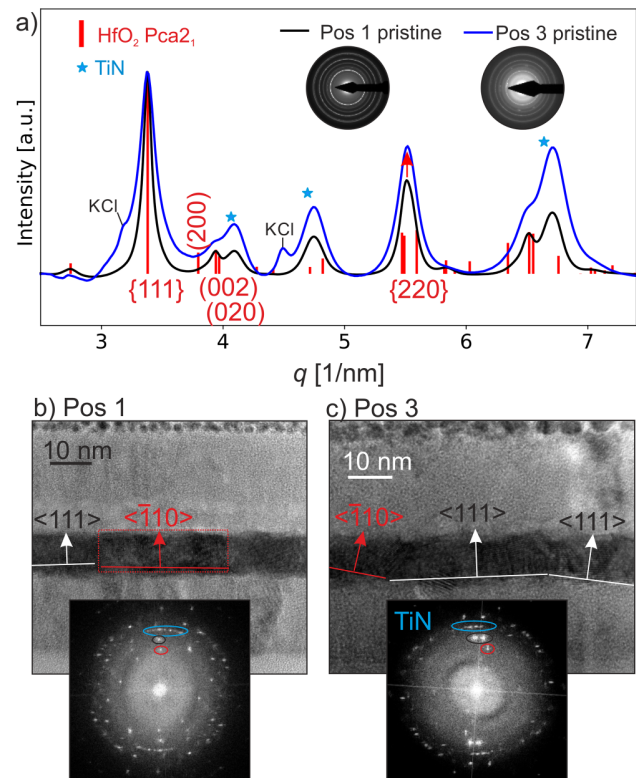


FIG. 6. (a) Plan-view rotational averages with background subtraction of SAED patterns from Pos 1 and Pos 3 are compared at 0 tilting and without TE. The original SAED patterns are shown in the insets. The intensity of the $\{220\}$ reflections of HfO_2 is higher in the sample from Pos 3 in comparison to Pos 1 (relative to $\{111\}$). The marked reflections stem from a KCl contamination. (b) and (c) show HRTEM micrographs of cross sections from Pos 1 and Pos 3. The Si substrate was tilted in the $[110]$ zone axis with the $[001]$ out-of-plane to guarantee plan-view on the cross sections. The out-of-plane directions are indicated for both positions. Pos 1 showed more $\langle 110 \rangle$ and Pos 3 more $\langle 111 \rangle$ out of plane directions. The insets show fast Fourier transformed images (FFT) of the entire micrograph.

$\{111\}$ and $\{220\}$ diffraction rings as indicated in Fig. S6 in the supplementary material. As revealed by texture analysis, HfO_2 has two predominant orientations: $\langle 111 \rangle$ and $\langle 110 \rangle$. Accordingly, the grains from $\{111\}$ reflections originate mainly from $\langle 110 \rangle$ out-of-plane directions and the grains from $\{220\}$ originate from both $\langle 111 \rangle$ and $\langle 110 \rangle$ out-of-plane directions. The statistics of three to six DF images are shown in Table I for Pos 1 and 3 and exemplary dark field images and histograms are shown in Fig. S6 in the supplementary material. The main difference is the mean grain size from the $\{220\}$ grains which increase their average size from 13.0 to 18.7 nm from Pos 1 to 3. The $\langle 111 \rangle$ oriented grains increase their average size while the $\langle 110 \rangle$ grains decreased by 0.7 nm in average which is measured from the $\{111\}$ reflections. This conclusion is supported by the higher deviation of the grain size in Pos 3 from $\{220\}$ reflections since the smaller grains are also included.

TABLE I. Statistical evaluation of DF images from Pos 1 and 3 and from {111} and {220} reflections of HfO₂. The mean grain size \bar{d} was determined from the reflections indicated in the brackets. Further, the standard deviation (SD) and the standard error (SE) are tabulated.

	$\bar{d}_{\{111\}}$ (nm)	SD (nm)	SE (nm)	$\bar{d}_{\{220\}}$ (nm)	SD (nm)	SE (nm)
Pos 1	16.3	7.8	0.28	13.0	7.0	0.43
Pos 3	15.6	6.7	0.32	18.7	9.8	0.93

Accordingly, the grain size analysis supports the conclusions from texture analysis that Pos 3 has a higher $\langle 111 \rangle$ texture and gives an explanation with Ostwald ripening of these grains.

To understand the strong wake-up behavior of the devices from Pos 1, we analyzed two trained devices in plan-view and from close regions without TE. The rotational averages in Fig. 7(a) compare a pristine HfO₂ region close to a trained TE of a device in Pos 1 after 10⁵ cycles at 6 Vpp with a triangular wave. The {002} reflections of HfO₂ shift to slightly larger d -values as well do the {113} reflections. Further, the intensity of the (110) reflections decreases. At the same time, all TiN reflections remain largely unchanged, despite an increased intensity which can be explained by the additional TiN TE. This structural transformation was observed in two trained devices in several rotational averages. An effect from the TE (or the TiO_xN_y interlayer) during training can be ruled out, as a pristine TE of Pos 1 shows no shifting of d -values [see Fig. S7(b) in the [supplementary material](#)].

Additionally, a device trained in the same way was analyzed in cross section. A HRTEM micrograph of one grain is shown in Fig. 7(b). The FFT analysis of the HRTEM micrograph suggests that the c -direction is in-plane on the left side of the grain, while on the right side, the b -direction is in-plane oriented. Two pieces of evidence were found in support of this thesis. First, in the left part, (110) planes can be observed in the FFT, while in the right part, only the (202) planes can be seen. This may be explained by the extinction by symmetry of the (101) reflections. Further, in the left part of the grain, the (001) lattice spacing is slightly larger compared to the right part (see line-scans in Fig. 7). Both features suggest the switching of the in-plane c -axis on the left side to the in-plane b -axis on the right side. Concluding, we observed a minor structural transformation after the field cycling evidenced by SAED in plan-view and in HRTEM in cross section. A more detailed discussion with reference to all structural results and the literature can be found below.

IV. DISCUSSION

An exclusive consideration of the polarization curves of thin ferroelectric layers can lead to misinterpretation as it is not simple to differentiate between switching currents and leakage currents. Therefore, a consideration of I(V) data is given in the [supplementary material](#), which unambiguously shows the ferroelectric character of this HfO₂ thin film. In addition, a corrected P(V) curve with the positive-up negative-down (PUND) method is shown in Fig. S2(a) in the [supplementary material](#).

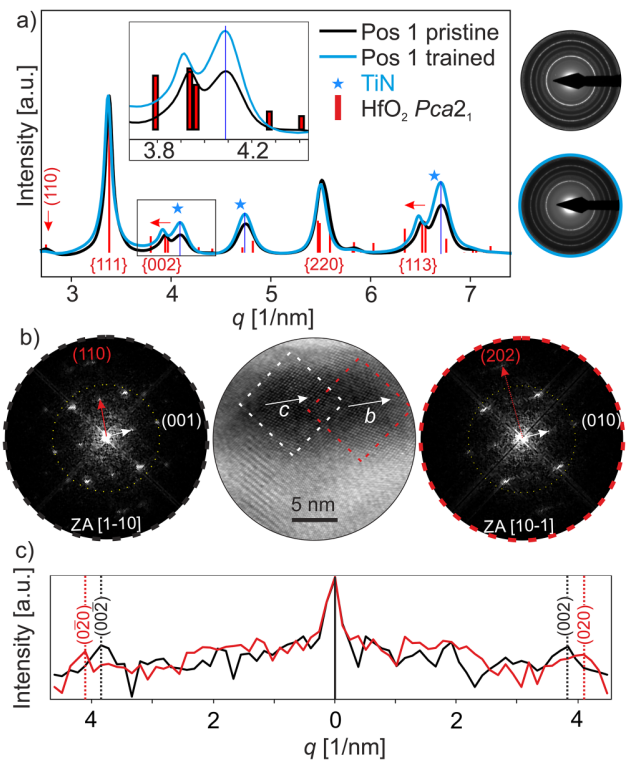


FIG. 7. The processed rotational average of a SAED pattern (original data shown on the right) in (a) compares a pristine region (black) next to a trained device (turquoise) in Pos 1 after 10⁵ cycles at 6 Vpp. The inset enlarges the diffraction pattern of the {002} reflections of HfO₂ where a shift to larger d -values can be observed (note the reciprocal scale). (b) shows a HRTEM micrograph (center) of a HfO₂ grain with both b and c in-plane next to each other. The dashed rectangles mark the regions used for the FFT analysis on the left (white) and on the right (red). In (c), line-scans are shown through the intensity peaks of the (002) planes (black) on the left and the (020) planes (red) on the right in the FFTs in (b). In these line-scans, a clear difference of the lattice spacings can be observed. Further, no intensity of the (101) planes is observable in the FFT on the right. Only the (202) planes can be observed, which fits to [10-1] zone axis of HfO₂ in the O-FE phase.

Stable ferroelectric switching was observed for at least 10⁵ cycles in Fig. 2 without shifts of the peaks in the I(V) curves and a fatigue or strong increase in the leakage currents, which can be estimated by the tail at high electric fields in Figs. 2(c) and 2(e). Therefore, we assume both electrode interfaces are stabilized against the generation of interfacial V_O as discussed next. At the interface to the BE, no oxidized interlayer could be observed in cross-sectional HRTEM micrographs (see Fig. 6). We suspect that a low Ti content (i.e., Ti_{1-x}N) in the TiN stabilizes the interface between HfO₂ and BE during deposition and during RTA. This can be explained with the N-saturation of the Ti-atoms. The low Ti content in the TiN electrodes can be correlated with the decreased d -values of the TiN structure in comparison to stoichiometric bulk TiN⁵⁷ and to Mittmann *et al.*, who sputtered TiN with a

lower N_2/Ar ratio (4/20 SCCM) than we did (6/18 SCCM).¹⁰ In the first place, an excess in N-content (e.g., as interstitials) leads to an increase in d -value, as shown in different reports.^{57–59} However, a Ti-deficiency can decrease the d -values in the same way as we observed, as shown for Ti-deficient nanoparticles.⁶⁰ Thus, the decreased lattice spacing of TiN (compared to bulk TiN and also to Mittmann *et al.*¹⁰) points toward a Ti-deficiency, which is equivalent to a N/Ti ratio > 1 . Different reports have shown that higher N/Ti ratios in TiN improve the endurance of ferroelectric HfO_2 ^{30–32} which can be assigned to the stabilization of the interfaces. Nevertheless, an interaction between HfO_2 and BE is expected during RTA. With the higher temperatures in Pos 3, diffusion processes should be faster. This should lead to a higher V_O concentration as the BE stronger oxidized during RTA. This higher V_O concentration in Pos 3 is also reflected by the higher leakage currents (see Figs. 2 and S1 in the [supplementary material](#)) which was also reported in the literature.^{51,61} However, the BE stays in its cubic TiN crystal structure and no interfacial oxidation could be observed in cross-sectional HRTEM micrographs (see Figs. 6 and S8 in the [supplementary material](#), by an amorphous interface). Accordingly, the oxygen ions may diffuse in the TiN structure, e.g., as interstitial or more likely along the grain boundaries.⁶²

In contrast to the BE, the interface to the TE is interrupted by an additional TiO_xN_y interlayer (see Fig. 3). In Pos 1, the interlayer is with 6 ± 2 nm almost as thick as the HfO_2 layer itself, while in Pos 3, the interlayer has a thickness of 4 ± 2 nm. The TiN TE must have oxidized during reactive sputtering of the TE since it is already present in the pristine state to the same extent (see Fig. 3). The only oxygen sources are the oxygen background pressure during sputtering and the HfO_2 layer. The background pressure should be the same for Pos 1 and 3. Seemingly, the different annealing temperatures of the HfO_2 affect the TiN TE deposition. Marchack *et al.* described a possible mechanism: reactive sputtering can generate vacancies in the substrate by sputtering atoms away,⁶³ and in HfO_2 , preferential O-ion sputtering is expected due to their smaller mass in comparison to Hf. These sputtered O-ions oxidize the growing TiN TE. Such a mechanism is supported by the observation of Matveyev *et al.*, who reported on a thicker oxidized interlayer between the sputtered TiN TE compared to the TiN BE deposited with ALD after RTA with both electrodes.⁶⁴ This observation might support our conclusion that the TiN TE is oxidized during reactive sputtering, and we hypothesize that the higher V_O concentration in Pos 3 with the higher RTA temperature leads to the thinner TiO_xN_y thickness. Thus, intentionally oxidizing the bottom of the top electrode appears to be a strategy to stabilize the interface to HfO_2 . In analogy, oxidizing the top of the BE³⁴ or inserting a diffusion barrier (like Al_2O_3 ,^{28,65} $HfON$,³⁶ or NH_3 -plasma treatments of both electrode interfaces³³) has already been shown to be beneficial for the ferroelectric polarization of HfO_2 . However, the latter approaches have the drawback that further deposition steps are required. In conclusion, both interfaces to the TiN electrodes are stabilized: one by an oxidized diffusion barrier and one by Ti deficiency.

Further, we discuss the different wake-up behavior of devices from Pos 1 and 3. The lower V_O concentration can explain the lower leakage and the higher breakdown voltage in Pos 1. However, the negligible pristine P_r and the strong increase during wake-up is

unlikely an effect from the lower V_O concentration. In comparison to Pos 3, the texture analysis has shown that Pos 1 has a stronger $\langle 110 \rangle$ texture without a -vector components in-plane (i.e., not $[011]$). To our knowledge, there is no structural reason why the b or c direction should be preferentially oriented in-plane (e.g., by local epitaxy with TiN during nucleation) as their d -values are almost identical. Another observation is that in the pristine state, no ferroelectric polarization is observed in Pos 1 which leads to the conclusion of an $[110]$ textured HfO_2 . Shimizu *et al.* argued that an in-plane polarization minimizes the electrostatic energy⁴⁶ what would favor the $[110]$ orientation over the $[101]$ orientation. In this case, no ferroelectricity is expected as the polar c -axis is orthogonal to the electric field.

Ex situ TEM experiments, both in plan-view and in cross section, of devices from Pos 1 of trained electrodes after 10^5 cycles at 6 Vpp have shown a small structural transformation. This is mainly indicated by an increased d -value of the $\{002\}$ reflections of HfO_2 . A similar shift to larger d -values of the $\{002\}$ reflection due to the wake-up of Gd-doped HfO_2 was observed with micro-spot XRD by Hoffmann *et al.* but was discussed as a minor effect. They proposed the de-trapping of domain walls at oxygen vacancies being responsible for the wake-up effect.²⁵ Fields *et al.* measured as well an increasing d -value accompanied by a reduction of the FWHM of reflections and assigned the here reported observations to a phase exchange from T to O-FE.⁶⁶ In contrast, our results suggest that the wake-up in our devices happens without phase transformations as discussed next. The presence of the T phase cannot be excluded entirely by electron diffraction but few indicators hint toward the O-FE phase. First, the observed (110) reflection of the O-FE phase [see Fig. 4(a)] is forbidden by symmetry in the T phase. However, the corresponding reflections in the T phase ($\{100\}$ without c -vector components) might be diffracted by double diffraction, which is a common phenomenon in the TEM.⁶⁷ Second, the $\{221\}$ and $\{230\}$ reflections (shoulders at 5.9 1/nm and at 7.0 1/nm in the rotational averages in Fig. 6) do not exist in the T but in the O-FE phase. Third, the electrical characterization proves the ferroelectricity, at least below the trained TEs, where the mentioned shoulders do not change significantly in intensity. Nevertheless, the coexistence of the T phase next to the verified O-FE phase cannot be excluded by our structural analysis. However, a look on the training data reveals no signature for the T phase. A T-to-O-FE phase transition is suspected for (initial) AFE-like behavior which is indicated by pinched hysteresis loops in Si^{5-} and Zr^{4-} -doped HfO_2 and by double peaks in $I(V)$ -characteristics.^{40,68} Grimley *et al.* and Cheng *et al.* observed interfacial, defect-rich T layers and these were discussed to form nonuniform internal bias fields at the interfaces, resulting in double peaks in the pristine $I(V)$ curves.^{38,69} In our experiments, no double peaks or AFE-like behavior were observed in either Pos 1 (see Fig. S3 in the [supplementary material](#)) or Pos 3. Thus, the combination of structural analysis by plan-view TEM and electrical characterization suggests a phase pure orthorhombic HfO_2 thin film deposited by RF sputtering. This thesis is supported by the observation by Chen *et al.* who prevented such AFE behavior from the interfacial T phase in the $I(V)$ -curves by NH_3 plasma treatments of both electrode interfaces.³³ In our case, the interfaces are stabilized by Ti-deficiency of the BE and the TiO_xN_y interlayer to the TE. Thus, we exclude a phase transition during wake-up.

We hypothesize a structural rearrangement being responsible for the observed wake-up effect, as discussed next. For this interpretation, we assume a correlation of the lattice and the atomic structure, which may not necessarily be the case in disordered defect distributions. Taking a deeper look on the structural transformation with respect of an [110] textured HfO_2 reveals a rather conclusive picture. As mentioned before, the (020)/(002) d -value increases. The same is true for the {113} reflections. Further, the (110) intensity decreases, while the {220} intensity is almost unaffected. All these changes can be correlated by a gradual transformation of the in-plane c axis to the b - or a -axis of the [110] out-of-plane oriented grains. This would explain the decrease of the (110) intensity, as the other {011} reflections are extinct from symmetry, while the intensity of all {220} reflections is unaffected. Such structural rearrangement can also explain the increasing d -values as the longer a -axis of the FE-O structure starts to contribute to the diffraction. This transformation must not be interpreted as a 90 rotation of the unit cell but rather as minor (electric field driven) rearrangements of the oxygen ions in the fluorite-type structure. These rearrangements should be facilitated by the presence of charged V_O in the structure which already induced structural distortions to compensate the missing negative charge.¹¹ A similar structural rearrangement was observed by Shimizu *et al.* in an epitaxial 7%-YO_{1.5}-substituted HfO_2 system with mainly [010] out-of-plane direction in the pristine state. They argued that the pristine thin film minimizes electrostatic energy with in-plane polarization (c -axis) and a depolarization field out-of-plane. This in-plane c -axis switches out-of-plane during electric field cycling. Shimizu *et al.* denoted this phenomenon to ferroelastic 90 domain switching.⁴⁶ This ferroelastic switching was also reported by Lederer *et al.* on polycrystalline HfO_2 based films.^{47–49}

We hypothesize that both the a - and the b -axes can exchange with the c -axis. In the first case, all oxygen ions in tetrahedron centers remain on their positions and only three of the oxygen ions on tetrahedron faces in the unit cell have to change their ligands and move through the tetrahedron center to the tetrahedron faces as indicated in Fig. 8(a). This scenario is likely, because in the actual ferroelectric switching the oxygen ions move also, electric

field driven, through the tetrahedron centers.¹⁸ However, in the case where the c and b axes exchange, half of the oxygen ions on tetrahedron faces move to tetrahedron centers and vice versa as depicted in Fig. 8(c). This exchange has the shorter distances for atomic movement in comparison to Fig. 8(a). These are, however, very simplistic considerations, which have to be verified by computational modeling like density functional theory taking also the V_O into account. This is out of the scope of this paper.

The cross-sectional analysis gives further hints for this interpretation of the structural changes. Figure 7(b) shows the HRTEM micrograph of one HfO_2 grain within which the switching of orientations may have happened. This observation is made after 10^5 cycles, before FIB preparation, where the maximum P_r is not reached yet which may indicate a gradual ferroelastic switching within single grains.

The wake-up effect by ferroelastic switching of the [110] oriented grains in Pos 1 is further supported by the different wake-up behavior of devices in Pos 3. Here, the mean grain size of $\langle 110 \rangle$ oriented grains has decreased while $\langle 111 \rangle$ oriented grains have increased as determined via DF images. The Ostwald ripening of the $\langle 111 \rangle$ oriented HfO_2 grains is supported by different reports in the literature. $\langle 111 \rangle$ textured HfO_2 was reported after extended RTA at 600 °C for 30 s or more,²⁹ 500 °C for 30 s,⁴⁴ and a HfO_2 thin film grown at 810 °C which in this case results in the M phase.⁷⁰ Additionally, the surface of {111} planes of the isostructural ZrO_2 has the lowest energy in the cubic, tetragonal, and monoclinic phases.⁷¹ Therefore, it seems likely that for HfO_2 , these surfaces are also energetically favored. In contrast to the $\langle 110 \rangle$, $\langle 111 \rangle$ orientated grains cannot minimize electrostatic energy with in-plane polarization, as the c -direction always points out-of-plane with an angle of 55.2°.⁵⁰ This can explain the ferroelectric polarization in the first cycle. Why this P_r value remains stable during field cycling until breakdown, we can only speculate because $\langle 110 \rangle$ grains are still present inside this HfO_2 thin film which should increase the P_r with field cycling. We suspect that the ferroelastic domain switching is prevented by the higher V_O concentration which might pin the in-plane domains or that the electric field is too low for the ion motion as the lower breakdown voltage limits the applicable voltage.

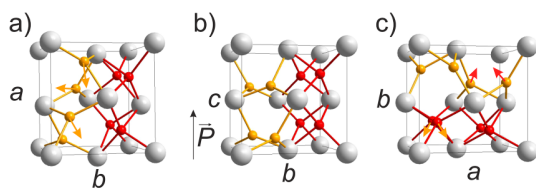


FIG. 8. The unit cells in (a) and (c) depict orientations with in-plane polarization while (b) shows out-of-plane polarization. Yellow arrows show the anion motion toward tetrahedron faces while red arrows toward tetrahedron centers. These motions are the presumed wake-up effect for devices in Pos 1. When a - and c -axes switch (a), anions on tetrahedron faces have to exchange their ligands. While for switching b - and c -axes (c), half of the anions exchange from tetrahedron centers to faces and vice versa. This exchange has the shorter distance in comparison to (a). For simplicity, the unit cells are oriented $\langle 100 \rangle$ out-of-plane and not as observed $\langle 110 \rangle$ oriented.

V. CONCLUSION

A temperature gradient in an RTA setup was applied to correlate the ferroelectric performance on a $10 \times 10 \text{ mm}^2$ chip with sputtered $\text{TiN}/\text{HfO}_2/\text{TiN}$ capacitors across the substrate. During RTA, the TiN BE scavenges oxygen from the HfO_2 and produces different concentrations of V_O . Depending on the temperature, the concentration of V_O increases macroscopically the leakage current by one order of magnitude in the hot region. While devices with a lower RTA, temperature produced a lower V_O concentration. During reactive sputtering of the TiN top electrode, a $6 \pm 2 \text{ nm}$ thick TiO_xN_y interlayer is formed, which appears less pronounced in the hot corner with higher V_O concentrations. No oxidized interlayer is observed at the back electrode, which is likely due to the presence of TiN with Ti-deficiency and with very fine columnar grains which can uptake oxygen ions along grain boundaries without forming an oxide interface. Therefore, we conclude that

both interfaces of HfO_2 to the electrodes are stabilized in terms of generating interfacial V_O during field cycling. This results in a stable leakage current during field cycling and during wake-up, no signatures of an interfacial tetragonal phase of HfO_2 [pinched hysteresis or double peaks in pristine $I(V)$ curves] were observed. The ferroelectric capacitors also show distinct wake-up behaviors depending on the RTA temperature. Devices from the corner with higher temperature exhibit wake-up free ferroelectricity with a P_r below $10 \mu\text{C}/\text{cm}^2$ (without leakage compensation), while the cold corner shows a strong wake-up from no polarization in the pristine state to an uncorrected P_r of up to $26 \mu\text{C}/\text{cm}^2$. Conventional structural analysis by plan-view and cross-sectional TEM in correlation with the electrical characterization revealed a dominantly orthorhombic HfO_2 thin film. In the cold corner, *ex situ* experiments after 10^5 cycles revealed a gradual ferroelastic 90 domain switching of $[110]$ oriented grains with in-plane polarization, which convincingly explains the evolution of the remnant polarization from 0 to up to $26 \mu\text{C}/\text{cm}^2$. In the hot corner, $\langle 111 \rangle$ oriented grains without the possibility of in-plane polarization become dominant. These occur due to Ostwald ripening and explain why the hot corner shows forming free ferroelectric polarization. Our findings underline the importance of temperature treatment, which affects the interfaces as well as the microstructural evolution of HfO_2 . Both have a strong impact on the ferroelectric behavior, especially on the wake-up effect. For device integration, the wake-up-free devices from Pos 3 are more promising due to their constant ferroelectric properties. We believe the lower endurance and lower breakdown voltage may be healed by a small admixture of oxygen during HfO_2 sputtering as proposed by Mittmann *et al.*¹⁰ or during RTA as proposed by Lee *et al.*²⁹

SUPPLEMENTARY MATERIAL

See the [supplementary material](#) for a more detailed description of the deposition parameters, electrical, as well as structural characterization.

ACKNOWLEDGMENTS

This work was funded by the Deutsche Forschungsgemeinschaft (DFG, German Research Foundation)—Project-ID 434434223—SFB 1461. Dr. Hendrik Gross is acknowledged for internal review and Mrs. Christin Szillus for TEM preparation. Further, Lena Saure is acknowledged for her assistance with thermal imaging.

AUTHOR DECLARATIONS

Conflict of Interest

The authors have no conflicts to disclose.

Author Contributions

O. Gronenberg: Conceptualization (equal); Formal analysis (lead); Investigation (lead); Methodology (equal); Software (lead); Visualization (equal); Writing – original draft (lead); Writing – review & editing (equal). **R. Marquardt:** Conceptualization (equal); Formal analysis (equal); Investigation (supporting); Methodology (supporting); Resources (lead); Writing – review & editing (equal).

R. Lamprecht: Formal analysis (equal); Investigation (equal); Resources (supporting); Writing – review & editing (equal). **Y. Ekici:** Formal analysis (supporting); Methodology (supporting); Writing – review & editing (equal). **U. Schürmann:** Methodology (equal); Supervision (equal); Validation (equal); Writing – original draft (equal); Writing – review & editing (equal). **H. Kohlstedt:** Conceptualization (equal); Funding acquisition (equal); Project administration (equal); Resources (equal); Validation (equal); Writing – review & editing (equal). **L. Kienle:** Funding acquisition (equal); Project administration (equal); Resources (equal); Supervision (equal); Validation (equal); Writing – review & editing (equal).

DATA AVAILABILITY

The data that support the findings of this study are available from the corresponding author upon reasonable request.

REFERENCES

- 1H. H. Radamson, H. Zhu, Z. Wu, X. He, H. Lin, J. Liu, J. Xiang, Z. Kong, W. Xiong, J. Li, H. Cui, J. Gao, H. Yang, Y. Du, B. Xu, B. Li, X. Zhao, J. Yu, Y. Dong, and G. Wang, “State of the art and future perspectives in advanced CMOS technology,” *Nanomaterials* **10**, 1555 (2020).
- 2M. S. Narula and A. Pandey, “Performance evaluation of stacked gate oxide/high K spacers based gate all around device architectures at 10 nm technology node,” *Silicon* **14**, 2397–2407 (2022).
- 3I.-S. Park, K.-R. Kim, S. Lee, and J. Ahn, “Resistance switching characteristics for nonvolatile memory operation of binary metal oxides,” *Jpn. J. Appl. Phys.* **46**, 2172–2174 (2007).
- 4J. Müller, T. S. Böscke, U. Schröder, S. Mueller, D. Bräuhäus, U. Böttger, L. Frey, and T. Mikolajick, “Ferroelectricity in simple binary ZrO_2 and HfO_2 ,” *Nano Lett.* **12**, 4318–4323 (2012).
- 5T. S. Böscke, J. Müller, D. Brauhäus, U. Schroder, and U. Böttger, “Ferroelectricity in hafnium oxide: CMOS compatible ferroelectric field effect transistors,” in *2011 International Electron Devices Meeting* (IEEE, Washington, DC, 2011), pp. 24.5.1–24.5.4.
- 6N. Du, N. Manjunath, Y. Li, S. Menzel, E. Linn, R. Waser, T. You, D. Bürger, I. Skorupa, D. Walczyk, C. Walczyk, O. G. Schmidt, and H. Schmidt, “Field-driven hopping transport of oxygen vacancies in memristive oxide switches with interface-mediated resistive switching,” *Phys. Rev. Appl.* **10**, 054025 (2018).
- 7B. Max, M. Pešić, S. Slesazeck, and T. Mikolajick, “Interplay between ferroelectric and resistive switching in doped crystalline HfO_2 ,” *J. Appl. Phys.* **123**, 134102 (2018).
- 8G. Niu, P. Calka, P. Huang, S. U. Sharath, S. Petzold, A. Gloskovskii, K. Fröhlich, Y. Zhao, J. Kang, M. A. Schubert, F. Bärwolf, W. Ren, Z.-G. Ye, E. Perez, C. Wenger, L. Alff, and T. Schroeder, “Operando diagnostic detection of interfacial oxygen ‘breathing’ of resistive random access memory by bulk-sensitive hard X-ray photoelectron spectroscopy,” *Mater. Res. Lett.* **7**, 117–123 (2019).
- 9M. Qi, Y. Tao, Z. Wang, H. Xu, X. Zhao, W. Liu, J. Ma, and Y. Liu, “Highly uniform switching of HfO_{2-x} based RRAM achieved through Ar plasma treatment for low power and multilevel storage,” *Appl. Surf. Sci.* **458**, 216–221 (2018).
- 10T. Mittmann, M. Materano, P. D. Lomenzo, M. H. Park, I. Stolichnov, M. Cavalieri, C. Zhou, C. Chung, J. L. Jones, T. Szyjka, M. Müller, A. Kersch, T. Mikolajick, and U. Schroeder, “Origin of ferroelectric phase in undoped HfO_2 films deposited by sputtering,” *Adv. Mater. Interfaces* **6**, 1900042 (2019).
- 11R. He, H. Wu, S. Liu, H. Liu, X. R. Wang, and Z. Zhong, “Charged oxygen vacancy induced ferroelectric structure transition in hafnium oxide,” *arXiv:2106.12159* (2021).

- ¹²S. Starschich, S. Menzel, and U. Böttger, "Evidence for oxygen vacancies movement during wake-up in ferroelectric hafnium oxide," *Appl. Phys. Lett.* **108**, 032903 (2016).
- ¹³P. Nukala, M. Ahmadi, Y. Wei, S. de Graaf, E. Stylianidis, T. Chakraborty, S. Matzen, H. W. Zandbergen, A. Björling, D. Mannix, D. Carbone, B. Kooi, and B. Noheda, "Reversible oxygen migration and phase transitions in hafnia-based ferroelectric devices," *Science* **372**, 630–635 (2021).
- ¹⁴M. H. Shao, H. F. Liu, R. He, X. M. Li, L. Wu, J. Ma, X. C. Hu, R. T. Zhao, Z. C. Zhong, Y. Yu, C. H. Wan, Y. Yang, C. W. Nan, X. D. Bai, T. L. Ren, and X. R. Wang, *arXiv:10.48550/ARXIV.2106.10837* (2021).
- ¹⁵R. Hann, P. Suitch, and J. Pentecost, "Monoclinic crystal structures of ZrO₂ and HfO₂ refined from x-ray powder diffraction data," *J. Am. Ceram. Soc.* **68**, 285–286 (1985).
- ¹⁶J. E. Jaffe, R. A. Bachorz, and M. Gutowski, "Low-temperature polymorphs of ZrO₂ and HfO₂: A density-functional theory study," *Phys. Rev. B* **72**, 144107 (2005).
- ¹⁷C. M. Fancher, L. Zhao, M. Nelson, L. Bai, G. Shen, and J. L. Jones, "Pressure-induced structures of Si-doped HfO₂," *J. Appl. Phys.* **117**, 234102 (2015).
- ¹⁸J.-H. Yuan, G.-Q. Mao, K.-H. Xue, N. Bai, C. Wang, Y. Cheng, H. Lyu, H. Sun, X. Wang, and X. Miao, "Ferroelectricity in HfO₂ from a chemical perspective," *arXiv:2201.00210* (2022).
- ¹⁹T. Mittmann, M. Michailow, P. D. Lomenzo, J. Gärtner, M. Falkowski, A. Kersch, T. Mikolajick, and U. Schroeder, "Stabilizing the ferroelectric phase in HfO₂-based films sputtered from ceramic targets under ambient oxygen," *Nanoscale* **13**(2), 912–921 (2021).
- ²⁰X. Sang, E. D. Grimley, T. Schenk, U. Schroeder, and J. M. LeBeau, "On the structural origins of ferroelectricity in HfO₂ thin films," *Appl. Phys. Lett.* **106**, 162905 (2015).
- ²¹S. Clima, D. J. Wouters, C. Adelman, T. Schenk, U. Schroeder, M. Jurczak, and G. Pourtois, "Identification of the ferroelectric switching process and dopant-dependent switching properties in orthorhombic HfO₂: A first principles insight," *Appl. Phys. Lett.* **104**, 092906 (2014).
- ²²P. Polakowski and J. Müller, "Ferroelectricity in undoped hafnium oxide," *Appl. Phys. Lett.* **106**, 232905 (2015).
- ²³P. Fan, Y. K. Zhang, Q. Yang, J. Jiang, L. M. Jiang, M. Liao, and Y. C. Zhou, "Origin of the intrinsic ferroelectricity of HfO₂ from ab initio molecular dynamics," *J. Phys. Chem. C* **123**, 21743–21750 (2019).
- ²⁴S. Estandía, N. Dix, J. Gazquez, I. Fina, J. Lyu, M. F. Chisholm, J. Fontcuberta, and F. Sánchez, "Engineering ferroelectric Hf_{0.5}Zr_{0.5}O₂ thin films by epitaxial stress," *ACS Appl. Electron. Mater.* **1**, 1449–1457 (2019).
- ²⁵M. Hoffmann, U. Schroeder, T. Schenk, T. Shimizu, H. Funakubo, O. Sakata, D. Pohl, M. Drescher, C. Adelman, R. Materlik, A. Kersch, and T. Mikolajick, "Stabilizing the ferroelectric phase in doped hafnium oxide," *J. Appl. Phys.* **118**, 072006 (2015).
- ²⁶T. Schenk, C. M. Fancher, M. H. Park, C. Richter, C. Künneth, A. Kersch, J. L. Jones, T. Mikolajick, and U. Schroeder, "On the origin of the large remanent polarization in La:HfO₂," *Adv. Electron. Mater.* **5**, 1900303 (2019).
- ²⁷H. J. Kim, M. H. Park, Y. J. Kim, Y. H. Lee, W. Jeon, T. Gwon, T. Moon, K. D. Kim, and C. S. Hwang, "Grain size engineering for ferroelectric Hf_{0.5}Zr_{0.5}O₂ films by an insertion of Al₂O₃ interlayer," *Appl. Phys. Lett.* **105**, 192903 (2014).
- ²⁸J. Wan, X. Chen, L. Ji, Z. Tu, H. Wu, and C. Liu, "Ferroelectricity of Hf_{0.5}Zr_{0.5}O thin films free from the influence of electrodes by using AlO capping layers," *IEEE Trans. Electron. Devices* **69**(4), 1–6 (2022).
- ²⁹Y. H. Lee, H. J. Kim, T. Moon, K. D. Kim, S. D. Hyun, H. W. Park, Y. B. Lee, M. H. Park, and C. S. Hwang, "Preparation and characterization of ferroelectric Hf_{0.5}Zr_{0.5}O₂ thin films grown by reactive sputtering," *Nanotechnology* **28**, 305703 (2017).
- ³⁰Z. Dang, S. Lv, Z. Gao, M. Chen, Y. Xu, P. Jiang, Y. Ding, P. Yuan, Y. Wang, Y. Chen, Q. Luo, and Y. Wang, "Improved endurance of Hf_{0.5}Zr_{0.5}O₂-based ferroelectric capacitor through optimizing the Ti:N ratio in TiN electrode," *IEEE Electron Device Lett.* **43**(4), 1 (2022).
- ³¹R. Athle, A. E. O. Persson, A. Irish, H. Menon, R. Timm, and M. Borg, "Effects of TiN top electrode texturing on ferroelectricity in Hf_{1-x}Zr_xO₂," *ACS Appl. Mater. Interfaces* **13**, 11089–11095 (2021).
- ³²Y. Li, R. Liang, B. Xiong, H. Liu, R. Zhao, J. Li, T. Liu, Y. Pang, H. Tian, Y. Yang, and T.-L. Ren, "TiN_x/Hf_{0.5}Zr_{0.5}O₂/TiN_x ferroelectric memory with tunable transparency and suppressed wake-up effect," *Appl. Phys. Lett.* **114**, 052902 (2019).
- ³³K.-Y. Chen, P.-H. Chen, R.-W. Kao, Y.-X. Lin, and Y.-H. Wu, "Impact of plasma treatment on reliability performance for HfZrO_x-based metal-ferroelectric-metal capacitors," *IEEE Electron Device Lett.* **39**, 87–90 (2018).
- ³⁴T. Szyjka, L. Baumgarten, T. Mittmann, Y. Matveyev, C. Schlueter, T. Mikolajick, U. Schroeder, and M. Müller, "Enhanced ferroelectric polarization in TiN/HfO₂/TiN capacitors by interface design," *ACS Appl. Electron. Mater.* **2**, 3152–3159 (2020).
- ³⁵L. Baumgarten, T. Szyjka, T. Mittmann, M. Materano, Y. Matveyev, C. Schlueter, T. Mikolajick, U. Schroeder, and M. Müller, "Impact of vacancies and impurities on ferroelectricity in PVD- and ALD-grown HfO₂ films," *Appl. Phys. Lett.* **118**, 032903 (2021).
- ³⁶B. Y. Kim, H. W. Park, S. D. Hyun, Y. B. Lee, S. H. Lee, M. Oh, S. K. Ryoo, I. S. Lee, S. Byun, D. Shim, D. Cho, M. H. Park, and C. S. Hwang, "Enhanced ferroelectric properties in Hf_{0.5}Zr_{0.5}O₂ films using a HfO_{0.61}N_{0.72} interfacial layer," *Adv. Electron. Mater.* **8**(6), 2100042 (2021).
- ³⁷J. F. Scott and C. A. Paz de Araujo, "Ferroelectric memories," *Science* **246**, 1400–1405 (1989).
- ³⁸E. D. Grimley, T. Schenk, X. Sang, M. Pešić, U. Schroeder, T. Mikolajick, and J. M. LeBeau, "Structural changes underlying field-cycling phenomena in ferroelectric HfO₂ thin films," *Adv. Electron. Mater.* **2**, 1600173 (2016).
- ³⁹T. Shimizu, Y. Tashiro, T. Mimura, T. Kiguchi, T. Shiraishi, T. J. Konno, O. Sakata, and H. Funakubo, "Electric-field-induced ferroelectricity in 5% Y-doped Hf_{0.5}Zr_{0.5}O₂: Transformation from the paraelectric tetragonal phase to the ferroelectric orthorhombic phase," *Phys. Status Solidi Rapid Res. Lett.* **15**, 2000589 (2021).
- ⁴⁰P. D. Lomenzo, C. Richter, T. Mikolajick, and U. Schroeder, "Depolarization as driving force in antiferroelectric hafnia and ferroelectric wake-up," *ACS Appl. Electron. Mater.* **2**, 1583–1595 (2020).
- ⁴¹M. Pešić, F. P. G. Fengler, L. Larcher, A. Padovani, T. Schenk, E. D. Grimley, X. Sang, J. M. LeBeau, S. Slesazek, U. Schroeder, and T. Mikolajick, "Physical mechanisms behind the field-cycling behavior of HfO₂-based ferroelectric capacitors," *Adv. Funct. Mater.* **26**, 4601–4612 (2016).
- ⁴²D. Zhou, J. Xu, Q. Li, Y. Guan, F. Cao, X. Dong, J. Müller, T. Schenk, and U. Schröder, "Wake-up effects in Si-doped hafnium oxide ferroelectric thin films," *Appl. Phys. Lett.* **103**, 192904 (2013).
- ⁴³P. Buragohain, C. Richter, T. Schenk, H. Lu, T. Mikolajick, U. Schroeder, and A. Gruverman, "Nanoscale studies of domain structure dynamics in ferroelectric La:HfO₂ capacitors," *Appl. Phys. Lett.* **112**, 222901 (2018).
- ⁴⁴A. Choupi, M. Spiridonov, S. Zarubin, R. Kirtaev, V. Mikheev, Y. Lebedinskii, S. Zakharchenko, and D. Negrov, "Wake-up in a Hf_{0.5}Zr_{0.5}O₂ film: A cycle-by-cycle emergence of the remnant polarization via the domain depinning and the vanishing of the anomalous polarization switching," *ACS Appl. Electron. Mater.* **1**, 275–287 (2019).
- ⁴⁵H. Chen, H. Luo, X. Yuan, and D. Zhang, "Constructing a correlation between ferroelectricity and grain sizes in Hf_{0.5}Zr_{0.5}O₂ ferroelectric thin films," *CrystEngComm* **24**, 1731–1737 (2022).
- ⁴⁶T. Shimizu, T. Mimura, T. Kiguchi, T. Shiraishi, T. Konno, Y. Katsuya, O. Sakata, and H. Funakubo, "Ferroelectricity mediated by ferroelastic domain switching in HfO₂-based epitaxial thin films," *Appl. Phys. Lett.* **113**, 212901 (2018).
- ⁴⁷M. Lederer, T. Kämpfe, R. Olivo, D. Lehninger, C. Mart, S. Kirbach, T. Ali, P. Polakowski, L. Roy, and K. Seidel, "Local crystallographic phase detection and texture mapping in ferroelectric Zr doped HfO₂ films by transmission-EBSD," *Appl. Phys. Lett.* **115**, 222902 (2019).
- ⁴⁸M. Lederer, R. Olivo, D. Lehninger, S. Abdulazhanov, T. Kämpfe, S. Kirbach, C. Mart, K. Seidel, and L. M. Eng, "On the origin of wake-up and

antiferroelectric-like behavior in ferroelectric hafnium oxide,” *Phys. Status Solidi Rapid Res. Lett.* **15**, 2100086 (2021).

⁴⁹M. Lederer, P. Bagul, D. Lehninger, K. Mertens, A. Reck, R. Olivo, T. Kämpfe, K. Seidel, and L. M. Eng, “Influence of annealing temperature on the structural and electrical properties of Si-doped ferroelectric hafnium oxide,” *ACS Appl. Electron. Mater.* **3**, 4115–4120 (2021).

⁵⁰K. Lee, K. Park, H.-J. Lee, M. S. Song, K. C. Lee, J. Namkung, J. H. Lee, J. Park, and S. C. Chae, “Enhanced ferroelectric switching speed of Si-doped HfO₂ thin film tailored by oxygen deficiency,” *Sci. Rep.* **11**, 6290 (2021).

⁵¹S. Mueller, J. Muller, U. Schroeder, and T. Mikolajick, “Reliability characteristics of ferroelectric Si:HfO₂ thin films for memory applications,” *IEEE Trans. Device Mater. Reliab.* **13**, 93–97 (2013).

⁵²F. Zahari, F. Schlichting, J. Strobel, S. Dirkmann, J. Cipo, S. Gauter, J. Trieschmann, R. Marquardt, G. Haberfehlner, G. Kothleitner, L. Kienle, T. Mussenbrock, M. Ziegler, H. Kersten, and H. Kohlstedt, “Correlation between sputter deposition parameters and *I-V* characteristics in double-barrier memristive devices,” *J. Vac. Sci. Technol. B* **37**, 061203 (2019).

⁵³J.-E. Sundgren, B.-O. Johansson, S.-E. Karlsson, and H. Hentzell, “Mechanisms of reactive sputtering of titanium nitride and titanium carbide II: Morphology and structure,” *Thin Solid Films* **105**, 367–384 (1983).

⁵⁴G. Lim, W. Parrish, C. Ortiz, M. Bellotto, and M. Hart, “Grazing incidence synchrotron X-ray diffraction method for analyzing thin films,” *J. Mater. Res.* **2**, 471–477 (1987).

⁵⁵T. Takayama and Y. Matsumoto, “Effects of refraction and reflection on analysis of thin films by the grazing-incidence X-ray diffraction method,” *Adv. in X-ray Anal.* **33**, 109–120 (1989).

⁵⁶A. Pandey, S. Dalal, S. Dutta, and A. Dixit, “Structural characterization of polycrystalline thin films by X-ray diffraction techniques,” *J. Mater. Sci. Mater. Electron.* **32**, 1341–1368 (2021).

⁵⁷J.-E. Sundgren, “Structure and properties of TiN coatings,” *Thin Solid Films* **128**, 21–44 (1985).

⁵⁸E. O. Ristolainen, J. M. Molarius, A. S. Korhonen, and V. K. Lindroos, “A study of nitrogen-rich titanium and zirconium nitride films,” *J. Vac. Sci. Technol. A* **5**, 2184–2189 (1987).

⁵⁹R. Qi, L. Pan, Y. Feng, J. Wu, W. Li, and Z. Wang, “Evolution of chemical, structural, and mechanical properties of titanium nitride thin films deposited under different nitrogen partial pressure,” *Results Phys.* **19**, 103416 (2020).

⁶⁰S. G. Seo, C.-H. Park, H.-Y. Kim, W. H. Nam, M. Jeong, Y.-N. Choi, Y. S. Lim, W.-S. Seo, S.-J. Kim, J. Y. Lee, and Y. S. Cho, “Preparation and visible-light

photocatalysis of hollow rock-salt TiO_{1-x}N_x nanoparticles,” *J. Mater. Chem. A* **1**, 3639 (2013).

⁶¹P. D. Lomenzo, Q. Takmeel, S. Moghaddam, and T. Nishida, “Annealing behavior of ferroelectric Si-doped HfO₂ thin films,” *Thin Solid Films* **615**, 139–144 (2016).

⁶²S. Logothetidis, E. Meletis, G. Stergioudis, and A. Adjaottor, “Room temperature oxidation behavior of TiN thin films,” *Thin Solid Films* **338**, 304–313 (1999).

⁶³N. Marchack, L. Buzi, D. B. Farmer, H. Miyazoe, J. M. Papalia, H. Yan, G. Totir, and S. U. Engelmann, “Plasma processing for advanced microelectronics beyond CMOS,” *J. Appl. Phys.* **130**, 080901 (2021).

⁶⁴Y. Matveyev, D. Negrov, A. Chernikova, Y. Lebedinskii, R. Kirtaev, S. Zarubin, E. Suvorova, A. Gloskovskii, and A. Zenkevich, “Effect of polarization reversal in ferroelectric TiN/Hf_{0.5}Zr_{0.5}O₂/TiN devices on electronic conditions at interfaces studied in operando by hard x-ray photoemission spectroscopy,” *ACS Appl. Mater. Interfaces* **9**, 43370–43376 (2017).

⁶⁵S. Im, S.-Y. Kang, Y. Kim, J. H. Kim, J.-P. Im, S.-M. Yoon, S. E. Moon, and J. Woo, “Ferroelectric switching in trilayer Al₂O₃/HfZrO_x/Al₂O₃ structure,” *Micromachines* **11**, 910 (2020).

⁶⁶S. S. Fields, S. W. Smith, P. J. Ryan, S. T. Jaszewski, I. A. Brummel, A. Salanova, G. Esteves, S. L. Wolfley, M. D. Henry, P. S. Davids, and J. F. Ihlefeld, “Phase-exchange-driven wake-up and fatigue in ferroelectric hafnium zirconium oxide films,” *ACS Appl. Mater. Interfaces* **12**, 26577–26585 (2020).

⁶⁷M. Yan, S. Luo, G. Schaffer, and M. Qian, “TEM and XRD characterisation of commercially pure-Ti made by powder metallurgy and casting,” *Mater. Lett.* **72**, 64–67 (2012).

⁶⁸P. D. Lomenzo, C.-C. Chung, C. Zhou, J. L. Jones, and T. Nishida, “Doped Hf_{0.5}Zr_{0.5}O₂ for high efficiency integrated supercapacitors,” *Appl. Phys. Lett.* **110**, 232904 (2017).

⁶⁹Y. Cheng, Z. Gao, K. H. Ye, H. W. Park, Y. Zheng, Y. Zheng, J. Gao, M. H. Park, J.-H. Choi, K.-H. Xue, C. S. Hwang, and H. Lyu, “Reversible transition between the polar and antipolar phases and its implications for wake-up and fatigue in HfO₂-based ferroelectric thin film,” *Nat. Commun.* **13**, 645 (2022).

⁷⁰S. Petzold, A. Zintler, R. Eilhardt, E. Piros, N. Kaiser, S. U. Sharath, T. Vogel, M. Major, K. P. McKenna, L. Molina-Luna, and L. Alff, “Forming-free grain boundary engineered hafnium oxide resistive random access memory devices,” *Adv. Electron. Mater.* **5**, 1900484 (2019).

⁷¹A. Christensen and E. A. Carter, “First-principles study of the surfaces of zirconia,” *Phys. Rev. B* **58**, 8050–8064 (1998).

II. Correlation between properties of direct current magnetron sputtered thin niobium nitride films and plasma parameters

Bibliographic Information

Marquardt, R., Cipo, J., Schlichting, F., Kolhatkar, G., Kohlstedt, H., Kersten, H.; Correlation between properties of direct current magnetron sputtered thin niobium nitride films and plasma parameters, *Thin Solid Films*, Volume 742, 2022, 139046, ISSN 0040-6090, <https://doi.org/10.1016/j.tsf.2021.139046>.

Author's contribution

The author contributed to:

- Conceptual work
- Guiding sample preparation
- Measurement and evaluation of the data
- Writing of the manuscript

Copyright Notice

This work is licensed under a Creative Commons Attribution 4.0 International License (CC BY 4.0).

II.1 Summary

The following manuscript presents results on the correlation between the structural and superconducting properties of NbN thin films deposited by DC-magnetron sputtering and the plasma parameters. NbN is known for its high transition temperature and superconducting energy gap. These attractive properties open a plethora of superconductive applications, such as bolometers, single-photon detectors, SIS (Superconducting-Insulator-Superconductor) tunnel junctions, SQUIDs (Superconducting QUantum Interference Devices), RF-cavities as well as non-superconducting applications e.g. tribological engineering. Moreover, DC-magnetron sputtering is a widely used deposition technique due to its many advantages in terms of deposition rate, scalability, and film density. However, the DC magnetron sputtering of NbN thin films is not yet fully understood.

Indeed, superconducting properties of NbN are strongly dependent on film properties such as crystallinity, grain size, and defect density, which in turn depend on the plasma environment prevailing during deposition. Thus, a comprehensive understanding of the evolution of the DC sputtering plasma parameters under different deposition conditions would provide the possibility of optimizing superconducting NbN thin films. To extract these relevant plasma parameters, we exploit two different diagnostics, i.e. a LP and PTP. This permits us to obtain crucial information regarding energy flux, electron temperature, ion current density, plasma and floating potential, which provide insight into the quantity and energy distribution of both the deposited neutral atoms and the ionized particles. Furthermore, we investigate the thin film structure by grazing incidence XRD, x-ray reflectometry, and atomic force microscopy, correlated with resistance measurements via temperature variation. We experimentally study the impact of the plasma parameters on the layer properties while varying process pressure, target-substrate distance, and sputtering power. Our results reveal that increasing process pressure induces a higher density of charged particles with lower mobility, which in turn results in a strong degradation of the structural layer and superconducting properties via grain size reduction.

Our findings show that by exploiting comprehensive plasma characterization, a deeper understanding of the deposition process of superconductive NbN can be reached. This will allow us to tune the films structural and therefore superconductive properties for the wide variety of applications of this material.



Correlation between properties of direct current magnetron sputtered thin niobium nitride films and plasma parameters

Richard Marquardt^{a,*}, Julia Cipo^b, Felix Schlichting^b, Gitanjali Kolhatkar^a, Hermann Kohlstedt^a, Holger Kersten^b

^a Nanoelectronics, Faculty of Engineering, Kiel University, Kiel 24143, Germany

^b Institute of Experimental and Applied Physics, Kiel University, Kiel 24098, Germany

ARTICLE INFO

Keywords:

Niobium nitride
Thin films
Superconductor
Langmuir probe
Passive thermal probe
Atomic force microscopy
Grazing incidence X-ray diffraction

ABSTRACT

Superconducting thin films of NbN on SiO₂ are prepared at ambient temperature by direct current magnetron sputtering with varying external deposition parameters, i.e. pressure, target-substrate distance, and power. Internal deposition parameters such as the plasma properties are determined with both a Langmuir probe and a calorimetric probe providing insight regarding the energy flux, the electron temperature, the plasma potential, and the ion current density of the plasma. Grazing incident x-ray diffraction and atomic force microscopy measurements reveal that the thin films have cubic polycrystalline structures with grain sizes of up to 51 Å, which define the superconducting behavior. Structural and electrical properties are related to the plasma parameters, showing a high correlation between the ion current density and the superconducting properties of the films. The results attest to the potential of plasma characterization as a powerful tool to optimize the deposition of thin NbN films and to predict their film properties.

1. Introduction

Niobium nitride (NbN) is a refractory Bardeen-Cooper-Schrieffer-type superconductor compound, exhibiting a large transition temperature and superconducting energy gap. In its thin film form, NbN is exploited in numerous applications, such as bolometers, single-photon detectors, superconductor-insulator-superconductor tunnel junctions for millimeter wave detectors, superconducting Quantum interference devices, radio frequency (RF) cavities [1–6] as well as non-superconductive applications, e.g. in tribological engineering [7]. NbN is commonly deposited by direct current (DC-) or RF-magnetron sputtering in an Ar/N₂(85%/15%) atmosphere and reaches a transition temperature of up to 14.2 K when deposited in ambient temperature on a structurally suitable substrate [8,9]. In previous studies, a relation between the deposition rate, pressure and nitrogen partial pressure and the transition temperature as well as the hardness, the stoichiometry and density of NbN could already be established [10]. In addition, the film thickness influences the orientation and structure of the NbN layer and, therefore, also its superconducting properties [11,12]. Although extensive information and studies on the influence of the deposition conditions on the layer properties of NbN have already been reported, the

present work focuses on plasma engineered thin NbN films. By exploring the relation between plasma parameters and film properties, a high degree of flexibility in the production of NbN thin films can be achieved. To extract relevant plasma properties during sputtering, two different diagnostics are exploited, i.e. a Langmuir probe (LP) and a passive thermal probe (PTP). While the former offers the opportunity to monitor the electron temperature, the plasma potential and the ion current density of the plasma, the latter measures the energy flux density from plasma to the wafer surface [13]. We show that the structural and electrical properties of the deposited NbN thin films are clearly related to the plasma parameters. In more general terms, the work presented here demonstrates that the tool box offered by plasma diagnostic is a powerful approach to optimize thin films towards particular applications.

2. Material and methods

2.1. Sputtering conditions and thin film diagnostics

All NbN films were deposited on a silicon substrate using a home-made DC magnetron sputtering system. In this system, a high vacuum

* Correspondence author.

E-mail addresses: rvm@tf.uni-kiel.de (R. Marquardt), julia.cipo@isit.fraunhofer.de (J. Cipo).

<https://doi.org/10.1016/j.tsf.2021.139046>

Received 30 April 2021; Received in revised form 15 November 2021; Accepted 7 December 2021

Available online 11 December 2021

0040-6090/© 2021 The Author(s).

Published by Elsevier B.V. This is an open access article under the CC BY-NC-ND license

(<http://creativecommons.org/licenses/by-nc-nd/4.0/>).

was obtained using a mechanical pump (Vacuumbrand, MD 4 NT) in combination with a turbo-molecular pump (Leybold, Turbovac 350i). The pressure was precisely controlled by adjusting the angle of the throttle valve of the turbo-molecular pump. A custom-designed substrate holder, able to accommodate a square substrate with a size of $10 \times 10 \text{ mm}^2$, was used for sample fabrication. Its configuration is illustrated in Fig. 1.

DC magnetron sputtering from a NbN-target (NbN, 99.99%) in a pure Ar atmosphere was employed for the deposition of the NbN layers. The NbN thin films were deposited at room temperature onto square Si-substrates ($10 \times 10 \text{ mm}^2$) coated with a 400 nm thick thermal SiO_2 . The base pressure was below $3 \cdot 10^{-5} \text{ Pa}$. Gas pressure, discharge power, and target-substrate distance were varied for the deposition processes of the sample, whereas the thickness of the deposited films was always kept constant at 50 nm. The variation of the mentioned process parameters can be found in Table 1.

Perfect conductivity is the first particular hallmark of superconductivity and a prerequisite for a large number of applications of superconductors such as high-current transmission lines or high-field magnets [14]. The phenomenon of perfect conductivity can be detected after a phase transition at a critical temperature T_C . The determination of the critical temperature is, therefore, an important method for characterizing a superconductor. To measure the critical temperature, the NbN films were lowered in liquid helium while their resistance was monitored. To ensure electrical contact, 0.25 mm radius circular Au top electrodes were deposited by DC magnetron sputtering with a stencil mask. The substrate was then attached with silver paste to the solid sample head of the deep temperature probe, which consisted of Copper (Cu). Wire bonding was used to contact the four Au pads with the measuring devices, and contact and lead resistance were eliminated by four-point sensing [15]. To determine the exact temperature of the phase transition during the resistance versus temperature (R-T) measurement, the cryogenic temperature sensor was placed at the same position as the sample, on the backside of the Cu-block.

Since both crystallinity and grain size affect the critical temperature and the critical current density of superconductors [16], a structural analysis of the NbN layers was also conducted. For this purpose grazing incidence x-ray diffraction (GIXRD), established in thin-film technology [17,18], was used to examine the important structural properties. The film thickness was analyzed by x-ray reflection (XRR). For both thin film analyses a Rigaku SmartLab 9 kW diffractometer at a wavelength of $\lambda = 1.5418 \text{ \AA}$ was used. For the GIXRD measurements a 9 kW copper X-ray

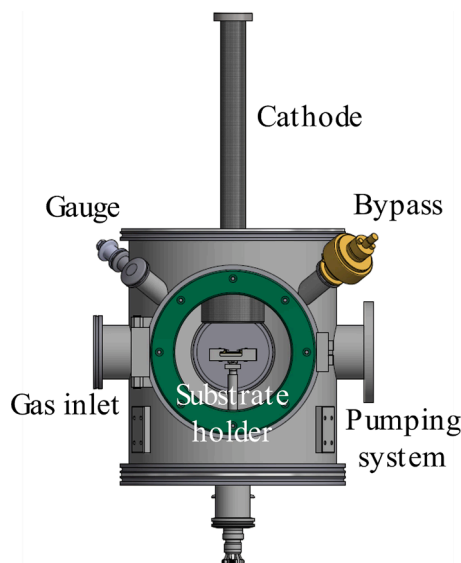


Fig. 1. Homemade sputtering system with 10 mm substrate holder and 2-inch target.

Table 1

Experimental deposition parameters.

Pressure variation @	Distance variation @	Power variation @
37 mm, 50W	0.5 Pa, 50 W	0.5 Pa, 37 mm
0.5 Pa	10 mm	20 W
1 Pa	15 mm	30 W
1.5 Pa	20 mm	40 W
2 Pa	25 mm	50 W
2.5 Pa	30 mm	60 W
3 Pa	35 mm	70 W
3.5 Pa	40 mm	80 W
4.5 Pa		90 W
5 Pa		100 W

source was used in a monochromatic parallel beam configuration focused with a length-limiting slit of 5 mm along the longitudinal axis. A typical GIXRD spectrum of polycrystalline Fm-3 m NbN is shown in Fig. 2. Topographic analyzes of the samples were made possible by atomic force microscopy (AFM). The AFM's ability to characterize nanoscale objects makes it a perfect tool to determine particle sizes and surface roughness. Hence, the sample surface was scanned using a Si AFM tip, attached to a cantilever. The tip was either repelled or attracted due to the atomic forces that occur when interacting with the sample surface. The bending caused by the atomic forces can be detected with the aid of a laser reflected onto the back of the cantilever and towards a photodetector. All AFM measurements were carried out on a SmartSPM 1000 from AIST-NT in a non-contact alternating current mode.

2.2. Measurement of plasma parameters

The plasma diagnostic was performed for the same deposition parameters, i.e. power, gas pressure, and probe-to-target distance, as the ones used for the NbN film deposition. Each process parameter was varied one at a time while keeping the others constant.

The PTP and LP measurements were carried out axially from the target. For the pressure and power variation the PTP was inserted vertically into the deposition chamber, while for the remaining measurements, the PTP and LP were inserted perpendicularly beneath the target, as shown for the LP in Fig. 3b. In both cases, the top of the probe pointed towards the target, yet, the different arrangement of the probe holder results in a different geometry, which in turn influences the energy flux of the plasma. The different installation of the PTP probe for power and pressure measurements in contrast to the distance measurement is due to the heating of the shutter by the plasma. Since the

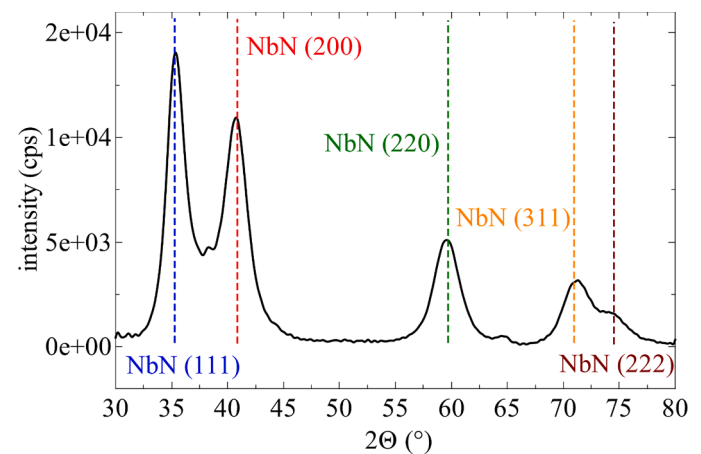


Fig. 2. Deflection spectrum with a grazing incidence angle (GIXRD) of NbN thin film with the following deposition parameters: $p = 0.5 \text{ Pa}$, $P = 50 \text{ W}$, $d = 37 \text{ mm}$ (black). The blue straight lines show the theoretical reflection peaks for Fm-3 m NbN. (For interpretation of the references to color in this figure legend, the reader is referred to the web version of this article.).

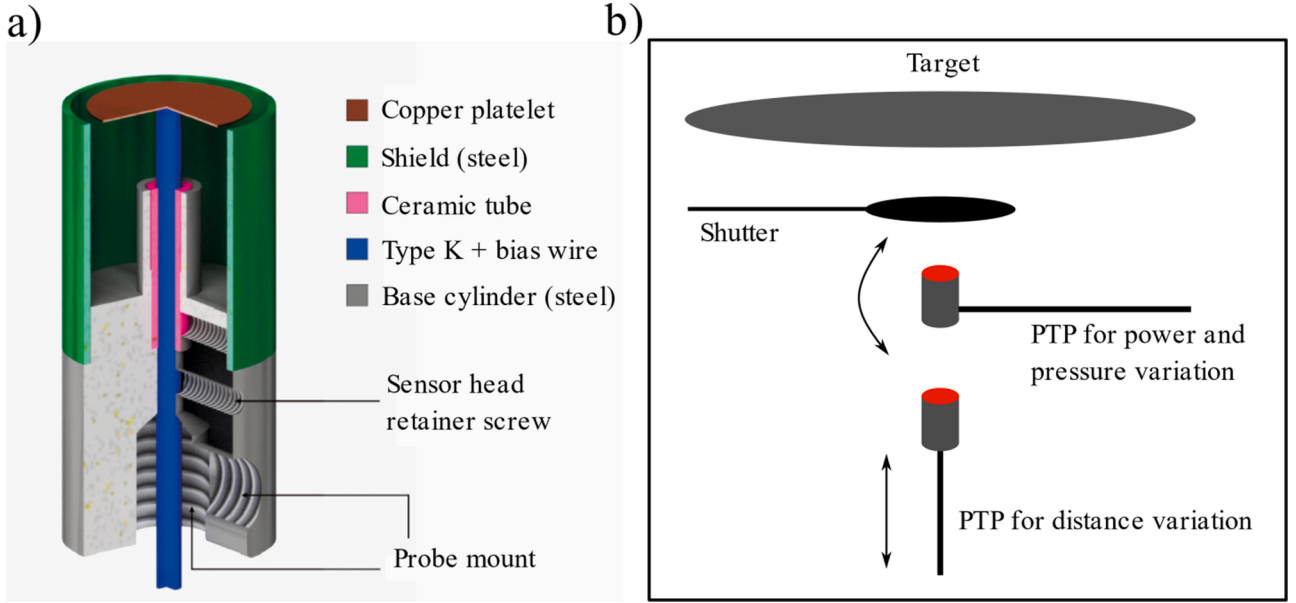


Fig. 3. (a) PTP design (used with permission of S. Gauter, F. Haase, and H. Kersten, Thin Solid Films 669, 8 (2019)). (b) Schematic drawing of the experimental setups of the PTP measurements for different process parameter variations. The PTP is positioned at 37, 67 and 97 mm from the NbN target for the distance variation. For the LP measurements, the experimental setup is analogous the PTP setup for the distance variation.

heat radiation of the shutter would affect the measurements, the probe was rotated 180° for power and pressure measurements, so that it was averted from the target during the cooling phase. This allowed the plasma to burn permanently during the measurement series. Due to the vertical installation of the probe, it was not possible to perform a 180° turn for cooling for the distance variation. Therefore, the plasma had to be switched off for the cooling phase. The PTP was oriented facing towards the cathode target for 20 s, while the plasma was switched off for 120 s, repeating this procedure for each varied process parameter (see Table 1). The LP measurements regarding the effect of power and pressure variation were repeated for probe-to-target distances of 37 mm, 67 mm and 97 mm. Since the magnetic field of the sputter-magnetron influences the LP measurements [13] for small distances (e.g. 37 mm), the influence of the magnetic field on the electrons was considered. For larger distances of 67 mm and 97 mm the magnetic field was expected to be weak and to have a much lower effect on the resulting plasma parameters.

2.2.1. Passive thermal probe

An effective diagnostic tool to record the energy flux towards a surface in a process plasma is the passive thermal probe (PTP). Its design is based on Thornton's idea of 1978 [19] and was recently improved [20]. The probe consisted of a copper plate with a diameter of 11 mm and a thickness of 100 μm (cf. Fig. 3a). On the back, a type K thermocouple (40 $\mu\text{V/K}$) and a copper bias wire are spot-welded. The probe is shielded by a housing made of stainless steel, so only the energy flux from the half-space above the substrate (probe) is detected. The wires are placed inside a ceramic tube, which is further installed inside a base cylinder. The cylinder is mounted on a vacuum feed-through, so the probe can be inserted into the process chamber by a vacuum flange.

When exposed to the plasma during the sputtering process, the PTP measures a temperature increase resulting from the incoming power towards it. This phase is known as the heating phase. It is mainly dominated by charged and neutral particles reaching the probe, surface processes like film formation, electron-ion recombination or chemical reactions as well as line radiation from the plasma and heat radiation from the target or the chamber walls. Inversely, the probe's temperature decreases when the power to the cathode target is turned off. This temperature course is characterized by the power leaving the probe and

is referred to as the cooling phase. The power loss contributions result mainly from heat conduction, convection, and radiation of the probe's surface. To obtain the energy flux during these phases, the overall change in the enthalpy \dot{H} has to be considered [21]:

$$\text{Heating : } \dot{H}_h = C_S = P_{in} - P_{out,h} \quad (1)$$

$$\text{Cooling : } \dot{H}_c = C_{Sc} = -P_{out,c} \quad (2)$$

where P_{in} is the input power from the plasma source, while $P_{out,h}$ and $P_{out,c}$ are the power losses and \dot{T}_h and \dot{T}_c the time derivatives of the temperature during the heating and cooling phase, respectively. The heat capacity C_S of the PTP is determined beforehand by calibration of the probe in an electron beam, as described in [22].

Only short time periods are investigated around the heating and cooling kinks when the plasma source is switched on and off. Thus, it can be assumed that the outgoing power remains the same during both phases such as $P_{out,h}(T_S) = P_{out,c}(T_S)$. The equations above can be combined, and the incoming power to the probe is obtained as follows:

$$P_{in} = \dot{H}_h - \dot{H}_c = C_S(\dot{T}_h - \dot{T}_c) \quad (3)$$

Based on the probe surface A_S , the incoming energy flux density is calculated:

$$J_{in} = \frac{P_{in}}{A_S} = \frac{C_S}{A_S} (\dot{T}_h - \dot{T}_c) \quad (4)$$

The evaluation method chosen for the measured temperature curves is the kink-method [20], where linear fits are used around the heating kink and cooling kink as demonstrated in Fig. 4a. By subtracting the slopes of the two linear fits, the term $\dot{T}_h - \dot{T}_c$ is obtained. Further parameters like heat capacity C_S and probe surface A_S in Eq. (6) are already known due to calibration and probe manufacturing, respectively. As a result, the energy flux can be easily determined. A detailed description of this evaluation method is given in the literature [20].

2.2.2. Langmuir probe

The Langmuir probe is a widespread and established plasma diagnostic method, which goes back almost a hundred years [13,23]. Its simplicity and easy fabrication allow for a wide range of applications in different plasma environments [24–26]. By bringing an additional

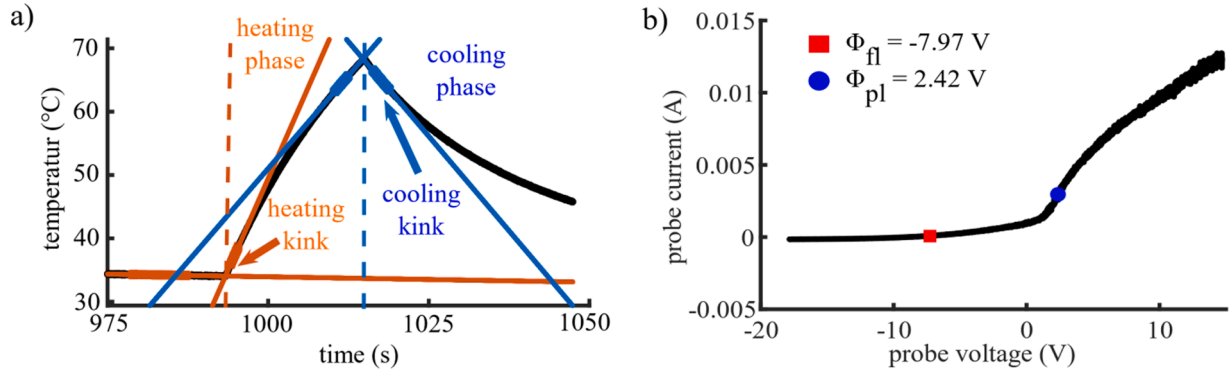


Fig. 4. (a) Example of a PTP measurement for position 37 mm, 50 W magnetron power and 0.5 Pa Ar gas pressure. The heating and cooling kink along with the linear fits are marked in red and blue, respectively. (b) Typical I - V characteristic measured by the LP at 97 mm probe-to-target distance, a magnetron power of 50 W and gas pressure of 0.5 Pa. (For interpretation of the references to color in this figure legend, the reader is referred to the web version of this article.).

electrode into the plasma and applying a voltage sweep, a typical current-voltage (I - V) characteristic can be obtained. The probe can have different geometries, cylindrical, planar or spherical. In this work, a 2.7 mm long cylindrical tungsten wire of 100 μ m diameter is used. The I - V characteristic can be employed to determine a variety of plasma parameters, such as the floating potential ϕ_{fl} , the plasma potential ϕ_{pl} , the electron temperature T_e , and the current density of the positive ions j_{ion} .

A typical I - V characteristic is presented in Fig. 4b. Starting at a high negative voltage, the plasma electrons are repelled and only positive ions can reach the probe. The resulting current is the ion saturation current.

When increasing the probe voltage, more electrons can reach the LP and the floating potential ϕ_{fl} , which is defined as the zero-crossing point of the I - V curve, is reached. Here, the electron current and the ion current flowing towards the probe are equal, resulting in a zero-net current at the probe. Further increase of the voltage increases the electron current towards the probe, which leads to an exponential rise in the electron current due to the Boltzmann factor. The turning point of this exponential rise marks the plasma potential, after which the electron current saturates. The plasma potential ϕ_{pl} can be obtained from the maximum of the first derivative of the I - V curve. The energy of the impinging positive ions in the plasma is largely defined by the plasma potential and is therefore, an important parameter in this study.

Looking at a semi-logarithmic plot of the I - V curve, the electron temperature T_e can be extracted from the slope of exponentially rising current. By combining T_e with the Bohm sheath criterion, the ion current density j_{ion} can be obtained [27].

3. Results and discussion

To better understand the interplay between the superconducting properties of NbN layers and the plasma parameters during deposition, electrical and structural information of the layers as well as plasma data were collected. In order to analyze the critical temperatures of the samples, a four-point measurement was carried out with a fixed current of 10 μ A on the outer electrodes, as the RT-probe head (Fig. 5a) was lowered into liquid helium. The superconducting properties of the samples were compared using two parameters that were derived from the RT measurements: the superconducting critical temperature (T_C , taken from the middle point of the resistive transition) and the residual resistivity ratio RRR (ratio of the film resistivity at 300 K to that at 20 K: $RRR = \rho(300\text{ K})/\rho(20\text{ K})$) [28].

3.1. Film and plasma properties versus sputtering pressure

Normalized resistance versus temperature dependence of NbN films (50 nm thick) deposited at four different process pressures are shown in Fig. 5b. The resistance versus temperature measurements were

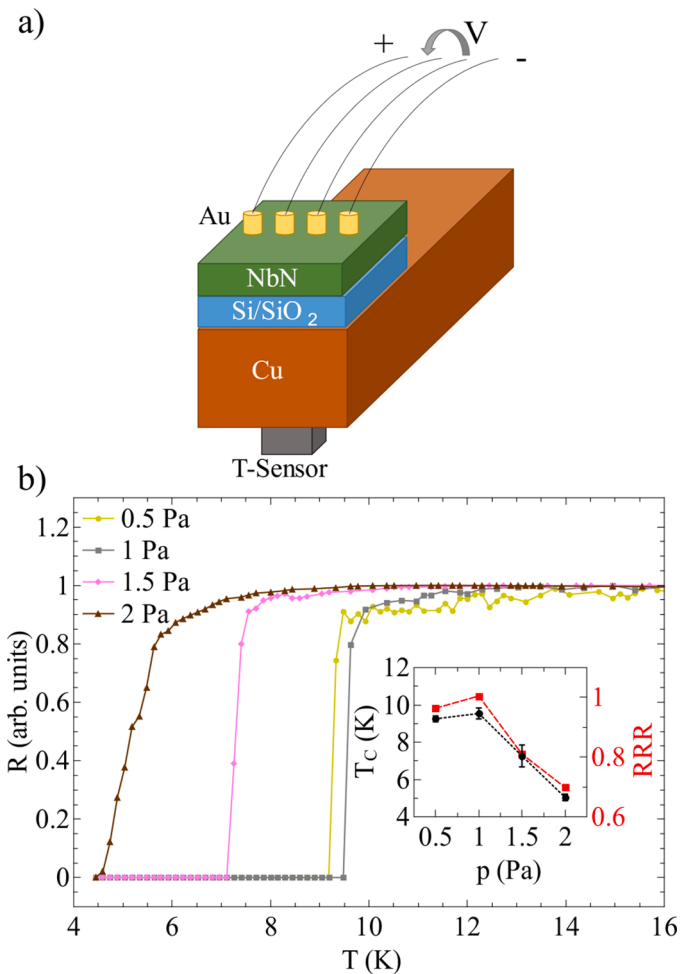


Fig. 5. (a) Schematic illustration of the sample fixed with conductive silver paste on a copper block. (b) RT-measurements for a variation in the deposition pressure for constant distance of 37 mm and deposition power of 50 W. Inset: Calculated T_C (black) and RRR (red) for the measured RT-curves. (For interpretation of the references to color in this figure legend, the reader is referred to the web version of this article.).

performed three times for each sample. For clarity, only one measurement per pressure variation was shown. The deviations can be seen in the error bars of T_C in the inset. The inset presents the parameters for T_C and RRR derived from the RT measurements. Samples that were deposited at a process pressure higher than 2 Pa showed no

superconducting properties and are therefore, not shown in Fig. 5b. A slight increase in the critical temperature is obtained when increasing the pressure from 0.5 Pa to 1 Pa. If the pressure rises further, a sharp drop in T_C and RRR occurs, down to a T_C of 5 K for a 2 Pa process pressure. Previous studies by Iosad et al. [29,30] observed similar relationships between deposition pressure and T_C of superconducting materials. Also, an optimal pressure (~ 1 Pa) for superconducting material deposition is found in our study, depending on the distance between the substrate and the target. A similar observation for structure and transition temperature between 0.47 Pa and 1.33 Pa was made by Bacon et al. [9]. At this optimum a transition from degrading factors is expected, which is related to destructive bombardment by fast neutrals at low pressure to highly thermalized conditions at high pressure [31]. With a transition temperature of 9.6 K, the optimal result obtained in this work is below the optimal values reported in other recent studies [12], which report up to 14.5 K for ambient temperature deposition. This can be due to two main factors: First, thin films of 50 nm are deposited in this work, which affects the structure and transition temperature. Second, the substrate used is not matched to the crystal lattice of NbN.

An investigation of the RRR for the different process pressures also shows that the conduction process changes from “metallic” ($RRR > 1$) to “thermally activated” ($RRR < 1$) for pressures around 1 Pa due to a much stronger grain boundary contribution as the grain size decreases [32]. The influence of the grain boundaries can be explained through a model with superconducting grains in a non-superconducting matrix. Here, the coherence length

$$\xi(T) = 0.74 \xi_0 \sqrt{\frac{T_C}{T_C - T}} \quad (5)$$

is defined for two different conditions, $\xi < d$ and $\xi > d$, where d is the diameter of the superconducting grain [33]. Since the superconducting properties are given more weight locally for the case $\xi > d$, they can be limited to the influence of the grains.

It should be noted here that both T_C and RRR show the same dependence on pressure. Such a correlation between RRR and T_C can be explained using a phenomenological approach of the above expounded model of superconducting grains in a non-superconductive matrix from Deutscher et al. [34]. In this approach the phase transition at the temperature T_C is defined as

$$\frac{1}{T_C} \approx \frac{1}{T_{C0}} + \frac{0.1N(E_F)}{T_{C0}^2 C_{ij}} \quad (6)$$

For this model a weakening of the coupling C_{ij} between the grains would lead to $T_C < T_{C0}$ and to an increased importance of the hopping conductance between the grains [33], which leads to a reduction in the total conductivity of the film. Therefore, T_C and RRR show the same functional relationship with respect to the grain size. For systems where the coherence length ξ is largely dependent on the grain size, Gurvitch et al. [35] suggested a method of calculating grain sizes by making an estimate of the mean free path l ,

$$l = v_F \cdot \tau \quad (7)$$

where v_F is the average Fermi velocity and τ is the relaxation time. The latter can be expressed as a function of the electron phonon coupling constant λ of NbN according to:

$$\frac{\hbar}{\tau} = 2\pi k_B T \lambda \quad (8)$$

Taking into consideration the study by Chockalingam et al. [36] the Fermi velocity v_F for our films can be estimated to $1.44 \cdot 10^6$ m/s and the electron phonon coupling $\lambda = 1.13$, resulting in $l(300\text{ K}) = 51$ Å. Taking $RRR = 1$ for 1 Pa we find $l(10\text{ K}) = l(300\text{ K}) \cdot RRR = 51$ Å and 37.7 Å for a pressure of 0.5 Pa.

The GIXRD method offers a more global analysis of the structural

features relevant to the superconducting properties, namely grain size, crystal structure, and crystallinity. Therefore, GIXRD scans are performed with an incidence angle omega of 0.5° from a 2θ in the 20° to 80° range.

The GIXRD patterns of all investigated NbN films show a face centered cubic phase for the deposited NbN (COD 1538667 [37] was used for fitting of the GIXRD patterns). For increasing sputtering pressure, a reduction in crystallinity can be observed (Fig. 6). The grain size of the films is determined by the Halder-Wagner [38] method used on the five reflections of the orientations within the scanning range (Figs. 2 and 6). A maximal grain size is achieved at a sputtering pressure of 1 Pa in agreement with the findings from the R-T measurements described above. The offset in the calculated values between GIXRD and R-T measurements suggests that there is an inhomogeneous distribution of grain sizes in the film. While a global recording of the film is made with a GIXRD analysis, the RT measurement collects the data exclusively from the local current path. Smaller grains which do not contribute to the current transport are, thus, recorded in the statistical averaging of the X-ray data, but remain insignificant in the R-T analysis. A relationship between the transition temperature and the layer thickness is often observed [39] and indicates an increase of the average total grain size with increasing film thickness.

An analysis of the orientation of the cubic structure also shows that we can find a preferential orientation in the (111) direction for a pressure of 1 Pa (gray line, Fig. 6). The ratio between the intensities of the (111) and (200) orientations changes from 1.3 for a process pressure of 0.5 Pa to 2.2 for a pressure of 1 Pa.

The observed variations in crystallization, grain size, and structuring orientation, together with collected data on surface roughness, allow a classification in Thornton's structure zone diagram (SZD) [40,41]. Due to the high roughness (Fig. 7a) in combination with low crystallization and small grain sizes for high process pressures, it can be concluded that the film displays a porous structure consisting of tapered crystallites separated by pits, as described in zone 1 of the SZD. With decreasing process pressure, a transition into the T-zone can be identified on the basis of decreasing roughness (Fig. 7b), increasing crystallization, and grain sizes. Adatom diffusion processes might occur, but their mobility and, thus, grain boundary migration is limited. The higher structure of the film at a process pressure of 1 Pa also indicates a transition into zone 2 of the SZD, in which the growth of columnar grains is described. Here, the adatom mobility is still high and the surface is smooth. Overall, it can

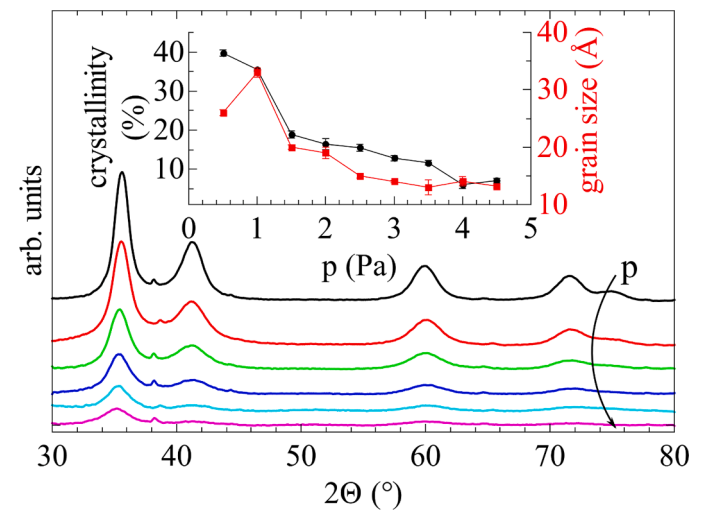


Fig. 6. GIXRD curves for deposition pressures in a 0.5 Pa to 5 Pa range for constant distance of 37 mm and deposition power of 50 W. Inset: Crystallinity (black) and grain size (red) extracted from the GIXRD. (For interpretation of the references to color in this figure legend, the reader is referred to the web version of this article.).

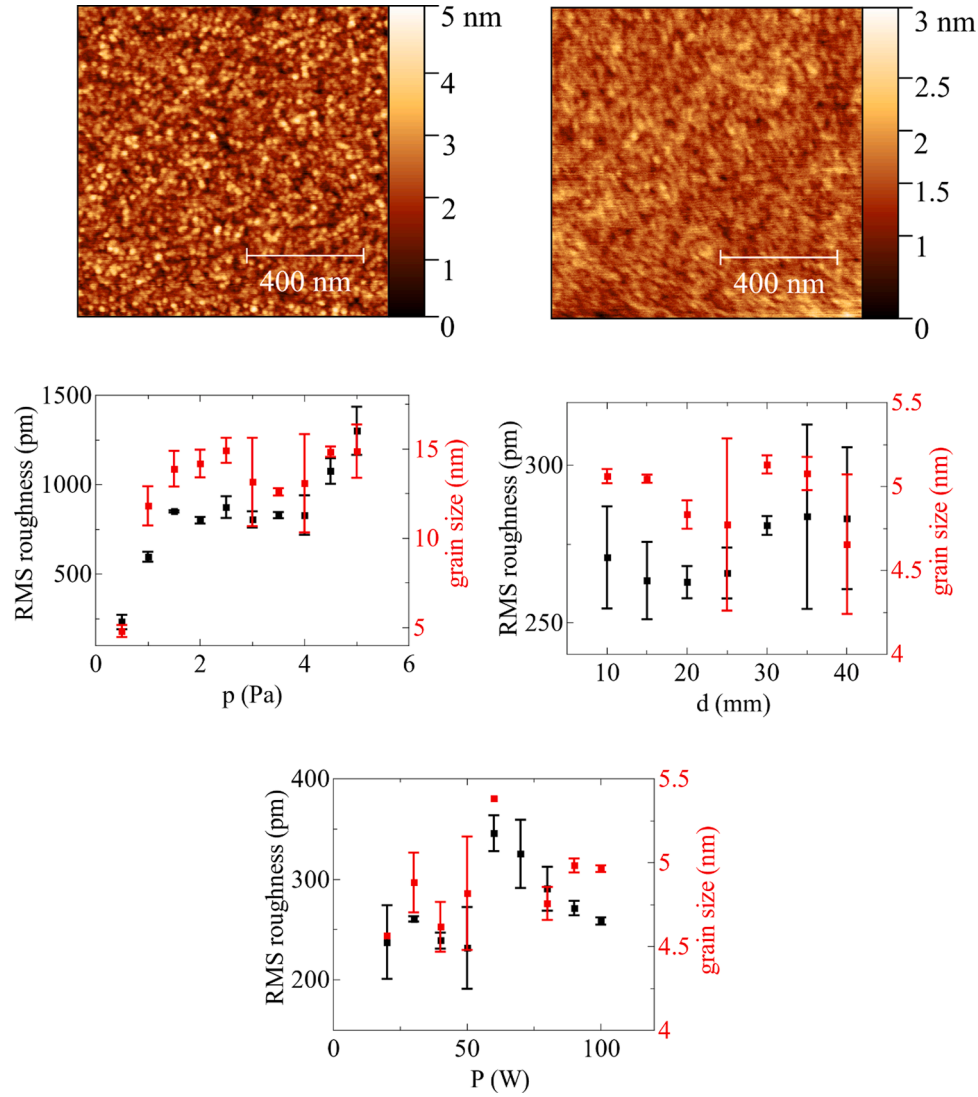


Fig. 7. Roughness of a thin film produced at a deposition pressure of a) 1.5 Pa and b) 0.5 Pa. RMS roughness (black) and grain size (red) dependence on c) the gas pressure, d) substrate-target distance and e) the magnetron power during deposition. (For interpretation of the references to color in this figure legend, the reader is referred to the web version of this article.).

be stated that, as expected according to Thornton et al. [41,42], increasing process pressure has a negative influence on the crystallinity and grain size of the layer.

Similar topography images for NbN films deposited by DC magnetron sputtering have been reported by other working groups, enabling an easier categorization into Thornton's SZD [42]. In addition, the grain size can be extracted from AFM topography measurements. Here, the grain size is determined using Otsu's method [43], which separates the pixels composing an image into two populations (noise and signal, or in this case grains and grain boundaries) using a mathematical method that minimizes the intra-class variance. The evolution of the grain size as a function of pressure, target-sample distance and sputtering power in shown in Fig. 7c–e. As the deposition pressure increases from 0.5 Pa to 2.5 Pa, the grains become larger, with values of 4.8 ± 0.2 nm and 14.9 ± 0.5 nm, respectively (Fig. 7c). When the pressure is further increased the grain size appears unchanged. As the target-substrate distance increases from 10 mm to 40 mm, the grain size remains constant with an average value of 4.94 ± 0.07 nm (Fig. 7d). Similarly, the grain size does not show any significant changes as the power increases from 20 W to 100 W, with an average grain size of 4.87 ± 0.09 nm (Fig. 7e). The increase in grain size with increasing process pressure contrasts with the observations of the XRD and current analysis (Fig. 7d). This can be explained by the

different methodology of the analysis methods. XRD depends on the size of the defect-free volume, while AFM determines the size of particles independently of defects, which can consist of several grains. For the influence of the distance (Fig. 7d) and process power (Fig. 7e), the same trends are obtained as with the other analysis methods.

In summary, it can be stated that the morphological properties show a strong dependence on the gas pressure, which affects the kinetic energies of impinging particles especially gas ions and sputtered neutrals. Therefore, the energy influx as well as the NbN deposition rate have been determined for the related pressure variation (Fig. 8).

The results for the energy influx show only a small variation, as seen in Fig. 7.

Beside the weak maximum of about 90 mW/cm^2 at 0.5 Pa, the energy flux remains almost constant during the pressure variation. This is due to a balance between the kinetic energies of sputtered and reflected particles, and their interaction with particles of the background gas:

When increasing the gas pressure, the collision rate between the neutral background gas particles and kinetic particles (e.g. sputtered and reflected particles) increases as well. Thus, the mean free path of the particles from the target and the ions decreases. This leads to energetic losses, resulting in lower energy fluxes of sputtered and reflected particles [44]. However, the total flux of kinetic particles is still high,

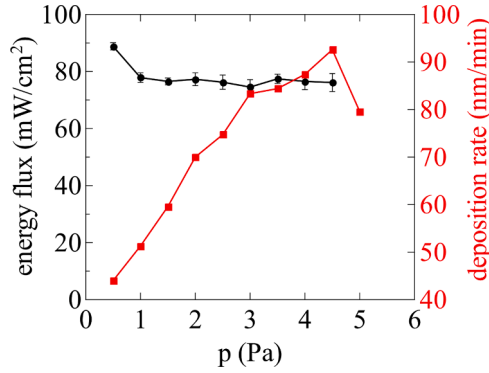


Fig. 8. Energy flux measured by passive thermal probe (PTP) as a function pressure (black). The mean values and the standard deviations are obtained from the two measurements acquired for each process pressure. The deposition rate for sputtered NbN thin films is determined by XRR (red). (For interpretation of the references to color in this figure legend, the reader is referred to the web version of this article.)

leading to an overall constant total energy flux in the pressure range investigated here.

Vice versa, the deposition rate first increases with increasing pressure, since a higher ionization rate and, thus, a higher number of sputtered particles is provided. For pressures between 3 Pa and 4.5 Pa the deposition rate increases just slowly. At higher pressures, the deposition rate decreases due to a decrease in the mean free path. The sputtered neutrals are no longer able to reach the substrate at the same rate as before, and the film thickness and, hence, the deposition rate are reduced [45].

Since the total energy flux showed a relatively constant behavior, it is important to understand the several energetic contributions to the integral energy flux and their correlation to specific film properties. Therefore, plasma parameters are measured by the LP at distances of 37 mm, 67 mm, and 97 mm while varying the pressure, as presented in Fig. 9.

Fig. 9a shows the electron temperature during pressure variation. The increasing gas pressure leads to a higher collision rate between the electrons and the gas particles. As a result, their mean thermal energy

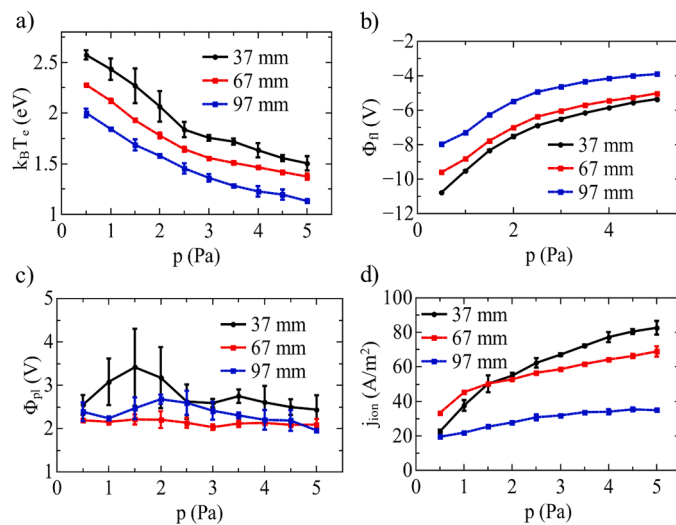


Fig. 9. Plasma parameters as a function of process pressure - the mean values and the standard deviations obtained from the three measurement points for each condition are depicted (squares with error bars). The solid and dashed lines are added as a guide to the eye for the mean values (37, 67 and 97 mm target to probe distance, respectively). (a) electron temperature, (b) floating potential of probe, (c) plasma potential, and (d) current density of positive ions.

and temperature is reduced, which is confirmed by the electron temperature T_e . This trend is reflected in further experimental work [46].

The floating potential ϕ_f shows the same behavior for all probe-to-target distances (Fig. 9b). Yet, for a distance of 37 mm (black curve), its values are more negative than for larger distances. This can be attributed to a stronger magnetic field closer to the magnetron, resulting in a larger amount of electrons being trapped in the plasma torus in front of the target cathode. Similar results on the enormous influence of the magnetron on film properties have already been shown by Zahari et al. [47].

Furthermore, ϕ_f becomes less negative with increasing pressure for all three probe-to-target distances. This behavior can qualitatively be compared to the ion current density j_{ion} in Fig. 8d. Since the ion density increases with increasing gas pressure it is possible for more positive ions to reach the probe (substrate) surface due to its negative bias voltage.

The plasma potential ϕ_{pl} in Fig. 9c shows a much less pronounced behavior and almost no dependence of the gas pressure. For a probe-to-substrate distance of 37 mm, a change between 0.5 Pa and 1.5 Pa is noticeable, but the values are still within the error margins. Thus, the plasma potential ϕ_{pl} can be correlated to the electron temperature T_e according to the Boltzmann relation [48]. Through the electron temperature, valuable information regarding the kinetic energy of particles is provided.

With increasing gas pressure, higher ion and electron densities are expected due to higher collision rates with the gas atoms. Therefore, an increasing ion current density is obtained, as seen in Fig. 9d. In summary, increasing pressure in the range studied results in more electrons and ions being present in the plasma but with reduced kinetic energies.

Plasma properties like the electron temperature T_e and the ion current density j_{ion} are further correlated to morphological and electrical film properties. The crystallinity and grain size shown in Fig. 6 decrease with increasing gas pressure, similarly to the T_e curve. As stated earlier, the number of charged particles in a plasma increases with increasing gas pressure, which is confirmed by the j_{ion} trend. Yet, their kinetic energies and temperatures are reduced due to the decreased mean free path. The sputtered particles undergo an increased collision rate as well, leading to lower kinetic energies and, consequently, to a lower adatom mobility. A limited boundary migration is expected, which results in smaller grain sizes and a lower crystallization rate. For small process pressures, bombardment by fast neutrals becomes the significant destructive process limiting the deposition of high quality NbN thin films.

Since these crystallographic features have an influence on the electrical film properties (e.g. critical temperature), it is possible to correlate them to plasma properties [28,49]. For instance, the critical temperature T_c decreases with increasing gas pressures resembling the behavior for the grain size and electron temperature T_e . Grain size is therefore, an indicator for the critical temperature (Fig. 5b).

3.2. Film and plasma properties versus target substrate distance

The influence of the target-substrate distance on the superconducting properties is shown in Fig. 10. An increase in the distance leads to an increase in the critical temperature, as depicted in the inset of Fig. 10, while RRR displays no dependence on a change in the distance. Comparable observations were also reported by Iosad et al. [30], where a modulation of the mean free path was achieved by adjusting the process pressure, resulting in transition temperatures > 14 K for both an 80 mm and a 40 mm separation. In contrast to the observations of the effect of varying gas pressure, RRR does not appear to have any direct influence on T_c in this case. Although a semiconductor-like type is demonstrated for the conduction flow, the RRR of all NbN samples is below 1 for all target-substrate distances, indicating that the previous assumption of superconducting grains in a non-superconducting matrix as limiting factor is no longer valid. In the case of a distance variation, the electrical

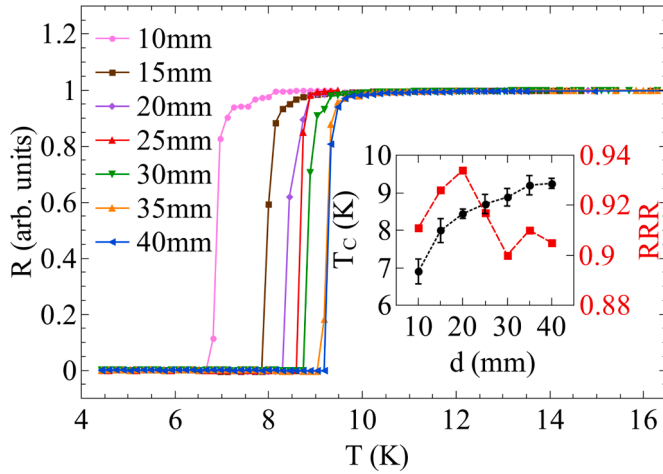


Fig. 10. RT-measurements for a variation in the distance (10 mm - 40 mm) between substrate and target with a constant pressure of 0.5 Pa and power 50 W. Inset: Calculated T_c (black) and RRR (red) for the measured RT-curves. (For interpretation of the references to color in this figure legend, the reader is referred to the web version of this article.).

resistance does not seem to be largely determined by the size of the grains. This absence of correlation between T_c and RRR could be due to an increased bombardment at shorter distances. Due to the mean free path of 33 mm between the neutrals in the gas phase at a pressure of 0.5 Pa, this effect would be stronger at smaller distances and lead to defects formation [50].

An increase in crystallinity can be seen as the target-substrate distance rises (Fig. 11). For distances $30 \text{ mm} < d < 40 \text{ mm}$, a saturation appears in the crystallinity. Although growth of larger grains can be detected with increasing distance, this growth seems to have a different dependence on the distance than the crystallinity. The increase in the general crystallinity in the films also indicates a reduction in the defect density.

Furthermore, the energy flux measured by the PTP can be compared to the deposition rate during distance variation (Fig. 12). Due to the different arrangement of the probe holder and the resulting anode geometry (Chapter 2.2), only a qualitative comparison can be made between the PTP measurements of the distance variation and the

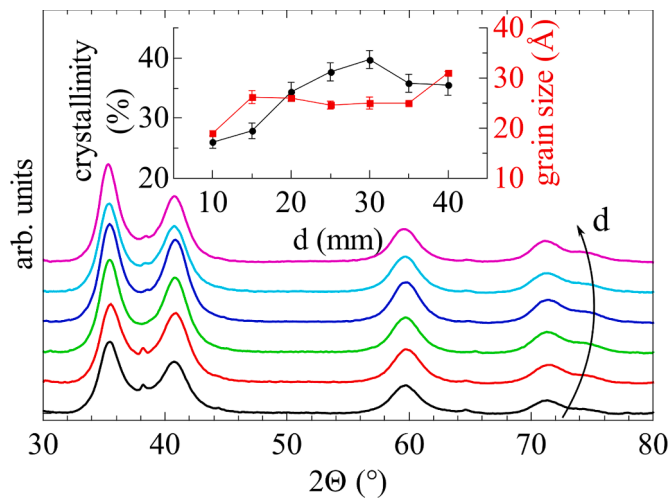


Fig. 11. GIXRD for a substrate-target distance between 10 mm and 40 mm for constant pressure of 0.5 Pa and deposition power of 50 W. Inset: Crystallinity (black) and Grain size (red) extracted from the GIXRD. (For interpretation of the references to color in this figure legend, the reader is referred to the web version of this article.).

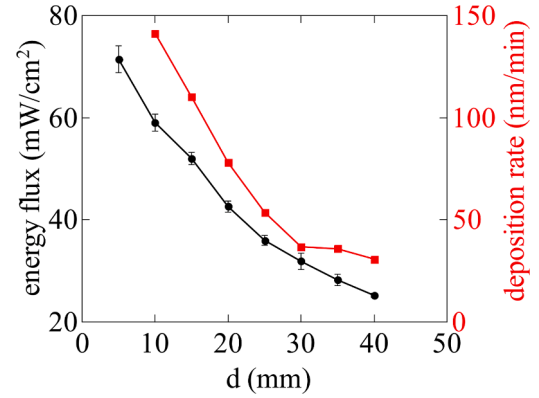


Fig. 12. Energy flux obtained from passive thermal probe (PTP) measurements as a function of the distance d between target and substrate (black). The mean values and the standard deviations are obtained from the two measurements for each distance. The black dashed line shows a fit of the mean values. The deposition rate for sputtered NbN thin films is determined by XRR (red). (For interpretation of the references to color in this figure legend, the reader is referred to the web version of this article.).

measurements of the pressure and power variation. The energy flux decrease results from the increased collision rate of sputtered particles at higher probe-to-target distances. Thus, a higher number of sputtered atoms are slowed down and unable to reach the substrate. This leads to thinner films and lower deposition rates.

The energy flux and consequently, the deposition rate show a quadratic decrease with increasing distances, suggesting that the heat intensity resembles that of a point-like source.

Here, the intensity decreases with increasing distance in a ratio of $I \sim 1/d^2$, with I being the intensity and d the distance between the probe and a point-like source. Since the distance $d = 5 \text{ mm} - 40 \text{ mm}$ is very small, we can no longer consider a close and comparably large plasma plume as a whole point-source, but instead we need to consider every point of it - especially beneath the race track - as a point-like source [21, 50].

3.3. Film and plasma properties versus sputtering power

When increasing the plasma power of the sputtering process from 20 W to 100 W, only slight variations on the superconducting properties of

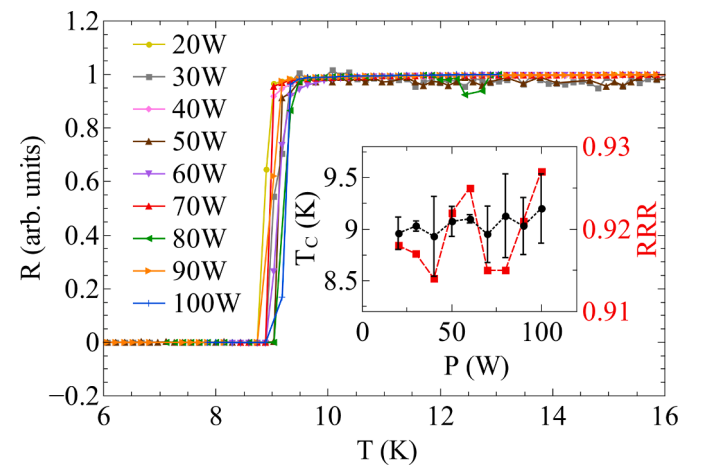


Fig. 13. RT-measurements for a variation in the deposition power (20 W - 100 W) with a constant pressure of 0.5 Pa and distance between target and sample of 37 mm. Inset: Calculated T_c (black) and RRR (red) for the measured RT-curves. (For interpretation of the references to color in this figure legend, the reader is referred to the web version of this article.).

the NbN films can be observed (Fig. 13). Only a marginal increase in T_c with increased sputtering power can be detected while RRR does not display any significant changes. Despite the minimal change in transition temperature, there is a clear linear increase in the deposition rate as a function of the increasing process power. Such an observation is surprising since, according to previous assumptions, the growth of the crystal layers of superconducting NbN is closely linked to the deposition rate [8] (Fig. 15).

At a process pressure of 0.5 Pa and a distance of 37 mm, the structure of the deposited NbN layers is independent of process power, as demonstrated by the GIXRD spectrum (Fig. 14). Neither crystallinity nor grain size show any dependence on sputtering power. This observation is in agreement with the investigation of the influence of the process power on the critical temperature, and confirms that the deposition rate cannot be directly correlated to the transition temperature and crystallinity of the NbN films.

A comparison between the energy flux and deposition rate for increasing magnetron power is shown in Fig. 15. The mean energy flux varies between 42 mW/cm² at a power of 20 W and 172 mW/cm² at 100 W. Moreover, the deposition rate increases from 15 nm/min at 20 W to 85 nm/min at 100 W. Both the energy flux and deposition rate show a linear increase for increasing power.

The energy flux being understood as a power transfer from the target/cathode to the substrate, a linear increase of the energy flux for increasing magnetron power is expected [20].

At higher power, the target's potential gets more negative compared to the substrate. Due to a higher potential difference, the positive ions accelerated towards the target obtain higher velocities and, thus, a higher kinetic energy. After momentum transfer, more target atoms will be sputtered resulting in a higher deposition rate.

Other plasma parameters like floating and plasma potential, electron temperature, and ion current density are obtained for probe-to-target distances of 37, 67, and 97 mm (Fig. 16).

The electron temperature shows an almost constant trend for $d > 37$ mm as seen in Fig. 16a. At higher probe-to-target distances, the electrons collide with more particles, losing kinetic energy and consequently reducing their temperature. As a result, the electron temperature at 67 mm and 97 mm is lower than at 37 mm.

Furthermore, the electron temperature increases from 2.2 eV at 20 W to about 3.1 eV at the maximum power for a distance of 37 mm. This is reflected by the plasma potential (Fig. 16c) and can be related to the

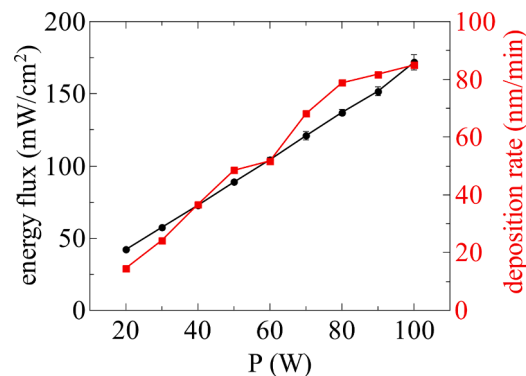


Fig. 15. Energy flux obtained by passive thermal probe (PTP) measurements as a function of deposition power (black). The mean values and the standard deviations are obtained from the two measurements for each deposition power. The black dashed line shows fits of the mean values. The deposition rate for sputtered NbN thin films is determined by XRR (red). (For interpretation of the references to color in this figure legend, the reader is referred to the web version of this article.).

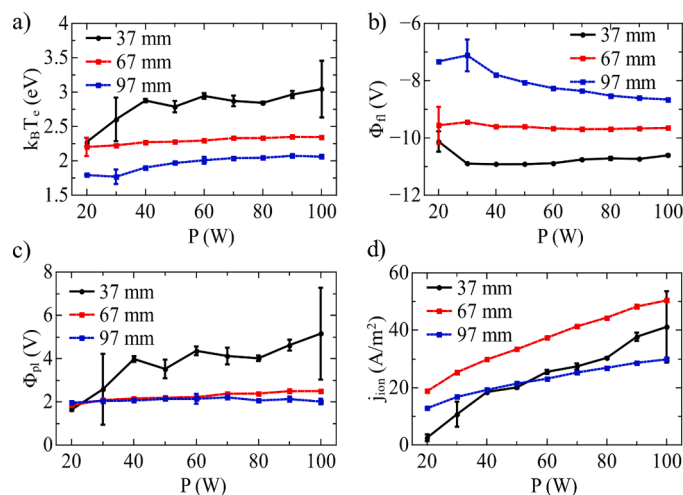


Fig. 16. Plasma parameters as a function of process power- the mean values and the standard deviations obtained from the three measurement points for each condition are depicted (squares with error bars). The solid and dashed lines are added as a guide to the eye for the mean values (37, 67 and 97 mm target to probe distance, respectively). (a) Electron temperature, (b) floating potential of probe, (c) plasma potential, and (d) current density of positive ions.

strong presence of the magnetic field.

Since the field strength of the magnetron is stronger at short distances, the floating potential is more negative resulting in a higher number of trapped electrons (Fig. 16b). With increasing magnetron power, the plasma density increases, leading to a higher number of electrons and ions. Yet, the floating potential of all three curves does not show a pronounced behavior, which is inconsistent with previous work on DC magnetron sputtering processes [51].

The plasma potential for distances of $d > 37$ mm behaves analogous to the floating potential, while for a probe-to-target distance of 37 mm it exhibits a total increase of 3.6 eV (1.6 eV to 5.2 eV) with increasing power (Fig. 16c). Here, the effect of the magnetic field is more pronounced, leading to a higher number of electrons in the plasma torus and, thus, a higher plasma density at a distance of 37 mm.

The current density of the positive ions is presented in Fig. 16d. With increasing magnetron power, the velocity and kinetic energy of the ions increases. As a result, a higher number of ions are accelerated towards the probe (substrate) leading to a higher ion current density.

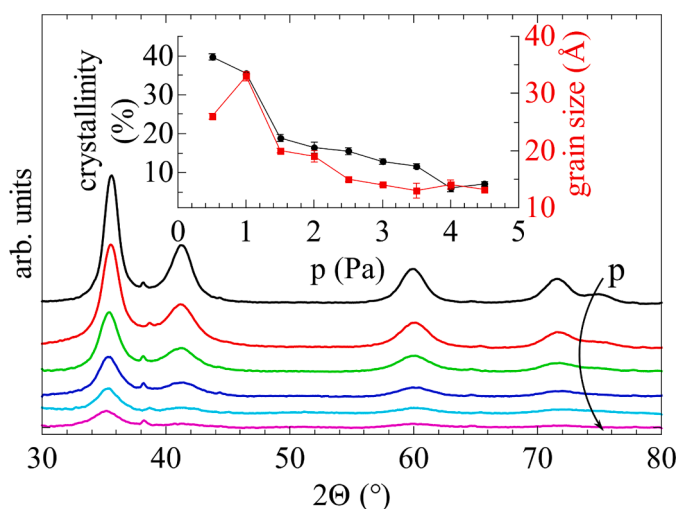


Fig. 14. GIXRD curves for a power range from 20 W to 100 W with a constant pressure of 0.5 Pa and distance between target and sample of 37 mm. Inset: Crystallinity (black) and grain size (red) extracted from the GIXRD. (For interpretation of the references to color in this figure legend, the reader is referred to the web version of this article.).

At 37 mm the increase of the current density is steeper (from 2.5 A/m² to 41.13 A/m²).

This can be attributed to smaller amounts of ions close to the magnetron and its magnetic field.

4. Conclusions

In summary, we show in this work that the analysis of the plasma parameters offers a comprehensive understanding of the effect of sputtering parameters on the layer growth of superconducting NbN. As the characterization of the energy flux alone provides insufficient information, further insight into the plasma parameters can be obtained by means of Langmuir probe measurements. This shows an increase of charged plasma particles with lower kinetic energies, resulting in a strong degradation of the structural layer properties via grain size reduction. This reduction in grain size is directly correlated to the transition temperature of the superconducting thin film. In addition, GIXRD and AFM structural analyses permitted film classification in Thornton's SZD, and demonstrating that the NbN film display the highest crystallinity for a pressure of 1 Pa.

A change in the substrate-target distance lower than the mean free path of the neutrals in the gas phase, induces an increase in the energy flux and a decrease in the transition temperature. The absence of correlation between RRR and T_c and the increase in energy flux suggests a higher defect density due to increased bombardment by neutrals.

The increase in plasma power shows a linear increase in deposition rate and energy flux, which are very highly correlated. No influence on the crystallinity and transition temperature of the layers could not be demonstrated under the given conditions, which together with the change in energy flux and sputtering rate can be explained by an increased amount of target atoms with constant energies.

CRedit authorship contribution statement

Richard Marquardt: Conceptualization, Writing – original draft, Investigation, Conceptualization, Methodology, Software, Visualization. **Julia Cipo:** Investigation, Software, Writing – original draft, Writing – review & editing. **Felix Schlichting:** Software, Investigation, Writing – review & editing. **Gitanjali Kolhatkar:** Data curation, Writing – review & editing. **Hermann Kohlstedt:** Project administration, Validation, Writing – review & editing, Funding acquisition, Supervision. **Holger Kersten:** Conceptualization, Writing – review & editing, Project administration, Validation, Supervision.

Declaration of Competing Interest

The authors declare that they have no known competing financial interests or personal relationships that could have appeared to influence the work reported in this paper.

Acknowledgements

One of the authors (G.K.) is thankful for a postdoctoral fellowship from the Alexander von Humboldt foundation. Funded by the Deutsche Forschungsgemeinschaft (DFG, German Research Foundation) – Project-ID 434434223 – SFB 1461.

References

- [1] A. Verevkin, J. Zhang, R. Sobolewski, A. Lipatov, O. Okunev, G. Chulkova, A. Korneev, K. Smirnov, G.N. Gol'tsman, A. Semenov, Detection efficiency of large-active-area NbN single-photon superconducting detectors in the ultraviolet to near-infrared range, *Appl. Phys. Lett.* 80 (Jun. (25)) (2002) 4687–4689, <https://doi.org/10.1063/1.1487924>.
- [2] G. Reithmaier, J. Senf, S. Lichtmannecker, T. Reichert, F. Flassig, A. Voss, R. Gross, J.J. Finley, Optimisation of NbN thin films on GaAs substrates for in-situ single photon detection in structured photonic devices, *J. Appl. Phys.* 113 (Apr. (14)) (2013), 143507, <https://doi.org/10.1063/1.4800838>.
- [3] V. Larrey, J. Villegier, M. Salez, F. Miletto-Granozio, A. Karpov, Processing and characterization of high Jc NbN superconducting tunnel junctions for THz analog circuits and RSFQ, *IEEE Trans. Appl. Supercond.* 9 (Jun. (2)) (1999) 3216–3219, <https://doi.org/10.1109/77.783713>.
- [4] Q. Zhang, H. Wang, X. Tang, W. Peng, Z. Wang, Fabrication and characteristics of all-NbN SQUID series array, *IEEE Trans. Appl. Supercond.* 30 (Apr. (3)) (2020) 1–3, <https://doi.org/10.1109/TASC.2019.2938582>.
- [5] I. Holzman, Y. Ivry, On-chip integrable planar NbN nanoSQUID with broad temperature and magnetic-field operation range, *AIP Adv.* 9 (Oct. (10)) (2019), 105028, <https://doi.org/10.1063/1.5100259>.
- [6] S. Leith, M. Vogel, J. Fan, E. Seiler, R. Ries, X. Jiang, Superconducting NbN thin films for use in superconducting radio frequency cavities, *Supercond. Sci. Technol.* 34 (Jan. (2)) (2021), 025006, <https://doi.org/10.1088/1361-6668/abc73b>.
- [7] C. s Sandu, M. Benkahoul, M. Parlinska-Wojtan, R. Sanjines, F. Lévy, Morphological, structural and mechanical properties of NbN thin films deposited by reactive magnetron sputtering, *Surf. Coat. Technol.* 200 (2006) 6544–6548, <https://doi.org/10.1016/j.surfcoat.2005.11.054>.
- [8] M.J. Deen, The effect of the deposition rate on the properties of d.c.-magnetron-sputtered niobium nitride thin films, *Thin Solid Films* 152 (Sep. (3)) (1987) 535–544, [https://doi.org/10.1016/0040-6090\(87\)90269-0](https://doi.org/10.1016/0040-6090(87)90269-0).
- [9] D.D. Bacon, A.T. English, S. Nakahara, F.G. Peters, H. Schreiber, W.R. Sinclair, R. B. van Dover, Properties of NbN thin films deposited on ambient temperature substrates, *J. Appl. Phys.* 54 (Nov. (11)) (1983) 6509–6516, <https://doi.org/10.1063/1.331881>.
- [10] M.S. Wong, W.D. Sproul, X. Chu, S.A. Barnett, Reactive magnetron sputter deposition of niobium nitride films, *J. Vac. Sci. Technol. A* 11 (Jul. (4)) (1993) 1528–1533, <https://doi.org/10.1116/1.578696>.
- [11] Y.M. Shy, L.E. Toth, R. Somasundaram, Superconducting properties, electrical resistivities, and structure of NbN thin films, *J. Appl. Phys.* 44 (Dec. (12)) (1973) 5539–5545, <https://doi.org/10.1063/1.1662193>.
- [12] T. Polakovic, S. Lendinez, J.E. Pearson, A. Hoffmann, V. Yefremenko, C.L. Chang, W. Armstrong, K. Hafidi, G. Karapetrov, V. Novosad, Room temperature deposition of superconducting niobium nitride films by ion beam assisted sputtering, *APL Mater.* 6 (Jul. (7)) (2018), 076107, <https://doi.org/10.1063/1.5031904>.
- [13] J. Benedikt, H. Kersten, A. Piel, Foundations of measurement of electrons, ions and species fluxes toward surfaces in low-temperature plasmas, *Plasma Sources Sci. Technol.* 30 (Mar. (3)) (2021), 033001, <https://doi.org/10.1088/1361-6595/abe4bf>.
- [14] M. Tinkham, *Introduction to Superconductivity*, Courier Corporation, 2004.
- [15] M.P. MacMartin, N.L. Kusters, A direct-current-comparator ratio bridge for four-terminal resistance measurements, *IEEE Trans. Instrum. Meas.* 15 (Dec. (4)) (1966) 212–220, <https://doi.org/10.1109/TIM.1966.4313542>.
- [16] J.H. Kim, S.X. Dou, J.L. Wang, D.Q. Shi, X. Xu, M.S.A. Hossain, W.K. Yeoh, S. Choi, T. Kiyoshi, The effects of sintering temperature on superconductivity in MgB₂/Fe wires, *Supercond. Sci. Technol.* 20 (May (5)) (2007) 448–451, <https://doi.org/10.1088/0953-2048/20/5/007>.
- [17] S. Banerjee, A.A.I. Aarnink, R. van de Kruijs, A.Y. Kovalgin, J. Schmitz, PEALD AlN: controlling growth and film crystallinity, *Phys. Status Solidi c* 12 (7) (2015) 1036–1042, <https://doi.org/10.1002/pssc.201510039>.
- [18] P.D. Edmondson, Y. Zhang, S. Moll, F. Namavar, W.J. Weber, Irradiation effects on microstructure change in nanocrystalline ceria - phase, lattice stress, grain size and boundaries, *Acta Mater* 60 (Sep. (15)) (2012) 5408–5416, <https://doi.org/10.1016/j.actamat.2012.07.010>.
- [19] J.A. Thornton, Substrate heating in cylindrical magnetron sputtering sources, *Thin Solid Films* 54 (Oct. (1)) (1978) 23–31, [https://doi.org/10.1016/0040-6090\(78\)90273-0](https://doi.org/10.1016/0040-6090(78)90273-0).
- [20] S. Gauter, F. Haase, H. Kersten, Experimentally unraveling the energy flux originating from a DC magnetron sputtering source, *Thin Solid Films* 669 (2019) 8–18, <https://doi.org/10.1016/j.tsf.2018.10.021>.
- [21] S. Bornholdt, H. Kersten, Transient calorimetric diagnostics for plasma processing, *Eur. Phys. J. D* 67 (Aug. (8)) (2013) 176, <https://doi.org/10.1140/epjd/e2013-40148-8>.
- [22] M. Stahl, T. Trottenberg, H. Kersten, A calorimetric probe for plasma diagnostics, *Rev. Sci. Instrum.* 81 (Feb. (2)) (2010), 023504, <https://doi.org/10.1063/1.3276707>.
- [23] H.M. Mott-Smith, I. Langmuir, The theory of collectors in gaseous discharges, *Phys. Rev.* 28 (Oct. (4)) (1926) 727–763, <https://doi.org/10.1103/PhysRev.28.727>.
- [24] R.H. Huddleston, S.L. Leonard, Plasma diagnostic techniques, *J. Plasma Phys.* 1 (1) (1965) 156, <https://doi.org/10.1017/S0022377800003160>.
- [25] B.B. Sahu, J.G. Han, M. Hori, K. Takeda, Langmuir probe and optical emission spectroscopy studies in magnetron sputtering plasmas for Al-doped ZnO film deposition, *J. Appl. Phys.* 117 (Jan. (2)) (2015), 023301, <https://doi.org/10.1063/1.4905541>.
- [26] X. Wang, Q. Li, Z. Chen, W. Wang, C. Xie, J. Wang, Q. Gao, W. Peng, X. Geng, G.-N. Luo, A newly designed actively water-cooled Langmuir probe for tokamak devices, *Rev. Sci. Instrum.* 90 (2019) 6.
- [27] A. Piel, *Plasma Physics: an Introduction to Laboratory, Space, and Fusion Plasmas*, Springer, 2017.
- [28] Z. Wang, A. Kawakami, Y. Uzawa, B. Komiyama, Superconducting properties and crystal structures of single-crystal niobium nitride thin films deposited at ambient substrate temperature, *J. Appl. Phys.* 79 (May (10)) (1996) 7837–7842, <https://doi.org/10.1063/1.362392>.
- [29] N.N. Iosad, A.V. Mijiritskii, V.V. Roddatis, N.M. van der Pers, B.D. Jackson, J. R. Gao, S.N. Polyakov, P.N. Dmitriev, T.M. Klapwijk, Properties of (Nb_{0.35}, Ti_{0.15}) xNi_{1-x} thin films deposited on silicon wafers at ambient substrate temperature,

- J. Appl. Phys. 88 (Nov. (10)) (2000) 5756–5759, <https://doi.org/10.1063/1.1319653>.
- [30] N.N. Iosad, N.M. van der Pers, S. Grachev, V.V. Roddatis, B.D. Jackson, S. N. Polyakov, P.N. Dmitriev, T.M. Klapwijk, Texture formation in sputter-deposited (Nb_{0.7}Ti_{0.3})N thin films, J. Appl. Phys. 92 (Nov. (9)) (2002) 4999–5005, <https://doi.org/10.1063/1.1510589>.
- [31] M. Wittmer, Properties and microelectronic applications of thin films of refractory metal nitrides, J. Vac. Sci. Technol. A 3 (Jul. (4)) (1985) 1797–1803, <https://doi.org/10.1116/1.573382>.
- [32] F. Marsili, A. Gaggero, L.H. Li, A. Surrente, R. Leoni, F. Lévy, A. Fiore, High quality superconducting NbN thin films on GaAs, Supercond. Sci. Technol. 22 (Aug. (9)) (2009), 095013, <https://doi.org/10.1088/0953-2048/22/9/095013>.
- [33] H.C. Jones, Some properties of granular thin films of high-field superconductors, Appl. Phys. Lett. 27 (8) (1975) 471, <https://doi.org/10.1063/1.88532>.
- [34] G. Deutscher, Y. Imry, L. Gunther, Superconducting phase transitions in granular systems, Phys. Rev. B 10 (Dec. (11)) (1974) 4598–4606, <https://doi.org/10.1103/PhysRevB.10.4598>.
- [35] M. Gurvitch, M. Washington, H. Huggins, J. Rowell, Preparation and properties of Nb Josephson junctions with thin Al layers, IEEE Trans. Magn. 19 (May (3)) (1983) 791–794, <https://doi.org/10.1109/TMAG.1983.1062296>.
- [36] S.P. Chockalingam, M. Chand, J. Jesudasan, V. Tripathi, P. Raychaudhuri, Superconducting properties and Hall effect of epitaxial NbN thin films, Phys. Rev. B 77 (Jun. (21)) (2008), 214503, <https://doi.org/10.1103/PhysRevB.77.214503>.
- [37] R. Kieffer, H. Nowotny, P. Ettmayer, G. Dufek, Neue Untersuchungen über die Mischbarkeit von Übergangsmetallnitriden und -karbiden, Metall (26) (1972) 701.
- [38] N.C. Halder, C.N.J. Wagner, Separation of particle size and lattice strain in integral breadth measurements, Acta Cryst. 20 (Feb. (2)) (1966) 312–313, <https://doi.org/10.1107/S0365110X66000628>.
- [39] S. Kubo, M. Asahi, M. Hikita, M. Igarashi, Magnetic penetration depths in superconducting NbN films prepared by reactive dc magnetron sputtering, Appl. Phys. Lett. 44 (Jan. (2)) (1984) 258–260, <https://doi.org/10.1063/1.94690>.
- [40] J.A. Thornton, Influence of apparatus geometry and deposition conditions on the structure and topography of thick sputtered coatings, J. Vac. Sci. Technol. 11 (Jul. (4)) (1974) 666–670, <https://doi.org/10.1116/1.1312732>.
- [41] J.A. Thornton, Influence of substrate temperature and deposition rate on structure of thick sputtered Cu coatings, J. Vac. Sci. Technol. 12 (Jul. (4)) (1975) 830–835, <https://doi.org/10.1116/1.568682>.
- [42] O. Kluth, G. Schöpe, J. Hüpkes, C. Agashe, J. Müller, B. Rech, Modified Thornton model for magnetron sputtered zinc oxide: film structure and etching behaviour, Thin Solid Films 442 (Oct. (1)) (2003) 80–85, [https://doi.org/10.1016/S0040-6090\(03\)00949-0](https://doi.org/10.1016/S0040-6090(03)00949-0).
- [43] N. Otsu, A threshold selection method from gray-level histograms, in: IEEE Transactions on Systems, Man, and Cybernetics, 9, 1979. Art. no. 1.
- [44] S.M. Rossnagel, Energetic particle bombardment of films during magnetron sputtering, J. Vac. Sci. Technol. A 7 (May (3)) (1989) 1025–1029, <https://doi.org/10.1116/1.576223>.
- [45] E.G. Sheikin, The pressure dependence of the deposition rate in a magnetron sputtering system, Thin Solid Films 574 (2015) 52–59, <https://doi.org/10.1016/j.tsf.2014.11.043>. Jan.
- [46] S.N. Mazhir, M.K. Khalaf, S.K. Taha, H.K. Mohsin, Measurement of plasma electron temperature and density by using different applied voltages and working pressures in a magnetron sputtering system, IJET 7 (Jun. (3)) (2018) 1177, <https://doi.org/10.14419/ijet.v7i3.9459>.
- [47] F. Zahari, F. Schlichting, J. Strobel, S. Dirkmann, J. Cipo, S. Gauter, J. Trieschmann, R. Marquardt, G. Haberfehlner, G. Kothleitner, L. Kienle, T. Mussenbrock, M. Ziegler, H. Kersten, H. Kohlstedt, Correlation between sputter deposition parameters and I-V characteristics in double-barrier memristive devices, J. Vac. Sci. Technol. B 37 (Nov. (6)) (2019), 061203, <https://doi.org/10.1116/1.5119984>.
- [48] K.L. Cartwright, J.P. Verboncoeur, C.K. Birdsall, Nonlinear hybrid Boltzmann-particle-in-cell acceleration algorithm, Phys. Plasmas 7 (Jul. (8)) (2000) 3252–3264, <https://doi.org/10.1063/1.874191>.
- [49] Z. Wang, H. Terai, A. Kawakami, Y. Uzawa, Interface and tunneling barrier heights of NbN/AlN/NbN tunnel junctions, Appl. Phys. Lett. 75 (Jul. (5)) (1999) 701–703, <https://doi.org/10.1063/1.124487>.
- [50] P. Gu, X. Zhu, H. Wu, D. Yang, Regulation of substrate-target distance on the microstructural, optical and electrical properties of CdTe films by magnetron sputtering, Materials 11 (Dec. (12)) (2018), <https://doi.org/10.3390/ma11122496>.
- [51] E. Martinez, R. Cavazzana, G. Serianni, M. Spolaore, L. Tramontin, M. Zuin, V. Antoni, Electrostatic fluctuations in a direct current magnetron sputtering plasma, Phys. Plasmas 8 (May (6)) (2001) 3042–3050, <https://doi.org/10.1063/1.1369657>.

III. Domain Wall Movement in Undoped Ferroelectric HfO₂: A Rayleigh Analysis

Bibliographic Information

Marquardt, R., Petersen, D., Gronenberg, O., Zahari, F., Lamprecht, R., Popkirov, G., Carstensen, J., Kienle, K., and Kohlstedt, H. (2023). Domain Wall Movement in Undoped Ferroelectric HfO₂: A Rayleigh Analysis. *ACS Applied Electronic Materials* 2023, 5, 6, 3251–3260.
<https://doi.org/10.1021/acsaelm.3c00336>

Author's contribution

The author contributed to:

- Conceptual work
- Partial construction of the measurement setup
- Guiding sample preparation
- Electrical and XRD Measurements
- Evaluation of the data
- Writing of the manuscript

Copyright Notice

This work is licensed under a Creative Commons Attribution 4.0 International License (CC BY 4.0). Read the license text:

<https://creativecommons.org/licenses/by/4.0/legalcode>.

III.1 Summary

In this manuscript, we present our results of a Rayleigh analysis performed by impedance spectroscopy on a ferroelectric undoped HfO_2 layer (~ 10 nm) sandwiched between two superconducting NbN electrodes and prepared by sputter deposition. Due to its great potential, given by its CMOS compatibility and scalability, ferroelectric HfO_2 has been of great interest since its discovery about a decade ago. Various applications of the newly discovered property of HfO_2 are already found in ferroelectric field effect transistors, ferroelectric tunnel junctions, as well as neuromorphic devices, thus expanding the technological scope toward memory applications. Although numerous applications of ferroelectric HfO_2 exist, some of the underlying mechanisms of ferroelectric phase stabilization and ferroelectric switching are not yet fully understood.

The nature and movement of the domain walls within the ferroelectric layer provide information about the switching behavior and are assumed to be the cause of good scalability. Through our experiments, we demonstrate the applicability of Rayleigh's law to the domain wall behavior of HfO_2 . The data relevant to the Rayleigh analysis is extracted by impedance spectroscopy, a non-destructive and fast measurement technique. Results of Rayleigh analysis provide information on the flexibility of the domain walls, which in turn gives insight into scattering processes that impede domain wall motion. Furthermore, a structural and chemical analysis is provided, which focuses on the chemical properties of the interfaces between the electrodes and the active layer. In particular, the electrodes contain a low oxygen content compared to other typically used electrode materials. A low interdiffusion between the electrodes and the oxide layer allows more precise tuning of the oxygen content, which is essential for stabilizing the ferroelectric phase in the undoped HfO_2 layers and is, therefore, favorable. A further benefit of superconducting electrode materials lies in the potential development of low-energy electronics for low-energy computing.

Our findings show that stabilizing undoped HfO_2 on NbN by sputtering position is possible. In addition, we demonstrate that a deeper understanding of the processes of ferroelectric switching can be obtained by employing impedance spectroscopy. These insights are beneficial for the effective tuning of the ferroelectric layer properties.

Domain Wall Movement in Undoped Ferroelectric HfO₂: A Rayleigh Analysis

Richard Marquardt,* Deik Petersen, Ole Gronenberg, Finn Zahari, Rouven Lamprecht, George Popkirov, Jürgen Carstensen, Lorenz Kienle, and Hermann Kohlstedt*



Cite This: <https://doi.org/10.1021/acsaelm.3c00336>



Read Online

ACCESS |

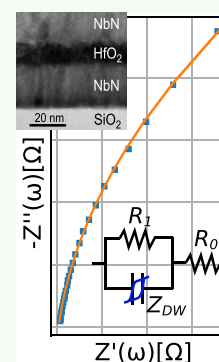
Metrics & More

Article Recommendations

Supporting Information

ABSTRACT: The discovery of ferroelectricity in doped HfO₂ in 2011 gave rise to quite a stir in the scientific world that persists up to this day. The complementary metal oxide semiconductor compatibility, as well as good scalability, enables versatile applications ranging from ferroelectric field effect transistors to ferroelectric tunnel junctions and neuromorphic devices. Stabilizing the metastable polar orthorhombic phase with space group *Pca*2₁-phase, which is responsible for the ferroelectricity in HfO₂, is still challenging. We demonstrate for the first time a sputter deposition of undoped ferroelectric HfO₂ on superconducting NbN electrodes, with a remanent polarization of 6.4 $\mu\text{C}/\text{cm}^2$. Grazing incident X-ray diffraction on the layer structure, dynamic hysteresis measurements, and electron energy loss spectroscopy on fabricated devices indicate a HfO₂ layer with low oxygen deficiency. Furthermore, no evidence of interdiffusion of oxygen or nitrogen at the interfaces is found. A sudden “wake-up” for the transition from the dielectric state to the ferroelectric state as well as no classical fatigue effect for the degradation of the ferroelectric performance are observed. These analyses are extended by an investigation of Rayleigh behavior using impedance spectroscopy. In that way, the domain wall flexibility is quantified and classified within different regimes of the various domain wall motions.

KEYWORDS: Ferroelectricity, Impedance Spectroscopy, Domain Wall, Hafnium Oxide, Superconductivity



INTRODUCTION

The discovery of ferroelectricity in HfO₂ sparked new interest in the ferroelectric information storage research field,¹ which lost popularity due to the lack of complementary metal oxide semiconductor (CMOS) compatibility of the widely used ferroelectric perovskites.² The scalability of hafnia-based devices and the compatibility of HfO₂ with CMOS technology, known through its use as a high-K gate dielectricum, demonstrate the great potential for HfO₂-based ferroelectric devices as semiconductor components in diverse device types.³ Accordingly, research on the integration of ferroelectric HfO₂ has already been carried out on a variety of different device types, such as ferroelectric random access memory (FRAM), ferroelectric tunnel junctions (FTJs), and ferroelectric field effect transistors (FeFETs).^{4,5} For the fabrication of undoped and doped ferroelectric HfO₂ layers, atomic layer deposition (ALD), sputtering, pulsed laser deposition, and chemical solution deposition can be used as deposition methods.⁶

Even though there have been almost twice as many publications on ALD for HfO₂ production as on sputtering deposition in the past three years,⁷ the sputtering process offers advantages such as more adjustable process parameters and, thus, a high degree of flexibility as well as a larger deposition rate.⁸ Furthermore, combining undoped HfO₂ as a ferroelectric with superconducting NbN as electrode material has several benefits. From an engineering point of view, the advantage of undoped HfO₂ is the ease of handling compared to doped

HfO₂, where usually only a narrow range of doping concentration produces the desired ferroelectric effect.⁹ A system in which the oxygen defects act as dopants, as in the undoped ferroelectric HfO₂, allows a more flexible adjustment of the process independent of the target properties.¹⁰ Since future low-energy computing technologies may require cryogenic temperatures, using superconducting electrodes such as NbN is beneficial for very fast operation speed¹¹ and low energy consumption.¹² Furthermore, superconducting electrodes pave the way for Josephson junction (JJ) neurons based on ferroelectric HfO₂, which are considered promising candidates for neuromorphic computing.^{13,14} In addition, NbN shows desirable features compared to the most commonly used TiN electrodes in terms of resistance against oxidation,¹⁵ which in turn reduces the formation of oxidic interfaces, and favors the production of tunnel junctions with NbN electrodes.

For the characterization of the ferroelectric performance of the deposited HfO₂ layers, an analysis of the Rayleigh behavior is useful, which allows extracting information about the behavior of domain walls in interaction with pinning

Received: March 13, 2023

Accepted: May 3, 2023

centers.^{16,17} By the Rayleigh analysis method, it is possible to obtain information about defect densities and pristine structures of the domains, which are essential for optimizing the deposition process of ferroelectric layers and hence the development of efficient ferroelectric memory modules.

Domain wall motion is of particular interest in fluorite structures such as HfO_2 ,¹⁸ since such structures do not contain Ising walls as in perovskites, but instead domains down to the size of a unit cell with highly localized domain walls.¹⁹ This is possible due to flat phonon bands, which suppress an interaction between the dipoles and thus make them locally switchable.²⁰ Due to the phonon velocity approaching zero, the domain wall is assumed to have a thickness close to zero.²⁰ This special feature leads to a more sluggish behavior of the domains on one hand,^{20–22} but on the other hand it allows scale-free multilevel switching, which is especially interesting for memory applications. In addition to FeFETs, a novel form of brain-inspired memristor is currently being investigated for neuromorphic applications, which benefits the switching of conducting charged domain walls.^{23–26}

Impedance spectroscopy can be used to measure the field dependence of the domain wall motion and the frequency dispersion. The first Rayleigh law measurements on ferroelectric HfO_2 were published a few years after the discovery of ferroelectricity in HfO_2 .²⁷ Impedance spectroscopy on ferroelectric-doped HfO_2 was previously performed in 2016 by Grimley et al.²⁸ In the course of this analysis, interfacial effects and effects of a wake-up could have been defined.^{28,29} In 2018, the introduction of a Rayleigh element by Schenk et al. gave the possibility to extract information about the field-dependent behavior of domain walls (DW) by utilizing impedance spectroscopy.³⁰ An addition of frequency dispersion to the Rayleigh element due to the pinning of DW³¹ was later provided by Becker et al. and applied to epitaxial and polycrystalline ferroelectric $0.5(\text{Ba}_{0.7}\text{Ca}_{0.3})\text{TiO}_3\text{--}0.5\text{Ba}(\text{Zr}_{0.2}\text{Ti}_{0.8})\text{O}_3$ (BCZT) films.^{16,17}

This study shows an RF-sputtering process for undoped ferroelectric HfO_2 on superconducting NbN electrodes.³² Such a junction might be an attractive way to develop low-temperature, low-power superconducting electronics.³³ Both the HfO_2 and NbN are structurally and chemically analyzed for crystal phase, grain size, and oxygen content.

EXPERIMENTAL SECTION

The devices presented in this work consist of capacitor-like structures in which a ferroelectric layer of undoped HfO_2 is sandwiched between two NbN electrodes. All samples prepared for this study were deposited on a silicon substrate with a 400 nm thermally oxidized SiO_2 passivation layer at its surfaces. The NbN bottom electrode (BE) with a layer thickness of $d_{\text{BE}} = 30$ nm was deposited on the substrate by DC magnetron sputtering. The HfO_2 with a layer thickness of $d_{\text{FE}} = 9.5 \pm 0.5$ nm was deposited by RF magnetron sputtering in Ar atmosphere. An annealing step at 600 °C for 10 s under a N_2 atmosphere at atmospheric pressure is performed as an unconfined bake. Afterward, the top electrode (TE) was deposited with the same parameters as the BE, and a $d_{\text{Au}} = 10$ nm thick layer of gold was sputtered on top. The top electrodes were structured by a lift-off process. The fabrication parameters are summarized in Table 1.

X-ray diffraction patterns were obtained with a Rigaku SmartLab 9 kW diffractometer at a wavelength of $\lambda = 1.5418$ Å. For the grazing incident X-ray diffraction (GIXRD) measurements, a 9 kW copper X-ray source was used in a monochromatic parallel beam configuration focused with a length-limiting slit of 5 mm along the longitudinal axis. The grazing incidence angle was set to 0.5° for both presented measurements.

Table 1. Process Parameters

target	Nb(6")	HfO ₂ (4")	Au(4")
source	DC magnetron	RF magnetron	DC magnetron
power (W)	400	120	100
gas flow (sccm)	12 Ar + 3 N ₂	40 Ar	10 Ar
pressure (mbar)	1.3×10^{-2}	1.3×10^{-2}	1.3×10^{-2}
target-to-substrate distance (mm)	70	50	55
deposition rate (Å/s)	1.8	3.6	10
thickness (nm)	30	10.5	10

A trained device was prepared for cross-sectional TEM analysis by focused ion beam milling using an FEI Helios Nanolab system. TEM measurements, including Electron Energy Loss Spectroscopy (EELS), were performed at a FEI Tecnai F30 G² with 300 kV and a field emission gun.

Electrical I – V and P – V measurements were performed on an Aixacct TF2000 analyzer and a Precision Premier Pro II from Radiant. The C – V data were measured on a Precision LCR meter 4284A from Hewlett-Packard. A homemade impedance spectrometer was used to obtain the impedance of the ferroelectric films with frequency response analysis. For the amplitude of the electric field E_0 , a range from 0.05 up to 0.88 MV/cm was chosen for the measurement. The frequency range was between 0.76 and 358 Hz. Fitting the impedance data was performed with a customized version of the python library impedance.py.³⁴ For the fitting of the impedance data, only measuring points that showed a deviation of less than 5% according to the linear Kramers–Kronig theorem³⁵ were considered.

RESULTS AND DISCUSSION

Structural Analysis. GIXRD measurements before and after annealing reveal the crystallization and phase evolution of the devices analyzed in this work, as shown in Figure 1. For the undoped HfO_2 , an annealing-induced separation into several crystal phases is shown. A reflection at about 28° indicates a (1 1 $\bar{1}$) monoclinic phase fraction. The existence of a clearly visible monoclinic (1 1 $\bar{1}$) reflection is indicating that the HfO_2 is nearly stoichiometric, since the monoclinic phase is the energetically preferred phase of stoichiometric HfO_2 .⁸ Thus, there appears to be a low density of oxygen vacancies. This is also reported for other ferroelectric HfO_2 layers sputtered with an additional small amount of oxygen within the process gas.⁸

Based on the GIXRD scan, the orthorhombic/tetragonal/cubic (o/t/c) phase appears to be more dominant. Distinction of the o/t/c phases is difficult by XRD alone; therefore a phase mixture cannot be excluded. However, the existence of the o-phase is proven by the ferroelectric properties. The structure of the NbN electrodes is already shown to be polycrystalline cubic after deposition, and the crystal phase is not affected by the annealing step. The annealing step leads to an increase in the crystallinity of NbN and HfO_2 , which can be seen in the intensity increase of the GIXRD pattern normalized to the (200) reflection of NbN. Since all reflections increase almost equally, it is not assumed that a texture is formed. This is also proven by electron diffraction (data not shown).

The crystal size affects both the phase transformation process of HfO_2 ^{8,10,38} and the superconducting properties of NbN. For the superconducting properties of the NbN, a possible epitaxial growth is ideal since the coherence length depends essentially on the grain size.³² In contrast, a small grain size is advantageous to stabilize the ferroelectric orthorhombic phase. This can be achieved, for example, by

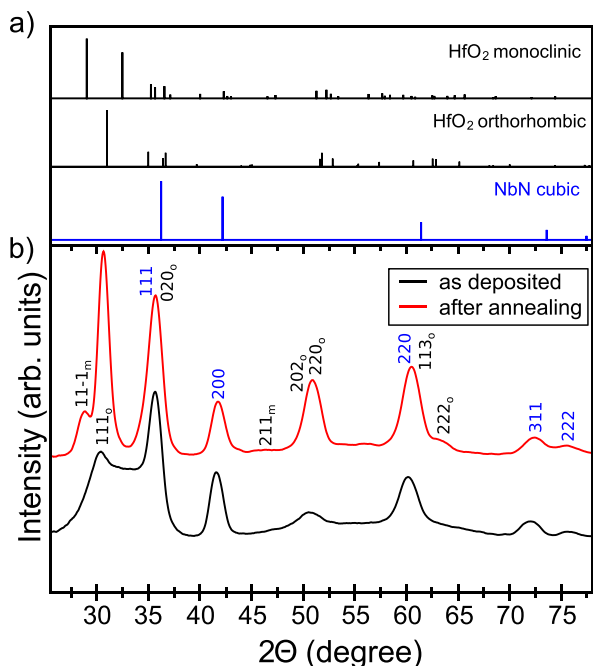


Figure 1. (a) Diffraction pattern for monoclinic³⁶ HfO₂ (black) as well as cubic NbN³⁷ (blue). The diffraction pattern for the orthorhombic *Pca*2₁ phase (black) of HfO₂ was generated with the cell lengths *a* = 5.27 Å, *b* = 5.04 Å, *c* = 5.07 Å. (b) GIXRD of the ferrielectric undoped HfO₂ sandwiched between NbN bottom and top electrodes.

reducing the film thicknesses of the HfO₂ layer⁸ as well as the bottom electrode. Thus, a conflict arises for the grain size optimization of the NbN.

From the GIXRD scan (Figure 1), the grain sizes of the NbN and HfO₂ layers can be determined using the Halder–Wagner method.³⁹ The deposited NbN has a grain size of 5.2 nm, which increases with the heat treatment to 6.8 nm. This is about twice the minimum grain size required for a sufficient coherence length to enable superconductivity.³² The crystallite size of HfO₂ is 7.2 nm, which is close to the theoretical optimum of 8–16 nm for stabilizing the orthorhombic phase, as calculated by density functional theory (DFT) of Materlik et al.³⁸ Smaller grains are assumed to be stable in the tetragonal phase and larger in the monoclinic phase.

The cross-sectional transmission electron spectroscopy (TEM) image of the MIM capacitor (Figure 2a) shows smooth interfaces. Further, a columnar structure of the NbN electrodes with a small column diameter, which fits well with the 6.8 nm determined by XRD, is detected. These NbN columns extend over the entire electrodes, arguing against oxidized interfaces with the HfO₂.

The EEL spectra in Figure 2b show a comparison of the BE and the TE) in the bulk and near the interfaces with HfO₂. No differences in the degree of oxidation can be evidenced from the O–K peak intensity. Hence, a low and uniform presence of oxygen in both TE and BE can be concluded, which is usual for cross-sectional samples prepared by focus ion beam etching due to the large surface exposed to air. Nevertheless, a transition temperature, from a conducting to a superconducting state, of about 9 K has been demonstrated for NbN electrodes deposited in such a manner, indicating a relatively small grain size and low oxygen content.³² Larger grains would

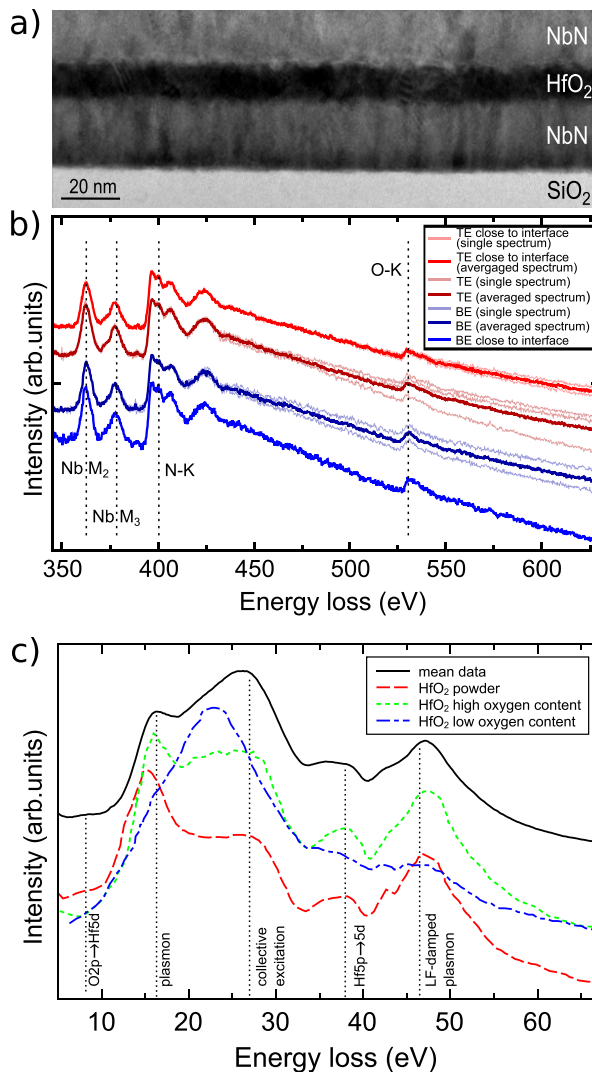


Figure 2. (a) Cross-sectional TEM image of the capacitor-like structure. (b) EELS measurements of NbN electrodes close to the interfaces with the HfO₂ and in the bulk. The solid curves show the averaged data of the individual scans, which are represented by the semitransparent curves. All spectra were background subtracted and normalized to the Nb M₂ edge. Peak positions were extracted from Guedj et al.⁴⁰ (c) Low-loss EELS of the HfO₂ layer, together with reference spectra for monoclinic HfO₂ (powder) and HfO₂ with high and low oxygen content prepared by atomic layer deposition (ALD).⁴¹

favor a higher transition temperature but suppress the growth of the metastable orthorhombic phase of HfO₂.

Furthermore, neither nitrogen nor niobium can be detected in the HfO₂ (Supporting Information, S3; Figure 5). Thus, an often observed interdiffusion of HfO₂ and the electrodes is not observed.⁴² This is preferable in the preparation of ferroelectric HfO₂, since stoichiometry is a crucial factor in achieving the ferroelectric crystal phase. Therefore, the use of NbN as electrode material allows a finer adjustment of the oxygen content in thin HfO₂ layers, in contrast to, for example, TiN.

The low-loss EEL spectrum of the HfO₂ layer is shown in Figure 2c, along with reference spectra of monoclinic HfO₂ (powder) and HfO₂ with low and high oxygen content deposited by ALD.⁴¹ The plasmon peak at about 16 eV is sensitive to oxygen concentration.^{41,43} It indicates an oxygen

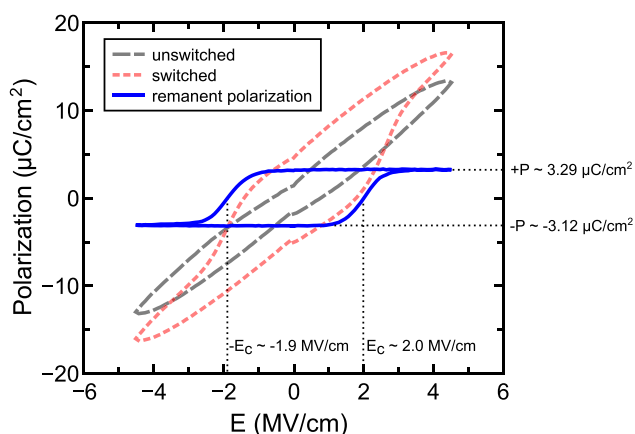


Figure 3. Remanent polarization measurement conducted with the PUND method at 5 kHz.

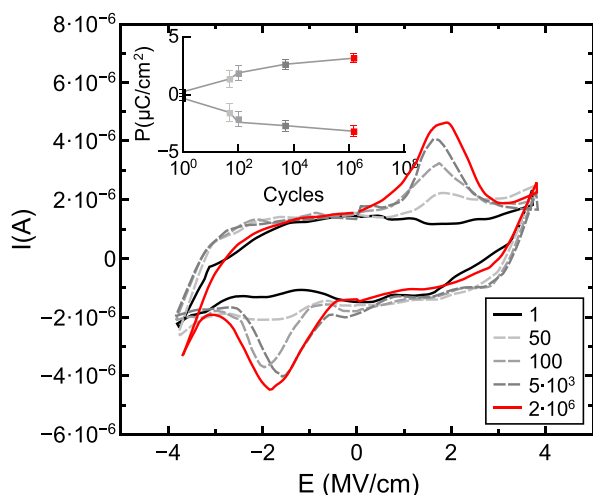


Figure 4. I – V measurements during wake-up at 5 kHz. Inset: The positive and negative polarization corrected for the leakage current component during wake-up taken from four samples.

content between that of the reference spectra with low and high concentrations and a phase portion of the m-phase. This fits well to the indicated phase mixture of monoclinic and orthorhombic by GIXRD.

Training: DC Measurements. For electrical characterization, polarization vs voltage (P – V) and capacitance vs voltage (C – V) curves, as well as impedance spectra, were measured on the ferroelectric NbN(30 nm)/HfO₂(9.5 nm)/NbN(30 nm) devices. From the uncorrected P – V curve of the ferroelectric capacitor, a remanent polarization of $2P_r = 9.6 \mu\text{C}/\text{cm}^2$ can be obtained (Figure 3). For the leakage current corrected P – V analysis, which uses the positive-up–negative-down (PUND) method, a reduced saturated P – V curve with a remanent polarization of $6.4 \mu\text{C}/\text{cm}^2$ is determined, with the negative coercive field of $-E_c = 1.9 \text{ MV}/\text{cm}$ and the positive coercive field of $E_c = 2.0 \text{ MV}/\text{cm}$. The offset between positive and negative coercive fields is called imprint and can have a variety of causes, ranging from domain pinning to degradation of the ferroelectric properties.⁴⁴ For HfO₂-based ferroelectrics, charge-injection-induced electron detrapping from oxygen vacancies is assumed to be the main cause of imprint.⁴⁵

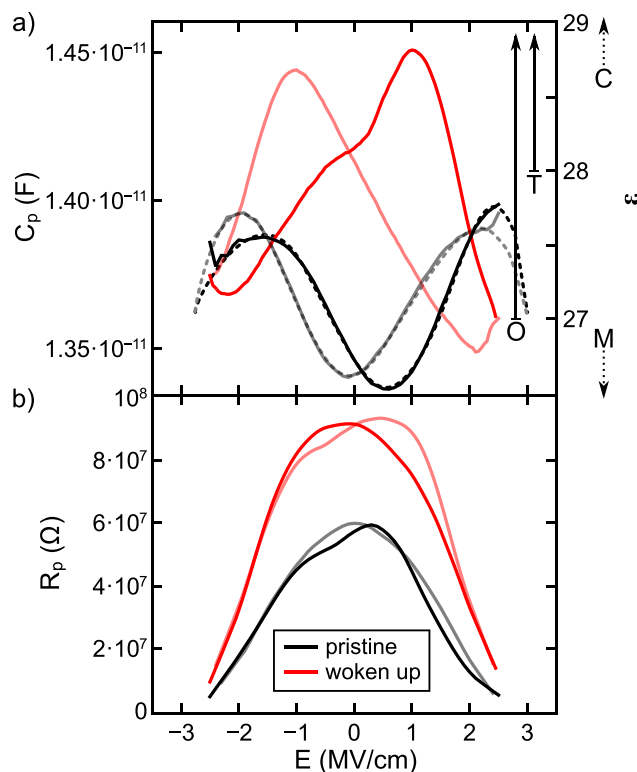


Figure 5. (a) Device capacitance C_p and relative permittivity ϵ dependent on the applied electric field for the pristine (black) and for the woken-up state (red) at 5 kHz and $V_{\text{amp}} = 50 \text{ mV}$. The permittivity ranges assigned to the different crystal phases are shown on the right side of the graph.²⁸ The dashed black lines show the sketched course of an antiferroelectric as an orientation. (b) Leakage resistance R_p . The full colors are for the sweep from a negative to a positive field, and the transparent colors are for the sweep from a positive field to a negative field.

There is a minimal imprint for the layers investigated here, which changes only marginally during the component's cycling. This, in turn, suggests a low density of oxygen defects.

The wake-up of the ferroelectric effect is investigated by consecutive I – V cycling with a frequency of 5 kHz, as shown in Figure 4. The cycling of the ferroelectric layer shows a wake-up phase before the ferroelectric characteristic becomes visible, like most polycrystalline HfO₂ layers.^{10,28,46} Both of the I – V curves shown in Figure 4 and the corrected remanent polarization curve in the inset show a sudden increase in polarization. It takes about 5×10^3 cycles until the sample is fully trained. Since no displacement currents can be measured for the pristine state, one speaks of a sudden wake-up.⁴⁷ Such wake-up behavior was first observed by Lederer et al. and was related to field-induced crystallization.⁴⁷ Recently, ferroelastic 90° domain switching was revealed as an additional possibility for a transition from a nonpolar direction to the polar (001) direction of the ferroelectric orthorhombic phase.⁴⁸

With increasing cycle number, an increase in leakage current can be observed at voltages above 3 V, eventually leading to a breakdown of the ferroelectric films between 5×10^6 and 8×10^6 cycles.

For all measurements performed, there was no decrease in the sample's polarization at any time during a fatigue measurement. Fatigue in ferroelectric HfO₂ layers is often observed, whether doped^{3,49,50} or undoped.^{50,51} This is one of

the major obstacles to implement ferroelectric hafnia into reliable information storage elements. It is associated with oxygen migration during cycling and phase transition.⁵²

C–V measurements of the undoped ferroelectric HfO₂ (Figure 5a) show a classic butterfly curve for the condition after the training (10⁵ cycles), which is caused by the movement of domain walls that are excited by the oscillation of the small signal amplitude (50 mV) of the C–V measurement.⁵³ However, a comparison with the pristine state reveals two unusual features. First, there is just a slight change in the minimum permittivity, which can mainly be attributed to the crystal phase. Therefore, a constant phase mixture is assumed and no phase transitions.²⁸ Such behavior can be explained by a ferroelastic 90° domain switching, which is also suspected to occur in undoped HfO₂ films on TiN electrodes.⁴⁸ Second, there are signs of antiferroelectric behavior in the C–V characteristics, manifested by a double peak (Figure 5a) in both the negative and positive regions of the applied electric field.⁵⁴ For the negative range of the electric field, an antiferroelectric typical double peak can be seen more clearly, whereas the coercive fields for the positive electric fields appear to be slightly higher (Figure 5). A possible explanation for this observation could be a phase transition from an orthorhombic phase with weak antiferroelectric behavior to an orthorhombic phase with ferroelectric behavior.⁵²

Furthermore, leakage resistance measurements show an increase in resistance for electric fields below 2.5 MV/cm with an increasing number of cycles, in addition to a slight change in the voltage dependency (Figure 5b). Such changes in resistivity during wake-up are attributed to oxygen vacancies moving out of the bulk material toward the electrode interfaces.⁵⁵

Rayleigh Analysis: AC Measurements. Theoretical Background. The Rayleigh analysis presented in this work is based on the logarithmic frequency dependence of domain wall motions in a rough energy landscape found by Becker et al.¹⁶ A detailed derivation of the origin of the Rayleigh model used can be found in the [Supporting Information](#), S1.

The assumption from Becker et al. of a frequency-dependent motion of a domain wall in a rough energy landscape leads to the following definition of the real and imaginary part of the relative permittivity:

$$\epsilon'_r(E_0, f) = \epsilon'_{r,in,0} + \alpha'_0 E_0 + [\Delta\epsilon'_{r,in} + \Delta\alpha' E_0] \ln\left(\frac{1\text{Hz}}{2\pi f}\right) \quad (1)$$

with $\epsilon'_{r,in,0}$ as the frequency-independent component of the reversible DW displacement, $\Delta\epsilon'_{r,in}$ as the zero-field contribution to the logarithmic dispersion strength, α'_0 as the frequency-independent component of the Rayleigh constant, and α' as the coupling strength between dielectric nonlinearity and frequency dispersion. The latter is defined as the change of logarithmic frequency dispersion strength with field amplitude or equivalently as the change of the irreversible Rayleigh parameter with the logarithm of the frequency.

For the imaginary part of the complex permittivity the following applies:

$$\epsilon''_r(E_0) = \epsilon''_{r,in} + \alpha'' E_0 \quad (2)$$

As can be seen in eq 2, the complex part of the permittivity responds independently of the changing electric field.

However, it contains a factor $\epsilon''_{r,in}$, which represents the zero-field contribution and is therefore 0 in nonstressed ferroelectrics without an internal field.

Linear equations for the three dispersion parameters can be derived from eq 1 and eq 2:

$$\epsilon'_{r,0}(E_0) = \epsilon'_{r,in,0} + \alpha'_0 E_0 \quad (3)$$

$$\epsilon''_{r,0}(E_0) = \epsilon''_{r,in} + \alpha'' E_0 \quad (4)$$

$$\Delta\epsilon'_{r,0} = \Delta\epsilon'_{r,in} + \Delta\alpha' E_0 \quad (5)$$

By analyzing these dispersion parameters, it is possible to define the behavior of ferroelectrics in different field frequency ranges. Three different behavioral ranges for ferroelectric domains could have been already defined solely from the dielectric response to differently high fields:^{16,17} (I) the subthreshold range, in which only reversible changes of the domain walls take place, (II) the Rayleigh-like region, in which irreversible shifts in domain wall mass centers result in nonlinearity in the dielectric response, and finally (III) the regime of partial switching, which is particularly interesting for the field of neuromorphic computing, in which the biological model of the synapse is emulated by partially switching memristive devices.⁵⁶ Due to the introduced coupling of field dependence and frequency dispersion, a further subdivision of the Rayleigh-like regime follows. The distinction is made between the stochastic behavior and the pinning of DWs, which will be discussed in more detail in the following analysis. As an equivalent circuit element, the so-called pinning element Z_{DW} :

$$Z_{\text{DW}} = \frac{\epsilon''_{r,0} - i \left[\epsilon'_{r,0} + \Delta\epsilon'_{r,in} \ln\left(\frac{1\text{Hz}}{2\pi f}\right) \right]}{2\pi f C_0 \left\{ \left[\epsilon'_{r,0} + \Delta\epsilon'_{r,in} \ln\left(\frac{1\text{Hz}}{2\pi f}\right) \right]^2 + \epsilon''_{r,0}^2 \right\}} \quad (6)$$

was extracted by Becker et al.¹⁷ from the above assumptions, which is used in the following for fitting the impedance data.

Analysis. For the investigated HfO₂ samples, utilizing three equivalent circuit elements is sufficient to generate a high quality fit in the used frequency range. When measuring the impedance at higher frequencies, interface effects can become visible, which are usually compensated by adding another resistor and a capacitor connected in parallel (RC element). To generate a fit of high quality despite the six degrees of freedom for the equivalent circuit shown in Figure 6a, a “prefit” was performed to determine starting values and bounds for the fit parameters. For this purpose, a simplified Randle’s circuit was used, which helped to estimate the parameters R_0 , R_1 , and C_0 . The frequency dispersion was approximated by the logarithmic fit error. Details on data fitting can be found in the [Supporting Information](#), S2.

The fit with the DW pinning element shows a significant improvement in terms of normalized error, which can also be seen in the plot of the Bode diagram ([Supporting Information](#), S2). The parameters of the example fit and two more impedance spectrum measurements inside the Rayleigh regime are shown in Table 2.

A nearly constant value (i.e., independent of the applied electric field) was fitted for the geometric constant of the capacitance C_0 , which is composed of contact size, layer thickness, and vacuum permittivity. A slightly lower value than expected ($C_0 \approx 5.8 \times 10^{-13}$) indicates a smaller contact size

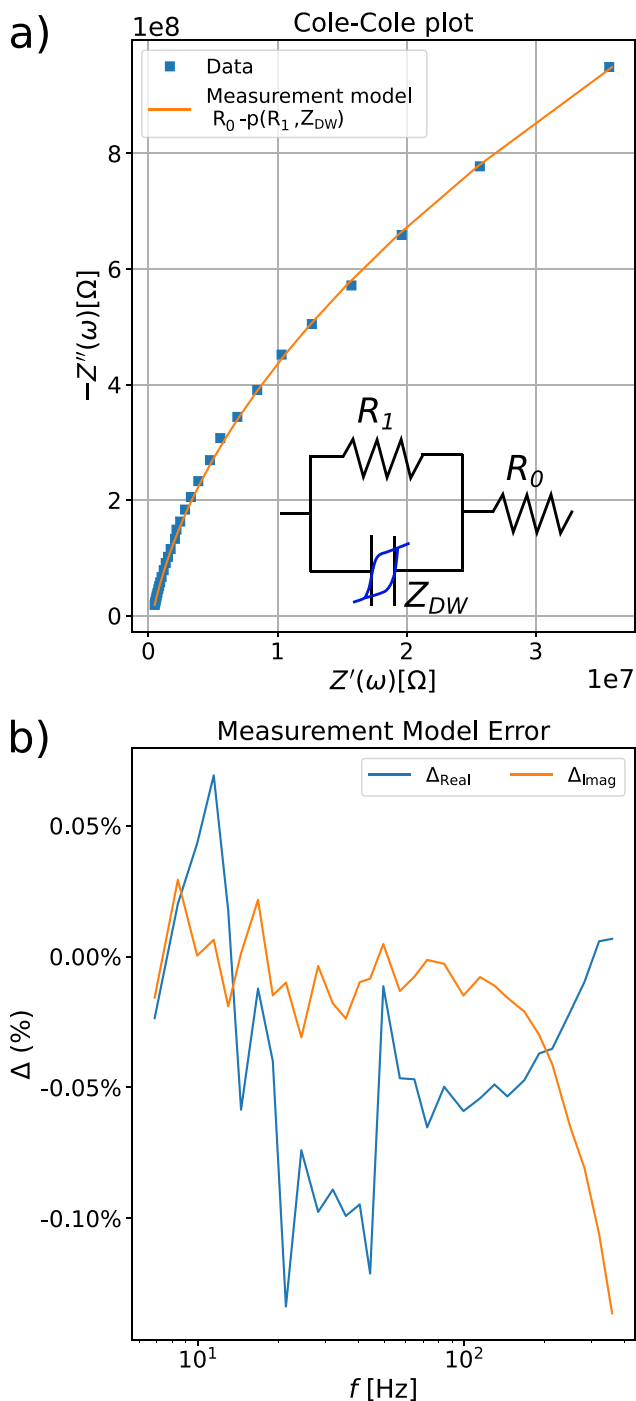


Figure 6. (a) Cole–Cole plot of the impedance of a ferroelectric HfO₂ layer between NbN electrodes at an electric field of $E_0 = 78.35 \times 10^6$ V/cm for a frequency range from 0.78 to 358 Hz shown in a Nyquist plot, along with a fit for an equivalent circuit containing two resistances and a DW pinning element. (b) Normalized error of the fit model divided into real and imaginary components plotted against frequency.

than the approximated $25 \times 25 \mu\text{m}^2$ after lift-off. The dispersion parameters are plotted against the electric field amplitude in Figure 7 to determine the Rayleigh range and

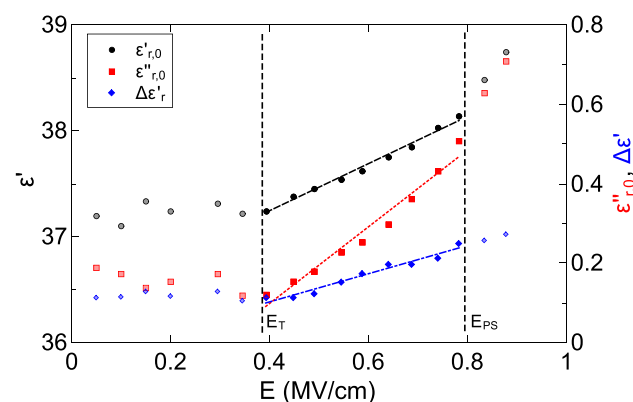


Figure 7. Field dependence of dispersion parameters $\epsilon_{r,0}'$, $\epsilon_{r,0}''$, and $\Delta\epsilon_{r,0}'$, along with linear fits in the Rayleigh range.

other parameters of the Rayleigh analysis. The three areas of subthreshold, Rayleigh-like, and partial switching can be identified. According to Hall,⁵⁷ the definition of the subthreshold region describes the region in which no irreversible DW motion takes place. The transition to the Rayleigh-like region occurs at the threshold field, which is $E_T = 0.4$ MV/cm for the measured HfO₂ layers. The definition of the Rayleigh-like region was chosen so that the coefficient of determination R^2 is greater than 0.95 for the linear fits of the three dispersion coefficients (eqs 3, 4, 5). This results in a field strength E_{PS} of about 0.8 MV/cm for the transition to the partial switching region.

The parameters obtained from the fits of the Rayleigh equations can be found in Table 3. With a zero-field value $\epsilon_{r,0}'$ of 36.35, the real fraction of relative permittivity is slightly above the assumed value of 35 for the orthorhombic phase.^{28,38} The value α_0' describes a nonlinear field interaction, which becomes most significant for fast-moving DWs. This field interaction thus includes the velocity of the fast-moving domain walls under the influence of an external field, which in turn depends on the flexibility of the domain wall. Thus, alpha can be understood as an indirect measure of domain wall flexibility. From the experiments, an α_0' of 2.22 MV/cm can be determined, which is about a factor of 4 lower than that of silicon-doped hafnium oxide²⁷ and orders of magnitude smaller than the value for ferroelectrics based on BCZT ($\approx 10^3$ MV/cm).¹⁶ It should be noted that the value for silicon-doped HfO₂ was not determined according to the method of Becker et al. and could therefore deviate from the values determined in this work due to the lack of consideration of parasitic losses of the frequency dispersion by Becker et al.

The deviation of the zero-field value of the imaginary part of the relative permittivity from zero indicates the presence of an

Table 2. Fitting Parameters for Three Different Field Strengths in the Rayleigh Range

E_0 (MV/cm)	R_0 (Ω)	R_1 (Ω)	C_0 (F)	$\epsilon_{r,0}''$	$\epsilon_{r,0}'$	$\Delta\epsilon_{r,0}'$
0.39	8.74×10^5	2.79×10^{10}	6.63×10^{-13}	0.1	37.4	0.176
0.59	4.91×10^5	1.39×10^{10}	6.64×10^{-13}	0.254	37.8	0.196
0.78	2.30×10^5	7.37×10^9	6.48×10^{-13}	0.55	39	0.213

Table 3. Dispersion Parameters Extracted from Figure 7

$\epsilon_{r,in,0}$	α_0' (MV/cm)	$\epsilon_{r,in}''$	α'' (MV/cm)	$\Delta\epsilon_{r,in}'$	$\Delta\alpha'$ (MV/cm)
36.35 ± 0.05	(2.22 ± 0.08)	-0.29 ± 0.04	(0.965 ± 0.068)	-0.04 ± 0.017	(0.355 ± 0.028)

internal bias or stress field.³⁰ According to eq 1 and eq 2, the α'' parameter represents the analogy to α' for the imaginary domain and thus also provides information about the field interaction of the fast-moving DW. Low values of the two α parameters, therefore, indicate parasitic effects such as scattering processes, which result in a low DW flexibility. We find the factor of $3\pi/4$ between α'' and α_0' , which is already indicating the Rayleigh frequency in the lower frequency spectrum. The coefficient $\Delta\epsilon_{r,in}'$ is the zero-field contribution to the logarithmic dispersion strength. A negative value for $\Delta\epsilon_{r,in}'$ means an increase of the reversible Rayleigh parameter $\epsilon_{r,in}'$ with increasing frequency according to eq 1. The reason for this could be a resonance behavior of the vibration of DWs, which would lead to an increase of $\epsilon_{r,in}'$ for low frequencies. Due to the high deviation of ± 0.017 from the fit for the $\Delta\epsilon_{r,in}'$ (Table 3), however, a fit error or measurement error for the dispersion parameter for the irreversible process would also be plausible. Therefore, an interpretation of this fit parameter should be considered cautiously.

The coupling parameter $\Delta\alpha'$ between dielectric field dependence and frequency dispersion is 0.355 MV/cm for the investigated films. From the determined parameters shown in Table 3, the frequency dependence of the Rayleigh constant can be represented with the help of eq 1 (Figure 8). The

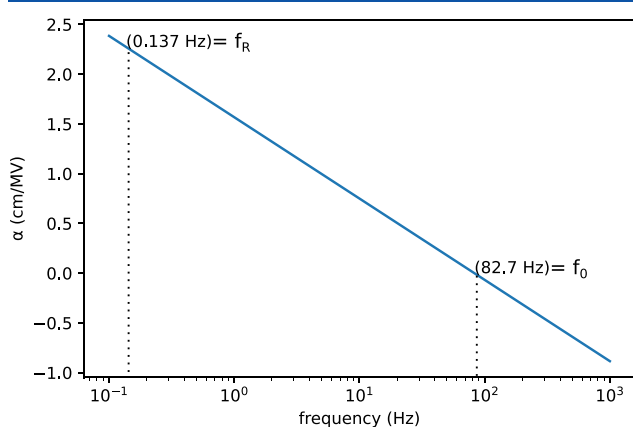


Figure 8. Irreversible Rayleigh parameter-dependent frequency. The Rayleigh frequency f_R and the crossover frequency f_0 are marked.

frequency, in which the symmetry criterion of $3\pi/4$ between the real and imaginary parts is fulfilled, is described as Rayleigh frequency. It is determined as $f_R \sim 0.14$ Hz. Rayleigh-like behavior is defined for the frequency range in which the Rayleigh constant is greater than zero. In this regime, it is assumed that the center of mass of a DW can jump between different potential minima. Since the center of mass of a DW passes through several potential minima within one electric field cycle, such behavior resembles the stochastic motion of particles in an RF environment.⁵⁸ Thus, it is called the stochastic regime.⁵⁹

In our data, a transition of the irreversible Rayleigh parameter to negative numerical values can be observed at a frequency of $f_0 \sim 83$ Hz. This frequency f_0 is thus called the transition frequency between the pinning and stochastic

regime. From this frequency on, a movement of the center of mass of a DW is only assumed between different metastable states since the exciting field period is too short for the center of mass to escape from the potential minimum. This area is called the pinning regime. For the investigated polycrystalline HfO_2 film the transition between the stochastic regime and pinning regime occurs at lower frequencies relative to epitaxial ferroelectric Y:HfO_2 films due to the low DW mobility and the relatively high coupling parameter $\Delta\alpha'$, which can be found in the Supporting Information S4. An obvious explanation for the different behaviors of the measured HfO_2 layers and ferroelectric BCZT layers lies in the different morphologies of the films. HfO_2 has a higher density of grain boundaries and different grain orientations due to its polycrystalline structure, which both greatly influence the switching behavior.⁶⁰ The influence of grain boundaries and their orientation can lead to the pinning of domain walls.^{61–63} However, grain boundaries do not affect the avalanche-like propagation of the influence of a domain wall displacement on the adjacent domain walls.⁶⁴ Nevertheless studies by Becker et al. have shown a reduction in the coupling factor of frequency dispersion and field dependence for epitaxial ferroelectric BCZT compared to polycrystalline BCZT films.^{16,17} This may be explained by the interplay between domain size and grain size of the polycrystalline films. If the grains are smaller than the domains, the film is less responsive to an external electrical field than a system with large grains and small domains.

To verify some of the results of the Rayleigh analysis, a check using the second Rayleigh relation for ferroelectric ceramics is helpful. The second Rayleigh relation is defined by⁶⁵

$$P = \epsilon_0 \left[\epsilon_r'(0) + \alpha E_0 \right] E \pm \frac{\alpha}{2} (E_0^2 - E^2) \quad (7)$$

For α equal to α_0 , eq 7, with the parameters determined from the Rayleigh analysis, yields a polarization of $2P = 5.21 \mu\text{C}/\text{cm}^2$. Since only the ferroelectric process with a logarithmic frequency dependence is considered by fitting the domain pinning element, and parasitic effects are thus neglected, this can be referred to as remanent polarization. This is in excellent agreement with the results ($2P_r = 6.4 \mu\text{C}/\text{cm}^2$) and, thus, indicates the quality of the Rayleigh analysis.

The behavior of the real fraction of the relative permittivity ϵ_r' for the analyzed HfO_2 films calculated by eq 1 is visualized in Figure 9 as a heat map from which gradients and the influence of the regimes can be observed. Figure 9a shows the transition from the stochastic region to the pinning region in a semilogarithmic representation. The parabolic course of the lines in Figure 9a shows the strong influence of the coupling factor on the behavior of the real part of the relative permittivity. It should be emphasized that eq 1 does not apply to the grayed-out areas $E_0 < E_T$ and $E_{PS} < E_0$. Furthermore, the influence of the dispersion parameter $\Delta\epsilon_{r,in}'$ can only be seen for very small fields in the grayed-out area. For fields below the threshold field $E_T = 0.4$ MV/cm, only reversible movements of the DW can be detected, which corresponds to the noncoupled pinning region. If the field is between the threshold field and the partial switching field (E_T

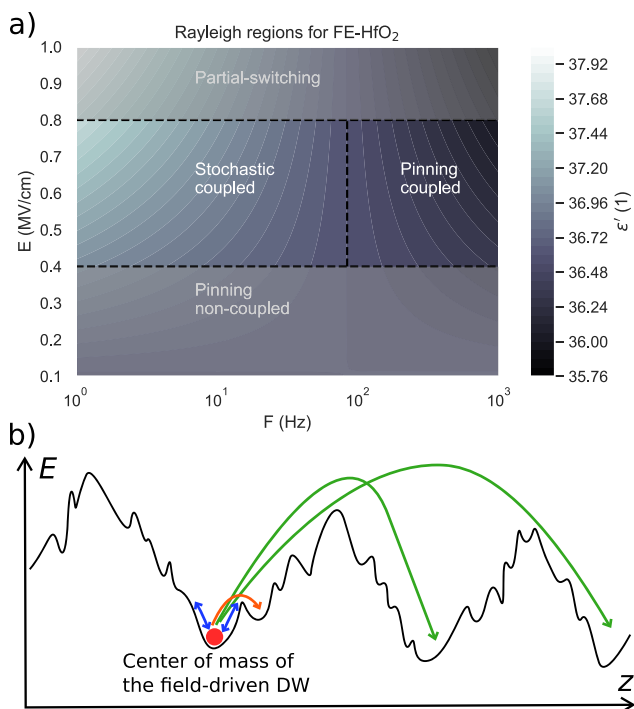


Figure 9. (a) Diagram of the different DW motion regimes with corresponding permittivity values of the polycrystalline HfO₂ thin film on NbN electrodes according to Becker et al.¹⁷ (b) Schematic of the motion of the center of mass of a DW in a rough energy landscape.^{30,59} The Z axis describes the spatial dimension in which the center of mass of the domain wall moves and the E axis describes the energy required for the movement. Blue arrows denote the reversible movement of the subthreshold or noncoupled pinning regime. The red arrows show the motion of the center of mass in different metastable states for the coupled pinning region, and the green arrows indicate the stochastic behavior.

$< E_0 < E_{ps}$), it is called the Rayleigh region, which is divided into the coupled stochastic and the coupled pinning regime. A schematic diagram showing the movement of the center of mass of a domain wall in the three different regimes is shown in Figure 9b. For the stochastic region, a possible motion of the center of mass into one of several potential minima is assumed, resulting in a coexistence of irreversible center-of-mass motion and relaxational motion of internal domain-wall segments.¹⁷ For our data, the transition of these two regions occurs at $f_0 = 84$ Hz, given that the irreversible Rayleigh parameter frequency above 84 Hz, the center of mass of the DW can no longer follow the alternating field and is therefore pinned.^{16,59,66} Nevertheless, a motion to nearby metastable states is assumed. However, it must be mentioned that there is still no definite understanding of the movement of DW in the coupled pinning regime.^{16,59} If the field is increased beyond $E_{ps} = 0.8$ MV/cm, partial switching of the ferroelectric domains takes place.^{16,30}

CONCLUSION

In this work, a novel material combination for ferroelectric devices was presented by stabilizing thin (9.5 nm) undoped ferroelectric HfO₂ films on superconducting NbN electrodes by magnetron sputtering.⁶ Such a combination of materials demonstrates the first steps toward ferroelectric tunnel barriers in superconducting Josephson junctions. This may offer an

attractive way to establish a highly integrable memory functionality in superconducting electronics, which is otherwise difficult to achieve.⁶⁷ In addition, NbN as an electrode material suppresses the interdiffusion of oxygen, allowing finer tuning of the oxygen content in thin HfO₂ films. The prepared films exhibited spontaneous wake-up, as well as no fatigue for a total of 2×10^6 cycles, with a maximum corrected polarization of $2P_r = 6.4 \mu\text{C}/\text{cm}^2$. Moreover, a more detailed analysis of the C–V characteristic hints at an antiferroelectric orthorhombic phase for the pristine state, together with a ferroelastic 90° domain switching for the phase transition during wake-up.

Furthermore, this work shows a Rayleigh analysis using the pinning element for thin ferroelectric HfO₂ films in a low-frequency range. The analysis presented in this work shows that the Rayleigh law, with its linear field dependence and logarithmic frequency dependence, can also be applied to highly localized domain walls whose thickness is close to zero. From the determined Rayleigh parameters for field and frequency dependence, different behavioral regimes can be defined, which provide information about the DW dynamics. We find much lower DW flexibility in polycrystalline ferroelectric HfO₂ films than in perovskite ferroelectrics, suggesting a higher density of pinning centers. Pinning centers are usually point defects, which, in ferroelectric HfO₂, mostly consist of oxygen vacancies⁴⁵ or pristine domain structures,⁶⁸ such as nonferroelectric spacer layers between the ferroelectric layers.^{20,21} EELS and electrical data show a chemically stable interface between HfO₂ and NbN electrodes, which exhibits no interdiffusion of oxygen or nitrogen. Furthermore, a rather high oxygen content in the HfO₂ film is detected. Thus, pristine domain structures and fractions of the nonferroelectric monoclinic crystal phase are suspected as the main cause for minor polarization values.

ASSOCIATED CONTENT

Supporting Information

The Supporting Information is available free of charge at <https://pubs.acs.org/doi/10.1021/acsaelm.3c00336>.

Additional experimental theoretical background, experimental details of impedance data, EEL spectra of HfO₂ layer and NbN electrodes, and dispersion parameters of epitaxial ferroelectric Y:HfO₂ (PDF)

AUTHOR INFORMATION

Corresponding Authors

Richard Marquardt – Nanoelectronics, Faculty of Engineering, Kiel University, 24143 Kiel, Germany; orcid.org/0000-0003-1105-9289; Email: rvm@tf.uni-kiel.de

Hermann Kohlstedt – Nanoelectronics, Faculty of Engineering, Kiel University, 24143 Kiel, Germany; Email: hko@tf.uni-kiel.de

Authors

Deik Petersen – Chair of Functional Nanomaterials, Faculty of Engineering, Kiel University, 24143 Kiel, Germany

Ole Gronenberg – Synthesis and Real Structure Group, Faculty of Engineering, Kiel University, 24143 Kiel, Germany

Finn Zahari – Nanoelectronics, Faculty of Engineering, Kiel University, 24143 Kiel, Germany

Rouven Lamprecht – Nanoelectronics, Faculty of Engineering, Kiel University, 24143 Kiel, Germany

George Popkirov – Central Laboratory of Solar Energy and New Energy Sources, Bulgarian Academy of Sciences, 1784 Sofia, Bulgaria

Jürgen Carstensen – Chair of Functional Nanomaterials, Faculty of Engineering, Kiel University, 24143 Kiel, Germany

Lorenz Kienle – Synthesis and Real Structure Group, Faculty of Engineering, Kiel University, 24143 Kiel, Germany

Complete contact information is available at:

<https://pubs.acs.org/10.1021/acsaelm.3c00336>

Notes

The authors declare no competing financial interest.

ACKNOWLEDGMENTS

Funded by the Deutsche Forschungsgemeinschaft (DFG, German Research Foundation)–Project-ID 434434223–SFB 1461.

REFERENCES

- (1) Böske, T.; Müller, J.; Bräuhäus, D.; Schröder, U.; Böttger, U. Ferroelectricity in hafnium oxide thin films. *Appl. Phys. Lett.* **2011**, *99*, 102903.
- (2) Fan, Z.; Chen, J.; Wang, J. Ferroelectric HfO₂-based materials for next-generation ferroelectric memories. *Journal of Advanced Dielectrics* **2016**, *6*, 1630003.
- (3) Park, M. H.; Lee, Y. H.; Mikolajick, T.; Schroeder, U.; Hwang, C. S. Review and perspective on ferroelectric HfO₂-based thin films for memory applications. *Mrs Communications* **2018**, *8*, 795–808.
- (4) Cheema, S. S.; Shanker, N.; Hsu, C.-H.; Datar, A.; Bae, J.; Kwon, D.; Salahuddin, S. One nanometer HfO₂-based ferroelectric tunnel junctions on silicon. *Advanced Electronic Materials* **2022**, *8*, 2100499.
- (5) Song, C.-M.; Kwon, H.-J. Ferroelectrics based on HfO₂ film. *Electronics* **2021**, *10*, 2759.
- (6) Hsain, H. A.; Lee, Y.; Materano, M.; Mittmann, T.; Payne, A.; Mikolajick, T.; Schroeder, U.; Parsons, G. N.; Jones, J. L. Many Routes to Ferroelectric HfO₂: A Review of Current Deposition Methods. *Journal of Vacuum Science & Technology A* **2022**, *40*, 010803.
- (7) Strobel, V. Pold87/academic-keyword-occurrence: First release. **2018**; DOI: 10.5281/zenodo.1218409.
- (8) Mittmann, T.; Materano, M.; Lomenzo, P. D.; Park, M. H.; Stolichnov, I.; Cavalieri, M.; Zhou, C.; Chung, C.-C.; Jones, J. L.; Szyjka, T.; Müller, M.; Kersch, A.; Mikolajick, T.; Schroeder, U. Origin of Ferroelectric Phase in Undoped HfO₂ Films Deposited by Sputtering. *Advanced Materials Interfaces* **2019**, *6*, 1900042.
- (9) Kim, K. D.; Park, M. H.; Kim, H. J.; Kim, Y. J.; Moon, T.; Lee, Y. H.; Hyun, S. D.; Gwon, T.; Hwang, C. S. Ferroelectricity in Undoped-HfO₂ Thin Films Induced by Deposition Temperature Control during Atomic Layer Deposition. *Journal of Materials Chemistry C* **2016**, *4*, 6864–6872.
- (10) Mittmann, T.; Michailow, M.; Lomenzo, P. D.; Gärtner, J.; Falkowski, M.; Kersch, A.; Mikolajick, T.; Schroeder, U. Stabilizing the ferroelectric phase in HfO₂-based films sputtered from ceramic targets under ambient oxygen. *Nanoscale* **2021**, *13*, 912–921.
- (11) Schneider, M. L.; Donnelly, C. A.; Russek, S. E. Tutorial: High-speed low-power neuromorphic systems based on magnetic Josephson junctions. *J. Appl. Phys.* **2018**, *124*, 161102.
- (12) Henry, M. D.; Smith, S. W.; Lewis, R. M.; Ihlefeld, J. F. Stabilization of Ferroelectric Phase of Hf_{0.58}Zr_{0.42}O₂ on NbN at 4 K. *Appl. Phys. Lett.* **2019**, *114*, 092903.
- (13) Goteti, U. S.; Zaluzhnyy, I. A.; Ramanathan, S.; Dynes, R. C.; Frano, A. Low-temperature emergent neuromorphic networks with correlated oxide devices. *Proc. Natl. Acad. Sci. U. S. A.* **2021**, *118*, No. e2103934118.
- (14) Chalkiadakis, D.; Hizanidis, J. Dynamical properties of neuromorphic Josephson junctions. *Phys. Rev. E* **2022**, *106*, 044206.
- (15) Barshilia, H. C.; Rajam, K. Nanolayered TiN/NbN Multilayers as New Superhard Materials. *Proceedings of the International Conference on Advances in Surface Treatment: Research and Applications*; ASTRA, 2003; p 129.
- (16) Becker, M. T.; Burkhardt, C. J.; Kleiner, R.; Koelle, D. Impedance Spectroscopy of Ferroelectrics: The Domain Wall Pinning Element. *J. Appl. Phys.* **2022**, *132*, 044104.
- (17) Becker, M.; Burkhardt, C. J.; Schröppel, B.; Kleiner, R.; Koelle, D. Rayleigh Analysis and Dielectric Dispersion in Polycrystalline 0.5(Ba_{0.7}Ca_{0.3})TiO₃–0.5Ba(Zr_{0.2}Ti_{0.8})O₃ Ferroelectric Thin Films by Domain-Wall Pinning Element Modeling. *J. Appl. Phys.* **2020**, *128*, 154103.
- (18) Lee, D. H.; Lee, Y.; Yang, K.; Park, J. Y.; Kim, S. H.; Reddy, P. R. S.; Materano, M.; Mulaosmanovic, H.; Mikolajick, T.; Jones, J. L.; Schroeder, U.; Park, M. H. Domains and domain dynamics in fluorite-structured ferroelectrics. *Applied Physics Reviews* **2021**, *8*, 021312.
- (19) Lederer, M.; Lehninger, D.; Ali, T.; Kämpfe, T. Review on the microstructure of ferroelectric hafnium oxides. *physica status solidi (RRL)–Rapid Research Letters* **2022**, *16*, 2200168.
- (20) Lee, H.-J.; Lee, M.; Lee, K.; Jo, J.; Yang, H.; Kim, Y.; Chae, S. C.; Waghmare, U.; Lee, J. H. Scale-free ferroelectricity induced by flat phonon bands in HfO₂. *Science* **2020**, *369*, 1343–1347.
- (21) Grimley, E. D.; Schenk, T.; Mikolajick, T.; Schroeder, U.; LeBeau, J. M. Atomic structure of domain and interphase boundaries in ferroelectric HfO₂. *Advanced Materials Interfaces* **2018**, *5*, 1701258.
- (22) Mulaosmanovic, H.; Ocker, J.; Müller, S.; Schroeder, U.; Müller, J.; Polakowski, P.; Flachowsky, S.; van Bentum, R.; Mikolajick, T.; Slesazek, S. Switching kinetics in nanoscale hafnium oxide based ferroelectric field-effect transistors. *ACS Appl. Mater. Interfaces* **2017**, *9*, 3792–3798.
- (23) Sharma, P.; Moise, T. S.; Colombo, L.; Seidel, J. Roadmap for ferroelectric domain wall nanoelectronics. *Adv. Funct. Mater.* **2022**, *32*, 2110263.
- (24) Salje, E. K. Mild and wild ferroelectrics and their potential role in neuromorphic computation. *APL Materials* **2021**, *9*, 010903.
- (25) McConville, J. P.; Lu, H.; Wang, B.; Tan, Y.; Cochard, C.; Conroy, M.; Moore, K.; Harvey, A.; Bangert, U.; Chen, L.-Q.; Gruverman, A.; Gregg, J. M. Ferroelectric domain wall memristor. *Adv. Funct. Mater.* **2020**, *30*, 2000109.
- (26) Jiang, A. Q.; Zhang, Y. Next-generation ferroelectric domain-wall memories: principle and architecture. *NPG Asia Materials* **2019**, *11*, 1–5.
- (27) Guan, Y.; Zhou, D.; Xu, J.; Liu, X.; Cao, F.; Dong, X.; Müller, J.; Schenk, T.; Schroeder, U. The Rayleigh Law in Silicon Doped Hafnium Oxide Ferroelectric Thin Films. *physica status solidi (RRL) – Rapid Research Letters* **2015**, *9*, 589–593.
- (28) Grimley, E. D.; Schenk, T.; Sang, X.; Pešić, M.; Schroeder, U.; Mikolajick, T.; LeBeau, J. M. Structural Changes Underlying Field-Cycling Phenomena in Ferroelectric HfO₂ Thin Films. *Advanced Electronic Materials* **2016**, *2*, 1600173.
- (29) Mittmann, T.; Fengler, F. P. G.; Richter, C.; Park, M. H.; Mikolajick, T.; Schroeder, U. Optimizing Process Conditions for Improved Hf_{1-x}Zr_xO₂ Ferroelectric Capacitor Performance. *Microelectron. Eng.* **2017**, *178*, 48–51.
- (30) Schenk, T.; Hoffmann, M.; Pešić, M.; Park, M. H.; Richter, C.; Schroeder, U.; Mikolajick, T. Physical Approach to Ferroelectric Impedance Spectroscopy: The Rayleigh Element. *Physical Review Applied* **2018**, *10*, 064004.
- (31) Damjanovic, D. Logarithmic Frequency Dependence of the Piezoelectric Effect Due to Pinning of Ferroelectric-Ferroelastic Domain Walls. *Phys. Rev. B* **1997**, *55*, R649–R652.
- (32) Marquardt, R.; Cipo, J.; Schlichting, F.; Kolhatkar, G.; Kohlstedt, H.; Kersten, H. Correlation between properties of direct current magnetron sputtered thin niobium nitride films and plasma parameters. *Thin Solid Films* **2022**, *742*, 139046.
- (33) Schneider, M. L.; Donnelly, C. A.; Russek, S. E.; Baek, B.; Pufall, M. R.; Hopkins, P. F.; Dresselhaus, P. D.; Benz, S. P.; Rippard, W. H. Ultralow power artificial synapses using nanotextured magnetic Josephson junctions. *Science advances* **2018**, *4*, No. e1701329.

- (34) Murbach, M. D.; Gerwe, B.; Dawson-Elli, N.; Tsui, L.-k. ImpedancePy: A Python Package for Electrochemical Impedance Analysis. *Journal of Open Source Software* **2020**, *5*, 2349.
- (35) Schönleber, M.; Klotz, D.; Ivers-Tiffée, E. A method for improving the robustness of linear Kramers-Kronig validity tests. *Electrochim. Acta* **2014**, *131*, 20–27.
- (36) Ruh, R.; Corfield, P. W. Crystal structure of monoclinic hafnia and comparison with monoclinic zirconia. *J. Am. Ceram. Soc.* **1970**, *53*, 126–129.
- (37) Becker, K.; Ebert, F. Die Kristallstruktur einiger binärer Carbide und Nitride. *Zeitschrift fuer Physik* **1925**, *31*, 268–272.
- (38) Materlik, R.; Künneth, C.; Kersch, A. The origin of ferroelectricity in Hf1-xZr_xO₂: A computational investigation and a surface energy model. *J. Appl. Phys.* **2015**, *117*, 134109.
- (39) Halder, N.; Wagner, C. Separation of particle size and lattice strain in integral breadth measurements. *Acta Crystallogr.* **1966**, *20*, 312–313.
- (40) Guedj, C.; Hung, L.; Zobelli, A.; Blaise, P.; Sottile, F.; Olevano, V. Evidence for anisotropic dielectric properties of monoclinic hafnia using valence electron energy-loss spectroscopy in high-resolution transmission electron microscopy and ab initio time-dependent density-functional theory. *Appl. Phys. Lett.* **2014**, *105*, 222904.
- (41) Jang, J. H.; Jung, H.-S.; Kim, J. H.; Lee, S. Y.; Hwang, C. S.; Kim, M. Investigation of oxygen-related defects and the electrical properties of atomic layer deposited HfO₂ films using electron energy-loss spectroscopy. *J. Appl. Phys.* **2011**, *109*, 023718.
- (42) Lee, Y. H.; Kim, H. J.; Moon, T.; Do Kim, K.; Hyun, S. D.; Park, H. W.; Lee, Y. B.; Park, M. H.; Hwang, C. S. Preparation and characterization of ferroelectric Hf_{0.5}Zr_{0.5}O₂ thin films grown by reactive sputtering. *Nanotechnology* **2017**, *28*, 305703.
- (43) Li, C.; Yao, Y.; Shen, X.; Wang, Y.; Li, J.; Gu, C.; Yu, R.; Liu, Q.; Liu, M. Dynamic observation of oxygen vacancies in hafnia layer by in situ transmission electron microscopy. *Nano Research* **2015**, *8*, 3571–3579.
- (44) Zhou, Y.; Chan, H.; Lam, C. H.; Shin, F. Mechanisms of imprint effect on ferroelectric thin films. *Journal of applied physics* **2005**, *98*, 024111.
- (45) Yuan, P.; Mao, G.-Q.; Cheng, Y.; Xue, K.-H.; Zheng, Y.; Yang, Y.; Jiang, P.; Xu, Y.; Wang, Y.; Wang, Y.; Ding, Y.; Chen, Y.; Dang, Z.; Tai, L.; Gong, T.; Luo, Q.; Miao, X.; Liu, Q. Microscopic mechanism of imprint in hafnium oxide-based ferroelectrics. *Nano Research* **2022**, *15*, 3667–3674.
- (46) Jiang, P.; Luo, Q.; Xu, X.; Gong, T.; Yuan, P.; Wang, Y.; Gao, Z.; Wei, W.; Tai, L.; Lv, H. Wake-Up Effect in HfO₂-Based Ferroelectric Films. *Advanced Electronic Materials* **2021**, *7*, 2000728.
- (47) Lederer, M.; Olivo, R.; Lehninger, D.; Abdulazhanov, S.; Kämpfe, T.; Kirbach, S.; Mart, C.; Seidel, K.; Eng, L. M. On the Origin of Wake-Up and Antiferroelectric-Like Behavior in Ferroelectric Hafnium Oxide. *physica status solidi (RRL)–Rapid Research Letters* **2021**, *15*, 2100086.
- (48) Gronenberg, O.; Marquardt, R.; Lamprecht, R.; Ekici, Y.; Schürmann, U.; Kohlstedt, H.; Kienle, L. The impact of rapid thermal annealing for the ferroelectricity of undoped sputtered HfO₂ and its wake-up effect. *J. Appl. Phys.* **2022**, *132*, 094101.
- (49) Li, X.; Li, C.; Xu, Z.; Li, Y.; Yang, Y.; Hu, H.; Jiang, Z.; Wang, J.; Ren, J.; Zheng, C.; Lu, C.; Wen, Z. Ferroelectric Properties and Polarization Fatigue of La: HfO₂ Thin-Film Capacitors. *physica status solidi (RRL)–Rapid Research Letters* **2021**, *15*, 2000481.
- (50) Shibayama, S.; Xu, L.; Migita, S.; Toriumi, A. Study of wake-up and fatigue properties in doped and undoped ferroelectric HfO₂ in conjunction with piezo-response force microscopy analysis, 2016 IEEE Symposium on VLSI Technology; 2016; pp 1–2.
- (51) Nittayakasetwat, S.; Kita, K. Evidence of ferroelectric HfO₂ phase transformation induced by electric field cycling observed at a macroscopic scale. *Solid-State Electron.* **2021**, *184*, 108086.
- (52) Cheng, Y.; Gao, Z.; Ye, K. H.; Park, H. W.; Zheng, Y.; Zheng, Y.; Gao, J.; Park, M. H.; Choi, J.-H.; Xue, K.-H.; Hwang, C. S.; Lyu, H. Reversible transition between the polar and antipolar phases and its implications for wake-up and fatigue in HfO₂-based ferroelectric thin film. *Nat. Commun.* **2022**, *13*, 1–8.
- (53) Bolten, D.; Lohse, O.; Grossmann, M.; Waser, R. Reversible and irreversible domain wall contributions to the polarization in ferroelectric thin films. *Ferroelectrics* **1999**, *221*, 251–257.
- (54) Thatikonda, S. K.; Huang, W.; Du, X.; Yao, C.; Ke, Y.; Wu, J.; Qin, N.; Bao, D. Ti-doping induced antiferroelectric to ferroelectric phase transition and electrical properties in Sm-PbZrO₃ thin films. *Curr. Appl. Phys.* **2021**, *24*, 12–18.
- (55) Li, R.; Zhu, H.; Liu, J.; Wang, S.; Xie, N.; Huang, Z.; Fang, Z. Research on the Wake-up Effect of Ferroelectric HfO₂-ZrO₂ Thin Films. *Journal of Physics: Conference Series* **2021**, *1907*, 012020.
- (56) Kinder, E. W.; Alessandri, C.; Pandey, P.; Karbasian, G.; Salahuddin, S.; Seabaugh, A. *Partial Switching of Ferroelectrics for Synaptic Weight Storage*, 2017 75th Annual Device Research Conference (DRC), 2017; pp 1–2.
- (57) Hall, D. A. Rayleigh Behaviour and the Threshold Field in Ferroelectric Ceramics. *Ferroelectrics* **1999**, *223*, 319–328.
- (58) Feigel'man, M. V.; Vinokur, V. M. On the Stochastic Transport in Disordered Systems. *J. Phys. (Paris)* **1988**, *49*, 1731–1736.
- (59) Fedorenko, A. A.; Mueller, V.; Stepanow, S. Dielectric Response Due to Stochastic Motion of Pinned Domain Walls. *Phys. Rev. B* **2004**, *70*, 224104.
- (60) Shu, W.; Wang, J.; Zhang, T.-Y. Effect of Grain Boundary on the Electromechanical Response of Ferroelectric Polycrystals. *J. Appl. Phys.* **2012**, *112*, 064108.
- (61) Zhang, W.; Bhattacharya, K. A Computational Model of Ferroelectric Domains. Part II: Grain Boundaries and Defect Pinning. *Acta Mater.* **2005**, *53*, 199–209.
- (62) Randall, C. A.; Barber, D. J.; Whatmore, R. W. Ferroelectric Domain Configurations in a Modified-PZT Ceramic. *J. Mater. Sci.* **1987**, *22*, 925–931.
- (63) Moulson, A. J.; Herbert, J. M. *Electroceramics: Materials, Properties, Applications*; John Wiley & Sons, 2003; pp 493–495.
- (64) Collective Dynamics Underpins Rayleigh Behavior in Disordered Polycrystalline Ferroelectrics — PNAS. <https://www.pnas.org/doi/abs/10.1073/pnas.0913172107>.
- (65) Hall, D. Review nonlinearity in piezoelectric ceramics. *J. Mater. Sci.* **2001**, *36*, 4575–4601.
- (66) Griggio, F.; Jesse, S.; Kumar, A.; Ovchinnikov, O.; Kim, H.; Jackson, T. N.; Damjanovic, D.; Kalinin, S. V.; Trolor-McKinstry, S. Substrate Clamping Effects on Irreversible Domain Wall Dynamics in Lead Zirconate Titanate Thin Films. *Phys. Rev. Lett.* **2012**, *108*, 157604.
- (67) Tsymbal, E. Y.; Kohlstedt, H. Tunneling across a ferroelectric. *Science* **2006**, *313*, 181–183.
- (68) Kim, Y.; Han, H.; Vrejoiu, I.; Lee, W.; Hesse, D.; Alexe, M. Origins of Domain Wall Pinning in Ferroelectric Nanocapacitors. *Nano Convergence* **2014**, *1*, 24.

IV. Trap-Assisted Memristive Switching in HfO₂-Based Devices Studied by In Situ Soft and Hard X-Ray Photoelectron Spectroscopy

Bibliographic Information

Zahari, F., **Marquardt, R.**, Kalläne, M., Gronenberg, O., Schlueter, C., Matveyev, Y., Haberfehlner, G., Diekmann, F., Nierhauve, A., Buck, J., Hanff, A., Kolhatkar, G., Kothleitner, G., Kienle, L., Ziegler, M., Carstensen, J., Rossnagel, K., Kohlstedt, H., Trap-Assisted Memristive Switching in HfO₂-Based Devices Studied by In Situ Soft and Hard X-Ray Photoelectron Spectroscopy. Adv. Electron. Mater. 2023, 0, 2201226.

<https://doi.org/10.1002/aelm.202201226>

Author's contribution

The author contributed to:

- Evaluation of the data
- Development of the physical model
- Partial writing of the manuscript

Copyright Notice

This work is licensed under a Creative Commons Attribution 4.0 International License (CC BY 4.0). Read the license text:

<https://creativecommons.org/licenses/by/4.0/legalcode>.

IV.1 Summary

In the following two papers, the same analog memristive devices composed of Nb/NbO_x/Al₂O₃/HfO₂/Au showing diode-like $|J|$ - V characteristics are investigated by two independent and distinct experimental approaches (in-situ synchrotron-based HAXPES/XPS in part I and impedance spectroscopy (ImpSpec) in part II).

In part I, in-situ synchrotron-based XPS and depth-dependent HAXPES are done to probe the device in different resistance states. Chemical analysis of the materials is supported by EELS. Additional structural information is provided by TEM. Spectroscopic evidence for an analog memristive switching mechanism based on the charge state of electron traps within HfO₂ is reported for the first time. Strong evidence for memristive switching was found based on a trap-assisted field effect. In particular, the charging and discharging of electron traps within an insulating HfO₂ alter the space charge region of a semiconducting NbO_x in a two-terminal metal-insulator-semiconductor (MIS) structure, which leads to resistive switching. The stoichiometry of the three oxide layers NbO_x, Al₂O₃, and HfO₂ is determined by EELS. The charging and discharging of the electron traps inside the HfO₂ layer were determined by observed core-level shifts which were dependent on the memristive state of the device. Furthermore, no evidence of ionic motion could be found in the experimental data.

The suggested model for the memristive device comprises of a two-terminal structure resembling MIS (Metal-Insulator-Semiconductor), where electron traps within the insulator control the space-charge region in the semiconductor, leading to alterations in the device resistance. These results shed light on the physical mechanism responsible for memristive switching in such devices, which are widely investigated as non-volatile memories for neuromorphic applications.

RESEARCH ARTICLE

Trap-Assisted Memristive Switching in HfO_2 -Based Devices Studied by In Situ Soft and Hard X-Ray Photoelectron Spectroscopy


Finn Zahari,* Richard Marquardt, Matthias Kalläne, Ole Gronenberg, Christoph Schlueter, Yury Matveyev, Georg Haberknecht, Florian Diekmann, Alena Nierhauve, Jens Buck, Arndt Hanff, Gitanjali Kolhatkar, Gerald Kothleitner, Lorenz Kienle, Martin Ziegler, Jürgen Carstensen, Kai Rossnagel, and Hermann Kohlstedt*

Memristive devices are under intense development as non-volatile memory elements for extending the computing capabilities of traditional silicon technology by enabling novel computing primitives. In this respect, interface-based memristive devices are promising candidates to emulate synaptic functionalities in neuromorphic circuits aiming to replicate the information processing of nervous systems. A device composed of $\text{Nb}/\text{NbO}_x/\text{Al}_2\text{O}_3/\text{HfO}_2/\text{Au}$ that shows promising features like analog switching, no electroforming, and high current-voltage non-linearity is reported. Synchrotron-based X-ray photoelectron spectroscopy and depth-dependent hard X-ray photoelectron spectroscopy are used to probe in situ different resistance states and thus the origin of memristive switching. Spectroscopic evidence for memristive switching based on the charge state of electron traps within HfO_2 is found. Electron energy loss spectroscopy and transmission electron microscopy support the analysis. A device model is proposed that considers a two-terminal metal–insulator–semiconductor structure in which traps within the insulator ($\text{HfO}_2/\text{Al}_2\text{O}_3$) modulate the space charge region within the semiconductor (NbO_x) and, thereby, the overall resistance. The experimental findings are in line with impedance spectroscopy data reported in the companion paper (Marquardt et al). Both works complement one another to derive a detailed device model, which helps to engineer device performance and integrate devices into silicon technology.

1. Introduction

Today's digital computers are based on a separation of memory and computation. Thus, data has to be continually transferred from the memory location to the location of computing and vice versa in traditional computing architecture, leading to high latency and energy consumption.^[1–3] One potential concept to overcome this so-called von Neumann bottleneck for certain applications is the development of neuromorphic computing architectures, which aim to emulate information processing in the human brain.^[4–7] In biology, information processing takes place in huge networks of neurons and synapses, without physical separation between computation and memory,^[8] leading to an impressive performance in tasks like sensory processing, motor control, and pattern recognition,^[9] while at the same time consuming less energy, orders of magnitude lower than digital computers require to conduct similar tasks.^[5,6,10,11]

F. Zahari, R. Marquardt, H. Kohlstedt
 Nanoelectronics
 Faculty of Engineering
 Kiel University
 24143 Kiel, Germany
 E-mail: fnz@tf.uni-kiel.de; hko@tf.uni-kiel.de

 The ORCID identification number(s) for the author(s) of this article can be found under <https://doi.org/10.1002/aelm.202201226>.

© 2023 The Authors. Advanced Electronic Materials published by Wiley-VCH GmbH. This is an open access article under the terms of the Creative Commons Attribution License, which permits use, distribution and reproduction in any medium, provided the original work is properly cited.

DOI: 10.1002/aelm.202201226

M. Kalläne, F. Diekmann, A. Nierhauve, J. Buck, A. Hanff, K. Rossnagel
 Institute of Experimental and Applied Physics
 Kiel University
 24098 Kiel, Germany
 M. Kalläne, F. Diekmann, A. Hanff, K. Rossnagel
 Ruprecht Haensel Laboratory
 Kiel University
 24098 Kiel, Germany
 M. Kalläne, L. Kienle, K. Rossnagel, H. Kohlstedt
 Kiel Nano Surface and Interface Science KiNSIS
 Kiel University
 24118 Kiel, Germany
 O. Gronenberg, L. Kienle
 Synthesis and Real Structure
 Faculty of Engineering, Kiel University
 24143 Kiel, Germany

Memristive devices are widely investigated as a key element for neuromorphic computing,^[3,10–13] and hybrid memristive-complementary metal-oxide-semiconductor (CMOS) circuits are examined to extend performance and reduce the energy consumption of traditional CMOS technology.^[9,14] Among other applications, memristive devices can be exploited to emulate functionalities of biological synapses, such as long-term potentiation (LTP), long-term depression (LTD), spike-timing-dependent plasticity (STDP), and paired-pulse facilitation (PPF).^[11,15–22] Memristive devices are often composed of a metal-insulator-metal (MIM) structure in which the resistance can be varied by electrical stimuli, allowing them to be used as non-volatile memory elements.^[5,13,23,24] Many different physical mechanisms leading to memristive behavior have been reported so far.^[5,13,24–26] Among them, devices based on a Schottky barrier height or width modulation^[22,27–36] are interesting candidates for neuromorphic circuits.^[11,25] These interface-based memristive devices show gradual, that is, analog switching, and do not require initial electro-forming.^[7,13,25] Moreover, arranging memristive devices in passive crossbar arrays for dense device integration requires selector devices to prevent parasitic current flows when a specific device is addressed,^[3,10,11] as recently reviewed in ref. [37]. Various kinds of selector devices, such as transistors^[38,39] or volatile memristive devices,^[40] can serve as selector elements when connected in series with the non-volatile memristive devices. In this respect, the high current-voltage (I - V) non-linearity of interface-type memristive devices allows passive crossbar integration^[29,41,42] without additional selector elements.^[3,10,11,37] Switching processes are reported to be caused by a rearrangement of ions or vacancies^[22,29,31–33,35] or by the charging and discharging of electron traps.^[27,28,30,34,36,43]

However, spectroscopic evidence for the proposed switching mechanism is often missing.

Among a multitude of different methods to probe memristive switching,^[44] transmission electron microscopy (TEM) together with energy electron loss spectroscopy (EELS),^[45] and photoelectron spectroscopy (PES)^[46] are widely used techniques to study structural, chemical and electronic properties of the material systems. In particular, X-ray photoelectron spectroscopy (XPS)^[46] and hard X-ray photoelectron spectroscopy (HAXPES)^[47] allow to probe film compositions, chemical states, band alignment as well as band bending in buried layers and their dependence on depth.^[46,48,49] Hard X-rays (>2 keV) from synchrotron sources with orders of magnitude higher photon flux compared to laboratory sources provide an information depth of up to a few 10 nm while simultaneously allowing for reasonable energy resolution.^[47] Furthermore, non-destructive depth profiling is possible with XPS/HAXPES by collecting photoelectrons that are ejected with different angles of emission.^[46,47] Thus, XPS and HAXPES allow in situ and in operando investigations of memristive switching processes^[50–55] in functional devices, where switching takes place within a few 10 nm below the sample surface.

Memristive devices based on metal oxides are often composed of oxide bi- or multi-layers sandwiched between two metal electrodes.^[22,33,42,43,55–62] One oxide serves as an active switching material, while the other oxides act, for example, as diffusion barriers,^[33,57,62] as oxygen ion reservoirs,^[22,55,59] as rectification layers,^[43,56,60,61,63] or affect the local heat distribution,^[59] thus significantly improving the device characteristics. Within this work, an analog switching interface-type memristive device consisting of the layer sequence Nb/NbO_x/Al₂O₃/HfO₂/Au (see **Figure 1**) is investigated. HfO₂ is widely investigated and applied as an active switching layer in memristive devices^[22,38,39,42,50–56,62,63] due to its CMOS compatibility.^[64] Among other applications, hafnia is used as a gate dielectric for metal-oxide-semiconductor field-effect transistors (MOS-FETs),^[64,65] as charge trapping layer in charge trap flash (CTF) memory,^[66] and as an active layer in CMOS-integrated filamentary-type resistive random access memory (RRAM) devices.^[38,39] On the other hand, Al₂O₃ is reported to serve as a diffusion barrier for oxygen ions^[33,57,58,62] which can lead to an enhanced retention time of interface-type memristive devices, and simultaneously suppress an oxygen exchange with adjacent layers.^[33] Alumina is also compatible with CMOS technology.^[62] Furthermore, stoichiometric Nb₂O₅ is known to be a good insulator,^[67] but oxygen-deficient films are reported to show n-type semiconducting behavior.^[67,68] Thus, a NbO_x layer can in principle be used to fabricate rectifying metal-semiconductor (MS) or metal-insulator-semiconductor (MIS) devices.^[69,70] The investigated Nb/NbO_x/Al₂O₃/HfO₂/Au device is based on similar devices with a NbO_y layer instead of HfO₂.^[33] The Schottky barrier of the NbO_y/Au interface was reported to be altered by the drift of negatively charged oxygen ions, while the probability for tunneling through the Al₂O₃ is simultaneously affected,^[33] as modeled by a kinetic Monte Carlo simulation,^[71] and a cloud-in-a-cell (CIC) scheme^[72] that also covers the device variability. Furthermore, the charging and discharging of interface trap states are also reported as a possible mechanism responsible for memristive switching.^[33] The integration into passive crossbar

C. Schlueter, Y. Matveyev
Deutsches Elektronen-Synchrotron DESY
22607 Hamburg, Germany
G. Haberfehlner, G. Kothleitner
Institute of Electron Microscopy and Nanoanalysis
Graz University of Technology
Graz 8010, Austria

A. Nierhaue, J. Buck, K. Rossnagel
Ruprecht Haensel Laboratory
Deutsches Elektronen-Synchrotron DESY
22607 Hamburg, Germany

G. Kolhatkar
Department of Engineering Physics
McMaster University, Hamilton
Ontario L8S 4L7, Canada

G. Kothleitner
Graz Centre for Electron Microscopy
Graz 8010, Austria

M. Ziegler
Department of Electrical Engineering and Information Technology
Technische Universität Ilmenau
98693 Ilmenau, Germany

M. Ziegler
Institute of Micro and Nanotechnologies MacroNano
Technische Universität Ilmenau
98693 Ilmenau, Germany

J. Carstensen
Functional Nanomaterials
Faculty of Engineering
Kiel University
24143 Kiel, Germany

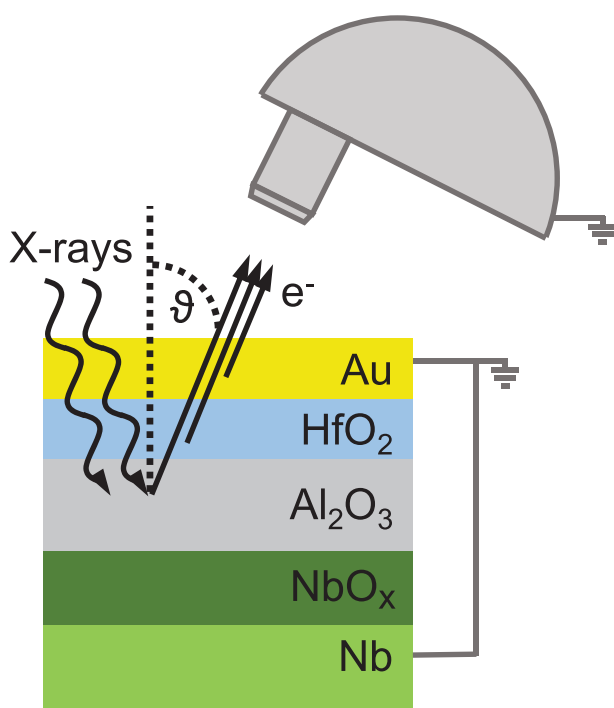


Figure 1. Schematic illustration of the HAXPES measurement setup and the probed devices: An X-ray beam is directed onto the sample surface. The kinetic energies of electrons ejected at specific polar angles of emission ϑ are measured. During HAXPES measurements, the device electrodes are connected to common ground with the analyzer to ensure charge compensation and to obtain defined electrostatic conditions within the device. The memristive state can be read out and switched in the vacuum chamber by connecting a source measurement unit to the electrodes. When voltages were applied, the beam was never directed onto the sample.

arrays^[41] and the utilization as artificial synapses in neuromorphic networks for pattern recognition tasks have already been reported for the devices based on NbO_y as the active layer.^[19,41]

Here, the origin of memristive switching in the HfO_2 -based devices is investigated by depth-dependent synchrotron-based HAXPES and synchrotron-based XPS with soft X-rays. Varying the recorded angle of emission ϑ allowed for non-destructive depth profiling of chemical and electronic properties. The measurement setup is schematically illustrated in Figure 1. In combination with structural data from TEM, chemical information from EELS, and current density versus voltage (J - V) characterizations, a model to qualitatively describe the physics of the interface-based memristive device is proposed in this manuscript: A two-terminal MIS structure, in which electron traps within the insulator modulate the space-charge region within the semiconductor and, thereby, the Schottky barrier height, is consistently used to explain the findings from all experiments. In particular, we identify a causal relationship between the charge-trapping state of HfO_2 and the overall device resistance. Spectroscopic evidence (by XPS/HAXPES) for such a switching mechanism has not been reported so far. Furthermore, impedance spectroscopy (ImpSpec)^[73] is exploited by Marquardt et al. in a companion paper^[74] to probe memristive switching in the same device. The findings presented in both papers indicate that the memristive switching can be attributed to a Schottky

barrier modulation by a charge-trapping mechanism. The obtained device model is advantageous for both device integration into silicon technology to exploit the benefits of hybrid memristive-CMOS neuromorphic circuits and engineering of device characteristics for specific applications. In this respect, some design rules for CMOS integration are provided at the end of this work.

2. Results

2.1. Electrical Characterization

Typical semi-logarithmic current density versus voltage ($|J|$ - V) characteristics of devices from the reference wafer (see Experimental Section for fabrication and characterization details) with a top electrode size of $625 \mu\text{m}^2$ are presented in Figure 2a. Here, the mean behavior of ten adjacent devices is depicted in black, while the characteristics of single devices are drawn in gray. The inset of Figure 2a shows the mean $|J|$ - V characteristics for low applied voltages (± 1.2 V). The hysteresis observed for small current densities arises from capacitive effects of the measurement setup since only noise is detected and no memristive switching takes place. As it is shown in Figure 2a, higher voltages (± 3.7 V) induce memristive switching. The diode-like electrical properties allow for integration into passive crossbar arrays without requiring additional selector devices.^[41] Furthermore, no initial electro-forming or current compliance is needed to operate the devices and the observed smooth hysteresis reveals analog switching. Such analog interface-type memristive devices can be used for emulating synaptic functionalities, as reported for various devices.^[15,17,19,22,42] In particular, devices with a similar material stack produced with the very same processes but containing a sputtered NbO_y layer instead of HfO_2 ^[33] show similar electrical characteristics. The possibility of using these NbO_y -based devices for the emulation of synaptic functionalities has been shown experimentally on both the device level^[18,19] and the network level.^[41]

The area-dependent current transport is shown in Figure 2b. Here, the resistance mean value and standard deviation of ten neighboring devices per area for a bias voltage of 1.2 V are depicted. The resistance scales linearly with the area of the device in the high resistance state (HRS) and in a low resistance state (LRS). Thus, homogeneous current transport through the whole device area is indicated for both HRS and LRS.

The relaxation of the LRS toward higher resistances is shown in Figure 2c as red circles. The device is set to an LRS by applying a positive voltage sweep with $V_{\text{max}} = 3.7$ V and the device resistance R is read out with 0.5 V voltage pulses of 4 s length after the set sweep, and with delay times of 300 (next 12 pulses), and 1800 s (all further pulses). R is further divided by the initial resistance R_0 , which is determined as the mean of ten consecutive read out pulses prior to switch the device. The resistance increases with time so that it approaches R_0 in ≈ 25.5 h and does not increase further in the next 13 h. The relaxation process can be fitted with a power law of the form $\propto t^\alpha$, as reported for other memristive devices,^[22,30,33,34] as well as for describing charge trapping under bias in HfO_2 .^[75] In

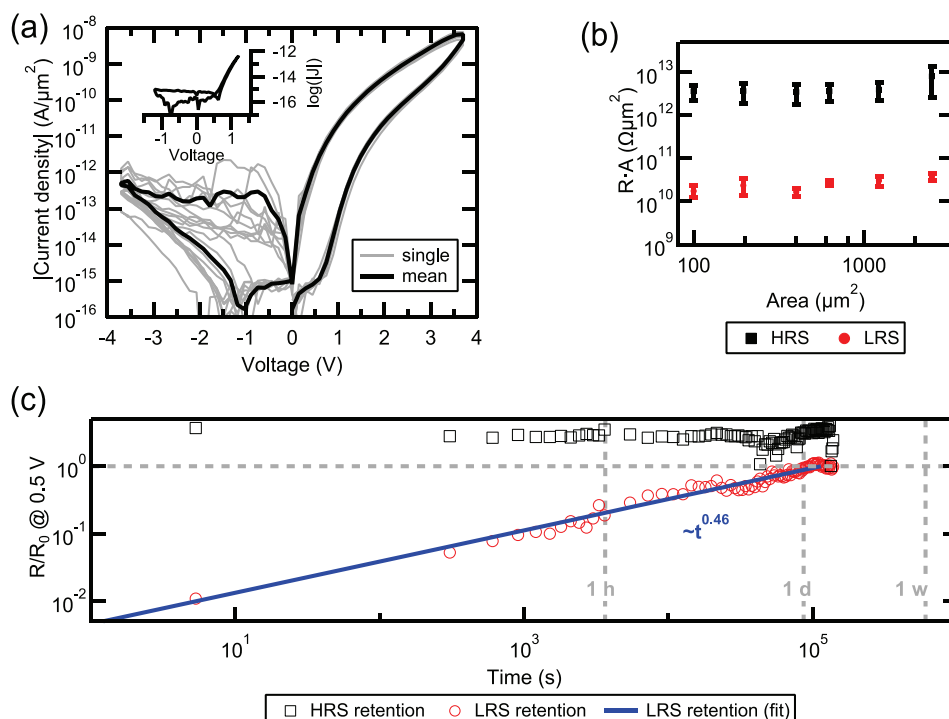


Figure 2. a) $|J|$ - V characteristics showing memristive switching of ten individual devices (gray) and their mean value (black). The inset shows a mean $|J|$ - V curve for lower voltages that do not induce memristive switching. b) Area dependency of the resistances in HRS (black squares) and LRS (red dots) for 1.2 V bias. Mean values and standard deviations of ten devices for each contact area are depicted. c) Retention time of the LRS (red circles) and HRS (black squares). The resistance evolution of a devices read out with 0.5 V is shown. A fit to the LRS data with a $\propto t^\alpha$ power law is further given as solid blue line. (a–c) Voltages are always applied to the Au top electrodes, while the Nb bottom electrodes are grounded.

particular, a power law with $\alpha = 0.46$ fits well the LRS retention characteristics. An α between 0.18 and 0.57 is reported for similar devices,^[22,30,33,34] while filamentary devices based on HfO_x show a much longer retention time with $\alpha = 0.02$.^[22] After measuring the relaxation process of the LRS resistance, the device is switched to an even higher resistance by applying a negative voltage sweep with $V_{\min} = -3.7$ V, and the resistance is read out with the same procedure as the LRS resistance. No distinct trend can be observed in the resistance evolution but a drift toward R_0 is expected on a longer time scale, since the resistance evolution of the LRS does not reveal a further drift toward the HRS resistance. The origin of the rather strong fluctuations in the HRS resistance evolution is unknown and needs to be further investigated in the future. It should be emphasized that the HRS resistance is rather close to the initial resistance ($R_{\text{HRS}} \approx 3 \times R_0$) while most of the switching window can be attributed to the difference between the initial resistance and the LRS ($R_{\text{LRS}} \approx 0.01 \times R_0$). A much longer retention time of typically more than 10 years is needed for memory applications,^[76] but shorter retention times are expected to be beneficial for certain neuromorphic applications.^[11] In particular, processing real-world data with spiking neural networks (SNNs) requires not only non-volatile memory elements but also volatile memristive devices with times-scales in the order of the time-scales of the data.^[14] One example is reported by Park et al., who utilize volatile analog memristive devices as short-term memory in leaky-integrate-and-fire (LIF) neurons to process sequential data.^[77] However, a long retention time is needed for inference

in a pattern recognition task.^[78,79] Thus, the retention time of the here reported devices has to be enhanced for this application. Nevertheless, the training of pattern recognition networks can be done with memristive devices with moderate retention times,^[78,79] as already shown with interface-type memristive devices.^[41]

Table 1 further provides a comparison between the devices presented here and those previously reported in literature with similar metal-oxide-based interface-type devices.^[30,32,33,42,77] We consider devices that comprise an area-dependent resistance in both HRS and LRS, and that require no external current compliance during switching. The first column of Table 1 shows the devices' material stacks. The electrical parameters extracted from the current-voltage hysteresis curves are the switching window $\Delta R = R_{\text{LRS}}/R_{\text{HRS}}$ measured with a typical read-out voltage V_{read} , the highest positive and lowest negative voltage used to record the evaluated hysteresis curves ($V_{\text{sw, LRS}}$ and $V_{\text{sw, HRS}}$), the maximum absolute value of the current density flowing during switching $|J_{\text{sw, max}}|$ (i.e., during switching to LRS for all compared devices, thus $|J_{\text{sw, max}}| = J_{\text{sw, LRS, max}}$), the ratios ΔJ_{sw} of the maximum absolute value of the current densities flowing during switching to LRS $|J_{\text{sw, LRS, max}}|$ and HRS $|J_{\text{sw, HRS, max}}|$, and the absolute value of the current density flowing during read-out the HRS $|J_{\text{read, HRS}}|$. Furthermore, the retention characteristics at room temperature are compared in two ways. The next to last column provides ΔR , measured after a certain time has elapsed since switching. The last column contains the coefficient α of the $\propto t^\alpha$ power law used for fitting the relaxation kinetics (if available).

Table 1. Comparison between different interface-type memristive devices.

Material stack	ΔR at V_{read}	V_{sw} [V]	$J_{\text{sw, max}}$ [A μm^{-2}]	ΔJ_{sw}	$J_{\text{read, HRS}}$ [A μm^{-2}]	Retention	
						$\alpha^a)$	
Nb/NbO _x /Al ₂ O ₃ /HfO ₂ /Au (This work)	100 at 1.2 V	± 3.7	7×10^{-9}	12 000	4×10^{-13}	$\Delta R \approx 1$ after 10^5 s	0.46
Nb/NbO _x /Al ₂ O ₃ /NbO _y /Au (ref. [33, 80])	500 at 0.5 V	+3/−2	2×10^{-7}	142 000	4×10^{-15}	$\Delta R \approx 40$ after 1.5 h ($\Delta R \approx 12$ after 10^6 s) ^{b)}	0.18
Al/Nb:SrTiO ₃ /Pt (ref. [30])	25 000 at 0.1 V	+2/−6	5×10^{-10}	6	2×10^{-15}	–	0.36
Pt/BiFeO ₃ /Au (ref. [32])	6400 at 2.0 V	± 8	2×10^{-9}	340	2×10^{-14}	$\Delta R \approx 600$ after 24 h ($\Delta R \approx 600$ after 10 y) ^{b)}	–
Ti/HfO ₂ /Al ₂ O ₃ /Pt (ref. [42])	80 at 0.7 V	± 2	6×10^{-7}	51 000	1×10^{-11}	ΔR constant for 600 s	–
TiN/TiO _x /TiO ₂ /Pt (ref. [77])	800 at 1.0 V	+4/−3	7×10^{-5}	84 000	3×10^{-10}	$\Delta R \approx 1$ after <1 s	–

^{a)}coefficient of the $\sim t^\alpha$ power law; ^{b)}projected values.

2.2. Transmission Electron Microscopy and Electron Energy Loss Spectroscopy

Figure 3a shows a spectral image of a device cross-section recorded with a scanning transmission electron microscope (STEM). Total NbO_x and HfO₂ thicknesses of $d_{\text{NbO}_x} = 5 \text{ nm} \pm 2 \text{ nm}$ and $d_{\text{HfO}_2} = 4.5 \text{ nm} \pm 0.4 \text{ nm}$ are determined, respectively. The NbO_x/Al₂O₃ interface is rough relative to the film size, leading to local Al₂O₃ thickness variations between ≈ 2 and 7 nm. Such roughness is also observed in Nb/Al-based tunnel junctions.^[85,86] All other interfaces are smooth due to the planning effect of Al on Nb.^[85,86] In a high-resolution (HR) STEM image (see Figure S1, Supporting Information), the HfO₂ appears to be polycrystalline, while Al₂O₃ and NbO_x are amorphous. It should be noted that HRTEM measurements of similar functional devices show amorphous HfO₂ (data not shown). Thus, it is expected that the crystalline state is not crucial for memristive switching.

EELS data of the entire layer sequence are shown in Figure 3b, Supporting Information. Here, a line scan of the O–K edge with a vertical step size of 1.75 nm is depicted. The whole HfO₂ and Al₂O₃ appear fully oxidized, and the Nb bottom electrode is also oxidized at the interface to Al₂O₃, as previously reported for similar devices.^[80] The spectra of the O–K edges indicate stoichiometric HfO₂ and Al₂O₃, as shown when compared to reference spectra.^[81,82] Moreover, an excess of oxygen may be indicated in the center of the Al₂O₃ layer by the pre-peak of the Al₂O₃-related O–K spectra in Figure 3b, Supporting Information. The O₂ seems to be molecular^[82,87] or incorporated as peroxide groups,^[88] that is, O–O bonds since both can produce the observed pre-peak. We, therefore, interpret this pre-peak as an excess of oxygen. It should be noted that the pre-peak is not stable within the electron beam, as shown in Figure S2, Supporting Information. Moreover, at the same position in the alumina layer, incorporated Ar is found by EELS (see Figure S3, Supporting Information) and energy-dispersive X-ray spectroscopy (data not shown). Since devices

without an Al₂O₃ layer show similar memristive switching, as shown in Section 3.1, the elements incorporated into alumina are expected to be not crucial for memristive switching. However, these defects could potentially decrease the overall electrical resistance of the Al₂O₃ layer. The electron energy-loss near-edge structure (ELNES) of NbO_x close to the Al₂O₃ interface can be attributed to a mixture of Nb₂O₅ and NbO₂ since fingerprints of both reference spectra can be found.^[67] Moreover, the intensity of the O–K edge decreases with an increasing distance to Al₂O₃, suggesting a continuously decreasing oxygen content in the NbO_x. Note that the ELNES of the NbO_x after the O–K pre-peak has vanished (due to electron irradiation) and now resembles more Nb₂O₅, which could suggest an in situ oxidation of the Nb electrode induced by the electron beam. The low-loss region of the hafnia layer is further analyzed. The corresponding spectra are shown in Figure 3c, together with reference spectra.^[83] Despite the broad peak at 34 eV, due to a collective excitation,^[89] the HfO₂ spectra show distinct peaks characteristic for the monoclinic structure. The intense plasmon peak at 23 eV, which is sensitive to the oxygen concentration,^[83,90] indicates stoichiometric rather than substoichiometric hafnia. Figure S3, Supporting Information shows the evolution of the low-loss regime within the HfO₂ layer. The intensity differences of the plasmon peaks might be due to an oxygen gradient^[91] or result from the overlapping low-loss regime of Au and Al₂O₃. These cases cannot be distinguished due to the very small dimensions and the roughness of the films. Figure 3d depicts the Al L₂₃ edge measured from the Al₂O₃, which matches well the ELNES of stoichiometric Al₂O₃.^[84] For comparison, the L₂₃ edge of metallic aluminum is shown, depicting an onset at 4 eV lower energies and a different ELNES than Al₂O₃.

2.3. X-Ray Photoelectron Spectroscopy

XPS and HAXPES measurements were performed at the synchrotron radiation facility PETRA III of DESY (Hamburg,

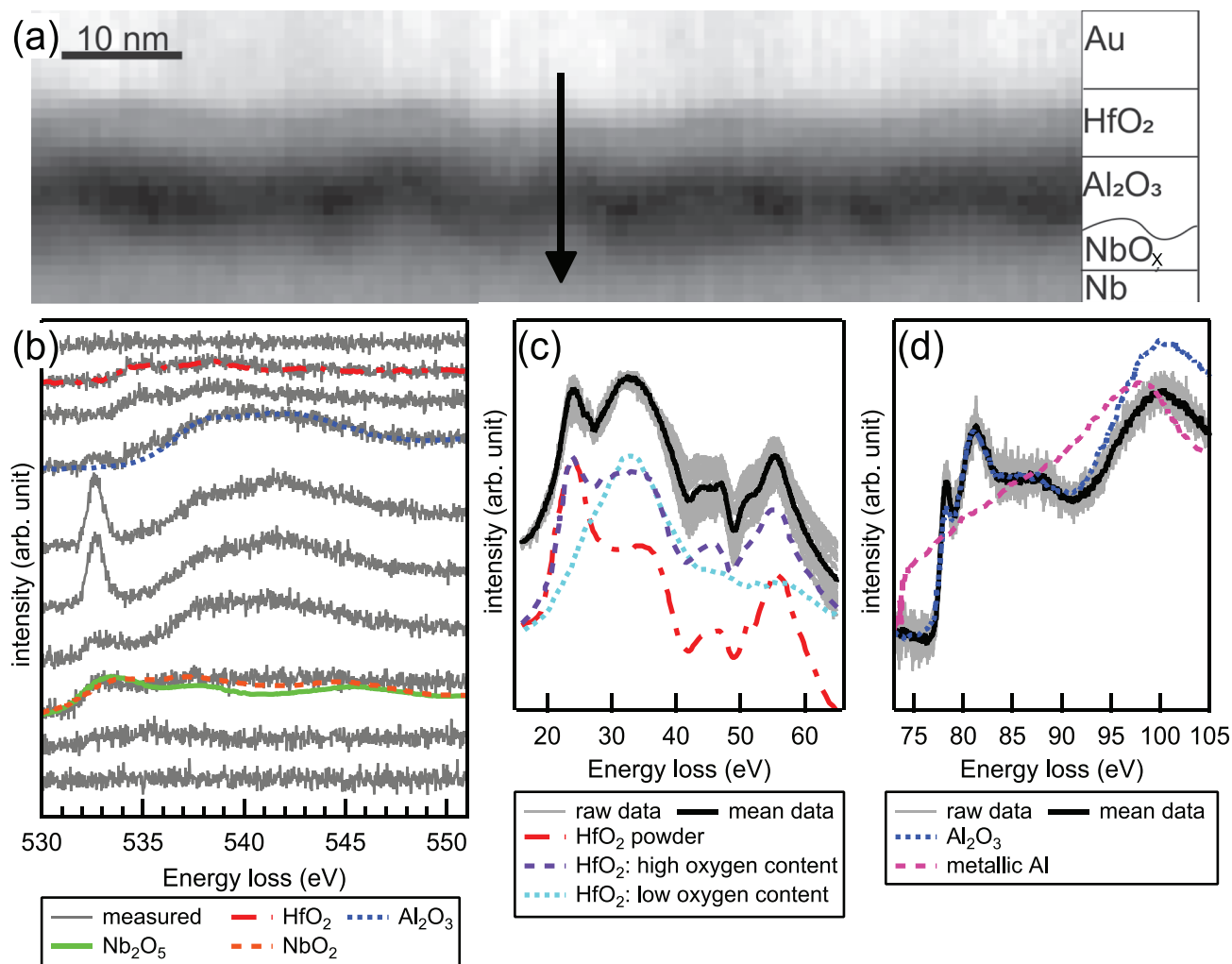


Figure 3. a) STEM recording of a focused ion beam cross section extracted from a functional device in HRS. The black arrow shows where the line scan in (b) was constructed from. In particular, all EELS data related to the pixels of two horizontal lines in (a) are combined as one spectral line in (b). b) EELS line scan of the O-K edge across the whole device stack extracted with a stepsize of 1.75 nm (gray solid lines) together with reference spectra for HfO₂,^[81] amorphous Al₂O₃,^[82] Nb₂O₅,^[67] and NbO₂.^[67] c) EELS low loss region of HfO₂ (black solid line: mean value of 36 measurements on adjacent positions, which are shown as gray solid lines) together with reference spectra.^[83] d) EELS Al L₂₃ of Al₂O₃ (black solid line: mean value of 36 measurements on adjacent positions, which are shown as gray solid lines) together with reference spectra for alumina and metallic aluminum.^[84]

Germany) by employing the experimental photoemission endstation ASPHERE III (beamline P04^[92]) and the HAXPES endstation at beamline P22,^[93] respectively. Details on energy referencing, peak fitting, and in situ electrical characterization can be found in Experimental Section, together with the sample design enabling PES on functional memristive devices (see also Figure S4, Supporting Information). The fabrication of the devices is also described in detail in Experimental Section.

2.3.1. Soft X-Ray Photoelectron Spectroscopy

A memristive device with a 6 nm thin Au top electrode is switched in situ from a high resistance state (HRS1) to a low resistance state (LRS) and back to a high resistance state (HRS2). Au 4f and Hf 4f core-level spectra for all resistance states are measured. A typical Au 4f spectrum is shown in

Figure S5, Supporting Information together with a I/V curve measured in situ, which indicates memristive switching. The Hf 4f spectra mainly stem from the Au/HfO₂ interface due to an inelastic mean free path λ of the Hf 4f electrons in Au of 1.8 nm estimated using the TPP-2M formula with the parameters provided in ref. [94]. Since $\approx 95\%$ of the signal intensity originates within 3λ ,^[95] only the HfO₂ near the Au interface can be probed. The Hf 4f spectra are shown in Figure 4. Here, a linear function models most accurately the background (gray solid lines). Full width at half maximum (FWHM) values of the doublet features of 1.20, 1.19, and 1.18 eV for HRS1, LRS, and HRS2, respectively, are obtained by fitting, while the Gaussian contribution dominates the Pseudo-Voigt function. Hf 4f_{7/2} binding energies (BEs) of 16.44 ± 0.01 , 16.56 ± 0.01 , and 16.45 ± 0.01 eV are measured for HRS1, LRS, and HRS2, respectively. The errors denote the standard deviation of the BE determined by the peak fitting algorithm. Thus, switching the devices from HRS to LRS and

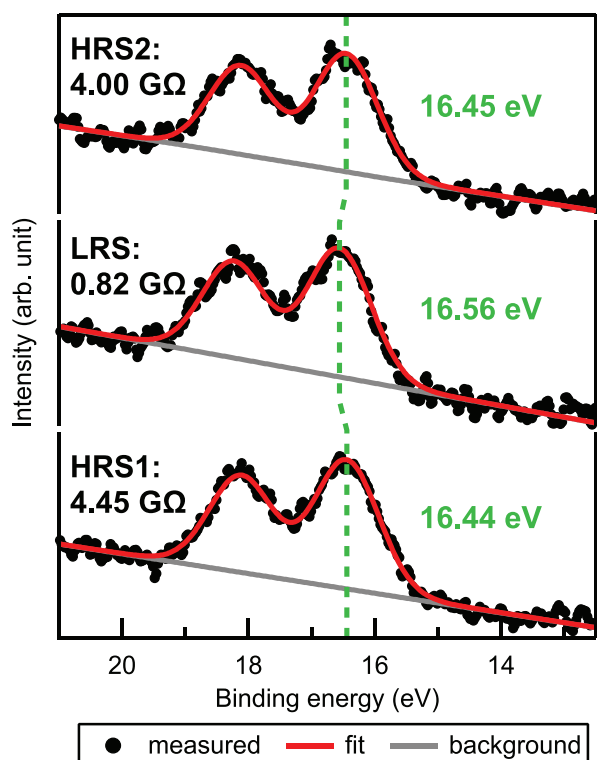


Figure 4. Measured Hf 4f spectra (black dots) in HRS1, LRS1, and HRS2, together with fitted peaks (red solid lines) and linear backgrounds (gray solid lines). The dashed green line indicates the shift of the Hf 4f_{7/2} position in the different memristive states. Resistances measured with 0.8 V and determined BEs for Hf 4f_{7/2} are also given in black and green, respectively.

back again leads to BE shifts of 110 ± 10 meV, with a higher BE for LRS. The difference between HRS1 and HRS2 being within the error margins shows that the core-level switches back to its initial BE. All peaks can be attributed to Hf⁴⁺ species in HfO₂ with reported BEs between 16.3 and 18.5 eV^[48,51–55,96–100] dependent on, for example, the band alignment with adjacent layers or the amount of charges within HfO₂ or adjacent layers. No additional spectral features attributed to sub-stoichiometric HfO_x can be seen, which appear at lower BEs corresponding to metallic Hf with a shift of 2.6–3.8 eV^[51–53,96,97] and to hafnium sub-oxide with smaller shifts.^[52–54,96,97,101] As such a signal is linked to filamentary-switching^[51–54] with an oxygen vacancy concentration of typically 10^{21} cm^{-3} ,^[102] this shows that the oxygen vacancy concentration in our devices is lower than in filamentary-based devices. This is in agreement with the EELS data indicating stoichiometric HfO₂. Also, additional spectral shape changes commonly observed in the case of chemical changes^[55,101] are absent from our spectra. Note that quantitative analyses of the material composition using XPS can lead to an error of less than 5% under best experimental conditions, while relative changes in the composition of less than 1% can be detected,^[103] which defines the resolution of XPS. Moreover, while BEs shift of the order of +100 meV, similar to these observed here between HRS and LRS, can be attributed to an additional amount of oxygen vacancies,^[101] the hypothesis of such a chemical change can be excluded for the devices studied

here (even though the signal-to-noise ratio of the presented Hf 4f peaks is low) as the positive bias applied to the Au top electrode cannot lead to an accumulation of (positively charged) oxygen vacancies near the Au interface. Hence, the BE shift toward higher energies in LRS can be attributed to an increased electrostatic potential near the Au interface, the origin of which is discussed in Section 3.2.

Finally, no defects caused by the X-ray radiation during XPS measurement are observed since no radiation-time dependent spectral shifts or additional spectral features, similar to those reported for in operando measurements on ferroelectric Pb(Mg_{1/3}Nb_{2/3})_{0.72}Ti_{0.28}O₃ (PMN-PT),^[104] are detected here.

2.3.2. Depth-Dependent Hard X-Ray Photoelectron Spectroscopy

Non-destructive depth profiling was done via HAXPES on a memristive device with a 13 nm thin Au top electrode. The measured angle of emission ϑ was varied (see Figure 1), leading to the highest information depth for small angles. All HAXPES spectra of Au 4f, Hf 3d_{5/2}, and Al 1s were recorded for three different ϑ and two different resistance states (HRS and LRS) switched in situ. The depth-dependent measurements are called “surface sensitive” ($\vartheta = 15^\circ$), “sub-surface sensitive” ($\vartheta = 41.4^\circ$), and “bulk sensitive” ($\vartheta = 60^\circ$) throughout this work. Since the Au top electrode is relatively thick (13 nm), the signal-to-noise ratio of Hf 3d_{5/2} and Al 1s decreases significantly with increasing surface sensitivity (i.e., increasing detection angles). The HAXPES recording of spectra with a good signal-to-noise ratio required approximately between 1 and 3 h. Since the LRS significantly relaxes toward the HRS within several hours (see Figure 2c), the measurement time had to be constant (≈ 1 h) to ensure that all measurements reflect the same memristive state. Hence, spectra for 41.4° (sub-surface sensitive) and 60° (surface sensitive) were measured two and three times, respectively, and were merged afterward to enhance the signal-to-noise ratio, while the memristive state was refreshed in between (see Experimental Section and Figure S6a, Supporting Information). No Al spectra were evaluated for 60° , and no NbO_x spectra were measured for any ϑ due to the limited information depth of HAXPES. Furthermore, no radiation-induced defects were observed in the HAXPES spectra.

A typical Au 4f spectrum is shown in Figure S6b, Supporting Information. Figures S7 and S8, Supporting Information show the raw spectra and the determined backgrounds for Hf 3d_{5/2} in HRS and LRS, respectively. The raw Al 1s spectra for HRS and LRS are shown in Figures S9 and S10, Supporting Information, respectively. The merged Hf 3d_{5/2} and Al 1s spectra, together with the peak fits, can be found in Figures 5a and 5b for Hf 3d_{5/2} and Al 1s, respectively, for both HRS and LRS. All spectra show single peaks. The BE and FWHM of the resulting fits are shown in Figure 5c for merged Hf 3d_{5/2} and Al 1s, respectively, in both HRS and LRS. Error bars denote standard deviations, which are determined by the fitting algorithm. All fitting parameters can be found in Table S11, Supporting Information.

The Hf 3d_{5/2} core-level is first investigated in HRS as a function of the angle of emission, revealing BEs between 1662.08 and 1662.28 eV, which can be attributed to Hf⁴⁺.^[51,100,105] Again, no indication of metallic Hf, and therefore no indication for

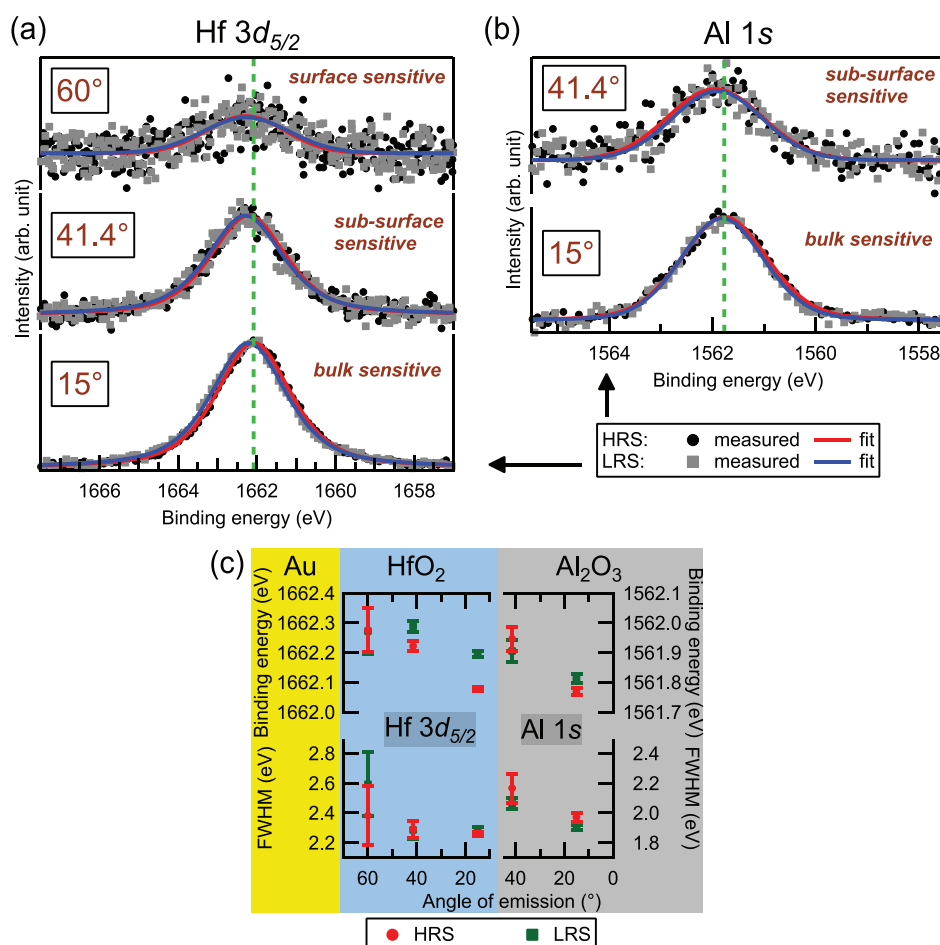


Figure 5. Merged and background-subtracted a) Hf 3d_{5/2} and b) Al 1s spectra in HRS (black dots) and LRS (gray squares). Fits of HRS (red solid lines) and LRS (blue solid lines) spectra are also shown. Green vertical dashed lines indicate the peak position in HRS for the bulk sensitive measurements at $\vartheta = 15^\circ$. c) BE and FWHM of Hf 3d_{5/2} and Al 1s as a function of the memristive state and depth (emission angle). Error bars denote the standard deviations, which are determined by the fitting algorithm.

a significant amount of vacancies is detectable. In contrast, filamentary-type Hf_xAl_{1-x}O_y memristive devices show a peak feature at 1660.6 eV.^[51] Furthermore, the BE increases at larger angles of emission, that is, closer to the Au interface. At the same time, the FWHM does not vary significantly between the sub-surface sensitive and the bulk sensitive measurement. The spectral shape also does not vary, and a chemical difference being responsible for the BE gradient can be excluded.^[55,101] Hence, a variation in the electrostatic potential is deduced to be accountable for the BE variation.^[48,49] Since the bulk sensitive spectrum is very noisy, the higher FWHM should not be attributed to a chemical change (see Table S11, Supporting Information).

For Al 1s in HRS, BEs of 1561.77 and 1561.95 eV are extracted for the bulk sensitive and the sub-surface sensitive measurement, respectively, indicative of Al₂O₃ since BEs for alumina (Al³⁺) are reported between 1562.6 and 1563 eV.^[106,107] No features of metallic Al are present, which are reported between 1559.6 and 1559.8 eV.^[107,108] A similar BE gradient as detected in HfO₂ is visible, suggesting a decreasing electrostatic potential with increasing distance to hafnia. It should again be noted that

the noise significantly impacts the peak form of the sub-surface sensitive Al 1s spectrum at 41.4° (see Table S11, Supporting Information).

Next, Hf 3d_{5/2} peaks are evaluated in the LRS. Again, no metallic Hf feature is present (see Figure 5a). BEs shift to higher energies by ≈ 120 and 70 meV for bulk sensitive and sub-surface sensitive measurements, respectively, as shown in Figure 5c. No significant BE shift can be measured for the surface sensitive spectrum. However, the standard deviations for both HRS and LRS are larger than 70 meV for the surface sensitive measurements so that any BE shift below this value cannot be reliably resolved. Nevertheless, an obvious trend is visible toward higher BE in LRS, with the most pronounced shift near Al₂O₃. The FWHM for bulk sensitive and sub-surface sensitive measurements do not change, and no additional peak features appear (Figure S12a, Supporting Information). Thus, no electrical bias-induced chemical change can be detected.^[55,101] The shifted BE is hence attributed to a change in the electrostatic potential within hafnia toward a higher potential in LRS. No additional peak features are present for Al 1s as well (see Figures 5b and S12b, Supporting Information). Here,

for 15° (bulk sensitive) and 41.4° (sub-surface sensitive), the BEs shift in opposite directions (see Figure 5c). Near HfO₂, the BE shifts by −40 meV (41.4°), and deeper in Al₂O₃, the BE shifts by +40 meV (15°). However, the BE difference between HRS and LRS for 41.4° (near HfO₂) is within one standard deviation of the uncertainty of the fit. The peak width is getting smaller in LRS (≈0.1 eV) for the bulk sensitive spectrum. The peak shape of the sub-surface sensitive measurement is not evaluated as explained above. Altogether, the BE variation in alumina can be ascribed to a variation in the electrostatic potential. In particular, the potential decreases at the HfO₂ interface and increases further inside in LRS.

3. Discussion

3.1. Current Transport Mechanism

The $|J|$ - V curves (Figure 2a) show a high non-linearity and a rectification of several orders of magnitude. This can be attributed to a Schottky-like contact which can form due to a direct metal/semiconductor contact but can also be established with a thin oxide layer between metal and semiconductor.^[69,70] In particular, a Pt/HfO₂(5 nm)/n-GaAs Schottky diode has already been reported.^[109] According to literature, current transport in the devices under study can thus be attributed to thermionic emission^[69,70,109] for low applied voltages (but above a memristive state-dependent threshold) in combination with an intrinsic current compliance dominant for high voltages (see Section S13, Supporting Information for a more detailed explanation), as also reported for similar devices.^[33] A positively charged space charge region (SCR) within an n-type semiconductor is consistent with the positive forward bias on the high

work function Au top electrode. Thus, the electrostatic potential in the semiconductor increases with the distance to Au. In contrast, the potential within HfO₂ and Al₂O₃ decreases with distance to the gold electrode for both memristive states, as revealed by HAXPES non-destructive depth profiling. Therefore, the NbO_x at the interface to Al₂O₃ is most probably responsible for the rectifying properties leading to a two-terminal MIS structure with a bilayer HfO₂/Al₂O₃ insulator. While stoichiometric Nb₂O₅ is known to be a good insulator,^[67] it is reported that even a small reduction leads to an n-type semiconducting behavior.^[67,68] Since EELS data indicate a mixture of Nb₂O₅ and NbO₂ with an oxygen gradient, semiconducting NbO_x can be expected.

Further information on the effect of the single material layers on the device functionality can be obtained by exchanging or omitting some of the layers and comparing the $|J|$ - V characteristics with those of the reference devices. To this end, three additional device compositions were investigated (see Experimental Section for fabrication details). The corresponding $|J|$ - V curves measured on devices with a top electrode size of 625 μm² are shown in Figure 6, where the insets show the respective material stack. Figure 6a displays the same data as shown in Figure 2a for a better comparison to the characteristics of the other devices. The $|J|$ - V switching characteristics of ten individual devices and the corresponding mean curve is shown, together with the mean read-out characteristics. Figure 6b depicts the $|J|$ - V characteristics of ten devices having a Hf bottom electrode instead of Nb. The Hf should be oxidized at the interface to Al₂O₃, similar to the Nb electrode. A significantly different performance is revealed compared to the reference devices in Figure 6a. For instance, a significant current can only be measured for positive voltages higher than 4.5 V when applying voltage sweeps with ±5 V amplitude. Moreover,

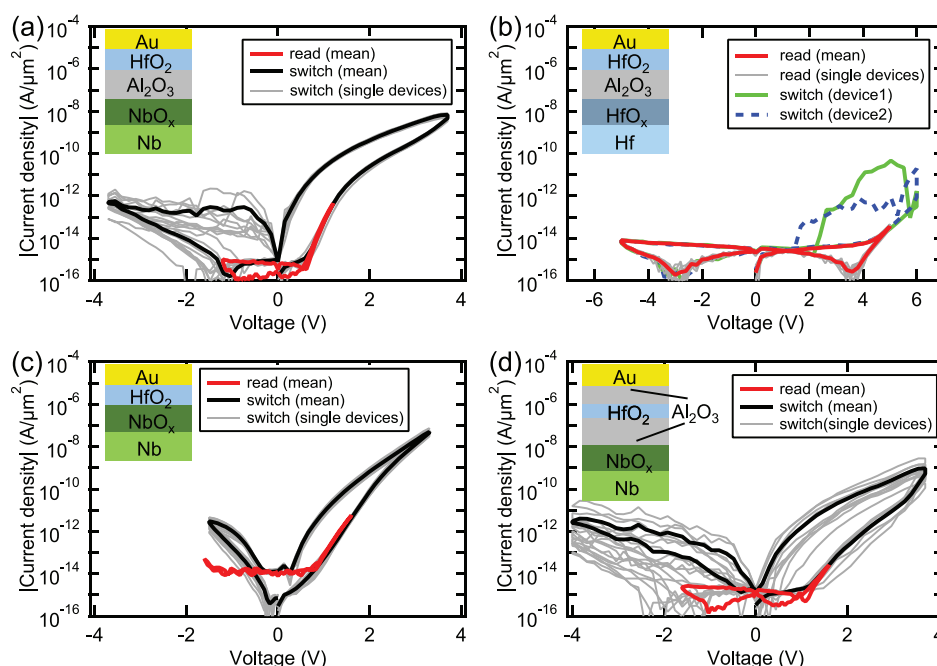


Figure 6. a) $|J|$ - V characteristic of reference devices and b–d) devices with different material stacks. The respective material stacks are shown as insets. Each black and red solid line shows the mean $|J|$ - V data of ten individual devices.

no analog memristive switching is observed even at higher voltages. However, a few devices show a threshold switching behavior^[110] when the positive bias is increased up to 6 V (see green solid line and blue dashed line). Note that this behavior differs strongly for different adjacent devices and is not well reproducible. Thus, replacing the Nb bottom electrode with Hf drastically changes the devices' I – V characteristics and the memristive switching process. This demonstrates the relevance of the bottom electrode on the device characteristics. Figure 6c shows I – V characteristics of ten devices without any Al_2O_3 . Here, the qualitative behavior is the same as for the reference devices, that is, diode-like current transport and analog memristive switching for voltages above a certain threshold. However, the devices do not allow to apply voltages with an absolute value as high as the other device types, especially for negative bias. Therefore, $V_{\text{max}} = 3.3$ V and $V_{\text{min}} = -1.5$ V are used to induce memristive switching. This clearly shows that memristive switching in the reported devices does not rely on the Al_2O_3 layer. However, the Al_2O_3 leads to less degradation of device performance over time (not shown) and significantly increases the retention time in similar devices.^[33] The I – V curves of ten device with an additional 2.5 nm thin Al_2O_3 layer between HfO_2 and Au can be found in Figure 6d. The lower Al_2O_3 and the HfO_2 layer are thinner so that the overall oxide thickness increases by ≈ 1 nm. The Nb bottom electrode is most probably oxidized again. These devices show qualitatively the same behavior as the other devices with Nb bottom electrodes. Thus, a device with an Au/ Al_2O_3 interface leads to similar performance as a device with an Au/ HfO_2 interface. The overall resistance, however, is increased compared to the reference devices and the device variability for positive and negative bias is significantly larger. For switching sweeps, voltage amplitudes of $V_{\text{max}} = 3.7$ V and $V_{\text{min}} = -4$ V are used.

We can conclude that current transport is dominated by the SCR within NbO_x while the $\text{HfO}_2/\text{Al}_2\text{O}_3$ double oxide layer acts as intrinsic current compliance. This is found by the tremendous change in the electrical characteristics when replacing the Nb bottom electrode with a Hf bottom electrode. It further agrees with the missing positively charged SCR in hafnia and alumina, as revealed by the depth-dependent HAXPES measurements, and with the composition of the NbO_x , as determined by EELS.

3.2. Memristive Switching Mechanism

The XPS and HAXPES spectra reflect the memristive switching mechanism in the following way. A net potential increase in HfO_2 is shown by a combination of the Hf $3d_{5/2}$ data (see Figure 5c) and the Hf $4f$ spectra (see Figure 4). In particular, Hf $3d_{5/2}$ spectra reveal a higher potential increase at $\vartheta = 15^\circ$ and thus near the Al_2O_3 interface than at the sub-surface sensitive measurements ($\vartheta = 41.4^\circ$). The measured signals are too noisy to distinguish a potential peak shift for surface sensitive measurements (near the Au interface). The Hf $4f$ spectra, which stem from the Au/ HfO_2 interface, indicate a potential increase near the Au interface as well. Movement of negatively charged oxygen ions or positively charged oxygen vacancies within hafnia would lead to an increased potential at one interface

together with a decreased potential at the opposite interface. Moreover, the exchange of negatively charged oxygen ions between HfO_2 and Al_2O_3 can also be excluded since the positive voltage applied to Au to switch to LRS would attract these ions, and the hafnia would charge negatively. Furthermore, positively charged oxygen vacancies cannot enter HfO_2 from Al_2O_3 when switching to LRS since the electric field under positive bias repels them. Thus, ion movement can be excluded with high probability.

Here, we suggest charging and discharging of localized traps within the HfO_2 layer or at the $\text{HfO}_2/\text{Al}_2\text{O}_3$ interface as an alternative switching mechanism. Probable candidates for these traps are oxygen vacancies. Simulations using a hybrid density functional suggest that these vacancies are singly positively charged (i.e., one electron is trapped) or neutrally charged (i.e., two electrons are trapped) if the Fermi level is located between 3.7 and 4 eV or 4 and 5.5 eV above the HfO_2 valence band maximum (VBM), respectively.^[111] The theoretical barrier height^[69,70] between HfO_2 and Au is 3.1 eV with an Au work function of 5.3 eV^[112] and a HfO_2 electron affinity of 2.2 eV^[99] leading to a Fermi level position of 2.6 eV above the VBM when considering a band gap of 5.7 eV.^[99] However, the actual barrier can deviate strongly (toward lower effective barriers) from these theoretical values,^[48,69,70] and this can be expected for the multi-layer device structure here. Thus, neutral or singly positively charged vacancies in thermodynamic equilibrium are reasonable since a lower effective barrier leads to an increased Fermi level with respect to the VBM. Applying a positive potential to Au can lead to a positive charging of the vacancies since electrons can be ejected.^[28,30,43] This agrees with the BE shifts toward higher energies in LRS. Moreover, additional positive charges within the HfO_2 layer influence the potential drop across the Al_2O_3 layer as well. Here, negative image charges may lead to the decreased potential at the $\text{HfO}_2/\text{Al}_2\text{O}_3$ in LRS and thus to the decreased potential drop across alumina as indicated by the depth- and state-dependent BEs of the Al 1s spectra (see Figure 5c). The decreasing FWHM of Al 1s spectra are consistent with a decreasing voltage drop across this layer (see Figure 5c) since the width of photoelectron spectra can increase due to an increased voltage drop across the probed layer.^[100,105] No significant changes in the FWHM of Hf $3d_{5/2}$ and Hf $4f$ are found. However, a potential of 0.9 V across HfO_2 is estimated to lead to a Hf $3d_{5/2}$ spectral broadening of 0.1 eV in ref. [100]. Thus, the smaller change in the potential in the HfO_2 layer cannot be detected through a change in FWHM within the standard deviation of the determined peak width.

The potential variation is used to estimate the amount of charges involved in switching, as shown in detail in Section S14, Supporting Information. Two scenarios are considered, that is, uniformly distributed bulk charges and charges located at the $\text{HfO}_2/\text{Al}_2\text{O}_3$ interface, in agreement with ref. [30]. A bulk charge density of $N_B = 1.6 \times 10^{19} \text{ cm}^{-3}$, and an interface charge density of $N_I = 4.7 \times 10^{12} \text{ cm}^{-2}$ are estimated. It should be noted that the estimated charges are not the maximum amount of charges involved in switching for two reasons. First, recording a single Hf $3d_{5/2}$ spectrum takes about 19 min, during which the respective energy range is scanned six times, and the single sweeps are then combined into a single spectrum. In this time span, a relaxation toward HRS takes place

(see Figure 2c). Thus, the determined BE shift between HRS and LRS reflects the mean potential difference within this time frame. Second, the BE shift at the bulk sensitive measurements (15°) is used to estimate the potential increase at the hafnia/alumina interface. Yet, the real potential increase is higher since the photoelectron spectra for 15° angle of emission include contributions from all parts of the HfO_2 layer. The potential only linearly contributes to the estimated charge densities (see Equations (S14.2) and (S14.4), Supporting Information). Thus, the order of magnitude calculated for both densities does only change if the actual potential increase deviates from the estimated increase by one order of magnitude, which is not to be expected. Since the oxygen vacancy density in physical vapor deposition (PVD) processed HfO_2 is reported to be in the order of 10^{19} cm^{-3} ,^[113] the estimated value of N_B is reasonable. Moreover, this vacancy density is too small to be detected by photoelectron spectroscopy, which allows for finding differences in the material composition down to $\approx 1\%$.^[103] This explains why no fingerprints of oxygen vacancies can be found in the spectra. The estimated value of N_I is also reasonable since charge densities of up to $7.8 \times 10^{12} \text{ cm}^{-2}$ at a HfO_2/GaN interface are reported.^[114] Thus, bulk charges in HfO_2 , interface charges at the alumina interface, or a combination of both can explain the potential variation.

In addition, filamentary switching is likely to be suppressed in the reported devices due to the low amount of vacancies compared to other devices showing filamentary switching together with spectral fingerprints of oxygen vacancies.^[50,51,54] In this respect, first principles-based simulations reveal that for efficient nucleation and growth of oxygen-deficient filaments in HfO_x an x in the range of 1.50–1.75 is optimal.^[115] This is experimentally supported by Park et al.,^[22] who show a filamentary-type switching for $x = 1.80$ and an area-type switching process for $x = 1.98$. HfO_2 films, which are stoichiometric after deposition, can also lead to filamentary switching if an initial electro-forming step reduces the HfO_2 locally.^[59] This is avoided in our devices by using a noble metal top electrode and an Al_2O_3 film acting as a diffusion barrier for oxygen ions^[33,57] as adjacent layers.

In summary, the memristive switching in the devices under study can be directly correlated with the electrostatic potential within HfO_2 and, thus, with the charge state of electron traps which are most probably oxygen vacancies. Indeed, HfO_2 is widely investigated as charge trapping layer in CTF memory.^[66] Here, trapped charges are assumed to modulate the conduction channel in MOSFETs. Moreover, memristive devices based on charging and discharging of traps within HfO_2 have already been reported^[42,56,63] without spectroscopic evidence. The influence of the potential variation on the device resistance is explained in the next section.

3.3. Device Model

A schematic band diagram of the qualitative device model can be found in Figure 7. A band diagram is used to visualize the involved potential profiles and barriers. The widths of the layers are drawn to scale, while the band alignment and the amount of band bending are drawn qualitatively. The current

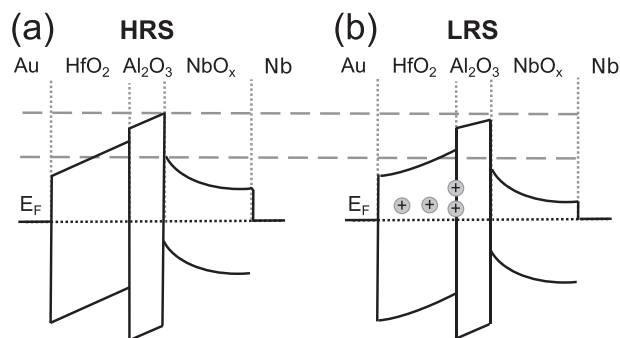


Figure 7. Band diagram of the device model in a) HRS and b) LRS. Only the additional positive charges in LRS arising from electron de-trapping are schematically indicated.

transport is dominated by the SCR within NbO_x while hafnia and alumina act as intrinsic current compliance. The current through the dielectrics can be assumed to be assisted by defects so that a significantly high current can flow even for $\approx 6.5 \text{ nm}$ insulators. In particular, the current through Al_2O_3 can be assumed to be dominated by the thinnest parts ($\approx 2 \text{ nm}$) of the layer (see the width of alumina relative to hafnia in Figure 7). The total charge distribution within the multi-layer stack is unknown. The HfO_2 and Al_2O_3 bands are drawn linearly in HRS in Figure 7a for simplicity but can have a more complex shape. The upward band bending in the dielectrics is indicated by the HAXPES data, while the downward band bending in the semiconducting NbO_x is extracted from the forward bias of the diode-like characteristics. A significant amount of negative charges at the $\text{Al}_2\text{O}_3/\text{NbO}_x$ interface is deduced to account for the band profile. Additional positive charges in the hafnia layer and at the $\text{HfO}_2/\text{Al}_2\text{O}_3$ interface in LRS, as qualitatively indicated in Figure 7b, are attributed to electron de-trapping from neutral or singly positively charged oxygen vacancies. Bulk traps, interface traps, or a combination of both can explain the switching.

The additional positive charges in the HfO_2 layer in LRS influence the charge distribution within the buried NbO_x such that the built-in potential decreases. This is similar to $\text{HfO}_2/\text{SiO}_2/\text{Si}$ gate stacks, in which positive charges within HfO_2 lead to a decreased upward band bending within silicon.^[116] Furthermore, positive charges within interfacial oxide layers in metal/semiconductor Schottky contacts are also reported to decrease the upward band bending.^[70] Thus, the effective barrier height and, thereby, the overall device resistance decrease due to positive charging of electron traps in HfO_2 . Switching the device back to HRS results in the initial charge distribution and, thereby, in the initial resistance. The proposed model can also explain the different current fluctuations for positive and negative bias (see Figure 2a and 6a). The devices are initially in the HRS, and the voltage is swept in positive direction first. For low voltages, the current transport is dominated by thermionic emission, and no memristive switching takes place. An intrinsic current compliance becomes dominant for voltages high enough to induce memristive switching (see Section S13, Supporting Information). The current density shows low fluctuations for both low and high positive voltages. When the voltage is swept back to 0 V, the device resistance relaxes toward HRS,

even without applied bias (see Figure 2c). Thus, switching toward HRS takes place for all negative biases. The electron trapping can be expected to cause the observed noise for negative bias.^[117] This effect is probably only visible for switching to HRS because the current density during switching to LRS is orders of magnitude higher. Besides, an additional higher variability for negative bias can potentially be explained by the inhomogeneous Al_2O_3 layer (see Section 2.2) if the current transport for negative bias is restricted by the alumina. Moreover, the proposed model does also explain why the device with Hf bottom electrode does not show interface-type memristive switching (see Figure 6b). In contrast to the NbO_x , no SCR exists in the HfO_2 below alumina. Thus, a variation in the charge distribution in HfO_2 does not impact the current transport as significantly as for the reference device since no SCR is modulated.

It is further estimated that the NbO_x cannot completely screen the built-in potential due to its thickness of $d_{\text{NbO}_x} \approx 5 \text{ nm}$. For an estimate, the standard formula for the Debye length λ_D is used^[69,118] (see Equation (S15.1) and Section S15, Supporting Information). The relative permittivity of NbO_x is assumed to be between 10 (NbO_2) and 41 (Nb_2O_5).^[68] Thus, 63% of the built-in potential can be screened in NbO_x (i.e., $\lambda_D = d_{\text{NbO}_x}$) if the doping concentration is between 2.9×10^{17} and $1.2 \times 10^{18} \text{ cm}^{-3}$. These are reasonable doping concentrations since concentrations of up to $6 \times 10^{19} \text{ cm}^{-3}$ for $\text{Nb}_2\text{O}_{5-x}$ are reported.^[68,119] However, a complete screening can be expected for $\approx 10\lambda_D = d_{\text{NbO}_x}$, as is the case for GaAs.^[69] This requires a doping concentration between 2.9×10^{19} and $1.2 \times 10^{20} \text{ cm}^{-3}$. Since an increase in charge density in the order of 10^{19} cm^{-3} in HfO_2 (with $d_{\text{HfO}_2} \approx d_{\text{NbO}_x}$) is estimated to have a significant impact on the charge distribution within NbO_x , such a doping concentration is unlikely in the reported devices, and part of the built-in potential should drop in the Nb bottom electrode. Moreover, in the latter case, $\approx 95\%$ of the built-in potential would be screened within 1.5 nm, and thus direct tunneling is expected to have a significant impact on current transport so that no diode-like behavior would occur. More details about these calculated results can be found in Section S15, Supporting Information.

In summary, the experimental findings consistently indicate that our devices consist of a two-terminal MIS-like structure in which electron traps within the insulator modulate the space-charge region of the semiconductor and, thereby, the overall device resistance. This is consistent with the results of ImpSpec conducted on the reference devices, performed by Marquardt et al. and reported in the companion paper.^[74] Here, the kinetics of the set process and of the retention imply charging of traps rather than ion movement. Furthermore, quantitative model parameters describing current transport in HRS and LRS and switching dynamics are given. In particular, current transport is described by thermionic emission with an effective barrier height of 0.84 and 0.675 eV, as well as an ideality factor of 3.71 and 4.9 in HRS and LRS, respectively. A series resistance of 12 k Ω and a reach-through^[120] complete the current transport model. The results from Marquardt et al. are in agreement with the qualitative model proposed here, which could be applied to explain memristive switching phenomena in other devices as well.

Similar device models have already been reported by other groups without spectroscopic evidence. In this respect, Mikheev

et al.^[30] explained memristive switching in Pt/Nb:SrTiO₃ (NSTO) by a modulation of the Schottky barrier height by a variation in trapped charges within an inter-layer consisting of carbon contamination between metal and semiconductor and a potentially damaged single crystalline NSTO interface. Kim et al. investigated TiN/ NbO_x /TiO₂/ NbO_x /Pt memristive devices.^[43] Here, electrons are reported to be ejected from traps ascribed to Ti-sites in the upper NbO_x layer (adjacent to Pt) by applying a positive voltage to the Pt electrode. This modulates the Schottky barrier of the NbO_x /Pt interface. The NbO_x is a mixture of $\approx 60\% \text{ Nb}_2\text{O}_5$ and $40\% \text{ NbO}_2$. Gao et al. report on an optoelectronic indium tin oxide (ITO)/NSTO junction in which memristive switching is induced by Schottky barrier modulation due to electron de-trapping while illuminated with light.^[36] Furthermore, charge trapping at an HfO_2 /Ti interface is reported as a memristive switching mechanism.^[42] In addition, devices are reported in which resistance switching is based on electron trapping in HfO_2 which changes the bulk conductivity of hafnia and, thereby, the overall resistance, while a rectifying barrier is unaffected.^[56,63] Moreover, an MIS model that explains memristive switching in Au/NSTO and Au/ BaTiO_3 /NSTO devices through electron trapping and de-trapping in an interfacial layer is given by Fan et al.^[34] Their model is supported by scanning Kelvin probe microscopy (SKPM) and piezoresponse force microscopy (PFM) studies on both the NSTO substrate and the BaTiO_3 layer, respectively. Thus, we show spectroscopic evidence on functional devices for Schottky barrier modulation by electron trapping/de-trapping in general and for electron trapping/de-trapping in HfO_2 in particular, in agreement with the other models.

The device model allows to propose methods for engineering the device characteristics for specific applications. In this respect, the defect density in the HfO_2 could be tuned by adjusting the sputter deposition parameters which affects the switching window.^[22,121] A strong impact of the top electrode's work function and metal-insulator interface quality on the read-out and switching parameters is further expected, since these properties crucially affect the current transport in interface-type devices. Reducing the roughness between the NbO_x and the Al_2O_3 might lead to less device variability. Finally, the device model can be exploited to deduce design rules for the integration of the devices into CMOS technology. First, the amount of charge traps involved in switching should be larger than the amount of charges in the SCR so that the traps can have a significant impact on the depletion region. Second, the insulator should guarantee an intrinsic current compliance to protect the device from dielectric breakdown while simultaneously allowing a significant current flow. Third, the density of oxygen vacancies in the insulator must be low enough to prevent filament formation. Fourth, for a back-end-of-line (BEOL) compatible process and, thereby, for a potential 3D integration and a more flexible chip design, CMOS-compatible semiconductors such as amorphous or poly-crystalline Si could be explored. Fifth, a fab-friendly metal that forms a rectifying barrier with the semiconductor should be used. Sixth, the overall current density should be orders of magnitude higher than in the reported devices to enable a geometrical scaling to the nanometer regime while obtaining a measurable read-out current (see inset of Figure 2a).

4. Conclusion

In summary, a comprehensive characterization of analog memristive switching devices composed of Nb/NbO_x/Al₂O₃/HfO₂/Au showing diode-like I – V characteristics is reported. The stoichiometry of HfO₂ and Al₂O₃ is confirmed by EELS and HAXPES, while an excess of oxygen and argon in the center of the Al₂O₃ is indicated by EELS. The oxidation state of the NbO_x is determined by EELS to be a mixture of Nb₂O₅ and NbO₂ with decreasing oxygen content toward the Nb bottom electrode. Non-destructive depth-dependent HAXPES and XPS measurements show that the space-charge region that accounts for the diode-like behavior is neither located in the HfO₂ nor in the Al₂O₃ layer. Memristive state-dependent core-level shifts indicate that the charging of vacancies within HfO₂ is responsible for switching. The experimental results suggest a purely electronic origin of memristive switching in the investigated devices. We could not find any hints of ionic drift as a source for the observed switching behavior. Devices with adjusted layer stacks reveal that the diode-like behavior is caused by the NbO_x layer, while Al₂O₃ is not crucial for the memristive switching. The proposed memristive device model consists of a two-terminal MIS-like structure in which electron traps within the insulator modulate the space-charge region within the semiconductor and, thereby, the overall device resistance. While similar memristive device models have been reported before, we present here spectroscopic evidence on functional devices for the charging and discharging of electron traps as the origin of memristive switching in such devices.

The worked-out model is in agreement with the companion paper Marquardt et al. that exploits ImpSpec to probe the current transport and switching kinetics of the same devices.^[74] Based on two different experimental approaches (XPS/HAXPES and ImpSpec), our findings strongly indicate an electronic charging and discharging of traps as the fundamental origin of resistive switching in our devices, instead of ionic drift.

5. Experimental Section

Device Fabrication: In the standard process, all layers were deposited using DC magnetron sputtering without breaking the vacuum with a base pressure of less than 5×10^{-7} mbar. The devices were fabricated on 100 mm Si wafers passivated by 400 nm thermally oxidized SiO₂. Metallic Nb and Al were first deposited in Ar atmosphere. The following deposition of HfO₂ in a reactive Ar/O₂ gas mixture using a metallic Hf target leads to the oxidation of the Al layer and, to some degree, of the Nb layer.^[80,121] The Au top electrode was deposited in an Ar atmosphere. The device patterning was performed by standard optical lithography, lift-off processes, and Au etching in potassium iodide to get different electrode areas. The fabrication process was developed by Hansen et al. for similar devices (with NbO_y instead of HfO₂)^[33] and is described in more detail in refs. [33, 121]. The HfO₂ layers investigated here were produced in exactly the same process as the NbO_x in refs. [33, 80, 121], that is, with a total process pressure of 1.21×10^{-2} mbar in poisoned mode (7 sccm Ar, 23 sccm O₂), a discharge power of 100 W and with a target to substrate distance of ≈ 53 mm. The Hf bottom electrode for the device shown in Figure 6b was deposited with the same sputter parameters as the Nb bottom electrode. The upper 2.5 nm thin Al₂O₃ layer for the device in Figure 6c was deposited with the same process pressure, gas composition, and power as the HfO₂. Here, the HfO₂ and

Al layers were deposited slightly thinner than for the reference device so that the overall Al₂O₃/HfO₂/Al₂O₃ tri-layer is ≈ 1 nm thicker than the insulator bi-layer of the reference devices.

Different device structures were built for this work:

- (i) Reference devices with structures described in ref. [33] were fabricated. Here, six different contact areas ranging from 100 to 2500 μm^2 are arranged across the wafer. Furthermore, a 720 nm thick Ti wiring layer covers the top electrodes and connects them to Ti contact pads. A SiO_x layer is needed as insulation between the wiring layer and the mesa structures. The devices shown in Figure 6 were also fabricated with the same design.
- (ii) Functional devices for the XPS and HAXPES measurements were fabricated with a different design. Here, the top electrode has to be much thinner and must not be covered with a wiring layer because the information depth of HAXPES is in the order of a few ten nm, while it is even less for lower energetic X-rays also used in this work.^[47,51] The device structure is shown in Figure S4, Supporting Information which is inspired by ref. [105]. The Au top electrodes are electrically connected to Ti contact pads by Ti wiring lines, which only cover a small percentage of the device area. The total top electrode areas of the investigated devices are 13650 μm^2 . 9000 μm^2 are not covered by insulation or wiring layers allowing to probe the devices with PES. To obtain functional devices, the top electrode has to form a continuous film. Since thin gold films are known to grow in an island-like structure on ceramics,^[122] an optimization of the top electrode deposition process has been performed. In the sputter deposition process, the thinnest continuous film produced has a thickness of 13 nm. A device produced that way was probed by HAXPES. The Au was thermally evaporated to get even thinner continuous films of 6 nm. Therefore, the respective wafer had to be transferred from the sputter deposition chamber to the evaporation chamber being exposed to normal atmosphere for less than 5 min. The wafers with structures (ii) not only contain devices with the described structures but also test structures as described in (i). These devices only work if the Ti wiring layer has no direct contact with HfO₂. Thus, measuring the electrical characteristics of these test structures verified that the deposited Au formed continuous layers.

Electrical Measurements and Memristive Switching: The bias voltage was applied to the Au top electrode while the bottom electrode was grounded. Trapezoid-shaped voltage sweeps were applied, where the voltage was increased from 0 V to the positive maximum bias V_{max} , then decreased to the negative bias V_{min} and increased again to 0 V. In total, 100 voltage steps with a total bias time of 220 s were used. The read-out characteristics of the devices with Nb/NbO_x/HfO₂/Au material stack were recorded with a total bias time of 16 s, which leads to the higher noise level in Figure 6(c) (red line). In situ switching to HRS or LRS in XPS/HAXPES experimental chambers was done with trapezoidal-shaped voltage sweeps of one polarity only (50 steps, 110 s). All data from the reference wafer (Figure 2) and the devices with alternative layer stacks (Figure 6) were measured with an HP4156A semiconductor parameter analyzer. Electrical characterization and memristive switching at the synchrotron beamlines were done with an Agilent E5260 source measurement unit (SMU) at beamline P04, and an Agilent B2912A SMU at beamline P22, respectively. The X-ray beam was never directed to the sample while applying bias to the devices.

The spectra for emission angles of 41.4° (sub-surface sensitive) and 60° (surface sensitive) were measured two and three times for each memristive state, respectively, and the state was refreshed in between. First, the spectra were recorded for HRS for all three angles. Afterward, the device was switched to an LRS with a unipolar voltage sweep with $V_{\text{max}} = 4$ V. To guarantee that all spectra for all detection angles were recorded for the same resistance state, a current compliance of 30 μA was utilized. Refreshing the resistance state to one and the same level was possible, and the device's retention was long enough to record data

for two distinct resistance states, as shown in Section S6, Supporting Information. The higher read-out voltage of 1.8 V was necessary because the noise level of the I – V measurement within the vacuum chamber did not allow to use lower voltages. However, the device state was not significantly affected by the higher read-out voltage (see Section S6, Supporting Information).

TEM and EELS: TEM characterization was performed using an FEI Titan³ at an acceleration voltage of 300 kV with spherical aberration (C_s) probe correction and monochromator. The EEL spectra were acquired with a GIF Quantum Dual EELS detector. To probe the whole material stack, a focused ion beam lamella was extracted from a functional device in HRS of structure (ii) with a 13 nm Au top electrode. The line scan in Figure 3b is constructed from a spectral image by summing all spectra horizontally and binning two of these lines to obtain a vertical step size of 1.75 nm.

XPS and HAXPES: The Au top electrode was electrically connected to a common ground with the analyzer during photoelectron spectroscopy. During HAXPES measurements, also the bottom electrode was connected to the common ground leading to defined electrical boundary conditions when evaluating potential profiles. All recorded Hf and Al spectra were aligned with the Au $4f_{7/2}$ peak of the top electrode at 84.0 eV BE. It should be emphasized that this provides an energy reference relative to the Fermi level of the Au rather than an exact alignment of the energy with $E_F = 0$ eV. All core-level spectra were fitted with the XPST add-on for IGOR Pro software (WaveMetrics), which utilized the Pseudo-Voigt function described in ref. [123]. Here, the Voigt profile was approximated by a Lorentzian–Gaussian sum function. Shirley-type backgrounds^[124] were used for spectra with a sufficient signal-to-noise ratio. Otherwise, linear backgrounds were used. The XPS measurements with soft X-rays were measured with an X-ray energy of 1550 eV, a beam spot diameter of <15 μm , and an energy resolution of ≈ 200 meV. The HAXPES spectra were obtained with an energy of 7000 eV, a beam spot of $20 \times 20 \mu\text{m}^2$, and a total experimental energy resolution of ≈ 300 meV. Depth-dependent information was obtained by measuring HAXPES spectra from different angles of emission. This was achieved by rotating the sample relative to the analyzer and also to the X-ray beam so that the footprint of the beam was elongated in one direction with a factor of $1/\sin(\vartheta)$ (i.e., a maximum footprint of $20 \times 80 \mu\text{m}^2$ for the bulk sensitive measurements at 15°). All PES measurements were conducted at 300 K.

Au $4f$ spectra were fitted with a fixed spin-orbit splitting of 3.7 eV, an intensity ratio of 0.75 for f-orbitals and the same FWHM for both components.^[125] For XPS measurements with the 6 nm top electrode, two doublet features assigned to surface states and bulk Au^[126] were detected (see Section S5, Supporting Information). For HAXPES measurements with a 13 nm Au top electrode, a single asymmetric doublet peak (see Section S6, Supporting Information) with additional features at higher BE was detected as it was usually observed for XPS spectra of gold and other metals.^[123] This asymmetry was incorporated into the fit by using an asymmetric Pseudo-Voigt function.^[123] No resistance state-dependent peak shift was observed for the Au $4f$ spectra, and no gold oxides^[127] were formed in both samples.

Hf $4f$ spectra were fitted with a fixed spin-orbit splitting of 1.67 eV, an intensity ratio of 0.75 for f-orbitals and the same FWHM for both components.^[96] The spectra were aligned to the respective bulk Au $4f_{7/2}$ peaks at 84.0 eV recorded for all resistive states.

Hf $3d_{5/2}$ and Al $1s$ spectra for an angle of emission of 41.4° (sub-surface sensitive) and 60° (surface sensitive) were measured two and three times, respectively. The spectra corresponding to the same angle and the same memristive state were combined afterward. To this end, the single spectra were aligned to the corresponding Au $4f_{7/2}$ peak at 84.0 eV, and the backgrounds of the single spectra were subtracted before the spectra taken at one and the same angle and resistive state were summed up. Raw spectra and fitted backgrounds can be found in Section S7–S10, Supporting Information. The merged Hf $3d_{5/2}$ and Al $1s$ spectra could be fitted best with single Pseudo-Voigt functions.

Supporting Information

Supporting Information is available from the Wiley Online Library or from the author.

Acknowledgements

This work was funded by the Deutsche Forschungsgemeinschaft (DFG, German Research Foundation) through FOR 2093. Funded by the Deutsche Forschungsgemeinschaft (DFG, German Research Foundation)—Project-ID 434434223—SFB 1461. The authors acknowledge DESY (Hamburg, Germany), a member of the Helmholtz Association HGF, for the provision of experimental facilities. Parts of this research were carried out at PETRA III using Beamlines P04 and P22. Beamtime was allocated for proposals I-20190542, I-20190474, and I-20210450. Funding for the photoemission spectroscopy instruments at P04 and P22 by the German Federal Ministry of Education and Research (BMBF) under the framework program ErUM is gratefully acknowledged. The TEM/EELS measurements were afforded by funding from the European Union Horizon 2020 research and innovation program under grant agreement No. 823717—ESTEEM3. Further, G.K. is thankful for a fellowship from the Alexander von Humboldt foundation.

Open access funding enabled and organized by Projekt DEAL.

Conflict of Interest

The authors declare no conflict of interest.

Data Availability Statement

The data that support the findings of this study are available from the corresponding author upon reasonable request.

Keywords

analog memristive devices, electron traps, hard X-ray photoelectron spectroscopy, HfO_2 , in situ photoelectron spectroscopy, memristive switching mechanisms, resistive switching

Received: November 11, 2022

Revised: February 6, 2023

Published online:

- [1] J. Backus, *Commun. ACM* **1978**, 21, 613.
- [2] M. Horowitz, in *2014 IEEE International Solid-State Circuits Conference Digest of Technical Papers (ISSCC)*, IEEE, Piscataway, NJ **2014**, pp. 10–14.
- [3] Q. Xia, J. J. Yang, *Nat. Mater.* **2019**, 18, 309.
- [4] C. Mead, *Proc. IEEE* **1990**, 78, 1629.
- [5] I. Chakraborty, A. Jaiswal, A. K. Saha, S. K. Gupta, K. Roy, *Appl. Phys. Rev.* **2020**, 7, 021308.
- [6] J. D. Kendall, S. Kumar, *Appl. Phys. Rev.* **2020**, 7, 011305.
- [7] D. V. Christensen, R. Dittmann, B. Linares-Barranco, A. Sebastian, M. L. Gallo, A. Redaelli, S. Slesazek, T. Mikolajick, S. Spiga, S. Menzel, I. Valov, G. Milano, C. Ricciardi, S.-J. Liang, F. Miao, M. Lanza, T. J. Quill, S. T. Keene, A. Salleo, J. Grollier, D. Marković, A. Mizrahi, P. Yao, J. J. Yang, G. Indiveri, J. P. Strachan, S. Datta, E. Vianello, A. Valentian, J. Feldmann, et al., *Neuromorph. Comput. Eng.* **2022**, 2, 022501.
- [8] G. Indiveri, S.-C. Liu, *Proc. IEEE* **2015**, 103, 1379.

- [9] E. Chicca, F. Stefanini, C. Bartolozzi, G. Indiveri, *Proc. IEEE* **2014**, 102, 1367.
- [10] G. W. Burr, R. M. Shelby, A. Sebastian, S. Kim, S. Kim, S. Sidler, K. Virwani, M. Ishii, P. Narayanan, A. Fumarola, L. L. Sanches, I. Boybat, M. Le Gallo, K. Moon, J. Woo, H. Hwang, Y. Leblebici, *Adv. Phys.: X* **2017**, 2, 89.
- [11] M. Ziegler, C. Wenger, E. Chicca, H. Kohlstedt, *J. Appl. Phys.* **2018**, 124, 152003.
- [12] M. Zhao, B. Gao, J. Tang, H. Qian, H. Wu, *Appl. Phys. Rev.* **2020**, 7, 011301.
- [13] R. Dittmann, S. Menzel, R. Waser, *Adv. Phys.* **2021**, 70, 155.
- [14] E. Chicca, G. Indiveri, *Appl. Phys. Lett.* **2020**, 116, 120501.
- [15] S. H. Jo, T. Chang, I. Ebong, B. B. Bhadviya, P. Mazumder, W. Lu, *Nano Lett.* **2010**, 10, 1297.
- [16] T. Ohno, T. Hasegawa, T. Tsuruoka, K. Terabe, J. K. Gimzewski, M. Aono, *Nat. Mater.* **2011**, 10, 591.
- [17] K. Seo, I. Kim, S. Jung, M. Jo, S. Park, J. Park, J. Shin, K. P. Biju, J. Kong, K. Lee, B. Lee, H. Hwang, *Nanotechnology* **2011**, 22, 254023.
- [18] M. Hansen, M. Ziegler, H. Kohlstedt, in *2016 IEEE International Conference on Rebooting Computing (ICRC)*, IEEE, Piscataway, NJ **2016**, pp 1–8.
- [19] M. Hansen, F. Zahari, M. Ziegler, H. Kohlstedt, *Front. Neurosci.* **2017**, 11, 1.
- [20] X. Yan, Y. Pei, H. Chen, J. Zhao, Z. Zhou, H. Wang, L. Zhang, J. Wang, X. Li, C. Qin, G. Wang, Z. Xiao, Q. Zhao, K. Wang, H. Li, D. Ren, Q. Liu, H. Zhou, J. Chen, P. Zhou, *Adv. Mater.* **2019**, 31, 1805284.
- [21] X. Yan, K. Wang, J. Zhao, Z. Zhou, H. Wang, J. Wang, L. Zhang, X. Li, Z. Xiao, Q. Zhao, Y. Pei, G. Wang, C. Qin, H. Li, J. Lou, Q. Liu, P. Zhou, *Small* **2019**, 15, 1900107.
- [22] S. Park, S. Klett, T. Ivanov, A. Knauer, J. Doell, M. Ziegler, *Front. Nanotechnol.* **2021**, 3, 16.
- [23] D. B. Strukov, G. S. Snider, D. R. Stewart, R. S. Williams, *Nature* **2008**, 453, 80.
- [24] D. Ielmini, R. Waser, *Resistive Switching: From Fundamentals of Nanoionic Redox Processes to Memristive Device Applications*, Wiley-VCH, Weinheim **2016**.
- [25] A. Sawa, *Mater. Today* **2008**, 11, 28.
- [26] H. Bian, Y. Y. Goh, Y. Liu, H. Ling, L. Xie, X. Liu, *Adv. Mater.* **2021**, 33, 2006469.
- [27] A. Sawa, T. Fujii, M. Kawasaki, Y. Tokura, *Appl. Phys. Lett.* **2004**, 85, 4073.
- [28] D.-j. Seong, M. Jo, D. Lee, H. Hwang, *Electrochem. Solid-State Lett.* **2007**, 10, H168.
- [29] S. Park, S. Jung, M. Siddik, M. Jo, J. Park, S. Kim, W. Lee, J. Shin, D. Lee, G. Choi, J. Woo, E. Cha, B. H. Lee, H. Hwang, *Phys. Status Solidi RRL* **2012**, 6, 454.
- [30] E. Mikheev, B. D. Hoskins, D. B. Strukov, S. Stemmer, *Nat. Commun.* **2014**, 5, 3990.
- [31] C.-W. Hsu, Y.-F. Wang, C.-C. Wan, I.-T. Wang, C.-T. Chou, W.-L. Lai, Y.-J. Lee, T.-H. Hou, *Nanotechnology* **2014**, 25, 165202.
- [32] T. You, N. Du, S. Slesazek, T. Mikolajick, G. Li, D. Bürger, I. Skorupa, H. Stöcker, B. Abendroth, A. Beyer, K. Volz, O. G. Schmidt, H. Schmidt, *ACS Appl. Mater. Interfaces* **2014**, 6, 19758.
- [33] M. Hansen, M. Ziegler, L. Kolberg, R. Soni, S. Dirkmann, T. Mussenbrock, H. Kohlstedt, *Sci. Rep.* **2015**, 5, 13753.
- [34] Z. Fan, H. Fan, L. Yang, P. Li, Z. Lu, G. Tian, Z. Huang, Z. Li, J. Yao, Q. Luo, C. Chen, D. Chen, Z. Yan, M. Zeng, X. Lu, X. Gao, J.-M. Liu, *J. Mater. Chem. C* **2017**, 5, 7317.
- [35] N. Du, N. Manjunath, Y. Li, S. Menzel, E. Linn, R. Waser, T. You, D. Bürger, I. Skorupa, D. Walczyk, C. Walczyk, O. G. Schmidt, H. Schmidt, *Phys. Rev. Appl.* **2018**, 10, 054025.
- [36] S. Gao, G. Liu, H. Yang, C. Hu, Q. Chen, G. Gong, W. Xue, X. Yi, J. Shang, R.-W. Li, *ACS Nano* **2019**, 13, 2634.
- [37] T. D. Dongale, G. U. Kamble, D. Y. Kang, S. S. Kundale, H.-M. An, T. G. Kim, *Phys. Status Solidi* **2021**, 15, 2100199.
- [38] D. Walczyk, C. Walczyk, T. Schroeder, T. Bertaud, M. Sowińska, M. Lukosius, M. Fräschke, B. Tillack, C. Wenger, *Microelectron. Eng.* **2011**, 88, 1133.
- [39] M. K. Mahadevaiah, E. Perez, C. Wenger, A. Grossi, C. Zambelli, P. Olivo, F. Zahari, H. Kohlstedt, M. Ziegler, in *2019 IEEE International Reliability Physics Symposium (IRPS)*, IEEE, Piscataway, NJ **2019**, pp. 1–4.
- [40] D. Kim, J. H. Park, D. S. Jeon, T. D. Dongale, T. G. Kim, *J. Alloys Compd.* **2021**, 854, 157261.
- [41] M. Hansen, F. Zahari, H. Kohlstedt, M. Ziegler, *Sci. Rep.* **2018**, 8, 8914.
- [42] S. Choi, Y. Kim, T. V. Nguyen, W. H. Jeong, K.-S. Min, B. J. Choi, *Adv. Electron. Mater.* **2021**, 7, 2100050.
- [43] K. M. Kim, J. Zhang, C. Graves, J. J. Yang, B. J. Choi, C. S. Hwang, Z. Li, R. S. Williams, *Nano Lett.* **2016**, 16, 6724.
- [44] Y. Yang, R. Huang, *Nat. Electron.* **2018**, 1, 274.
- [45] F. Hofer, F. P. Schmidt, W. Grogger, G. Kothleitner, *IOP Conf. Ser.: Mater. Sci. Eng.* **2016**, 109, 012007.
- [46] F. A. Stevie, C. L. Donley, *J. Vac. Sci. Technol., A* **2020**, 38, 063204.
- [47] C. Kalha, N. K. Fernando, P. Bhatt, F. O. L. Johansson, A. Lindblad, H. Rensmo, L. Z. Medina, R. Lindblad, S. Siol, L. P. H. Jeurgens, C. Cancellieri, K. Rossnagel, K. Medjanik, G. Schönhense, M. Simon, A. X. Gray, S. Nemšák, P. Lömker, C. Schlueter, A. Regoutz, *J. Phys.: Condens. Matter* **2021**, 33, 233001.
- [48] Y. Lebedinskii, A. Zenkevich, E. P. Gusev, *J. Appl. Phys.* **2007**, 101, 074504.
- [49] C. E. ViolBarbosa, C. Shekhar, B. Yan, S. Ouardi, E. Ikenaga, G. H. Fecher, C. Felser, *Phys. Rev. B* **2013**, 88, 195128.
- [50] T. Bertaud, M. Sowinska, D. Walczyk, S. Thiess, A. Gloskovskii, C. Walczyk, T. Schroeder, *Appl. Phys. Lett.* **2012**, 101, 143501.
- [51] Y. A. Matveyev, A. M. Markeev, Y. Y. Lebedinskii, A. A. Chouprik, K. V. Egorov, W. Drube, A. V. Zenkevich, *Thin Solid Films* **2014**, 563, 20.
- [52] S. U. Sharath, T. Bertaud, J. Kurian, E. Hildebrandt, C. Walczyk, P. Calka, P. Zaumseil, M. Sowinska, D. Walczyk, A. Gloskovskii, T. Schroeder, L. Alff, *Appl. Phys. Lett.* **2014**, 104, 063502.
- [53] A. S. Sokolov, Y.-R. Jeon, S. Kim, B. Ku, D. Lim, H. Han, M. G. Chae, J. Lee, B. G. Ha, C. Choi, *Appl. Surf. Sci.* **2018**, 434, 822.
- [54] G. Niu, P. Calka, P. Huang, S. U. Sharath, S. Petzold, A. Gloskovskii, K. Fröhlich, Y. Zhao, J. Kang, M. A. Schubert, F. Bärwolf, W. Ren, Z.-G. Ye, E. Perez, C. Wenger, L. Alff, T. Schroeder, *Mater. Res. Lett.* **2019**, 7, 117.
- [55] C. Baeumer, T. Heisig, B. Arndt, K. Skaja, F. Borgatti, F. Offi, F. Motti, G. Panaccione, R. Waser, S. Menzel, R. Dittmann, *Faraday Discuss.* **2019**, 213, 215.
- [56] J. H. Yoon, S. J. Song, I.-H. Yoo, J. Y. Seok, K. J. Yoon, D. E. Kwon, T. H. Park, C. S. Hwang, *Adv. Funct. Mater.* **2014**, 24, 5086.
- [57] C. Baeumer, C. Schmitz, A. H. Ramadan, H. Du, K. Skaja, V. Feyer, P. Müller, B. Arndt, C.-L. Jia, J. Mayer, R. A. De Souza, C. Michael Schneider, R. Waser, R. Dittmann, *Nat. Commun.* **2015**, 6, 8610.
- [58] S. Stathopoulos, A. Khiat, M. Trapatseli, S. Cortese, A. Serb, I. Valov, T. Prodromakis, *Sci. Rep.* **2017**, 7, 17532.
- [59] A. Hardtdegen, C. L. Torre, F. Cüppers, S. Menzel, R. Waser, S. Hoffmann-Eifert, *IEEE Trans. Electron Devices* **2018**, 65, 3229.
- [60] J. H. Lee, J. H. Park, T. D. Dongale, T. G. Kim, *J. Alloys Compd.* **2020**, 821, 153247.
- [61] J. H. Sung, J. H. Park, D. S. Jeon, D. Kim, M. J. Yu, A. C. Khot, T. D. Dongale, T. G. Kim, *Mater. Des.* **2021**, 207, 109845.

- [62] Q. Wang, Y. Wang, R. Luo, J. Wang, L. Ji, Z. Jiang, C. Wenger, Z. Song, S. Song, W. Ren, J. Bi, G. Niu, *Neuromorph. Comput. Eng.* **2022**, 2, 044012.
- [63] Y. Kim, Y. J. Kwon, D. E. Kwon, K. J. Yoon, J. H. Yoon, S. Yoo, H. J. Kim, T. H. Park, J.-W. Han, K. M. Kim, C. S. Hwang, *Adv. Mater.* **2018**, 30, 1704320.
- [64] J. Robertson, R. M. Wallace, *Mater. Sci. Eng.: R: Rep.* **2015**, 88, 1.
- [65] H. H. Radamson, H. Zhu, Z. Wu, X. He, H. Lin, J. Liu, J. Xiang, Z. Kong, W. Xiong, J. Li, H. Cui, J. Gao, H. Yang, Y. Du, B. Xu, B. Li, X. Zhao, J. Yu, Y. Dong, G. Wang, *Nanomaterials* **2020**, 10, 1555.
- [66] H.-W. You, W.-J. Cho, *Appl. Phys. Lett.* **2010**, 96, 093506.
- [67] D. Bach, R. Schneider, D. Gerthsen, J. Verbeeck, W. Sigle, *Microsc. Microanal.* **2009**, 15, 505.
- [68] C. Nico, T. Monteiro, M. Graça, *Prog. Mater. Sci.* **2016**, 80, 1.
- [69] S. Sze, K. K. Ng, *Phys. Semicond. Devices*, Wiley, Hoboken, NJ **2006**.
- [70] M. S. Tyagi, in *Metal-Semiconductor Schottky Barrier Junctions and Their Applications* (Ed: B. L. Sharma), Springer US, Boston, MA **1984**, pp. 1–60.
- [71] S. Dirkmann, M. Hansen, M. Ziegler, H. Kohlstedt, T. Mussenbrock, *Sci. Rep.* **2016**, 6, 35686.
- [72] S. Yarragolla, T. Hemke, J. Trieschmann, F. Zahari, H. Kohlstedt, T. Mussenbrock, *J. Appl. Phys.* **2022**, 131, 134304.
- [73] E. Barsoukov, J. R. Macdonald, editors, *Impedance Spectroscopy: Theory, Experiment, and Applications*, 3rd Edition, Wiley, Hoboken, NJ, USA **2018**.
- [74] R. Marquardt, F. Zahari, J. Carstensen, G. Popkairov, O. Gronenberg, G. Kolhatkar, H. Kohlstedt, M. Ziegler, *Adv. Electron. Mater.*, <https://doi.org/10.1002/aelm.202201227>.
- [75] S. Zafar, A. Callegari, E. Gusev, M. V. Fischetti, *J. Appl. Phys.* **2003**, 93, 9298.
- [76] H. Schroeder, V. V. Zhirnov, R. K. Cavin, R. Waser, *J. Appl. Phys.* **2010**, 107, 054517.
- [77] S.-O. Park, H. Jeong, J. Park, J. Bae, S. Choi, *Nat. Commun.* **2022**, 13, 2888.
- [78] S. Ambrogio, P. Narayanan, H. Tsai, R. M. Shelby, I. Boybat, C. di Nolfo, S. Sidler, M. Giordano, M. Bodini, N. C. P. Farinha, B. Killeen, C. Cheng, Y. Jaoudi, G. W. Burr, *Nature* **2018**, 558, 60.
- [79] E. A. Cartier, W. Kim, N. Gong, T. Gokmen, M. M. Frank, D. M. Bishop, Y. Kim, S. Kim, T. Ando, E. Y. Wu, P. Adusumilli, J. Rozen, P. M. Solomon, W. Haensch, M. J. BrightSky, A. Sebastian, G. W. Burr, V. Narayanan, in *2019 IEEE International Reliability Physics Symposium (IRPS)*, IEEE, Piscataway **2019**, pp. 1–10.
- [80] J. Strobel, M. Hansen, S. Dirkmann, K. K. Neelisetty, M. Ziegler, G. Haberfehlner, R. Popescu, G. Kothleitner, V. S. K. Chakravadhanula, C. Kübel, H. Kohlstedt, T. Mussenbrock, L. Kienle, *J. Appl. Phys.* **2017**, 121, 245307.
- [81] S. U. Sharath, S. Vogel, L. Molina-Luna, E. Hildebrandt, C. Wenger, J. Kurian, M. Duerrschabel, T. Niermann, G. Niu, P. Calka, M. Lehmann, H.-J. Kleebe, T. Schroeder, L. Alff, *Adv. Funct. Mater.* **2017**, 27, 1700432.
- [82] S. Fritz, A. Seiler, L. Radtke, R. Schneider, M. Weides, G. Weiß, D. Gerthsen, *Sci. Rep.* **2018**, 8, 1.
- [83] J. H. Jang, H.-S. Jung, J. H. Kim, S. Y. Lee, C. S. Hwang, M. Kim, *J. Appl. Phys.* **2011**, 109, 023718.
- [84] D. Bouchet, C. Colliex, *Ultramicroscopy* **2003**, 96, 139.
- [85] T. Imamura, S. Hasuo, *Appl. Phys. Lett.* **1991**, 58, 645.
- [86] X. Kang, L. Ying, H. Wang, G. Zhang, W. Peng, X. Kong, X. Xie, Z. Wang, *Phys. C* **2014**, 503, 29.
- [87] N. Jiang, J. C. H. Spence, *Ultramicroscopy* **2006**, 106, 215.
- [88] H. O. Ayoola, C.-H. Li, S. D. House, C. S. Bonifacio, K. Kisslinger, J. Jinschek, W. A. Saidi, J. C. Yang, *Ultramicroscopy* **2020**, 219, 113127.
- [89] C. Guedj, L. Hung, A. Zobelli, P. Blaise, F. Sottile, V. Olevano, *Appl. Phys. Lett.* **2014**, 105, 222904.
- [90] C. Li, Y. Yao, X. Shen, Y. Wang, J. Li, C. Gu, R. Yu, Q. Liu, M. Liu, *Nano Res.* **2015**, 8, 3571.
- [91] K. Lee, K. Park, H.-J. Lee, M. S. Song, K. C. Lee, J. Namkung, J. H. Lee, J. Park, S. C. Chae, *Sci. Rep.* **2021**, 11, 6290.
- [92] J. Viehhaus, F. Scholz, S. Deinert, L. Glaser, M. Ilchen, J. Seltmann, P. Walter, F. Siewert, *Nucl. Instrum. Methods Phys. Res., Sect. A* **2013**, 710, 151.
- [93] C. Schlueter, A. Gloskovskii, K. Ederer, I. Schostak, S. Piec, I. Sarkar, Y. Matveyev, P. Lömker, M. Sing, R. Claessen, C. Wiemann, C. M. Schneider, K. Medjanik, G. Schönhense, P. Amann, A. Nilsson, W. Drube, *AIP Conf. Proc.* **2019**, 2054, 040010.
- [94] S. Tanuma, C. J. Powell, D. R. Penn, *Surf. Interface Anal.* **2011**, 43, 689.
- [95] C. J. Powell, *J. Vac. Sci. Technol., A* **2020**, 38, 023209.
- [96] C. Morant, L. Galán, J. M. Sanz, *Surf. Interface Anal.* **1990**, 16, 304.
- [97] V. Kruchinin, V. Aliev, T. Perevalov, D. Islamov, V. Gritsenko, I. Prosvirin, C. Cheng, A. Chin, *Microelectron. Eng.* **2015**, 147, 165.
- [98] S. Kim, S. Woo, H. Kim, I. Kim, K. Lee, W. Jeong, T. P. a. H. Jeon, *J. Korean Phys. Soc.* **2008**, 52, 1103.
- [99] Y. Matveyev, A. Zenkevich, Y. Lebedinskii, S. Thiess, W. Drube, *Microelectron. Eng.* **2011**, 88, 1353.
- [100] Y. Abe, N. Miyata, E. Ikenaga, H. Suzuki, K. Kitamura, S. Igarashi, H. Nohira, *Jpn. J. Appl. Phys.* **2009**, 48, 041201.
- [101] T. Szyjka, L. Baumgarten, T. Mittmann, Y. Matveyev, C. Schlueter, T. Mikolajick, U. Schroeder, M. Müller, *ACS Appl. Electron. Mater.* **2020**.
- [102] C. Küneth, R. Batra, G. A. Rossetti, R. Ramprasad, A. Kersch, in *Ferroelectricity in Doped Hafnium Oxide: Materials, Properties and Devices*, Elsevier, New York **2019**, pp. 245–289.
- [103] A. G. Shard, *J. Vac. Sci. Technol., A* **2020**, 38, 041201.
- [104] E. Kröger, A. Petrar, A. Quer, R. Soni, M. Kalläne, N. A. Pertsev, H. Kohlstedt, K. Rossnagel, *Phys. Rev. B* **2016**, 93, 235415.
- [105] Y. Matveyev, D. Negrov, A. Chernikova, Y. Lebedinskii, R. Kirtaev, S. Zarubin, E. Suvorova, A. Gloskovskii, A. Zenkevich, *ACS Appl. Mater. Interfaces* **2017**, 9, 43370.
- [106] M. K. Mendes, E. Martinez, J. M. Ablett, M. Veillerot, R. Gassilloud, M. Bernard, O. Renault, J. P. Rueff, N. Barrett, *Sci. Rep.* **2018**, 8, 1.
- [107] V. Solokha, T.-L. Lee, A. Wilson, K. Hingerl, J. Zegenhagen, *J. Electron Spectrosc. Relat. Phenom.* **2018**, 225, 28.
- [108] A. Beni, N. Ott, M. Pawelkiewicz, M. Wardé, K. Young, B. Bauer, P. Rajput, B. Detlefs, J. Zegenhagen, R. McGrath, M.-G. Barthés-Labrousse, L. P. H. Jeurgens, P. Schmutz, *Electrochem. Commun.* **2014**, 46, 13.
- [109] A. Shetty, B. Roul, S. Mukundan, L. Mohan, G. Chandan, K. J. Vinoy, S. B. Krupanidhi, *AIP Adv.* **2015**, 5, 097103.
- [110] S. Petzold, E. Miranda, S. U. Sharath, J. Muñoz-Gorri, T. Vogel, E. Piro, N. Kaiser, R. Eilhardt, A. Zintler, L. Molina-Luna, J. Suñé, L. Alff, *J. Appl. Phys.* **2019**, 125, 234503.
- [111] P. Broqvist, A. Pasquarello, *Appl. Phys. Lett.* **2006**, 89, 262904.
- [112] H. Kawano, *Prog. Surf. Sci.* **2022**, 97, 100583.
- [113] X. Wang, K. Han, W. Wang, X. Ma, D. Chen, J. Zhang, J. Du, Y. Xiong, A. Huang, *Appl. Phys. Lett.* **2010**, 97, 062901.
- [114] A. Winzer, N. Szabó, J. Ocker, R. Hentschel, M. Schuster, F. Schubert, J. Gärtner, A. Wachowiak, T. Mikolajick, *J. Appl. Phys.* **2015**, 118, 124106.
- [115] K. P. McKenna, *Modelling Simul. Mater. Sci. Eng.* **2014**, 22, 025001.
- [116] X. Wang, K. Han, W. Wang, J. Xiang, H. Yang, J. Zhang, X. Ma, C. Zhao, D. Chen, T. Ye, *Appl. Phys. Lett.* **2012**, 100, 122907.
- [117] T. Grassler, *Microelectron. Reliab.* **2012**, 52, 39.
- [118] C. Lenser, A. Köhl, M. Patt, C. M. Schneider, R. Waser, R. Dittmann, *Phys. Rev. B* **2014**, 90, 115312.
- [119] A. de Sa, C. Rangel, P. Skeldon, G. Thompson, *Port. Electrochim. Acta* **2006**, 24, 305.

- [120] A. J. Bard, L. R. Faulkner, *Electrochem. Methods: Fundam. Appl.*, 2nd edition, Wiley, New York **2001**.
- [121] F. Zahari, F. Schlichting, J. Strobel, S. Dirkmann, J. Cipo, S. Gauter, J. Trieschmann, R. Marquardt, G. Haberehner, G. Kothleitner, L. Kienle, T. Mussenbrock, M. Ziegler, H. Kersten, H. Kohlstedt, *J. Vac. Sci. Technol., B* **2019**, 37, 061203.
- [122] J.-Y. Kwon, T.-S. Yoon, K.-B. Kim, S.-H. Min, *J. Appl. Phys.* **2003**, 93, 3270.
- [123] M. Schmid, H.-P. Steinrück, J. M. Gottfried, *Surf. Interface Anal.* **2014**, 46, 505.
- [124] D. A. Shirley, *Phys. Rev. B* **1972**, 5, 4709.
- [125] J. Leiro, E. Minni, E. Suoninen, *J. Phys. F: Met. Phys.* **1983**, 13, 215.
- [126] P. H. Citrin, G. K. Wertheim, Y. Baer, *Phys. Rev. Lett.* **1978**, 41, 1425.
- [127] H. Tsai, E. Hu, K. Perng, M. Chen, J.-C. Wu, Y.-S. Chang, *Surf. Sci.* **2003**, 537, L447.

V. Impedance Spectroscopy on Hafnium Oxide-Based Memristive Devices

Bibliographic Information

Marquardt, R., Zahari, F., Carstensen, J., Popkirov, G., Gronenberg, O., Kolhatkar, G., Kohlstedt, H., Ziegler, M., Impedance Spectroscopy on Hafnium Oxide-Based Memristive Devices. Adv. Electron. Mater. 2023, 0, 2201227. <https://doi.org/10.1002/aelm.202201227>

Author's contribution

The author contributed to:

- Partial construction of the measurement setup
- Electrical Measurements
- Evaluation of the data
- Development of the physical model
- Writing of the manuscript

Copyright Notice

This work is licensed under a Creative Commons Attribution 4.0 International License (CC BY 4.0). Read the licence text:

<https://creativecommons.org/licenses/by/4.0/legalcode>.

V.1 Summary

As well as the afore-presented companion paper, this work investigates an interface-based memristive device consisting of the layer sequence Nb/NbO_x/Al₂O₃/HfO₂/Au. The device exhibits promising electronic properties suitable for neuromorphic applications, characterized by a high I-V non-linearity, facilitating integration into passive crossbar arrays. Switching from a high-resistance state (HRS) to a low-resistance state (LRS) is achieved by applying a positive voltage to the top electrode.

The devices consist of a semiconducting partially oxidized Nb back electrode (NbO_x, approximately 5 nm thick) and an Al₂O₃ layer with varying thickness and nano-scale roughness at the interface with NbO_x. Spectral analysis of ImpSpec measurements reveals a single half circuit in the EC. A simplified Randle's circuit adequately represents the EC, with the two parallel elements significantly affected by the applied DC voltage. The current transport mechanism is attributed to thermionic emission, which presupposes the existence of a SCR. An analysis of the capacitance indicates a superposition of an insulator capacitance together with an SCR capacitance which is influenced by surface states. Changing the resistive state does not require altering the EC but involves a quantitative change in the physical process of charge carrier transport. This change in the barrier height and ideality factor is associated with variations in the SCR, leading to changes in the resistive state. The change in the ideality factor of the thermionic emission theory is found to be mirrored in the dimensionless capacitance factor. Temperature measurements show an increase in the ideality factor with increasing temperature, as well as a valid fit for the Richardson constant, further supporting the assumption of a dominant thermionic emission process.

Resistive switching occurs for voltages above 1V after a 30-second measurement interval, while voltages above 2V exhibit an "inductive hook." This behavior might be explained by a slow process that gradually reduces resistance over time. Transient analysis is employed to extract more information about the switching process, revealing the presence of two time constants represented by a bi-exponential function. Similarly, two time constants for the retention of the memristive state can be determined. Based on the indications of surface states found in the capacitance data, the time constants found are fitted with the Shockley-Read-Hall model. A single electron trap depth of approximately 0.89 eV, matching the measured depth of VO²⁺, can thus be determined for all time constants, which exhibit multiple time constants. Additionally, it is suggested that interface traps with smaller capture cross-sections are responsible for long-time memory, while bulk traps are responsible for short-time memory.

Finally, a physical model indicating the charging and discharging of electron trap states as the main resistive switching mechanism is proposed. Electronic traps located in the HfO_2 layer (caused by VO) can change their charge state, which modulates the space charge region of the semiconducting NbO_x and thus affects the overall resistance of the device.

RESEARCH ARTICLE

Impedance Spectroscopy on Hafnium Oxide-Based Memristive Devices

Richard Marquardt,* Finn Zahari, Jürgen Carstensen, George Popkirov, Ole Gronenberg, Gitanjali Kolhatkar, Hermann Kohlstedt,* and Martin Ziegler

Memristive devices for neuromorphic computing have been attracting ever growing attention over the last couple of years. In neuromorphic electronics, memristive devices with multi-level resistance states are required to accurately reproduce synaptic weights. Here, a memristive device based on a multilayer oxide system (Nb/NbO_x/Al₂O₃/HfO₂/Au), which features a filamentary-free, homogenous interfacial resistive switching mechanism, is investigated. To gain a deeper insight into the switching mechanism, impedance spectroscopy (ImpSpec), X-ray photoelectron spectroscopy (XPS), and transmission electron microscopy (TEM) are exploited. While this work focuses on the analysis of impedance and current-voltage characteristics, XPS and TEM investigations can be found in a companion paper (Zahari et al.). In the course of this investigation, potentiodynamic impedance spectroscopy (PD-ImpSpec) and time resolved impedance spectroscopy (TR-ImpSpec) in combination with transient analysis are used. Evidence is presented of switching kinetics at voltages above 2.1 V directly related to changes in Schottky barrier resistance. These switching kinetics can in turn be interpreted by the charging and discharging of double positively charged oxygen vacancies $V_O^{2+} \approx 0.9$ eV. The results of the impedance analysis are translated into a more general model for memristive devices to map the physical processes during switching.

1. Introduction

Memristive devices have been attracting considerable interest for applications in advanced computing architectures, such as in-memory computing or neuromorphic circuits.^[1–4] A memristive device, which is based on resistive switching, typically consists of a metal-insulator-metal capacitor-like structure.^[5] A special feature of memristive devices is that they can display several resistance states which can be adjusted by suitable current or voltage signals.^[6] Although at first glance memristive devices are simple structures, the underlying elementary physical and chemical mechanisms leading to resistive switching are notoriously complicated. Furthermore, the development of highly integrated circuits is challenging as many material systems cannot be technologically integrated into the prevailing silicon technology, while the devices exhibit often high variability.

R. Marquardt, F. Zahari, H. Kohlstedt
 Nanoelectronics, Faculty of Engineering
 Kiel University
 24143 Kiel, Germany
 E-mail: rvm@tf.uni-kiel.de; hko@tf.uni-kiel.de

J. Carstensen
 Chair of Functional Nanomaterials
 Faculty of Engineering
 Kiel University
 24118 Kiel, Germany

G. Popkirov
 Central Laboratory of Solar Energy and New Energy Sources
 Bulgarian Academy of Sciences
 Sofia 1784, Bulgaria

O. Gronenberg
 Synthesis and Real Structure Group
 Faculty of Engineering
 Kiel University
 24118 Kiel, Germany

G. Kolhatkar
 Department of Engineering Physics
 McMaster University
 Hamilton, Ontario L8S 4L7, Canada

H. Kohlstedt
 Kiel Nano, Surface and Interface Science KiNSIS
 Kiel University
 24118 Kiel, Germany

M. Ziegler
 Micro- and Nanoelectronic Systems
 Electrical Engineering and Information Technology
 Ilmenau University of Technology
 98693 Ilmenau, Germany

M. Ziegler
 Institute of Micro and Nanotechnologies MacroNano
 Technische Universität Ilmenau
 98693 Ilmenau, Germany

 The ORCID identification number(s) for the author(s) of this article can be found under <https://doi.org/10.1002/aelm.202201227>.

© 2023 The Authors. Advanced Electronic Materials published by Wiley-VCH GmbH. This is an open access article under the terms of the Creative Commons Attribution License, which permits use, distribution and reproduction in any medium, provided the original work is properly cited.

DOI: 10.1002/aelm.202201227

To overcome these hurdles, a deep and detailed understanding of the underlying resistive switching effects is mandatory for the fabrication and integration of memristive devices in electronic systems.

Impedance spectroscopy (ImpSpec) has proven to be a powerful electrical diagnostic tool to analyze the origin of resistive switching due to its potential for probing the dynamics of trapped and mobile charges in both bulk and interfacial regions.^[7] As a result, it is possible to collect pertinent information about redox processes, defect structures, and barrier properties related to resistive switching by ImpSpec.^[8–13]

While ImpSpec can provide insight regarding carrier transport mechanisms, the interpretation of impedance data remains challenging, particularly in oxide-based memristive devices due to time-dependent resistance reduction which is often seen as positive impedance phase shifts.^[11] In these devices, the resistance change is usually attributed to the displacement of oxygen vacancies^[14,15] or charging and discharging of traps,^[16–18] and several equivalent circuits^[13] have been proposed. Interpretations for positive impedance phase shifts vary, ranging from inductance^[9] to negative RC-elements.^[19] To correctly interpret a system's ImpSpec response and identify the dominating physical mechanism, an equivalent circuit (EC) diagram that accurately represents such a device is mandatory. A thorough understanding of the physical processes behind the switching mechanisms is important as it will allow for the efficient tuning of memristive devices.

This study aims to develop a realistic EC diagram for the hafnium oxide-based memristive devices. Starting from a simplified Randles circuit,^[20] the model is extended and a complex EC diagram tailored to the memristive device is proposed. While potentiodynamic ImpSpec (PD-ImpSpec) is employed to characterize current transport dynamics for different switching states, time resolved ImpSpec (TR-ImpSpec) is used to access slower time constants that are outside the used frequency spectrum via transient analyses in the time domain. In this context, a positive phase shift, also called “inductive” behavior, is discussed.

In particular, we aim to better understand the complex physics of Nb/NbO_x/Al₂O₃/HfO₂/Au memristive devices, which show a filament-free interface-type, analog resistive switching, a high current–voltage (*I*–*V*) non-linearity, and a low power consumption, comparable to other oxide multi-layer devices.^[16,18,21,22] In particular, devices based on a similar material stack but with NbO_y instead of HfO₂ were reported in the past.^[18,21] The analog switching dynamics and the possibility to emulate the functionality of biological synapses were investigated in detail on the device level,^[22] and the integration into passive crossbar-arrays together with an experimental realization of a bio-inspired learning scheme has already been shown.^[23] Furthermore, the switching process was modeled with kinetic Monte Carlo simulations^[24] and the device-to-device and cycle-to-cycle variability was modeled with a cloud-in-a-cell (CIC) scheme.^[25] The correspondence between the memristive behavior of those oxide multi-layer devices can be concluded from the area-dependent switching (Figure 2b in Zahari et al.^[26]), the diode-like *I*–*V* characteristics, a high device resistance (even in the low resistive state (LRS)), and the analog switching process.

For homogeneous switching devices, the *I* – *V* behavior and the switching mechanism have been attributed to various causes. First, a distinction is made between the existence of one or more potential barriers and their interaction with charge carrier flow.^[14,16,27,28] Second, the diffusion of ions and the change of the charge state of electron traps are discussed as the cause of the memristive effect.^[16,17,27,29,30] In this work, clear evidence of the existence of a single potential barrier and the charging and discharging of electron traps as the origin of the memristive effect is presented for the discussed device.

Since multiple spectroscopy characterizations are required for a comprehensive memristive device analysis, as suggested by Yang et al.,^[31] the X-ray photoelectron spectroscopy (XPS) and electron energy loss spectroscopy (EELS) in the transmission electron microscopy (TEM) are results presented in detail in the companion paper Zahari et al.^[26] While only a brief summary is given here, the results of the companion paper will be discussed in more detail in comparison to the ImpSpec data in the course of this work. EELS analyses by Zahari et al.^[26] show a NbO_x oxidation state from a mixture of Nb₂O₅ and NbO₂ with decreasing oxygen content toward the bottom electrode. Using the hard X-ray photoelectron spectroscopy (HAXPES) data, a space charge region (SCR) in the HfO₂ and Al₂O₃ can be excluded. In addition, core level shifts, which are dependent on the memristive state of the device, indicate charge and discharge of electron traps as a memristive mechanism. No evidence of ionic drifts is found in the HAXPES data.

2. Material and Methods

2.1. Electrical Measurements

This work aimed to carry out transient analyses of individual impedance parameters during the switching process of the memristive devices. A homemade impedance spectrometer based on the fast Fourier transform (FFT) of time-domain data was used to obtain the complete impedance spectrum over all excitation frequencies in a very short time interval, instead of the commonly used frequency response analysis (FRA). As sketched in **Figure 1**, a multi sine perturbation signal was applied to the sample as perturbation voltage. Both the applied voltage perturbation and the current response of the sample were simultaneously recorded and subsequently transformed into the frequency domain by FFT. This allows the individual Fourier components to be determined and the impedance of the sample to be calculated.^[32] The impedance data experimentally obtained were validated by comparing the response spectrum to the perturbation spectrum.^[33,34] An adjustable bias voltage V_{bias} in the range of –5 to +5 V could additionally be applied and the respective DC was measured. The sample holder was temperature-controlled in the range from –5 to 80 °C. The FFT-impedance spectrometer was designed and built by one of the authors in our laboratory. A schematic of the experimental setup can be seen in Figure 1. The perturbation signal used for all measurements in the stationary voltage region had an amplitude of 55 mV, and the frequency range was from 600 mHz to 20 kHz. Agreement with linear response theory was verified after each

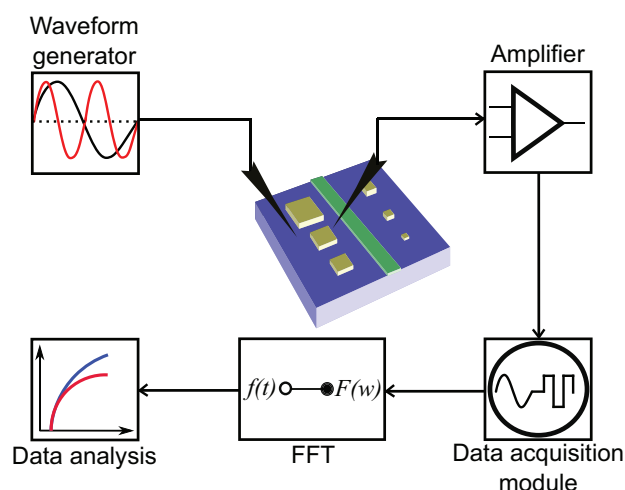


Figure 1. Principle of the ImpSpec setup which uses a preamplifier and a FFT.

measurement. For measurements at a higher voltage bias, or for TR-ImpSpec measurements, a narrower frequency band was used to improve the resolution at lower frequencies (2 Hz - 1 kHz). The design was adapted to the specific properties of particularly highly resistive memristive devices. Two essential requirements had to be taken into account: i) high amplification for the current response (up to 10^9 – 10^{12}); ii) matching the perturbation spectrum to the characteristic slow time constants of the memristive devices. More detailed information on the ImpSpec measurement setup can be found in ref. [31#32] by Popkirov and Schindler.

2.2. Memristive Device

The hafnium oxide-based memristive devices consisted of a partially oxidized (NbO_x (5 nm)) Nb back electrode assumed to be semiconducting (Figure 2a), followed by an insulating double oxide layer (Al_2O_3 (2–7 nm)/ HfO_2 layer (4.5 nm)) and a Au top electrode. Al and Nb layers were deposited by DC magnetron sputtering in an inert Ar plasma, before depositing the HfO_2 layer using an active O_2/Ar plasma. The reactive plasma leads to an oxidation of Al and partly of Nb, as shown in the companion paper (Zahari et al.)^[26] and also for similar devices.^[35] For the Al_2O_3 layer, a varying layer thickness and a roughness in the nano-scale could be observed at the interface with NbO_x (Figure 2a). An explanation of how the roughness at the interface of Al_2O_3 and NbO_x was determined can be found in Supporting Information S1. A detailed analysis of the TEM data can be found in Figure 3 in Zahari et al.^[26]

The device showed a homogeneous area-dependent switching behavior, suggesting a non-filamentary switching mechanism.^[28] Switching from the high resistive state (HRS) to the LRS could be achieved by applying a positive voltage to the top electrode with respect to the bottom electrode and inversely for switching back to HRS (Figure 2b). An illustration of the I - V characteristics of the memristive device depending on various voltage ramp speeds to switch the device are shown in Figure 2b. The corresponding I - V curves for reading the

resistive state are shown in the inset. It can be seen that the switching dynamics can be manipulated in the millisecond to second range and that the resistive state is reduced by using longer switching periods. A variance in memristive behavior among devices can be taken from Figure 2a in Zahari et al.^[26]

3. Results and Discussion

3.1. Steady-State Analysis by PD-ImpSpec

To obtain information about the electronic transport phenomena, an impedance analysis is performed in a steady-state voltage range where no resistive switching can be induced. Here, the operating point is systematically varied by adjusting V_{bias} (PD-ImpSpec). This allows insight into the voltage dependence of the particular EC elements. For the steady-state case, a single semicircle can be found in the Nyquist graph of the recorded impedance spectra with an offset on the real axis (Figure 3). This hints toward the existence of a single RC—element for the EC for the stationary voltage region. Since

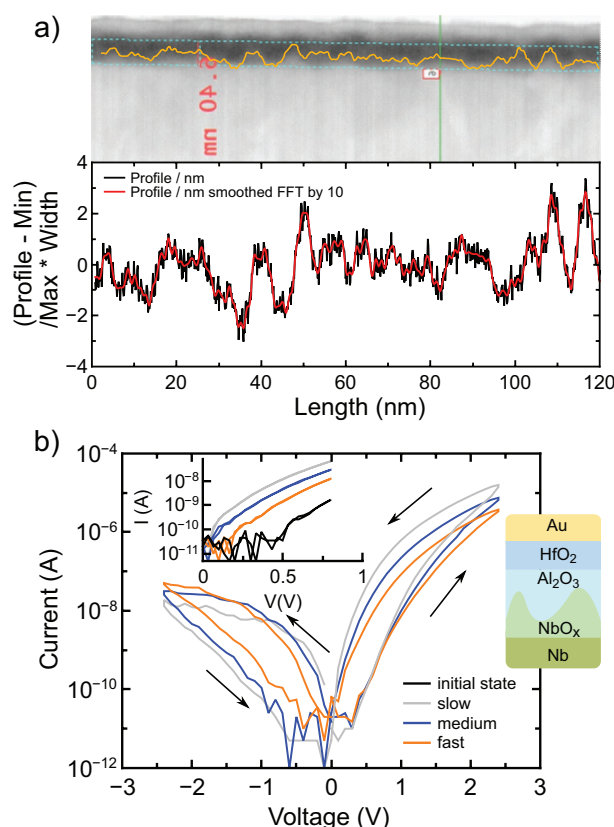


Figure 2. a) STEM image showing the cross section of the device. The roughness at the interface between Al_2O_3 and NbO_x is indicated. The roughness profile was estimated by the intensity of the cross-sectional scan. b) Characteristic I - V curves of a memristive device switching from the HRS to the LRS and back. Voltage ramps at three different speeds: grey—slow—43.6 mV s^{-1} , blue—medium—480 mV s^{-1} , orange—fast—4.8 V s^{-1} . Inset: Read-out I - V characteristics of different resistance states depending on the ramp speed of the switching. A sketch of the layer stack of the memristive device is given on the right side. All measurements were performed on the same device.

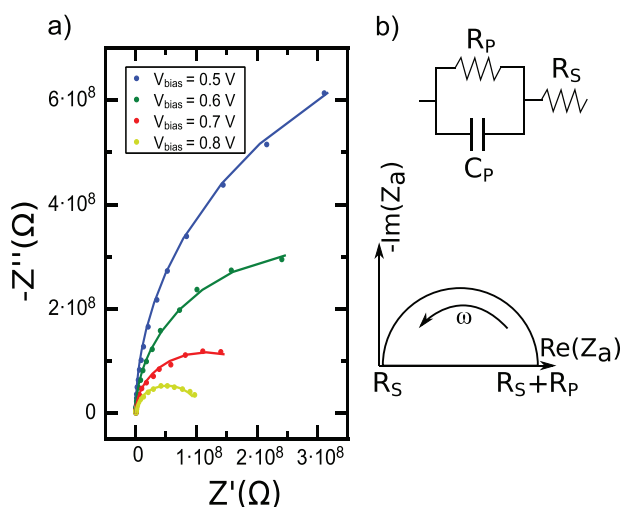


Figure 3. a) Nyquist diagram of the PD-ImpSpec of the memristive device for V_{bias} ranging from 0.5 to 0.8 V. b) Simulated Nyquist graph for the simplified Randles circuit.

the Nyquist curves do not pass through the origin, it can be assumed that the associated EC must be an arrangement of two resistors and one capacitor.

The usual EC, which is most commonly used for such an impedance spectrum, is the simplified Randles circuit^[20] and consists of a serial resistance followed up by an RC element (Figure 3b). The impedance of such a simplified Randles circuit in a Voigt configuration^[7] is described by:

$$Z = R_s + \frac{1}{\frac{1}{R_p} + j\omega C_p} \quad (1)$$

with R_s as serial ohmic component, and R_p and C_p as parallel RC element. A frequent observation in impedance analyses of solid electrolytes is a frequency dispersion, which can be represented by a constant phase element (CPE).^[36] The impedance of such a CPE is described as:

$$Z_{CPE} = \frac{1}{Q(j\omega C)^\phi} \quad (2)$$

where Q is related to the electrode capacitance ($\text{Fs}^{\phi-1} \text{cm}^{-2}$) and ϕ is the constant phase exponent ($0 < \phi < 1$).^[37] A CPE of 1 reduces Equation (2) to the definition of an ideal capacitor. Frequency dispersions are often a result of inhomogeneity, which can originate from both material composition and layer thickness.^[37] Using a CPE instead of a capacitance to fit the presented data results in a phase exponent ϕ of nearly 1 (>0.99). A CPE was therefore not used for the following data fits. Furthermore, a linear area dependence for all fitted EC elements is found (Figure S2, Supporting Information). The simplicity of the physical EC is surprising for such a complex stack of conducting, semiconducting, and insulating layers and suggests current transport is affected by a single barrier. In addition, the accuracy of the fits presented in Figure 3 shows that the proposed EC is an appropriate choice.

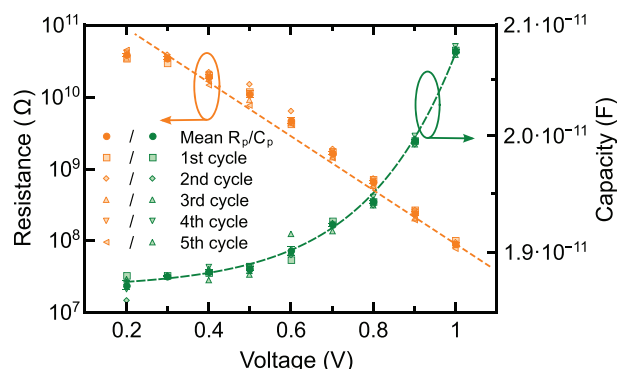


Figure 4. Parameters of the differential RC (R_p , C_p) element of the PD-ImpSpec of the memristive device versus applied V_{bias} . R_p (yellow) is displayed on a semi logarithmic scale on the left axis and C_p (green) is displayed on a linear scale on the right axis. The measurements were performed for five cycles on a single device.

To assign the discrete circuit elements of the EC to physical mechanisms within the memristive device that determine the current transport, it is necessary to take a closer look at functional relations between the elements and the varying parameters. For this purpose, the $R-V$ and $C-V$ curves of the single EC elements provide insight into the nature of the EC elements. In Figure 4, such an analysis is presented for each Randles circuit element in Voigt configuration. The PD-ImpSpec is performed in a bias voltage range from 200 to 1000 mV. Since no voltage dependence can be found for the serial resistance R_s , it can be described as a strictly real non-differential resistor. In addition, a serial resistance of $R_s \approx 12 \text{ k}\Omega$ is determined, about two orders of magnitude larger than the expected lead resistances for the electrode and contact materials. This phenomenon hints at bulk resistances and will be discussed in more detail in a later part of this study. Moreover, a clear voltage dependence can be seen for the serial RC elements R_p and C_p , as depicted in Figure 4. Here, a diode-like characteristic is obtained for the parallel differential resistor R_p . This exponential voltage dependence can be described by the thermionic emission model of a Schottky barrier:^[38,39]

$$I_D = I_S (e^{\frac{qV_D}{nk_B T}} - 1) \quad (3)$$

where k_B is the Boltzmann factor and T is the temperature. The elementary charge q is the reverse current I_S described below, and V_D is the voltage drop across the diode. As most real Schottky diodes show deviations from the ideal thermionic emission, a dimensionless correction factor n is inserted. By fitting the slope of the logarithmic current through the parallel resistor R_p , the ideality factor can be determined according to:

$$n = \frac{q}{k_B T} \frac{dV}{d(\ln I)} \quad (4)$$

The fits of the PD-ImpSpec analysis presented in Figure 4 show a remarkably small deviation from the data, attesting to the accuracy of the mathematical model employed in this study. For the parallel resistor R_p , an ideality factor of 3.71 is

determined, which gives insight into the voltage drop across the depletion region of the diode.

Various explanations for the ideality factor can be found in the literature. One possibility is the partitioning of the current transport into different paths, for example, a superposition of thermionic emission and thermionic-field emission where n describes the partitioning ratio between the different paths.^[40] Assuming a single current transport mechanism associated with a SCR, n can be used to describe the position of the mean generation of charge carriers within the SCR. For $n = 2$, the average generation of charge carriers in the center of the SCR is derived.^[41] Lateral fluctuations in barrier height and inhomogeneities in the depletion layer are possible causes for ideality factors much larger than unity.^[42–46] An alternative cause of an ideality factor greater than 1 may be a superposition of recombination currents via thermionic emission, or the presence of an interfacial layer together with surface states.^[47,48]

The reverse current I_s mentioned in Equation (3) is given by

$$I_s = A^* A T^2 e^{\frac{-\phi_{B,eff} q}{k_B T}} \quad (5)$$

where $\phi_{B,eff}$ is the effective barrier height, A the contact area, and A^* is the Richardson constant (usually approximated with $1.20173 \times 10^6 \text{ Am}^{-2}\text{K}^{-2}$ ^[49]). The occurrence of excess currents indicated by the high ideality factor, whether due to inhomogeneities or superposition of other charge transport processes, impedes accurate barrier height determination. For this reason, the barrier height determined here is referred to as the effective barrier height. Van Otterloo and Gerritsen suggest that the total barrier height $\phi_{B,r}$ can be defined as the product of n and $\phi_{B,eff}$.^[50]

The equation for calculating the effective barrier height can be derived from the reverse current definition in Equation (5):

$$\phi_{B,eff} = -\frac{k_B T}{q} \ln \left(\frac{A^* A T^2}{I_s} \right) \quad (6)$$

For the PD-ImpSpec shown in Figure 4, we find an effective barrier height of 0.84 eV for the HRS of the device. An evaluation of impedance data is more suitable for determining a barrier height than quasi-static $I-V$ curves, since series resistances and other artifacts do not have to be taken into account.

The analysis of the R_p for the steady-state case together with the rectifying behavior of the static $I-V$ curve (Figure 2b) shows a clear indication of the presence of a SCR in the memristive device, which affects the charge carrier flow in the measured voltage range. Operation of the diode in the forward direction when a positive voltage is applied to the top electrode, together with the high gold work function, suggests the formation of an SCR with an n -type semiconductor.

For the $C-V$ analysis of the memristive device, we find that the capacitance increases with V_{bias} , indicating a reduction in the SCR width due to the applied field. However, no typical asymptotic dependence of the measured capacitance is found in the voltage range investigated here which suggests that not all potential charges have been accumulated in the capacitance at this point. Instead, an exponential relationship extended by

a dimensionless divisor between voltage and measured capacitance is found, described as:

$$C_p(V) = C_j(0) + C_i^{\frac{V}{m_c}} \quad (7)$$

with an offset $C_j(0) = 1.92 \cdot 10^{-11} \text{ F}$, the initial capacitance $C_i = 2.66 \cdot 10^{-14} \text{ F}$, and the dimensionless parameter $m_{HRS} = 0.247$ and $m_{LRS} = 0.221$. This observation together with the voltage independence of C_p for negative voltage range implies a superposition of the SCR capacitance with another geometric capacitance. The latter is shown by the added offset, which is additionally influenced by the double oxide layer and arranged parallel to the SCR capacitance. The voltage dependence of the capacitance of an SCR can be expressed by the solution of Poisson's equation for a defined distribution of space charges:

$$-\frac{d^2 \varphi(x)}{dx^2} = \frac{dE(x)}{dx} = \frac{\rho(x)}{\epsilon_0 \epsilon_s} = \frac{qN(x)}{\epsilon_0 \epsilon_s} \quad (8)$$

Here, φ describes the electrostatic potential, E the electric field, ρ the total electric spatial charge density, $N(x)$ the doping concentration, x the position relative to the SCR transition, and ϵ_0 and ϵ_s the permittivity of the vacuum and the relative static permittivity, respectively. A derivation of the solution for an arbitrary doping profile yields:^[51]

$$C_s(V) = \frac{C_j(0)}{(1 - V / v_{bi})^p} \quad (9)$$

where v_{bi} is the built-in potential and p is the grading coefficient of the doping profile. Finally $N(x)$ is given by:

$$N(x) = N_D \left(\frac{x}{d} \right)^{\frac{1}{p-2}} \quad (10)$$

with N_D as donor doping concentration and d as length scale for donors.^[52]

Therefore, in the conventional representation of the SCR capacitance, a plot of the reciprocal of C_p versus applied voltage is used. However, this ideal model assumes a charge distribution in the SCR as described in Equation (10), which is often disturbed by the presence of serial resistors or oxide interlayers between the semiconductor and the metal, which lead to charge reversal phenomena at the interfaces due to surface states.^[53,54] In addition, the high roughness at the interface with Al_2O_3 (Figure 2a) leads to a superposition of both geometric and space charge capacitances. Due to these factors, capacitance–voltage plots often deviate from the given expectation.

A visualization of the arrangement of the capacitors and the other EC elements, which summarizes the findings of this work and the companion paper Zahari et al.^[26] can be seen in Figure 12. This geometric capacitance is largely determined by the Al_2O_3 layer due to its geometry ($d = 2\text{--}7 \text{ nm}$) and permittivity (≈ 9.1) and can be estimated to be $C_{\text{Al}_2\text{O}_3} \approx 1.26 \times 10^{-11} \text{ F}$. A higher capacitance is obtained for the HfO_2 layer ($C_{\text{HfO}_2} \approx 4 \times 10^{-11} \text{ F}$, with $\epsilon_{\text{HfO}_2} = 25$ and

$d_{\text{HfO}_2} = 4.5 \text{ nm}$), suggesting that the capacitance of the Al_2O_3 layer in a series interconnection is dominant. An increased capacitance value compared to the estimated one as well as the parallel arrangement of the capacities can be explained by the roughness at the $\text{NbO}_x/\text{Al}_2\text{O}_3$ interface. Together with the roughness seen in TEM analyses (Figure 2a) and by using spatial averaging,^[55] an excess capacitance of $C_{\text{geo}} \approx 1.6 \times C_{\text{smooth}}$ can be computed. The roughness determined from the cross-sectional TEM analysis may differ from the actual roughness, due to the thickness of the lamella (approximately 30–60 nm). While the capacitances comprised in $C_j(0)$ cannot be accurately deconvoluted, it can be assumed that the largest fraction is given by the Al_2O_3 layer and smaller fractions are due to HfO_2 , the SCR in NbO_x , and possible surface states.

The lack of insight regarding time constants associated with the double oxide layer in this analysis may be due to the spectrum of the signal being limited to 20 kHz. Therefore, it is not possible to resolve smaller time constants (with $R_{\text{ox}} < 10^5 \Omega$, $C_{\text{ox}} \approx 10^{-11} \text{ F} \rightarrow \tau_{\text{ox}} < 100 \text{ ns}$) that would possibly describe the RC elements of the double oxide layer. Since the current flow is dominated by only one barrier, which has already been defined as the Schottky barrier inside the NbO_x , there must be a sufficiently small resistance in the following double oxide layer to limit the current to high field strengths only. From the TEM results (Figure 2a) and the previously mentioned high serial ohmic ratio, we can assume that there is a high spatial density of current paths (shunt resistors) in the oxide double layer (Figure 12).

To further understand the dependence of circuit parameters on the memristive switching mechanisms of the device, steady-state PD-ImpSpec is performed for the HRS and LRS of the device. For this purpose, a positive voltage ramp ($V_{\text{max}} = 3.2 \text{ V}$) is applied to set the device from HRS to LRS between the PD-ImpSpec measurements. For both states, the same symmetry in the Nyquist graphs of the impedance could be observed, revealing that the EC describing the measured data is not affected by changing the state. Thus, the charge carrier transport appears to quantitatively vary due to the change in state but continues to be described qualitatively by the same physical process, which is further confirmed by the accuracy of the fits seen in Figure 5. Both R_p and C_p are significantly affected by switching from HRS to LRS. In particular, a change in R_p of up to two orders of magnitude can be observed for low voltage ranges. Thus, we can conclude that the diode interface is sensitive to the memristive state of the device. The parameters for the HRS and LRS states determined using Equations (4), (6), and (7) and their percentage change between the states are given in Table 1.

For the resistive part of the diode interface, represented by the differential R_p , there is a significant reduction in the effective barrier height of around 17%, and the accompanying increase in n of about 13% which suggests a low variation in total barrier height compared to the effective barrier height. The aforementioned changes lead to the drop in total resistance shown in Figure 5b) on a semi-logarithmic scale for R_p . The increase in total capacity obtained when switching from HRS to LRS, together with the reduction in effective barrier height, can be explained by a reduction in the SCR width. According to the simulations on metal-insulator-semiconductor diodes by Green

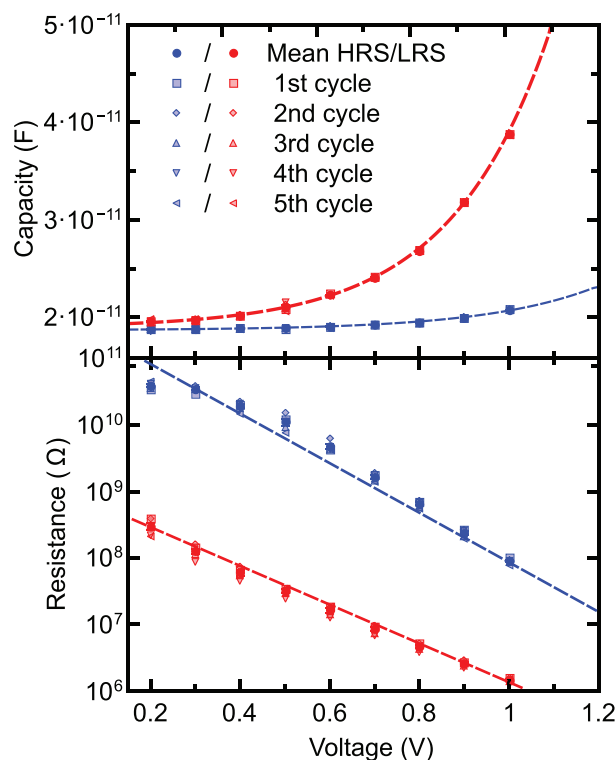


Figure 5. HRS (blue) versus LRS (red) analysis of fitted circuit parameters C_p (a) and R_p (b). C_p is shown on an linear scale in the upper graph and R_p is displayed on an semi logarithmic scale in the lower graph. The measurements were performed for five cycles on a single device.

and Shewchun, the change in the slope of the $C - V$ curves after switching indicates an increase in the amount of surface states at the insulator–semiconductor interface.^[53] The $C - V$ data are again fitted with Equation (7) and the voltage pre-factor m is determined and shown to vary proportionally to the reciprocal of the ideality factor n (Table 1). Since the inhomogeneous voltage drop across the SCR of a diode is defined via the ideality factor, which is often caused by parallel charge carrier transport mechanisms, it is necessary to introduce this parameter when analyzing the diode capacitance.

3.2. Temperature Variation

In addition to the electric field dependence, a temperature change influences most charge carrier transport phenomena. The temperature dependencies of the state-sensitive diode are determined by heating the memristive device while performing

Table 1. Calculated values of $\phi_{B,\text{eff}}$, n , m for HRS and LRS, and percentage variation between both states.

State	$\phi_{B,\text{eff}}$ (eV)	n	m
HRS	0.866 ± 0.013	3.98 ± 0.18	0.247
LRS	0.716 ± 0.007	4.49 ± 0.16	0.221
Change(%)	17.3	12.8	11.7

PD-ImpSpec. Since this device suffers dielectric breakdown under applied bias even for moderate heating, a small temperature range up to 50 °C is chosen.

For this purpose, a temperature variation from 20 up to 50 °C was performed five times in steps of 5 °C and under different voltages V_{bias} . The plot of the logarithmic current flow versus different voltages through the EC element R_p at different temperatures is shown in **Figure 6a**. Fitting the curves with a linear function gives information about the ideality factor and

the reverse bias current of the Schottky-like diode, while the effective barrier height is determined for each temperature using Equation (6).

Figure 6a shows a current increase with temperature, consistent with charge carrier transport by thermionic emission. The parameters determined from these curves show a decrease in the effective barrier height and an increase in the ideality factor with increasing temperature, in accordance with literature.^[56,57] The decrease in effective barrier height with

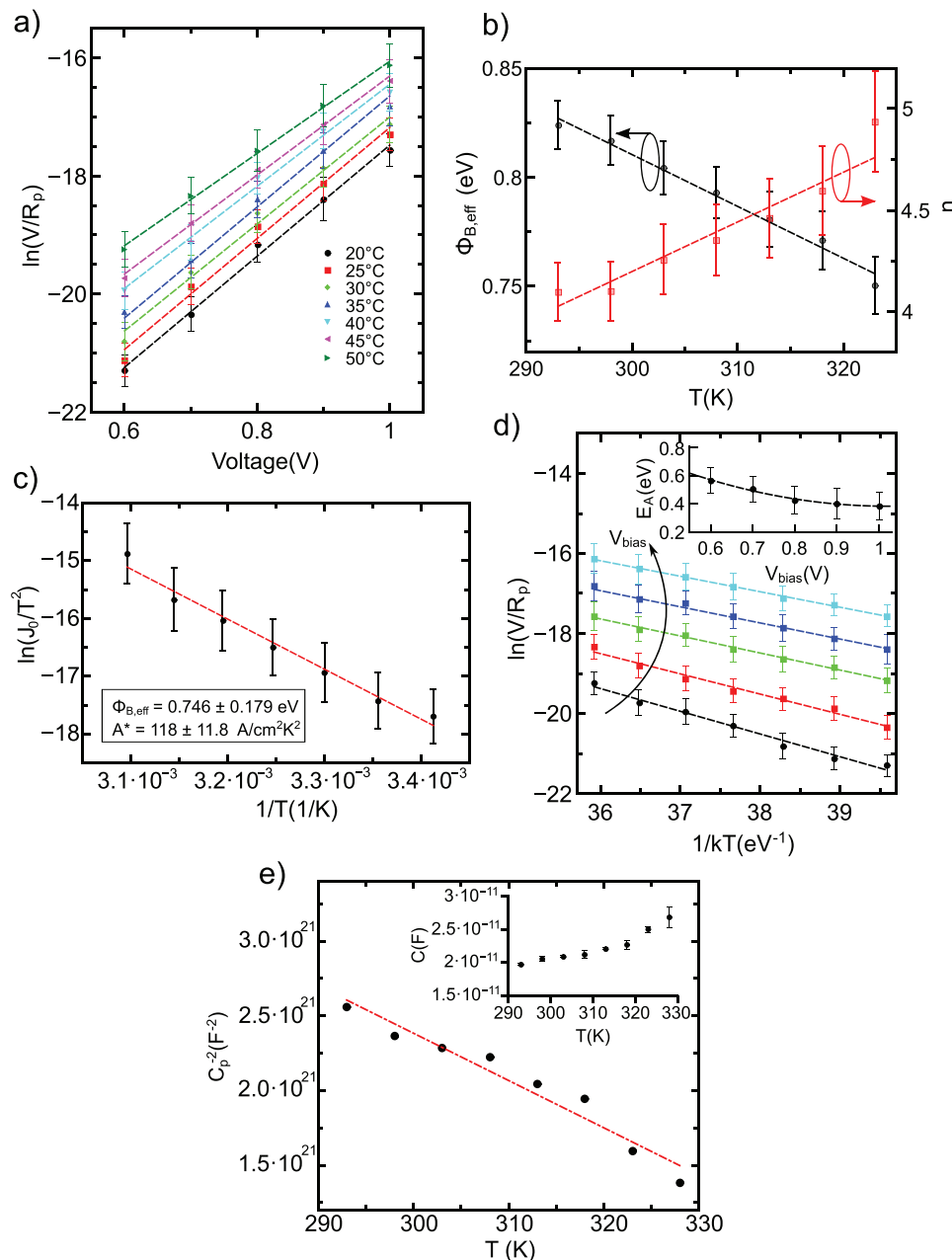


Figure 6. a) Linear plot of the natural logarithm of the current flow through R_p versus the applied voltage V_{bias} at different sample temperatures for the HRS. The temperature measurements were performed five times for one device. b) Barrier height $\phi_{B,eff}$ and ideality factor n of the diode interface extracted from fitted $I-V$ characteristics in Figure 6a versus temperature. c) Richardson plot of the reverse current of V/R_p . d) Current-temperature characteristics of a memristive device at applied voltages V_{bias} between 0.6 and 1 V plotted linearly as the natural logarithm of the current flow through R_p . Inset: Activation energy as a function of V_{bias} . e) Modified Mott plot of C_p^{-2} versus temperature. Inset: Differential parallel capacity as a function of temperature.

increasing temperature can be explained by a change in the band gap E_g .^[58] According to Werner and Güttler,^[59] after linearizing the temperature dependence of E_g , a linear behavior of the Schottky barrier height is obtained:

$$\phi_B(T) = \phi_B(T = 293) + T\alpha_\phi \quad (11)$$

Together with Tersoff's theoretical prediction of the Schottky barrier height,^[60] a reduction of barrier height with increasing temperature with a temperature coefficient

$$\alpha_B(T) = \frac{d\phi_B}{dT} = \frac{dE_g}{2dT} \quad (12)$$

follows. From the linear fit of the effective barrier height as a function of temperature (Figure 6b), the temperature coefficient can be determined using Equations (11) and (6): $\alpha_\phi = 2.38 \pm 0.46 \times 10^{-3}$ eV K⁻¹ for the reduction of the barrier height ($d\phi_B/dT$) and effective barrier height at room temperature $\phi_B(T = 293) = 0.82$ eV.^[61]

TEM images show local inhomogeneity in the barrier (Figure 2a) that most likely causes spatial potential fluctuations and thus leads to an effective barrier increase with temperature.^[42] Yet, this effect seems to be dominated by band narrowing (Varshni shift^[62]), which can be explained by two causes. First, semiconductors show a higher band-narrowing coefficient at temperatures above room temperature, along with a decrease in local inhomogeneities. Second, the presented studies show an unusually high band-narrowing coefficient, which is considerably larger than observed by Sakai et al.^[63]

Since transport mechanisms such as field emission and trap-assisted tunneling strongly depend on the effective barrier height, they become dominating charge transport mechanisms, as illustrated by the increase of the ideality factor with decreasing effective barrier height. Furthermore, at low temperatures, the ideality factor would be expected to approach unity, since superimposed charge carrier transport processes would cancel out.

An effective barrier height of 0.746 eV, determined from the Richardson plot (Figure 6c), is in agreement with the effective barrier height calculated from the $I - V$ data. The estimated Richardson constant of $A^* = 1.18 \times 10^6$ Am⁻² K⁻²^[46,64] is in good agreement with the usually used value 1.20173×10^6 Am⁻² K⁻².^[49] Small deviations from the commonly used value of 1.20173×10^6 Am⁻² K⁻² should not affect the calculations, since the barrier height is not particularly sensitive to a deviation in the Richardson constant (Equation (6)), a 100% increase of A^* at room temperature will only cause an increase of 0.018 eV in ϕ_B .^[49] A correction of the previously calculated barrier heights with the newly determined Richardson constant would therefore barely impact the result.

As shown in Figure 6d, the current follows an Arrhenius-type^[65] temperature dependence at all voltages according to

$$\frac{V}{R_p} = A \times e^{-\frac{E_A}{k_B T}} \quad (13)$$

where A is the pre-exponential factor and E_A is the activation energy. The temperature data can be fitted using a single linear

function, indicating only one activation energy for the entire temperature range investigated here. This indicates the presence of a single potential barrier.

From the inset in Figure 6d, it can be seen that the activation energy decreases with increasing applied voltage which may be due to the lowering of the potential barrier. The zero-field activation energy $E_A(E = 0) \approx 1.21$ eV can be calculated from Figure 6d.^[66,67] Since the investigations are in a stationary voltage and temperature range, the determined activation energies can be understood as the barrier height of a single potential barrier.

As the temperature increases, the band gap decreases along with the built-in potential. The reduction of the built-in potential affects the width of the SCR and thus causes an increase in capacitance with increasing temperature (Figure 6e, inset). Alternatively, the capacitance increase can be attributed to a change in the charge states of electron traps in HfO₂ following an SCR narrowing. This change would have a great influence on the SCR width due to the lack of charges. This last hypothesis is the most probable since indications of surface states can already be found in the voltage-dependent capacitance characteristics.

3.3. Verification of ImpSpec Parameters

Since a derivation of the results from an AC to DC configuration is valid for the EC elements of the serial resistor and the diode, a first model can be created from the previous analysis. Since the previously shown $I - V$ curve (Figure 2b) already shows a diode reach-through due to the high reverse current, the diode model with serial resistance is extended by the dimensionless transfer coefficient α .^[41] This transfer coefficient is then fitted by the quasi-static $I - V$ curve. The resulting current of this model is described as:

$$I = I_s \times \left(e^{\frac{\alpha(V - (R_s I)q)}{nk_B T}} - e^{-\frac{(1 - \alpha)(V - (R_s I)q)}{nk_B T}} \right) \quad (14)$$

The reverse current I_s is defined in Equation (5). For the fit of the static $I - V$ curve, the parameter α is varied in the range $0 < \alpha < 1$, while R_s and n are set to 12 k Ω and 3.71, respectively, as previously determined from the ImpSpec-analysis. From the static $I - V$ curve, we focus on the data recorded in the LRS (Figure 7) as they allow for a wider range of positive voltage values to be used for fitting without considering the memristive set behavior, which is not implemented in this model. From the fit, shown in Figure 7, a reach-through parameter of 0.77 can be determined. A fit of the data presented in Figure 7, taking into account an additional current transport by thermionic-field emission in addition to the assumed transport by thermionic emission, according to Rideout,^[40] showed no agreement. Thus, we can conclude that the fitted ideality factor refers to a generation of charge carriers within an SCR and not to the division of the current between thermionic emission and thermionic-field emission.

An adequate description of the charge carrier transport for stationary states of the device is obtained by fitting with the function described in Equation (14), thus confirming that the current is dominated by a diode interface for the DC case. In

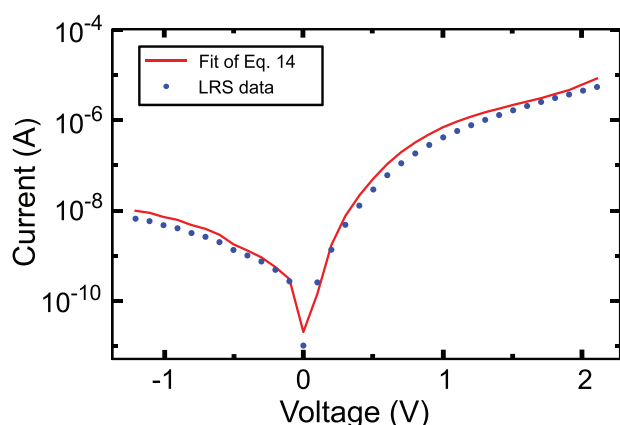


Figure 7. Fit of the quasi-static $I - V$ curve of the LRS of a memristive device with Equation (14) and extracted ImpSpec parameters in a semi-logarithmic plot.

addition, we are able to determine a reach-through parameter that, together with the ideality factor, provides information about the imperfection of this diode.

To further characterize the memristive device, a deeper understanding of the switching mechanism is required, as discussed in the following section.

3.4. Non-Stationary Analysis

Applying a voltage above 1 V can cause a resistance change in the memristive device. A distinction is made between a short and long-term resistance change. Hansen et al.^[28] attribute a short-term change in the state of a similar device to charging and discharging of interfacial trap states, while long-term retention is associated with ionic motion.

To gain insight into the mechanisms involved in the non-stationary region, two different DC voltages (1.2 and 2.1 V) are applied to the device in the HRS while ImpSpec is carried out at 1 s intervals. Such a TR-ImpSpec has two main advantages. First, slow time constants that would otherwise be outside the detection range can be resolved since slow kinetic processes are not able to follow the frequencies. Second, saturation processes can be tracked. This methodology allows a combined investigation in the frequency and time domain within a single measurement.

The impedance spectra presented in **Figure 8** indicate a change in the differential resistance R_p for a low setting voltage (1.2 V) measured after applying the voltage bias 1 and 30 s. The complex plane plot of higher setting voltage (2.1 V) shows a second semicircle with a positive imaginary part, which is often misleadingly referred to in the literature as an “inductive” feature and therefore called “inductive loop.”^[68] Splitting the impedance characteristics into quadrants shows that the additionally occurring time constant τ_{mem} must be considerably smaller than that of the already observed Schottky-like interface. From the part of the impedance with a positive phase shift, a transition to a smaller total resistance can be obtained, starting with a time constant of $\tau_{mem} = 10^{-2}$ s going down to 10^{-4} s after roughly one second at 2.1 V.

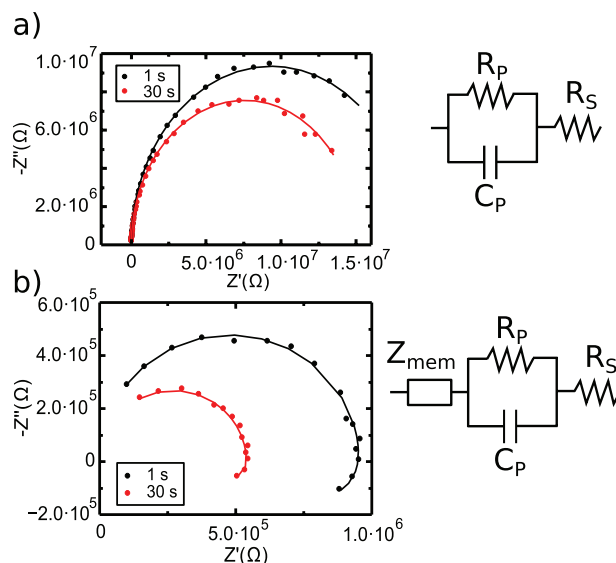


Figure 8. Nyquist TR-ImpSpec graphs showing an “inductive” loop after applying a) 1.2 V for 1 and 30 s, and b) 2.1 V for 1 and 30 s.

Such impedance behavior is often found in memristive device analyses, regardless of whether they display binary or analog switching,^[8–10] and is most commonly attributed to memristive switching. The “inductive” loop decreases when the memristive devices change from the HRS to LRS. Such behavior can be seen in the TR-ImpSpec of the examined memristive device. Usually, the additional semicircle in memristive devices is explained as an inductivity^[68] or mem-inductivity.^[9] However, inductance in such memristive thin-film systems is inconceivable, simply because of the geometric conditions. Implementing windings of an inductance of corresponding size (>10 mH), in a multi-layer system of about 10 nm thickness, is physically impossible.

A much more appropriate assumption was made by Taibl et al.^[19] who studied epitaxial SrTiO₃ thin films (100–413 nm) at temperatures between 325 and 700 °C employing ImpSpec. In this work, an “inductive” loop is found which affects the overall resistance of the thin film and shows a dependency on the applied DC-bias. Taibl et al. discuss an additional impedance feature showing as a semicircle in the complex plane plot as a frequency-dependent transport process of charged carriers that is responsible for a varying resistance Z_{mem} , which can either be positive or negative depending on the resistance change direction.^[19] Like every transport process, this follows the Boltzmann equation and consists of a resistance R_{mem} and a capacitance C_{mem} , needed to mathematically model this slower process. Consequently, the RC element must have a negative sign if it is used for the modeling of the “inductive” loop. The transfer function of this slow resistance changing process can be defined as:

$$F(\omega) = \frac{1}{1 + j\omega C_{mem} R_{mem}} \quad (15)$$

Thus, an “inductive” loop can be defined as a decrease in resistance over time under an applied voltage that follows slow frequencies, and in our case describes the kinetics of the

slow setting process. Bou and Bisquert^[11] already predicted the existence of a time-dependent resistance reduction in their memristive device modeling approach together with three different general EC memristor models, which are analogous to the assumptions made by Taibl et al. The model developed in this work is in agreement with both aforementioned models but extended by the sensitive Schottky-like interface and a geometric capacitance. Similar to the stationary analysis, the Schottky-like contact is affected by device switching. It is therefore evident that the RC element of the Z_{mem} slow process is in series with the Schottky-like contact. As a result, the EC diagram, created with the results of the stationary impedance measurement, can be expanded by adding Z_{mem} , represented by an additional RC element (see Figure 8). The extended EC is thus close to an EC developed by Yan et al. in 2010,^[69] which describes the memristive switching of a binary switching memristive device with an additional RC-Element. However, the interpretation and relevance of the individual EC elements is somewhat different, since Yan et al. analyzed a filamentary switching memristive device ion movement as memristive cause.^[69]

To gain further insights into the physical processes related to Z_{mem} , an additional modified TR-ImpSpec measurement is carried out. For this measurement, a device in the HRS is used and set to the LRS, while impedance measurements are acquired under different bias voltages. As sketched in Figure 9, the measurement series consists of 30 alternating read (0.6 V_{bias}/1.8 s) and set measurements (2.1 V_{bias}/0.3 s), starting with a read measurement to determine the initial state (HRS) of the device.

In addition to the time-dependent resistance reduction occurring at low frequencies, two further time constants of the

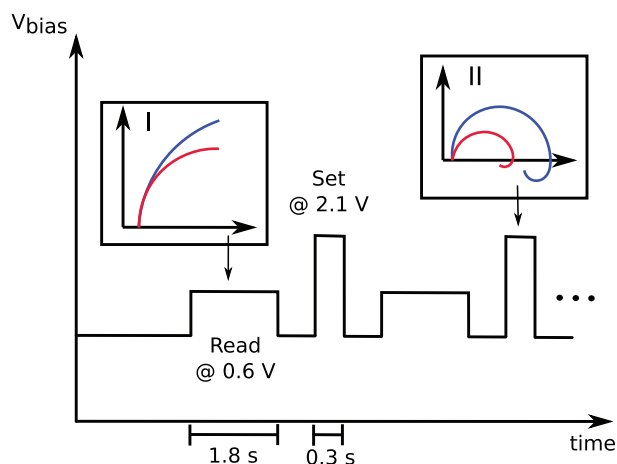


Figure 9. Principle sketch of the measurement sequence of a TR-ImpSpec experiment for a read voltage (0.6 V) and a set voltage (2.1 V). I) Sketch of the impedance data of the read voltage which show a single time constant with negative phase shift, while (II) sketch of the impedance data of the set voltage reveal a further time constant with positive phase shift. The blue curve describes the beginning of the measurement sequence (start interval), whereas the red curve describes a later interval of the sequence. A total of 13 measurement points were recorded for the set voltage and another 13 measurement points for the read voltage. A visualization of the impedance data together with the fits can be found in Supporting Information S5.

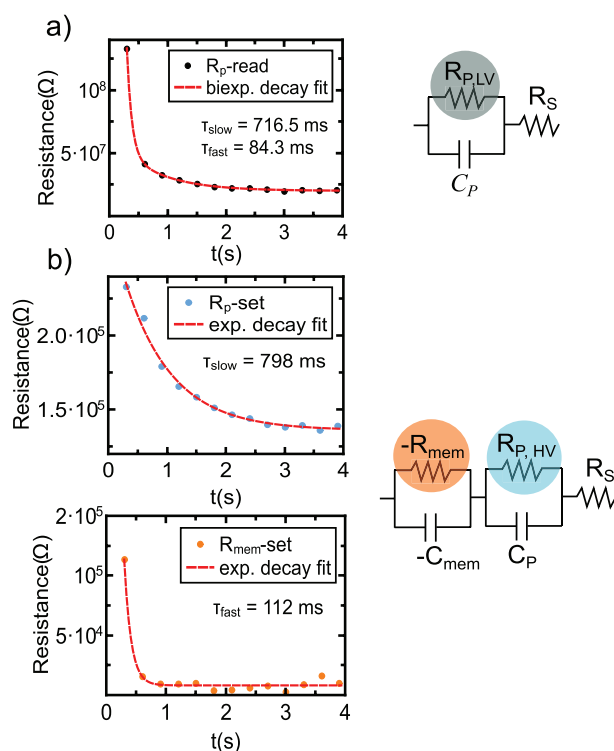


Figure 10. Resistance decay over time extracted from TR-ImpSpec and displayed in a semi-logarithmic plot. The measurement sequence consists of 15 set pulses, each combined with a read pulse. a) $R_{p,LV}$ resistance change at 0.6 V over time fitted with a second order exponential decay (red) for the corresponding EC. b) $R_{p,HV}$ and $-R_{mem}$ variation over time at 2.1 V fitted with a first order exponential decay for the corresponding EC.

setting mechanism can be identified. These can be determined by transient analysis of the impedance spectra at set and read voltages. In addition, this method can be used to obtain information about the arrangement of the EC elements. Thus, a serial arrangement of the memristive elements in the EC can be directly inferred instead of a parallel one. The impedance data of the EC element $R_{p,LV}$ captured during the lower read voltage (LV) of the TR-ImpSpec sequence follows a second-order exponential decay over time (Figure 10a),

$$\gamma = \gamma_0 + a_1 \frac{-x}{\tau_{slow,LV}} + a_2 \frac{-x}{\tau_{fast,LV}} \quad (16)$$

where the time constants $\tau_{slow,LV} = 716$ ms and $\tau_{fast,LV} = 84$ ms can be extracted from the transient analysis. For the set voltage, the previously mentioned feature of a positive phase shift for low frequencies can be observed (Figures 8 and 9). Therefore, the EC is further extended by the RC term defined in Equation (15). The transients of the two EC elements $-R_{mem}$ and $R_{p,HV}$ measured at a higher set voltage (HV) can be fitted by a first-order exponential decay.

$$\gamma = \gamma_0 + a \frac{-x}{\tau} \quad (17)$$

The two time constants $\tau_{fast,HV} = 112$ ms and $\tau_{slow,HV} = 798$ ms are derived from $-R_{mem}$ and $R_{p,HV}$ in the transient analyses

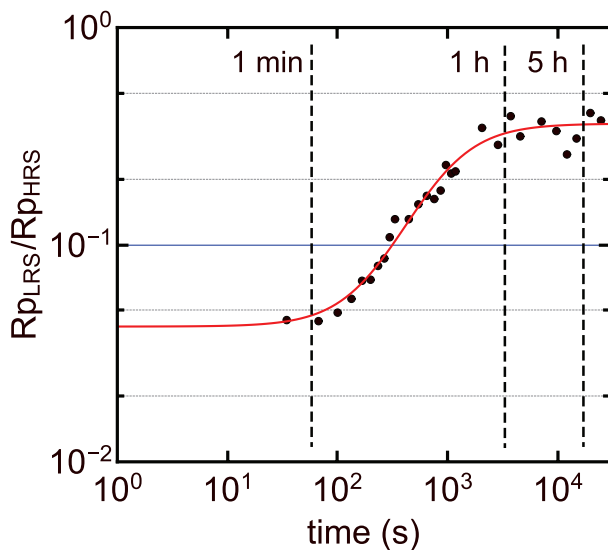


Figure 11. Retention measurement at 500 mV for the status sensitive differential resistance R_p over a period of 8 h displayed in a double logarithmic plot, and fitted with a biexponential growth.

(Figure 10b). These results match the quasi-static $I - V$ measurements of the memristive devices, where the voltage ramp time changes from 4.8 V s^{-1} to 480 mV s^{-1} , strongly influencing the magnitude of the switching process (Figures S3 and S4, Supporting Information).

A comparison of the transient analyses for the read and set measurements show excellent agreement between the determined time constants $\tau_{\text{fast}, \text{HV}}$ and $\tau_{\text{fast}, \text{LV}}$, as well as $\tau_{\text{slow}, \text{HV}}$ and $\tau_{\text{slow}, \text{LV}}$. This shows that an increased voltage makes it possible to separate two processes occurring at lower voltages and combined within $R_{p, \text{LV}}$.

Retention measurements are conducted to relate the time constants of the set process to the resetting of the device back to its initial state. For these measurements, the initial HRS of the memristive device is first determined, before setting the device in the LRS using a positive voltage ramp. Subsequently, the temporal state change is studied with a 0.5 V read pulse. The change in the $R_{p, \text{LRS}} / R_{p, \text{HRS}}$ ratio over time during the reset process is shown in **Figure 11**.

From the biexponential fit of the retention measurements, two time constants $\tau_1 = 133 \text{ s}$ and $\tau_2 = 896 \text{ s}$ are determined. When comparing the time constants for the set processes ($\tau_{\text{set}, \text{fast}}$) and ($\tau_{\text{set}, \text{slow}}$) and the back drift (τ_1) and (τ_2), the same scale factor of three orders of magnitude lies between the respective processes (**Table 2**). This suggests that both the slow and fast set process are caused by similar phenomena.

Since indications of surface states were found in the capacitance analysis of the impedance, the measured time constants are assigned to electron traps. The time constants for

Table 2. Extracted time constants from transient analysis of set and back drift process.

Constants	LV _{set} [ms]	HV _{set} [ms]	Retention [s]
τ_{slow}	716	798	896
τ_{fast}	84	112	133

the electron discharging from defects at an energy E_t below the conduction band E_C can be described using the Shockley–Read–Hall model^[70] as follows:^[71]

$$\tau_e = \frac{1}{N_C \sigma v_{th}} \exp\left(\frac{E_C - E_t}{k_B T}\right) \quad (18)$$

with N_C as effective density of states, σ as capture cross section, and v_{th} as average carrier thermal velocity.

A twofold time constant in a current transient for discharging of electron traps was previously reported for Si/SiO_x junctions.^[72] The existence of two time constants for switching into the LRS and drifting back into the HRS can be attributed to an energetic and spatial distribution of electron traps.^[73] The same scale factor between the two-time constants for switching and drifting back suggests that the electron traps can be separated into two types, with different discharging prefactors and the same exponential factors. Since both the density of states and the thermal velocity of the charge carriers can be assumed to be constant at the same temperature, this observation can be attributed to a change in the capture cross section. Possible spatial distribution of electron traps between bulk HfO₂ and the HfO₂/Al₂O₃ interface would affect the capture cross section and thus lead to a dispersion of the time constants for the capture and discharging of electrons. If the expected electron trap depth is determined from the retention measurement using Equation (18) with the following parameters: $N_C = 10^{19} \text{ cm}^{-3}$,^[74] $\sigma = 1.8 \times 10^{-14} \text{ cm}^2$,^[75] $2.4 \times 10^{-15} \text{ cm}^2$,^[76] $v_{th} = 3.7 \times 10^7 \frac{\text{cm}}{\text{s}}$,^[77] two different electron trap capture cross sections are assumed for the switching processes in the HfO₂ layer. The electron traps with $\sigma_B = 1.8 \times 10^{-14} \text{ cm}^2$ are expected to be located in the bulk of the HfO₂ and are responsible for a short storage time, while the traps with $\sigma_I = 2.4 \times 10^{-15} \text{ cm}^2$ are supposed to be located at the interface with the Al₂O₃ and maintain the state over a longer time scale. An evaluation of the amplitudes of the biexponential fits shows a clear majority of the traps located in the bulk with a 4 to 1 ratio compared to the interface traps. This conclusion assumes spatial non-uniformity and does not consider spatial energetic non-uniformity. A trap depth of about 0.89 eV, which is between those of 0.6 and 1 eV previously reported for HfO₂-based memristive devices,^[16] can be directly correlated to double positively charged ($V_O^{+2} \approx 0.9 \text{ eV}$) oxygen vacancies.^[78] The formation of such defects in the HfO₂ can potentially be explained by high energetic negatively charged oxygen ions in the sputter process plasma,^[79] with a density of $\rho \approx 10^{19} \text{ cm}^{-3}$ in the physical vapour deposition processes.^[80]

Furthermore, the consistency with the Shockley–Read–Hall model (Equation (18)) indicates an exponential dependence of the Boltzmann factor, which would not be expected according to Fick's diffusion laws for the movement of ions.^[81]

The conclusion of this ImpSpec study and the proposed physical model are in good agreement with those of the companion paper Zahari et al.^[26] Both analyses provided strong evidence of electron trap charging and discharging being the cause of the memristive switching process and concluded on their influence on an SCR. Additionally, the spatial arrangement of the SCR and electron traps can be inferred from the results of Zahari et al.^[26] Since depth-resolved HAXPES measurements reported by Zahari et al.^[26] (Figure 5c) show an increase in the binding

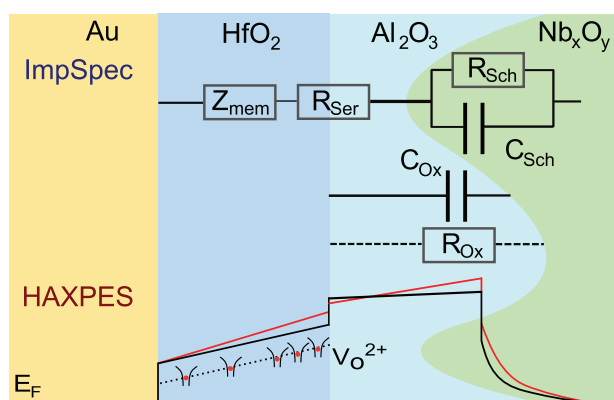


Figure 12. Model of the memristive device in terms of the spectroscopy methods used. Top: Complete EC of the memristive device in spatial order determined by ImpSpec. Bottom: Band diagram determined by HAXPES proposed by Zahari et al.^[26] (Figure 7).

energy of the HfO₂ layer toward the Au electrode, the formation of an SCR with an n-type semiconductor inside the HfO₂ can be excluded. TEM investigations reveal a mixture of Nb₂O₅ and NbO₂ in the partly oxidized back electrode (Figure 2a)), suggesting that the Schottky-like behavior described in detail in this work originates from the SCR located in the NbO_x. This is further reinforced by replacing the Nb with Hf, leading to significantly different *I*–*V* characteristics (Figure 6b in Zahari et al.^[26]).

Combining both observations lead to a physical model depicted in **Figure 12** along with a sketched band diagram of the memristive device. A rough Schottky-like transition at the NbO_x/Al₂O₃ provides a parallel superposition of the capacitances of the SCR and the bulk oxide. The flow of charge carriers through the double oxide layer is enabled by a large number of shunt resistors at thinner junction parts, which can be modeled as a serial linear ohmic component. *Z*_{mem} serves as a description of the differential resistance representing the charging and discharging of traps in the HfO₂, in turn influencing the space charge of the Schottky interface. The SCR in the NbO_x is affected by this net charge change in the HfO₂ layer and thus acts as an amplifier for the charging and discharging of electron traps. This can be described as a trap-assisted field effect that alters the Schottky barrier height. Thus, the existence of an SCR is necessary for a high LRS/HRS ratio in the switching behavior of such a memristive device. A possible further development of the memristive components described here, which with high probability also have a positive influence on the poor temperature stability, can be found in section 3.3 in Zahari et al.^[26]

4. Conclusions

In summary, we show that the ImpSpec analysis of memristive devices offers a comprehensive understanding of the state-sensitive interfaces and their functionalities. Using PD-ImpSpec at room temperature and under heating, a single barrier due to an imperfect Schottky contact is identified, with a SCR sensitive to the state of the device. Furthermore, we present evidence of electron traps by examining the capacitance

analysis and the interconnection between the time constants of switching states and relaxation, as a dependency on the Boltzmann factor is revealed.

The occurrence of an “inductive” loop in the non-stationary analysis is correlated to the switching state of the device. Employing TR-ImpSpec together with retention analysis, the kinetics of this state-switching process are described in more detail, revealing the contribution of two processes. The time constants ratio of these processes inferred a common trap depth or species (V_0^{2+}) with different capture cross sections. Therefore, trap-assisted field-effect altering the SCR is identified as the dominant switching mechanism for the HfO₂-based memristive device investigated here, which behaves like an amplifier for the charge state change of the traps. The ImpSpec results are in good agreement with the HAXPES and TEM experiments presented by Zahari et al.^[26] and combining both allows to construct a more complete picture of the physical process.

Supporting Information

Supporting Information is available from the Wiley Online Library or from the author.

Acknowledgements

This work was funded by the Deutsche Forschungsgemeinschaft (DFG, German Research Foundation)—Project number RU 2093 and Project-ID 434434223—SFB 1461. G.K. is thankful for a postdoctoral fellowship from the Alexander von Humboldt foundation.

Open access funding enabled and organized by Projekt DEAL.

Conflict of Interest

The authors declare no conflict of interest.

Data Availability Statement

The data that support the findings of this study are available from the corresponding authors upon reasonable request.

Keywords

analog memristive devices, combining methods, electron traps, impedance spectroscopy HfO₂

Received: November 11, 2022

Revised: February 10, 2023

Published online:

- [1] S. Nandakumar, S. R. Kulkarni, A. V. Babu, B. Rajendran, *IEEE Nanotechnol. Mag.* **2018**, 12, 19.
- [2] A. Sebastian, M. Le Gallo, R. Khaddam-Aljameh, E. Eleftheriou, *Nat. Nanotechnol.* **2020**, 15, 529.
- [3] G. W. Burr, R. M. Shelby, A. Sebastian, S. Kim, S. Kim, S. Sidler, K. Virwani, M. Ishii, P. Narayanan, A. Fumarola, L. L. Sanches,

- I. Boybat, M. Le Gallo, K. Moon, J. Woo, H. Hwang, Y. Leblebici, *Adv. Phys. X* **2017**, 2, 89.
- [4] D. V. Christensen, R. Dittmann, B. Linares-Barranco, A. Sebastian, M. Le Gallo, A. Redaelli, S. Slesazeck, T. Mikolajick, S. Spiga, S. Menzel, I. Valov, G. Milano, C. Ricciardi, S.-J. Liang, F. Miao, M. Lanza, T. J. Quill, S. T. Keene, A. Salleo, J. Grollier, D. Marković, A. Mizrahi, P. Yao, J. J. Yang, G. Indiveri, J. P. Strachan, S. Datta, E. Vianello, A. Valentian, J. Feldmann, et al., *Neuromorph. Comput. Eng.* **2022**, 2, 022501.
- [5] H.-S. P. Wong, S. Salahuddin, *Nat. Nanotechnol.* **2015**, 10, 191.
- [6] J. J. Yang, M. D. Pickett, X. Li, D. A. Ohlberg, D. R. Stewart, R. S. Williams, *Nat. Nanotechnol.* **2008**, 3, 429.
- [7] E. Barsoukov, J. R. Macdonald, 2nd ed., John Wiley & Sons, Hoboken, NJ **2005**.
- [8] J. D. Greenlee, W. L. Calley, M. W. Moseley, W. A. Doolittle, *IEEE Trans. Electron Devices* **2012**, 60, 427.
- [9] G. U. Kamble, N. P. Shetake, S. D. Yadav, A. M. Teli, D. S. Patil, S. A. Pawar, M. M. Karanjkar, P. S. Patil, J. C. Shin, M. K. Orlowski, et al., *Int. Nano Lett.* **2018**, 8, 263.
- [10] L. Qingjiang, A. Khia, I. Salaoru, C. Papavassiliou, X. Hui, T. Prodromakis, *Sci. Rep.* **2014**, 4, 4522.
- [11] A. Bou, J. Bisquert, *J. Phys. Chem. B* **2021**, 125, 9934.
- [12] R. Schmitt, M. Kubicek, E. Sediva, M. Trassin, M. C. Weber, A. Rossi, H. Hutter, J. Kreisel, M. Fiebig, J. L. M. Rupp, *Adv. Funct. Mater.* **2019**, 29, 1804782.
- [13] C. Gonzales, A. Guerrero, J. Bisquert, *Appl. Phys. Lett.* **2021**, 118, 073501.
- [14] N. Du, N. Manjunath, Y. Li, S. Menzel, E. Linn, R. Waser, T. You, D. Bürger, I. Skorupa, D. Walczyk, et al., *Phys. Rev. Appl.* **2018**, 10, 054025.
- [15] T. Chang, S.-H. Jo, K.-H. Kim, P. Sheridan, S. Gaba, W. Lu, *Appl. Phys. A* **2011**, 102, 857.
- [16] J. H. Yoon, S. J. Song, I.-H. Yoo, J. Y. Seok, K. J. Yoon, D. E. Kwon, T. H. Park, C. S. Hwang, *Adv. Funct. Mater.* **2014**, 24, 5086.
- [17] Y. Kim, Y. J. Kwon, D. E. Kwon, K. J. Yoon, J. H. Yoon, S. Yoo, H. J. Kim, T. H. Park, J.-W. Han, K. M. Kim, et al., *Adv. Mater.* **2018**, 30, 1704320.
- [18] S. Choi, Y. Kim, T. Van Nguyen, W. H. Jeong, K.-S. Min, B. J. Choi, *Adv. Electronic Mater.* **2021**, 2100050.
- [19] S. Taibl, G. Faflek, J. Fleig, *Nanoscale* **2016**, 8, 13954.
- [20] W. Choi, H.-C. Shin, J. M. Kim, J.-Y. Choi, W.-S. Yoon, *J. Electrochem. Sci. Technol.* **2020**, 11, 1.
- [21] S. Park, S. Klett, T. Ivanov, A. Knauer, J. Doell, M. Ziegler, *Front. Nanotechnol.* **2021**, 3, 29.
- [22] K. M. Kim, J. Zhang, C. Graves, J. J. Yang, B. J. Choi, C. S. Hwang, Z. Li, R. S. Williams, *Nano Lett.* **2016**, 16, 6724.
- [23] M. Hansen, F. Zahari, H. Kohlstedt, M. Ziegler, *Sci. Rep.* **2018**, 8, 8914.
- [24] S. Dirkmann, M. Hansen, M. Ziegler, H. Kohlstedt, T. Mussenbrock, *Sci. Rep.* **2016**, 6, 35686.
- [25] S. Yarragolla, T. Hemke, J. Trieschmann, F. Zahari, H. Kohlstedt, T. Mussenbrock, *J. Appl. Phys.* **2022**, 131, 134304.
- [26] F. Zahari, R. Marquardt, M. Kalläne, O. Gronenberg, C. Schlueter, Y. Matveyev, G. Haberehner, F. Diekmann, A. Nierhauve, J. Buck, A. Hanff, G. Kolhatkar, G. Kothleitner, L. Kienle, M. Ziegler, J. Carstensen, K. Rosnagel, H. Kohlstedt, *Adv. Electron. Mater.*, <https://doi.org/10.1002/aem.202201226>.
- [27] M. Hansen, F. Zahari, M. Ziegler, H. Kohlstedt, *Front. Neurosci.* **2017**, 11, 91.
- [28] M. Hansen, M. Ziegler, L. Kolberg, R. Soni, S. Dirkmann, T. Mussenbrock, H. Kohlstedt, *Sci. Rep.* **2015**, 5, 13753.
- [29] D.-j. Seong, M. Jo, D. Lee, H. Hwang, *Electrochem. Solid-State Lett.* **2007**, 10, H168.
- [30] D. Ielmini, R. Waser, *Resistive Switching: From Fundamentals of Nanoionic Redox Processes to Memristive Device Applications*, John Wiley & Sons, New York **2015**.
- [31] Y. Yang, R. Huang, *Nat. Electron.* **2018**, 1, 274.
- [32] G. Popkurov, R. Schindler, *Rev. Sci. Instrum.* **1992**, 63, 5366.
- [33] G. Popkurov, R. Schindler, *Electrochim. Acta* **1993**, 38, 861.
- [34] G. Popkurov, R. Schindler, *Electrochim. Acta* **1994**, 39, 2025.
- [35] J. Strobel, M. Hansen, S. Dirkmann, K. K. Neelisetty, M. Ziegler, G. Haberehner, R. Popescu, G. Kothleitner, V. S. K. Chakravadhanula, C. Kübel, et al., *J. Appl. Phys.* **2017**, 121, 245307.
- [36] M. S. Abouzari, F. Berkemeier, G. Schmitz, D. Wilmer, *Solid State Ionics* **2009**, 180, 922.
- [37] A. Lasia, in *Modern Aspects of Electrochemistry*, Springer, **2002**, pp. 143–248.
- [38] S. Cheung, N. Cheung, *Appl. Phys. Lett.* **1986**, 49, 85.
- [39] S. M. Sze, Y. Li, K. K. Ng, *Physics of Semiconductor Devices*, John Wiley & Sons, New York **2021**.
- [40] V. Rideout, *Solid-State Electron.* **1975**, 18, 541.
- [41] A. J. Bard, L. R. Faulkner, J. M. Loayza, *Electrochem. Meth.* **2001**, 2, 96.
- [42] J. H. Werner, H. H. Güttler, *J. Appl. Phys.* **1991**, 69, 1522.
- [43] S. Chand, J. Kumar, *J. Appl. Phys.* **1997**, 82, 5005.
- [44] S. Chand, J. Kumar, *Semicond. Sci. Technol.* **1997**, 12, 899.
- [45] R. Schmitsdorf, W. Mönch, *Eur. Phys. J. B* **1999**, 7, 457.
- [46] H. von Wenckstern, G. Biehne, R. A. Rahman, H. Hochmuth, M. Lorenz, M. Grundmann, *Appl. Phys. Lett.* **2006**, 88, 092102.
- [47] A. Bhuiyan, A. Martinez, D. Esteve, *Thin. Solid Films* **1988**, 161, 93.
- [48] R. Hackam, P. Harrop, *IEEE Trans. Electron Devices* **1972**, 19, 1231.
- [49] S. M. Sze, Y. Li, K. K. Ng, *Physics of Semiconductor Devices*, John Wiley & Sons, New York **2021**.
- [50] J. Van Otterloo, L. Gerritsen, *J. Appl. Phys.* **1978**, 49, 723.
- [51] S.-M. Kang, Y. Leblebici, *CMOS Digital Integrated Circuits*, Tata McGraw-Hill Education, New York **2003**.
- [52] V. Milovanović, H. Zimmermann, in *2012 28th Int. Conf. on Microelectronics Proc.*, IEEE, Piscataway, NJ **2012**, pp. 73–76.
- [53] M. Green, J. Shewchun, *J. Appl. Phys.* **1975**, 46, 5185.
- [54] P. Chattopadhyay, B. Raychaudhuri, *Solid-State Electron.* **1993**, 36, 605.
- [55] N. C. Bruce, A. García-Valenzuela, D. Kouznetsov, *J. Phys. D: Appl. Phys.* **1999**, 32, 2692.
- [56] A. Tataroglu, H. Tanrikulu, E. Tanrikulu, A. B. Uluşan, et al., *Indian J. Pure Appl. Phys. (IJPAP)* **2018**, 56, 142.
- [57] Z. Xiaoling, L. Fei, L. Changzhi, X. Xuesong, L. Ying, S. Mohammad, *J. Semiconductors* **2009**, 30, 034001.
- [58] C. Crowell, S. Sze, W. Spitzer, *Appl. Phys. Lett.* **1964**, 4, 91.
- [59] J. H. Werner, H. H. Güttler, *J. Appl. Phys.* **1993**, 73, 1315.
- [60] J. Tersoff, *Phys. Rev. Lett.* **1984**, 52, 465.
- [61] A. Jadhav, L. A. Lyle, Z. Xu, K. K. Das, L. M. Porter, B. Sarkar, *J. Vac. Sci. Technol., B: Nanotechnol. Microelectron.: Mater., Process., Meas., Phenom.* **2021**, 39, 040601.
- [62] Y. P. Varshni, *Physica* **1967**, 34, 149.
- [63] Y. Sakai, N. Tsuda, T. Sakata, *J. Phys. Soc. Jpn.* **1985**, 54, 1514.
- [64] W. Mtangi, F. D. Auret, C. Nyamhere, P. J. van Rensburg, A. Chawanda, M. Diale, J. M. Nel, W. E. Meyer, *Phys. B* **2009**, 404, 4402.
- [65] K. J. Laidler, *J. Chem. Educ.* **1984**, 61, 494.
- [66] L. Kungumadevi, K. Rajasekar, A. Subbarayan, R. Sathyamoorthy, *Ionics* **2008**, 14, 63.
- [67] O. Mitrofanov, M. Manfra, *J. Appl. Phys.* **2004**, 95, 6414.
- [68] D. Klotz, *Electrochem. Commun.* **2019**, 98, 58.
- [69] X. Yan, Y. Xia, H. Xu, X. Gao, H. Li, R. Li, J. Yin, Z. Liu, *Appl. Phys. Lett.* **2010**, 97, 112101.
- [70] W. Shockley, W. Read Jr, *Phys. Rev.* **1952**, 87, 835.
- [71] M. Miczek, C. Mizue, T. Hashizume, B. Adamowicz, *J. Appl. Phys.* **2008**, 103, 104510.
- [72] T. Wang, T. Chang, L. Chiang, C. Huang, *IEEE Electron Device Lett.* **1996**, 17, 398.
- [73] A. Balasinski, J. Worley, K. Huang, J. Walters, F. Liou, *IEEE Electron Device Lett.* **1995**, 16, 460.

- [74] C. Künneth, R. Batra, G. A. Rossetti Jr., R. Ramprasad, A. Kersch, in *Ferroelectricity in Doped Hafnium Oxide: Materials, Properties and Devices*, Elsevier, Amsterdam **2019**, pp. 245–289.
- [75] C. Zhao, J. Zhang, M. Zahid, B. Govoreanu, G. Groeseneken, S. De Gendt, *J. Appl. Phys.* **2006**, *100*, 093716.
- [76] F.-C. Chiu, *Adv. Mater. Sci. Eng.* **2013**, *2013*, 71.
- [77] S. Monaghan, P. Hurley, K. Cherkaoui, M. Negara, A. Schenk, *Solid-State Electron.* **2009**, *53*, 438.
- [78] P. Broqvist, A. Pasquarello, *Appl. Phys. Lett.* **2006**, *89*, 262904.
- [79] F. Zahari, F. Schlichting, J. Strobel, S. Dirkmann, J. Cipo, S. Gauter, J. Trieschmann, R. Marquardt, G. Haberfehlner, G. Kothleitner, L. Kienle, T. Mussenbrock, M. Ziegler, H. Kersten, H. Kohlstedt, *J. Vac. Sci. Technol., B: Nanotechnol. Microelectron.: Mater., Process., Meas., Phenom.* **2019**, *37*, 061203.
- [80] X. Wang, K. Han, W. Wang, X. Ma, D. Chen, J. Zhang, J. Du, Y. Xiong, A. Huang, *Appl. Phys. Lett.* **2010**, *97*, 062901.
- [81] T. R. Yu, *Chemistry of Variable Charge Soils*, Oxford University Press, Oxford **1997**.

Appendix

Complete list of publications	147
Eidesstattliche Erklärung	149

Complete List of Publications

1. Zahari, F., Schlichting, F., Strobel, J., Dirkmann, S., Cipo, J., Gauter, S., Trieschmann, J., **Marquardt, R.**, Haberfehlner, G., Kothleitner, G., Kienle, L., Mussenbrock, T., Ziegler, M., Kersten, H., Kohlstedt, H.; Correlation between sputter deposition parameters and I-V characteristics in double-barrier memristive devices. *Journal of Vacuum Science and Technology B* 1 November 2019; 37 (6): 061203. <https://doi.org/10.1116/1.5119984>
2. **Marquardt, R.**, Cipo, J., Schlichting, F., Kolhatkar, G., Kohlstedt, H., Kersten, H.; Correlation between properties of direct current magnetron sputtered thin niobium nitride films and plasma parameters, *Thin Solid Films*, Volume 742, 2022, 139046, ISSN 0040-6090, <https://doi.org/10.1016/j.tsf.2021.139046>
3. Gronenberg, O., **Marquardt, R.**, Lamprecht, R., Ekici, Y., Schürmann, U., Kohlstedt, H., Kienle, L.; The impact of rapid thermal annealing for the ferroelectricity of undoped sputtered HfO₂ and its wake-up effect. *Journal of Applied Physics* 7 September 2022; 132 (9): 094101. <https://doi.org/10.1063/5.0100562>
4. Zahari, F., **Marquardt, R.**, Kalläne, M., Gronenberg, O., Schlueter, C., Matveyev, Y., Haberfehlner, G., Diekmann, F., Nierhauve, A., Buck, J., Hanff, A., Kolhatkar, G., Kothleitner, G., Kienle, L., Ziegler, M., Carstensen, J., Rossnagel, K., Kohlstedt, H., Trap-Assisted Memristive Switching in HfO₂-Based Devices Studied by In Situ Soft and Hard X-Ray Photoelectron Spectroscopy. *Adv. Electron. Mater.* 2023, 0, 2201226. <https://doi.org/10.1002/aelm.202201226>
5. **Marquardt, R.**, Zahari, F., Carstensen, J., Popkirov, G., Gronenberg, O., Kolhatkar, G., Kohlstedt, H., Ziegler, M., Impedance Spectroscopy

on Hafnium Oxide-Based Memristive Devices. *Adv. Electron. Mater.* 2023, 0, 2201227. <https://doi.org/10.1002/aelm.202201227>

6. **Marquardt, R.**, Petersen, D., Gronenberg, O., Zahari, F., Lamprecht, R., Popkirov, G., Carstensen, J., Kienle, K., and Kohlstedt, H., Domain Wall Movement in Undoped Ferroelectric HfO₂: A Rayleigh Analysis. *ACS Applied Electronic Materials* 2023, 5, 6, 3251–3260. <https://doi.org/10.1021/acsaelm.3c00336>

Eidesstattliche Erklärung

Hiermit erkläre ich:

Diese Dissertation mit dem Titel “Hafnium dioxide for memristive applications“ habe ich noch nie, weder ganz noch teilweise im Rahmen eines anderen Promotionsverfahrens vorgelegt oder veröffentlicht. Ich habe mich bislang noch keiner mündlichen Prüfung im Rahmen eines Promotionsverfahrens unterzogen. Die vorliegende Arbeit habe ich ohne unzulässige Hilfe Dritter und ohne Benutzung anderer als der angegebenen Hilfsmittel angefertigt; die aus fremden Quellen direkt oder indirekt übernommenen Gedanken sind als solche kenntlich gemacht. Die Arbeit ist unter Einhaltung der Regeln guter wissenschaftlicher Praxis der Deutschen Forschungsgemeinschaft entstanden. Bei der Auswahl und Auswertung des Materials sowie bei der Herstellung des Manuskripts habe ich nur Unterstützungsleistungen meines Betreuers erhalten. Weitere Personen waren an der geistigen Herstellung der vorliegenden Arbeit nicht beteiligt. Insbesondere habe ich nicht die Hilfe eines Promotionsberaters in Anspruch genommen. Dritte haben von mir weder unmittelbar noch mittelbar geldwerte Leistungen für Arbeiten erhalten, die im Zusammenhang mit dem Inhalt der vorgelegten Dissertation stehen.

Kiel, den

Richard Volker Marquardt